Sandia National Laboratories

Operated for the United States Department of Energy
by National Technology and Engineering
Solutions of Sandia, LLC.

P.O. Box 5800
Albuquerque, NM 87185-0101

Phone: (615) 318-5284
Email: jhoganc@sandia.gov

Joshua Hogancamp, PhD
Postdoctoral Appointee

August 23, 2018

Dear: Huan Li

Subject: ***A Detailed Assessment of the Finite Element Analysis of Reinforced Concrete Structures Impacted by Large Missiles***

This letter report fulfills the final commitment for JCN N6741, "Aircraft Impact Assessment Research to Support the CSNI/NEA (Committee on the Safety of Nuclear Installations / Nuclear Energy Agency) Project." This report is required as dictated in the Statement of Work, Section 8. This report constitutes the final deliverable from Sandia National Laboratories to the US Nuclear Regulatory Commission for JCN N6741.

Attachment I documents the culmination of the research conducted for JCN N6741 and is captured in a draft NUREG/CR format. Attachment I references all relevant information, research, analyses, and conclusions pertaining to JCN N6741 from Sandia National Laboratories

Sincerely,

Joshua Hogancamp, PhD
Sandia National Laboratories
Org. 8853
Structural & Thermal Analysis

List of Recipients: Hernando Candra (NRC), Huan Li (NRC), Patrick Mattie (SNL), Joshua Hogancamp (SNL)

Attachment I: Draft Report for Program IRIS: Improving the Robustness of the Assessment of Structures Impacted by a Large Missile

Sandia National Laboratories is a multimission laboratory managed and operated by National Technology & Engineering Solutions of Sandia, LLC, a wholly owned subsidiary of Honeywell International Inc., for the U.S. Department of Energy's National Nuclear Security Administration under contract DE-NA0003525. SAND#TBD

National Nuclear Security Administration
U.S. DEPARTMENT OF ENERGY NNSA

Exceptional Service in the National Interest

Sandia National Laboratories

U.S.NRC
United States Nuclear Regulatory Commission
Protecting People and the Environment

NUREG-XXXX

Draft Report for Program IRIS: Improving the Robustness of the Assessment of Structures Impacted by a Large Missile

[Comments]

Sandia National Laboratories

AVAILABILITY OF REFERENCE MATERIALS IN NRC PUBLICATIONS

NRC Reference Material

As of November 1999, you may electronically access NUREG-series publications and other NRC records at the NRC's Public Electronic Reading Room at http://www.nrc.gov/reading-rm.html. Publicly released records include, to name a few, NUREG-series publications; *Federal Register* notices; applicant, licensee, and vendor documents and correspondence; NRC correspondence and internal memoranda; bulletins and information notices; inspection and investigative reports; licensee event reports; and Commission papers and their attachments.

NRC publications in the NUREG series, NRC regulations, and Title 10, "Energy," in the *Code of Federal Regulations* may also be purchased from one of these two sources.

1. **The Superintendent of Documents**
   U.S. Government Publishing Office
   Mail Stop SSOP
   Washington, DC 20402-0001
   Internet: http://bookstore.gpo.gov
   Telephone: 1-866-512-1800
   Fax: (202) 512-2104

2. **The National Technical Information Service**
   5301 Shawnee Road
   Alexandria, VA 22161-0002
   http://www.ntis.gov
   1-800-553-6847 or, locally, (703) 605-6000

A single copy of each NRC draft report for comment is available free, to the extent of supply, upon written request as follows:

U.S. Nuclear Regulatory Commission
Office of Administration
Publications Branch
Washington, DC 20555-0001
E-mail: distribution.resource@nrc.gov
Facsimile: (301) 415-2289

Some publications in the NUREG series that are posted at the NRC's Web site address http://www.nrc.gov/reading-rm/doc-collections/nuregs are updated periodically and may differ from the last printed version. Although references to material found on a Web site bear the date the material was accessed, the material available on the date cited may subsequently be removed from the site.

Non-NRC Reference Material

Documents available from public and special technical libraries include all open literature items, such as books, journal articles, transactions, *Federal Register* notices, Federal and State legislation, and congressional reports. Such documents as theses, dissertations, foreign reports and translations, and non-NRC conference proceedings may be purchased from their sponsoring organization.

Copies of industry codes and standards used in a substantive manner in the NRC regulatory process are maintained at—

The NRC Technical Library
Two White Flint North
11545 Rockville Pike
Rockville, MD 20852-2738

These standards are available in the library for reference use by the public. Codes and standards are usually copyrighted and may be purchased from the originating organization or, if they are American National Standards, from—

American National Standards Institute
11 West 42nd Street
New York, NY 10036-8002
http://www.ansi.org
(212) 642-4900

Legally binding regulatory requirements are stated only in laws; NRC regulations; licenses, including technical specifications; or orders, not in NUREG-series publications. The views expressed in contractor-prepared publications in this series are not necessarily those of the NRC.

The NUREG series comprises (1) technical and administrative reports and books prepared by the staff (NUREG-XXXX) or agency contractors (NUREG/CR-XXXX), (2) proceedings of conferences (NUREG/CP-XXXX), (3) reports resulting from international agreements (NUREG/IA-XXXX), (4) brochures (NUREG/BR-XXXX), and (5) compilations of legal decisions and orders of the Commission and Atomic and Safety Licensing Boards and of Directors' decisions under Section 2.206 of NRC's regulations (NUREG-0750).

U.S.NRC
United States Nuclear Regulatory Commission
Protecting People and the Environment

NUREG-XXXX

Draft Report for Program IRIS: Improving the Robustness of the Assessment of Structures Impacted by a Large Missile

[Comments]

Manuscript Completed:
Date Published:

SNL Contributors:
Joshua Hogancamp
Jonathan Rath
Stewart Silling
Jason Petti
John Bignell
Christopher Jones
Michael Hessheimer

Sandia National Laboratories
1515 Eubank SE
Albuquerque, NM 87123

NRC Contributors:
Syed Ali
Richard Rivera-Lugo
Hernando Candra

US Nuclear Regulatory Commission
11555 Rockville Pike
Rockville, Maryland 20852

Sandia National Laboratories

ABSTRACT

This document consolidates the work performed by Sandia National Laboratories and the US Nuclear Regulatory Commission in participation of Program IRIS: "Improving the Robustness of the Assessment Methodologies for Structures Impacted by Missiles". Three round-robin benchmark exercises on improving the robustness of the assessment of structures impacted by large missiles at medium to high velocities were organized by either the IAGE Subgroup on Ageing of Concrete Structures of the Organization for Economic Co-operation and Development Nuclear Energy Agency (NEA) or Électricité de France (EDF). The objectives of the exercises were to develop guidance for conducting impact analyses including issues related to computer codes, modeling approaches, and analysis techniques. The full project was comprised of three phases: Phase I, impact of walls; Phase II, impact of larger structures; and Phase III, transmission of shock and vibration to internal components.

The portions pertaining to Phase I describe in detail the numerical simulations and comparisons to existing experimental data of three impact scenarios involving a steel missile striking a concrete target heavily reinforced with steel bars. The first impact modeling scenario was related to the Meppen test (II-4) performed in Germany in 1980 (Brandes 1988), (Meppen 2010), and the two other simulations were related to two different tests performed at the VTT facility (VTT 2012): flexural and punching. The final numerical model for each of the three Phase I impact scenarios were constructed using finite element meshes of each structural component (*i.e.,* target, reinforcing steel, and missile). All Phase I impact scenario calculations were performed using the LS-DYNA finite element analysis code (LSTC, LS-DYNA 2011).

The portions pertaining to Phase II describe analyses and numerical results obtained from simulations of a steel missile impacting a concrete target reinforced with steel bars using two different computer codes: LS-DYNA and EMU. Phase II of the IRIS program was implemented to continue the activity developed in Phase I. The objectives were as follows:

- To give the opportunity to IRIS 2010 participants (plus newcomers) to update and improve the simulations with the knowledge of the test results and with the experience gained by one's own 1st computation and by others' computations using a single set of material properties;
- To give the opportunity to each participant to develop, test, and share the means and tools for alternative approaches ("simplified models");
- To gather all the results from the new simulations and all the proposals of simplified models and to issue a new set of recommendations.

This section introduces the two different numerical analyses, define the three test conditions, compare and contrast several numerical code simulation results of the three tests, and discuss the advantages and limitation of each computational approach.

The portions pertaining to Phase III describe analyses and numerical results obtained from simulations of a hollow steel missile impacting a concrete target reinforced with steel bars. Phase III was completed using the finite element analysis code SIERRA. Various material models were tested in the simulation including pure elastic, Holmquist-Johnson-Cook concrete model (Holmquist, Johnson and Cook 1993), and Karagozian & Case concrete model (Malvar, et al. 1997). A first benchmark workshop was held in Paris-Saclay, France, in June 2017. The results for Phase III presented herein describe the second iteration of effort (post June 2017) resulting in improved material model understanding and simulations.

FOREWARD

The Committee on the Safety of Nuclear Installations (CSNI) and the Committee on Nuclear Regulatory Activities jointly issued in February 2011 a Joint Strategic Plan taking into account the evolving status of nuclear industry worldwide and the main challenges that will face the regulatory bodies and technical safety organizations over the next several years.

The clear safety priority of the CSNI Committees is on existing nuclear installations and the design and construction of new reactors and installations. In particular, the CSNI provides a forum for improving the safety related knowledge and promotes joint research. The interest in nuclear energy has expanded worldwide, however public acceptance of existing and new nuclear installations in part depends on demonstrating adequate structural robustness of the installation and the effectiveness of emergency response strategies to avoid or mitigate the effects of severe accident including missiles impact.

Many countries have performed missiles impact analyses, but due to their sensitivity, the results are not easily shared. Therefore, it was considered important and worthwhile to perform a study that can be publicly vetted as a means of validating the evaluation techniques used in these analyses. The Committee on the Safety of Nuclear Installations (CSNI) approved in December 2008 a proposal of the Working Group on Integrity and Ageing of Components and Structures (WGIAGE) to conduct a round robin study, called Improving Robustness Assessment Methodologies for Structures Impacted by Missiles (IRIS), where the different computer codes, modelling approaches methods and results were to be compared to data and other codes used to determine effective means of analyzing the structural and vibrational effects of a postulated missiles impact on a NPP.

This report documents the results and conclusions of the work performed by Sandia National Laboratories and the US Nuclear Regulatory Commission in support of the IRIS program.

TABLE OF CONTENTS

LIST OF FIGURES

LIST OF TABLES

LIST OF EQUATIONS

EXECUTIVE SUMMARY

The power generation industry, and the nuclear power generation industry in particular, is constantly developing new and improved methods for maintaining and escalating the safety of power generation structures. The Committee on the Safety of Nuclear Installations (CSNI) maintains a clear safety priority on existing nuclear installations and the design and construction of new reactors and installations. In particular, the CSNI provides a forum for improving the safety related knowledge and promotes joint research. The interest in nuclear energy has expanded worldwide, however public acceptance of existing and new nuclear installations in part depends on demonstrating adequate structural robustness of the installation and the effectiveness of emergency response strategies to avoid or mitigate the effects of severe accident including missiles impact.

Many countries have performed missiles impact analyses, but due to their sensitivity, the results are not easily shared. Therefore, it was considered important and worthwhile to perform a study that can be publicly vetted as a means of validating the evaluation techniques used in these analyses. The CSNI approved in December 2008 a proposal of the Working Group on Integrity and Ageing of Components and Structures (WGIAGE) to conduct a round robin study, called Improving Robustness Assessment Methodologies for Structures Impacted by Missiles (IRIS), where the different computer codes, modelling approaches methods and results were to be compared to data and other codes used to determine effective means of analyzing the structural and vibrational effects of a postulated missiles impact on a NPP.

This document consolidates the work performed by Sandia National Laboratories and the US Nuclear Regulatory Commission in participation of Program IRIS: “Improving the Robustness of the Assessment Methodologies for Structures Impacted by Missiles”. Three round-robin benchmark exercises on improving the robustness of the assessment of structures impacted by large missiles at medium to high velocities were organized by either the IAGE Subgroup on Ageing of Concrete Structures of the Organization for Economic Co-operation and Development Nuclear Energy Agency (NEA) or Électricité de France (EDF). The objectives of the exercises were to develop guidance for conducting impact analyses including issues related to computer codes, modeling approaches, and analysis techniques. The full project was comprised of three phases: Phase I, impact of walls; Phase II, impact of larger structures; and Phase III, transmission of shock and vibration to internal components.

The portions pertaining to Phase I describe in detail the numerical simulations and comparisons to existing experimental data of three impact scenarios involving a steel missile striking a concrete target heavily reinforced with steel bars. The first impact modeling scenario was related to the Meppen test (II-4) performed in Germany in 1980 (Brandes 1988), (Meppen 2010), and the two other simulations were related to two different tests performed at the VTT facility (VTT 2012): flexural and punching. The final numerical model for each of the three Phase I impact scenarios were constructed using finite element meshes of each structural component (i.e., target, reinforcing steel, and missile). All Phase I impact scenario calculations were performed using the LS-DYNA finite element analysis code (LSTC, LS-DYNA 2011).

The portions pertaining to Phase II describe analyses and numerical results obtained from simulations of a steel missile impacting a concrete target reinforced with steel bars using two different computer codes: LS-DYNA and EMU. Phase II of the IRIS program was implemented to continue the activity developed in Phase I. The objectives were as follows:

- To give the opportunity to IRIS 2010 participants (plus newcomers) to update and improve the simulations with the knowledge of the test results and with the experience gained by one's own 1st computation and by others' computations using a single set of material properties;
- To give the opportunity to each participant to develop, test, and share the means and tools for alternative approaches ("simplified models");
- To gather all the results from the new simulations and all the proposals of simplified models and to issue a new set of recommendations.

This section introduces the two different numerical analyses, define the three test conditions, compare and contrast several numerical code simulation results of the three tests, and discuss the advantages and limitation of each computational approach.

The portions pertaining to Phase III describe analyses and numerical results obtained from simulations of a hollow steel missile impacting a concrete target reinforced with steel bars. Phase III was completed using the finite element analysis code SIERRA. Various material models were tested in the simulation including pure elastic, Holmquist-Johnson-Cook concrete model (Holmquist, Johnson and Cook 1993), and Karagozian & Case concrete model (Malvar, et al. 1997). A first benchmark workshop was held in Paris-Saclay, France, in June 2017. The results for Phase III presented herein describe the second iteration of effort (post June 2017) resulting in improved material model understanding and simulations.

ABBREVIATIONS AND ACRONYMS

CSNI	Committee on the Safety of Nuclear Installations
EDF	Électricité de France
EOS	Equation of state
FEA	Finite element analysis
FEM	Finite element method
HJC	Holmquist, Johnson, Cook
IRIS	Improving Robustness Assessment Methodologies for Structures Impacted by Missiles
IRSN	Institut de Radioprotection et de Sureté Nucléaire
K&C	Karagozian & Case
NEA	Nuclear Energy Agency
NRC	US Nuclear Regulatory Commission
SNL	Sandia National Laboratories
VTT	Technical Research Centre of Finland
WGIAGE	Working Group on Integrity and Ageing of Components and Structures

1 INTRODUCTION

This report consolidates the results of Sandia National Laboratories analyses in support of the U.S. Nuclear Regulatory Commission's participation in the Committee on the Safety of Nuclear Installations (CSNI) Working Group on Integrity and Ageing of Components and Structures (IAGE), Concrete Subgroup's activities in Program IRIS: "Improving the Robustness of the Assessment Methodologies for Structures Impacted by Missiles". Three round-robin benchmark exercises on improving the robustness of the assessment of structures impacted by large missiles at medium to high velocities were organized by either the IAGE Subgroup on Ageing of Concrete Structures of the Organization for Economic Co-operation and Development Nuclear Energy Agency (NEA) or Électricité de France (EDF). These activities were approved by the CSNI. The objectives of the exercises were to develop guidance for conducting impact analyses including issues related to computer codes, modeling approaches, and analysis techniques. The full project was comprised of three phases: Phase I, impact of walls; Phase II, impact of larger structures; and Phase III, transmission of shock and vibration to internal components. This report contains in entirety the information developed by Sandia National Laboratories during each Phase of the program.

Program IRIS consisted of three phases. Phase I included three separate tests of missile impact against a reinforced concrete wall. Each participating agency was required to model the impact scenario using a finite element analysis (FEA) code of the agency's choosing and compile a report on the findings. Phase II did not include additional missile impact tests; participating agencies were allowed to modify their FEA codes to better simulate the missile impact tests of Phase I and compile a report on the findings. Phase III included a trio of missile impact tests against a reinforced concrete structure. Participating agencies were required to model the impact scenario using an FEA code; predict displacements, damage, accelerations, and damping in the structure and missile; and compile a report on the findings. After each phase, a workshop was held for the participating agencies to meet and present/discuss findings.

2 PHASE I: IMPACT OF WALLS

2.1 Phase I Test Overview

The portions pertaining to Phase I describe in detail the numerical simulations and comparisons to existing experimental data, relative to the CSNI Phase I exercise, of three impact scenarios involving a steel missile striking a concrete target heavily reinforced with steel bars. The first impact modeling scenario was related to the Meppen test (II-4) performed in Germany in 1980 (Brandes 1988), (Meppen 2010), and the two other simulations were related to two different tests performed at the VTT facility (VTT 2012): flexural and punching. The final numerical model for each of the three Phase I impact scenarios; hereby denoted as Meppen II-4, VTT flexural mode, and VTT punching mode; were constructed using finite element meshes of each structural component (*i.e.,* target, reinforcing steel, and missile). All Phase I impact scenario calculations were performed using the LS-DYNA finite element analysis code (LSTC, LS-DYNA 2011), version: mpp971d Dev, revision: 6922, date: 06/October/2011. This report documents the test overview, the test data and material properties provided, the finite element representation of each impact test scenario, the results summary, and the conclusions and recommendations in subsequent chapters. The report summarizes the third iteration of effort resulting from the CSNI funding of the Phase I activities. The analyses and numerical results presented herein are the final evolution of the best computational models and material models using knowledge gained throughout the entire exercise.

2.1.1 Meppen II-4 Test

The Meppen test may be described as a soft impact with a thin shelled missile striking a relatively thin (in the transverse direction) reinforced concrete target. The 1016 kg missile impacted the target at 247.7 m/sec. The steel missile was 5.99 m in length and roughly 0.6 m in diameter and is shown in Figure 2-1. The target was 6.5 x 6.0 x 0.7 m thick and is shown in Figure 2-2. The Meppen test reinforcing steel bar geometry is shown in Figure 2-3.

Missile:

made by steel RSt 37-2 Ø600mm tubes

Mass: 1016kg

Velocity at impact: 247.7m/s

Shock duration: 26ms

Load peak: 13.1 MN

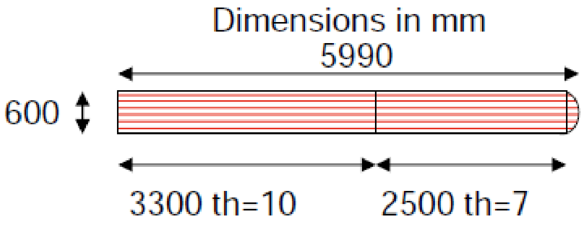

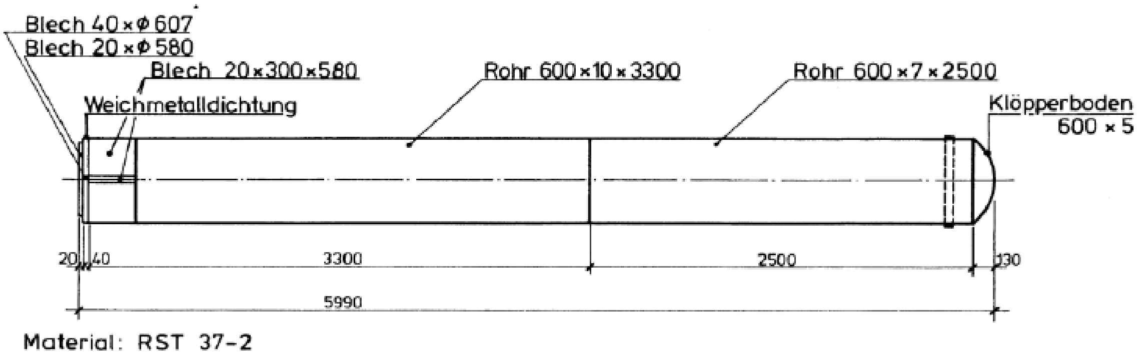

Figure 2-1: Meppen II-4 Test Missile Engineering Drawing.

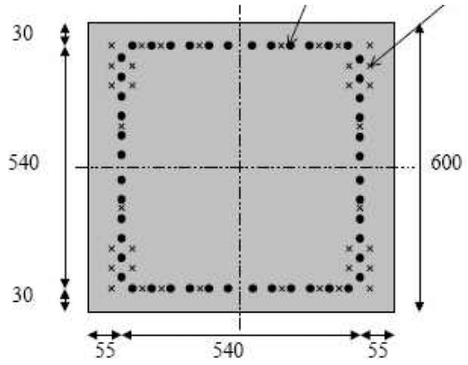

Slab

Geometry

Outer dimension:	6.5x6.0 mxm
Span dimensions:	5.4x5.4 mxm
Thickness:	0.7 m

Supported on 48 equally spaced points

Figure 2-2: Meppen II-4 Target Geometry and Support Geometry.

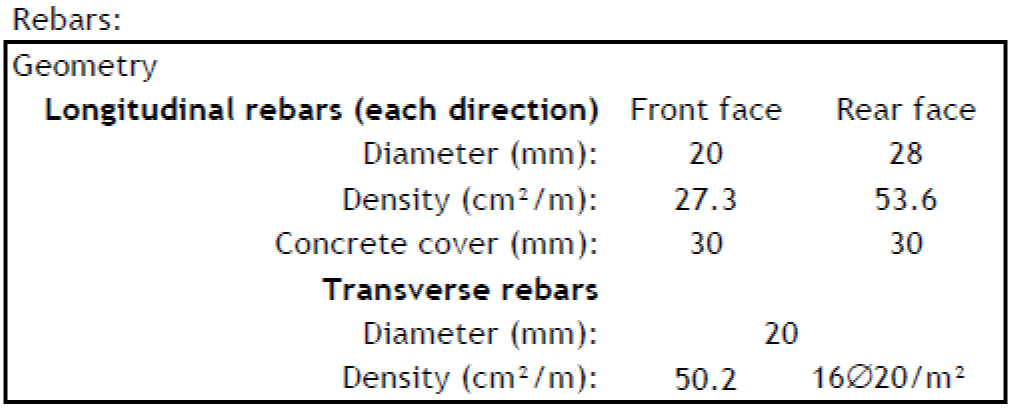

Rebars:

Geometry

Longitudinal rebars (each direction)	Front face	Rear face
Diameter (mm):	20	28
Density (cm^2/m):	27.3	53.6
Concrete cover (mm):	30	30
Transverse rebars		
Diameter (mm):	20	
Density (cm^2/m):	50.2	16∅20/m^2

Figure 2-3: Meppen II-4 Test Reinforcing Bar Geometry.

2.1.2 IRSN VTT Flexural Test

The flexural test is similar to the Meppen test and involves a soft impact of a thin shelled steel missile hitting a thin steel reinforced concrete target. The 50 kg steel missile impacted the target at 110.885 m/sec. The steel missile was 2.111 m in length and roughly 0.254 m in diameter, comprised mostly of a long stainless steel tube with a carbon steel end pipe, and is shown in Figure 2-4 and Figure 2-5. The target had outer dimensions of 2.10 x 2.10 x 0.15 m thick that was simply supported along a 2.0 m side square. The test target mounting schematic and target engineering drawing are shown in Figure 2-6 and Figure 2-7. The flexural test reinforcing steel bar geometry and areal density are shown in Figure 2-8 and Figure 2-9 (Vepsä 2010a), and the reinforcing steel bar cross-section geometry (Vepsä 2010a) is shown in Figure 2-10.

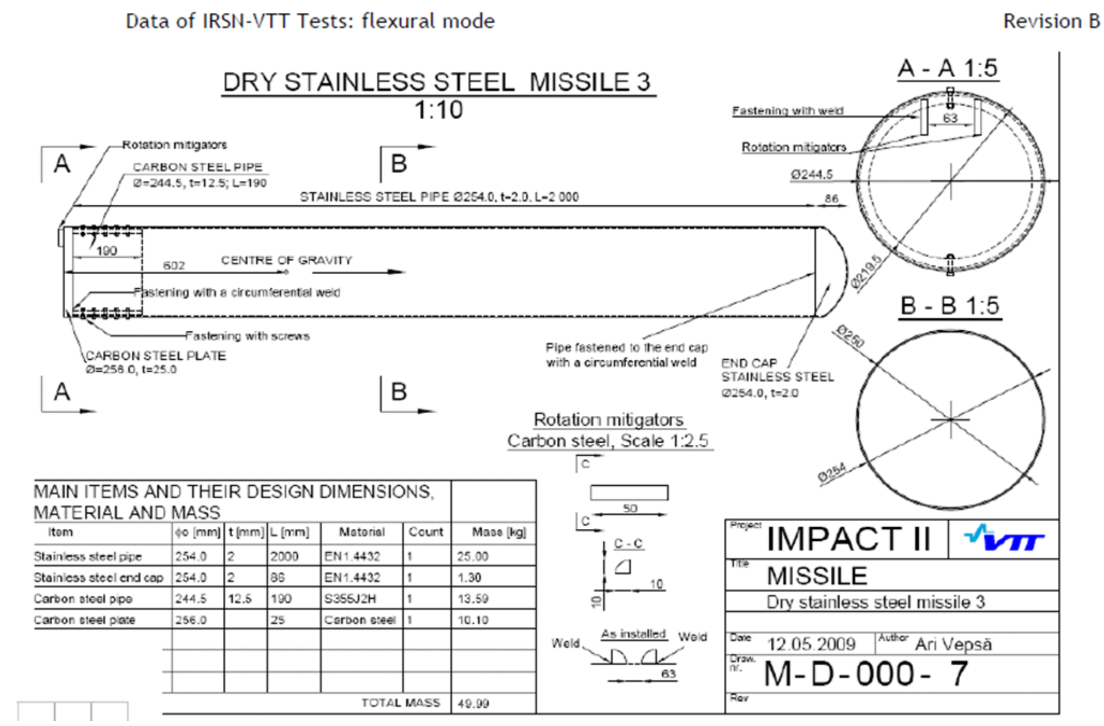

MAIN ITEMS AND THEIR DESIGN DIMENSIONS, MATERIAL AND MASS

Item	ϕo [mm]	t [mm]	L [mm]	Material	Count	Mass [kg]
Stainless steel pipe	254.0	2	2000	EN1.4432	1	25.00
Stainless steel end cap	254.0	2	86	EN1.4432	1	1.30
Carbon steel pipe	244.5	12.5	190	S355J2H	1	13.59
Carbon steel plate	256.0		25	Carbon steel	1	10.10
					TOTAL MASS	49.99

Project IMPACT II VTT
Title MISSILE
Dry stainless steel missile 3
Date 12.05.2009 Author Ari Vepsä
Draw. nr. M-D-000- 7
Rev

Figure 2-4: IRSN VTT Flexural Test Steel Missile Engineering Drawing.

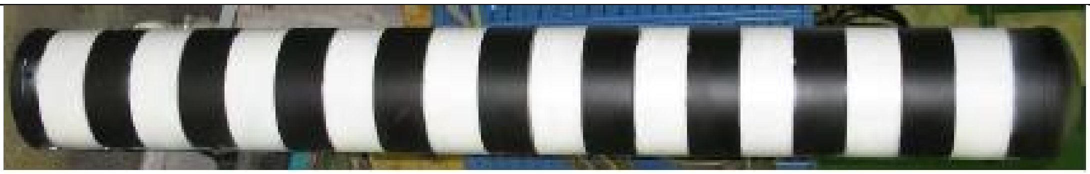

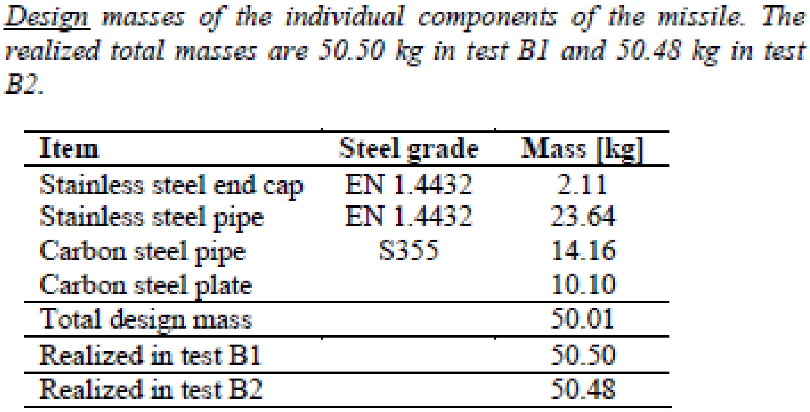

Design masses of the individual components of the missile. The realized total masses are 50.50 kg in test B1 and 50.48 kg in test B2.

Item	Steel grade	Mass [kg]
Stainless steel end cap	EN 1.4432	2.11
Stainless steel pipe	EN 1.4432	23.64
Carbon steel pipe	S355	14.16
Carbon steel plate		10.10
Total design mass		50.01
Realized in test B1		50.50
Realized in test B2		50.48

Figure 2-5: IRSN VTT Flexural Test Missile and Missile Component Mass (Vespä 2010b).

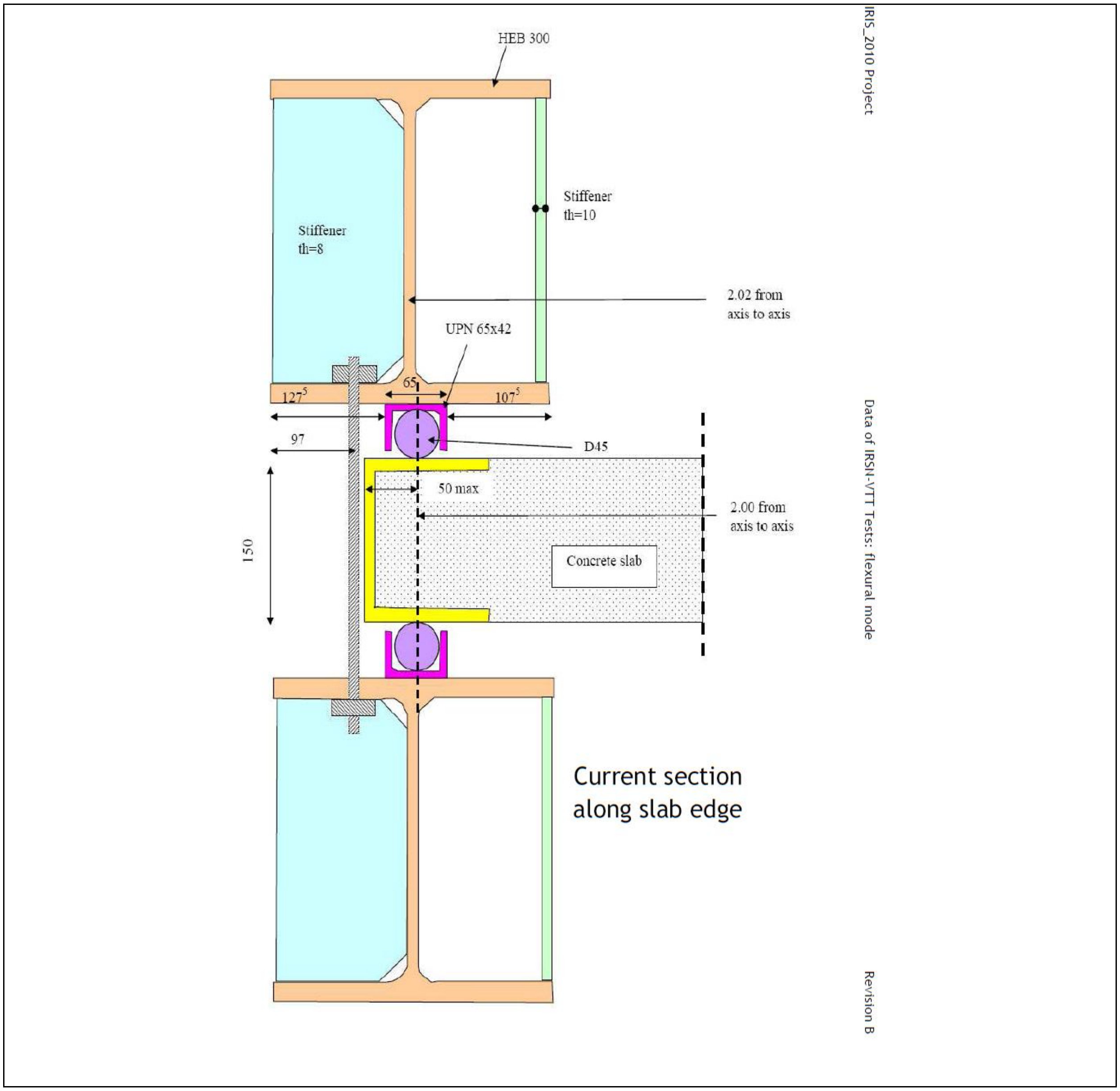

Figure 2-6: IRSN VTT Flexural Test Fixture Schematic.

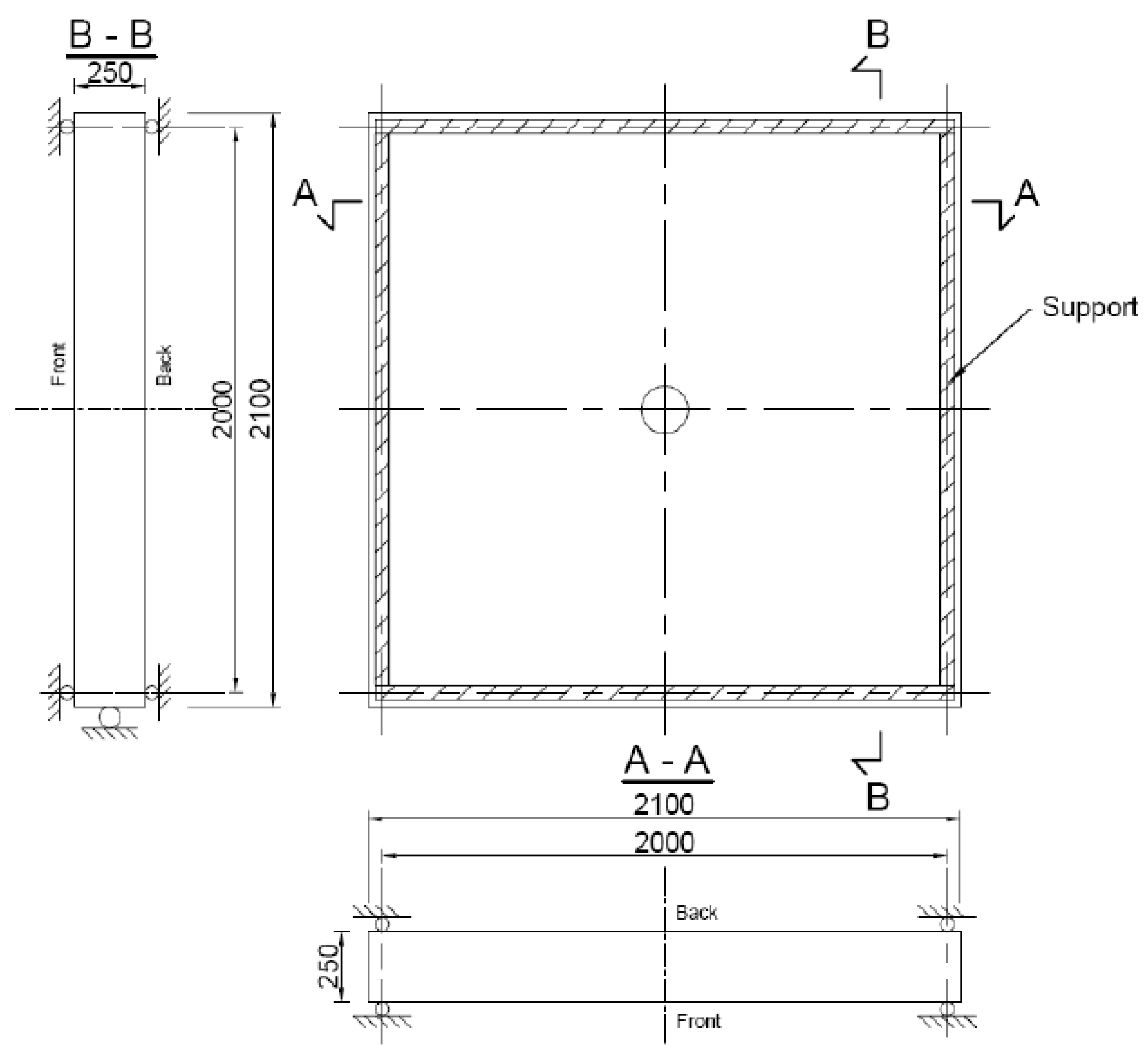

Figure 2-7: IRSN VTT Flexural Test Target Engineering Drawing.

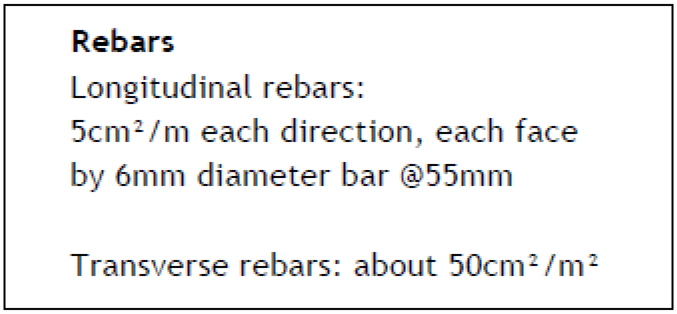

Rebars
Longitudinal rebars:
5cm²/m each direction, each face
by 6mm diameter bar @55mm

Transverse rebars: about 50cm²/m²

Figure 2-8: IRSN VTT Flexural Test Reinforcing Bar Density and Geometry.

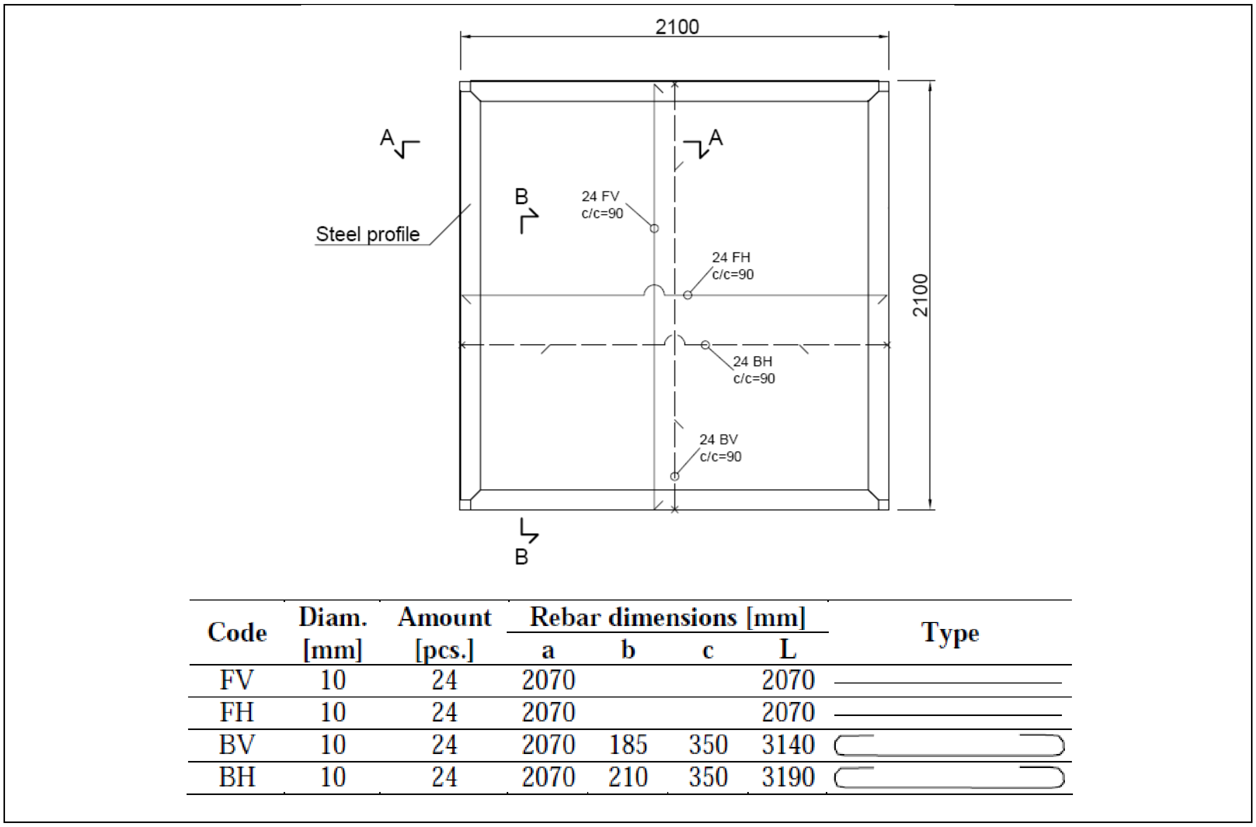

Code	Diam. [mm]	Amount [pcs.]	Rebar dimensions [mm] a	b	c	L	Type
FV	10	24	2070			2070	
FH	10	24	2070			2070	
BV	10	24	2070	185	350	3140	
BH	10	24	2070	210	350	3190	

Figure 2-9: IRSN VTT Flexural Test Reinforcing Steel Bar Layout Specifications.

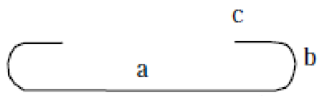

*Dimension codes used in Table 1. L is the total theoretical length of the rebar, computed as a+2*b+2*c.*

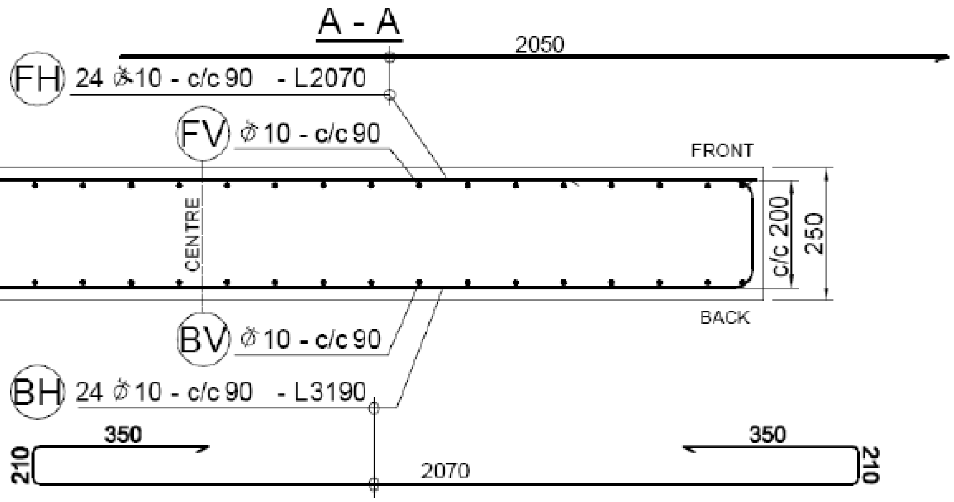

Horizontal cross section A-A of the wall.

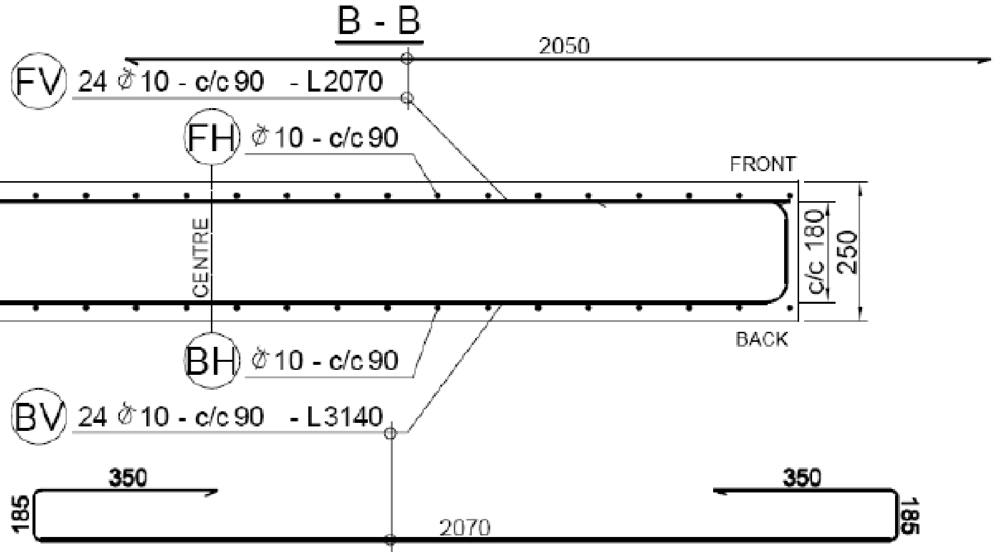

Vertical cross section B-B of the wall.

Figure 2-10: IRSN VTT Flexural Test Reinforcing Steel Bar Cross-section Geometry.

2.1.3 IRSN VTT Punching Test

The punching test is a hard impact involving a penetrating missile (i.e., a concrete cylinder encapsulated in steel) striking a thick reinforced concrete target, without any transverse direction steel reinforcement. The 47 kg steel and concrete missile impacted the target at 135 m/sec. The steel missile was 0.64 m in length and roughly 0.168 m in diameter, comprised of a light weight concrete cylinder surrounded by steed, and is shown Figure 2-11 and Figure 2-12. The target had outer dimensions of 2.10 x 2.10 x 0.25 m thick that was simply supported along a 2.0 m side square, and the target slab mounting schematic and target engineering drawing are shown in Figure 2-13 and Figure 2-14. The flexural test reinforcing steel bar geometry and areal density is shown in Figure 2-15 and Figure 2-16 (Vepsä 2010a), and the reinforcing steel bar cross-section geometry (Vepsä 2010a) is shown in Figure 2-17.

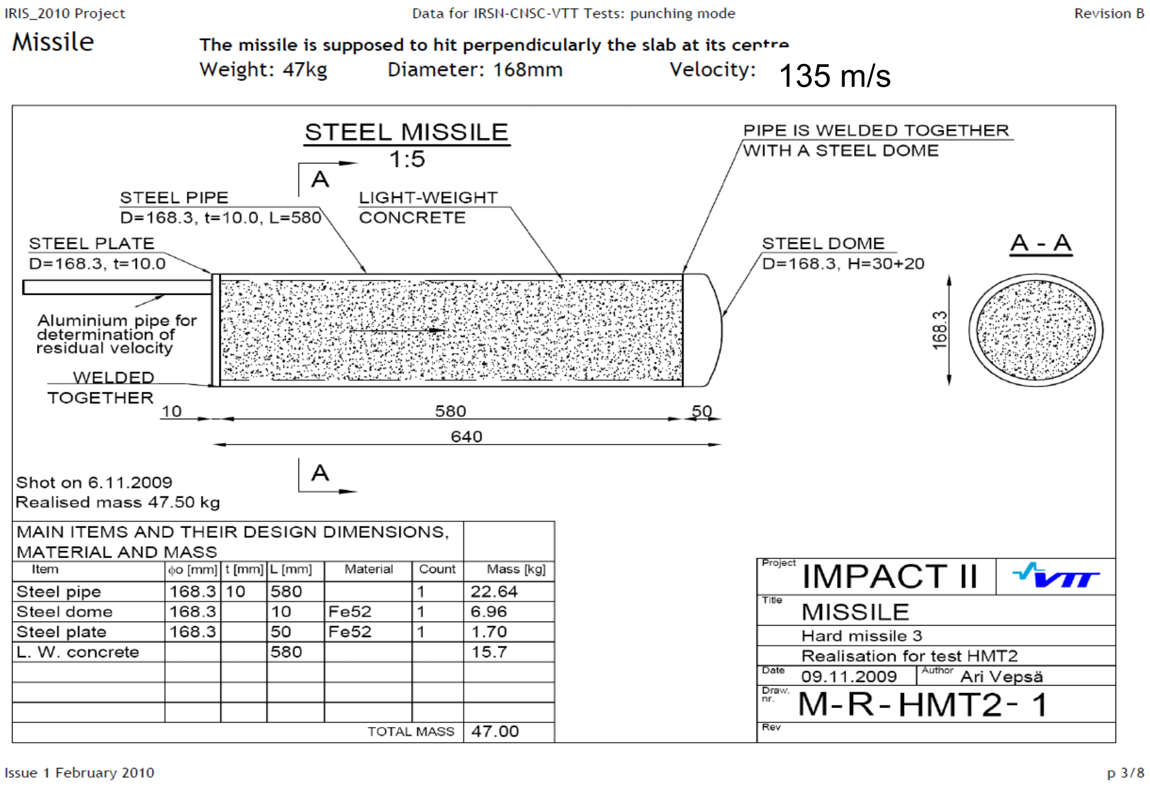

IRIS_2010 Project Data for IRSN-CNSC-VTT Tests: punching mode Revision B

Missile

The missile is supposed to hit perpendicularly the slab at its centre

Weight: 47kg Diameter: 168mm Velocity: 135 m/s

Shot on 6.11.2009
Realised mass 47.50 kg

MAIN ITEMS AND THEIR DESIGN DIMENSIONS, MATERIAL AND MASS

Item	ϕo [mm]	t [mm]	L [mm]	Material	Count	Mass [kg]
Steel pipe	168.3	10	580		1	22.64
Steel dome	168.3		10	Fe52	1	6.96
Steel plate	168.3		50	Fe52	1	1.70
L. W. concrete			580			15.7
					TOTAL MASS	47.00

Project	IMPACT II VTT
Title	MISSILE Hard missile 3 Realisation for test HMT2
Date	09.11.2009
Author	Ari Vepsä
Draw. nr.	M-R-HMT2- 1
Rev	

Issue 1 February 2010 p 3/8

Figure 2-11: IRSN VTT Punching Test Missile Engineering Drawing.

Figure 2-12: IRSN VTT Punching Test Missiles.

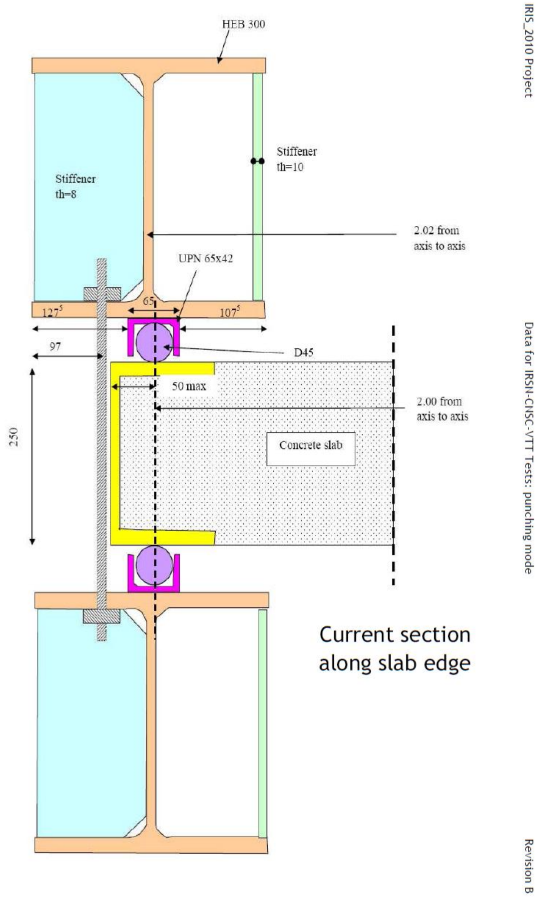

Figure 2-13: IRSN VTT Punching Test Fixture Schematic

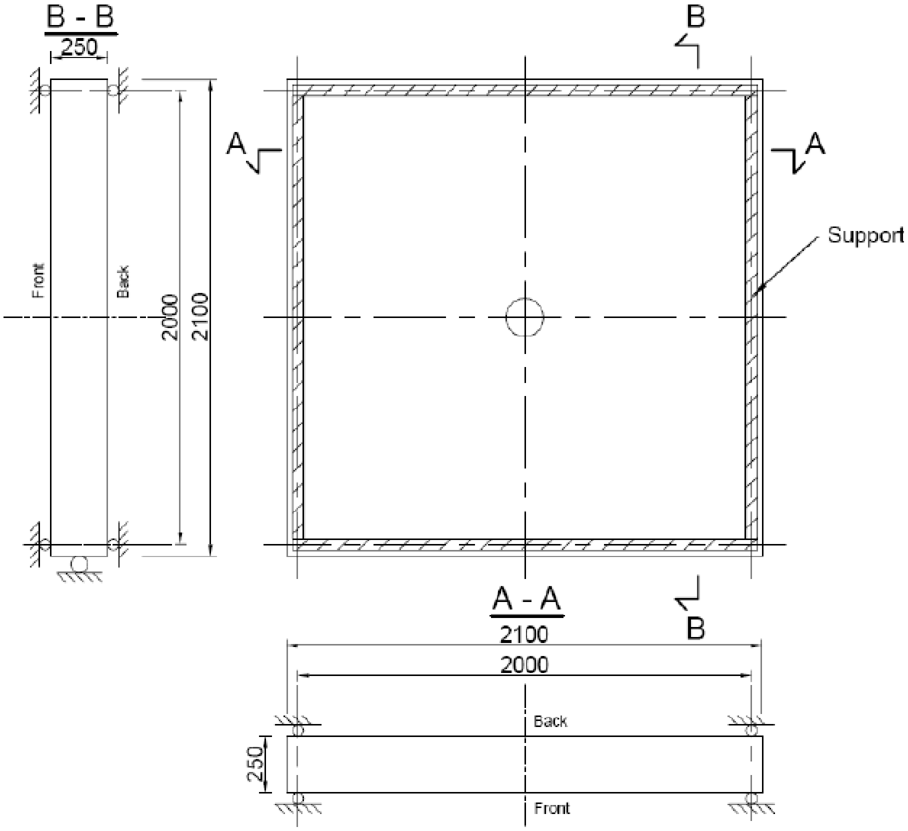

Figure 2-14: IRSN VTT Punching Test Target Engineering Drawing.

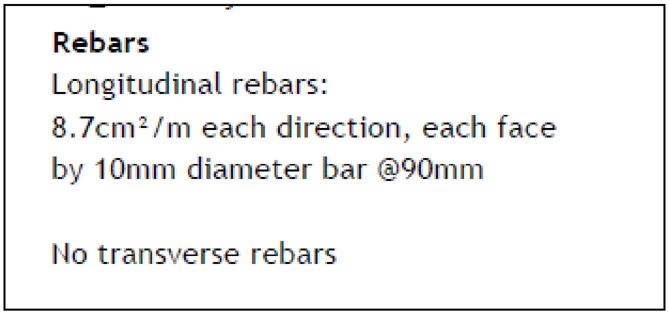

Rebars

Longitudinal rebars:

8.7cm²/m each direction, each face

by 10mm diameter bar @90mm

No transverse rebars

Figure 2-15: IRSN VTT Punching Test Reinforcing Steel Bar Density and Geometry.

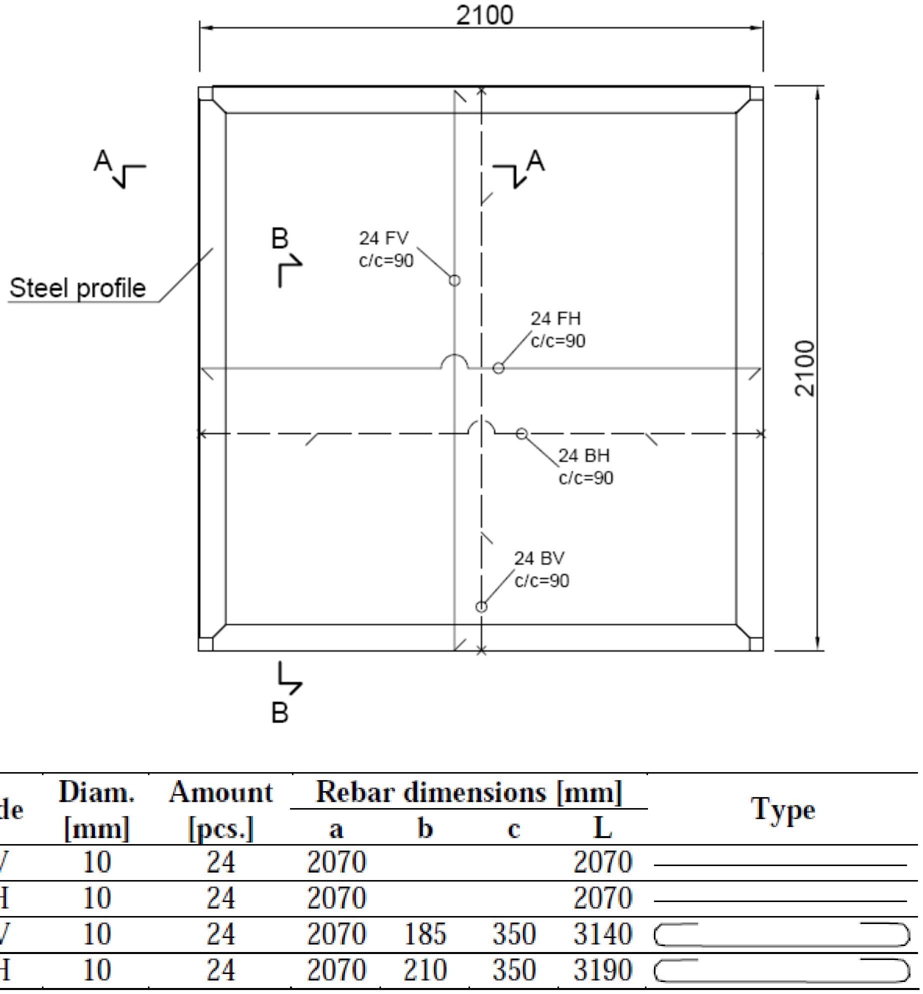

Code	Diam. [mm]	Amount [pcs.]	Rebar dimensions [mm]				Type
			a	b	c	L	
FV	10	24	2070			2070	
FH	10	24	2070			2070	
BV	10	24	2070	185	350	3140	
BH	10	24	2070	210	350	3190	

Figure 2-16: IRSN VTT Punching Test Reinforcing Steel Bar Layout Specifications.

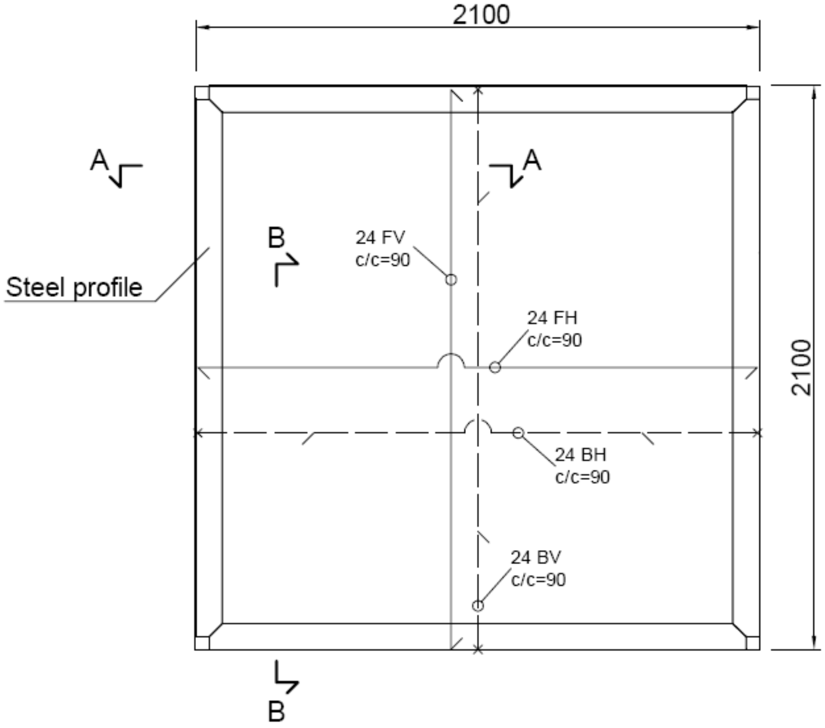

Code	Diam. [mm]	Amount [pcs.]	Rebar dimensions [mm]				Type
			a	b	c	L	
FV	10	24	2070			2070	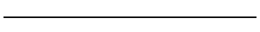
FH	10	24	2070			2070	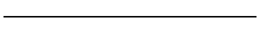
BV	10	24	2070	185	350	3140	
BH	10	24	2070	210	350	3190	

Figure 2-17: IRSN VTT Punching Test Reinforcing Steel Bar Cross-section Geometry.

2.2 Phase I Test Data and Material Properties

During Phase I, the material property data used in the Meppen II-4 impact scenario simulations was derived from values listed in the Meppen Test II-4 report provided by the IRIS 2010 project committee (Meppen 2010). Similarly, all material property data used in the flexural mode simulations was taken from the Technical Research Centre of Finland (VTT) Report VTT-R-05587-10 (Vepsä 2010a). Lastly, the material property values used in the Punching mode calculations were derived from the second Report VTT-R-05588-10 (Vespä 2010b). During the FY 2012, additional concrete material property data was made available to all benchmark participants (CSNI 2012) which included unconfined and triaxial compression test data to be used in improving the numerical models representing the target concrete.

2.2.1 Concrete Test Data

Shown in Figure 2-18 is the concrete property provided from the Meppen test.

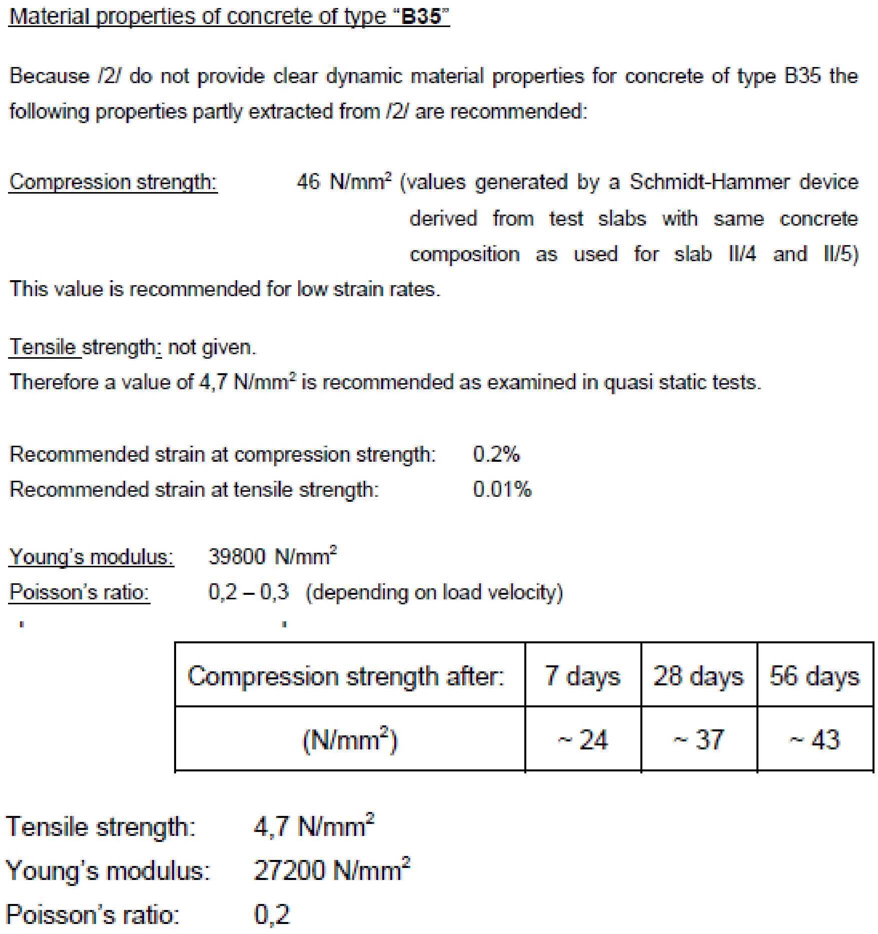

Material properties of concrete of type "**B35**"

Because /2/ do not provide clear dynamic material properties for concrete of type B35 the following properties partly extracted from /2/ are recommended:

Compression strength: 46 N/mm² (values generated by a Schmidt-Hammer device derived from test slabs with same concrete composition as used for slab II/4 and II/5)

This value is recommended for low strain rates.

Tensile strength: not given.
Therefore a value of 4,7 N/mm² is recommended as examined in quasi static tests.

Recommended strain at compression strength:	0.2%
Recommended strain at tensile strength:	0.01%

Young's modulus:	39800 N/mm²
Poisson's ratio:	0,2 – 0,3 (depending on load velocity)

Compression strength after:	7 days	28 days	56 days
(N/mm²)	~ 24	~ 37	~ 43

Tensile strength:	4,7 N/mm²
Young's modulus:	27200 N/mm²
Poisson's ratio:	0,2

Figure 2-18: Meppen II-4 Test Target Concrete Strength Properties

An updated data set for the flexural and punching tests was provided and some key information is presented in this section. Several uniaxial and triaxial compression tests were performed on standard 70 mm diameter by 140 mm long concrete specimens (CSNI 2012). The test geometry for these standard tests is shown in Figure 2-19. The unconfined, and five triaxial compression tests, each with a different confinement pressure, axial stress vs. pressure response plots are presented in Figure 2-20, Figure 2-21, Figure 2-22, and Figure 2-23. Shown in Figure 2-24 is the Mohr's circle representation of these tests and demonstrate the quality of the tests. Also, to help visualize the post-peak response, final deformed shapes from all of these standard cylinder tests are presented in Figure 2-25. Lastly, another image showing the over-laid unconfined compression test and the four triaxial compression tests, showing the axial stress vs. axial strain is shown in Figure 2-26.

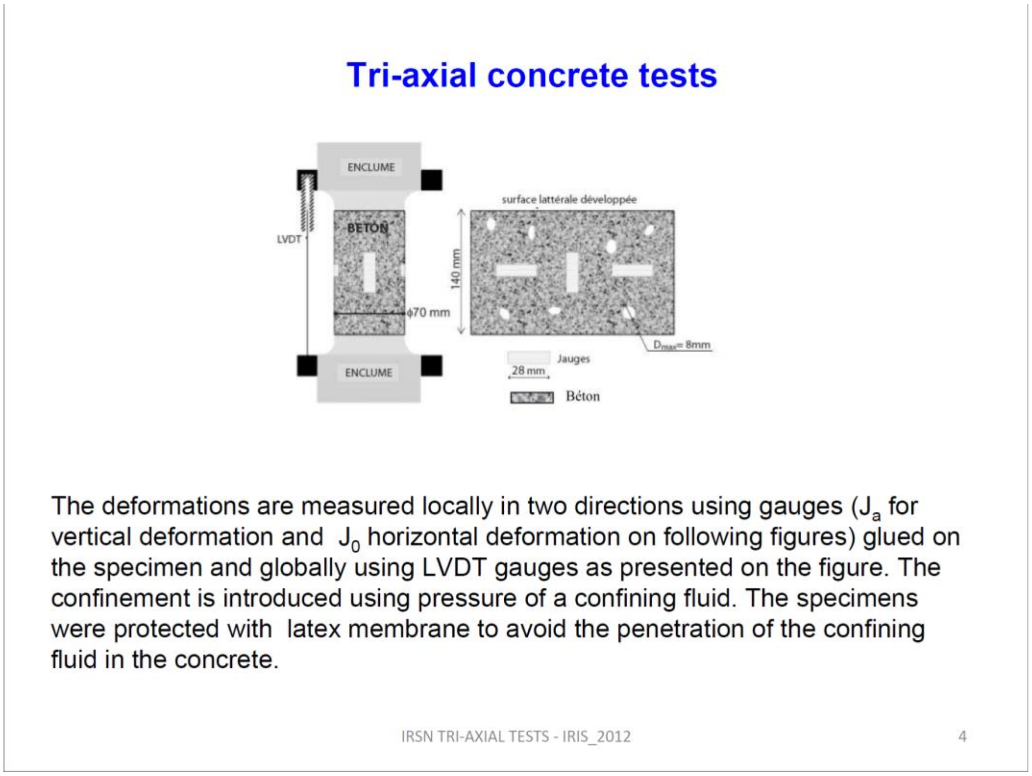

Tri-axial concrete tests

The deformations are measured locally in two directions using gauges (J_a for vertical deformation and J_0 horizontal deformation on following figures) glued on the specimen and globally using LVDT gauges as presented on the figure. The confinement is introduced using pressure of a confining fluid. The specimens were protected with latex membrane to avoid the penetration of the confining fluid in the concrete.

IRSN TRI-AXIAL TESTS - IRIS_2012 4

Figure 2-19: IRSN Cylinder Test Geometry and Description.

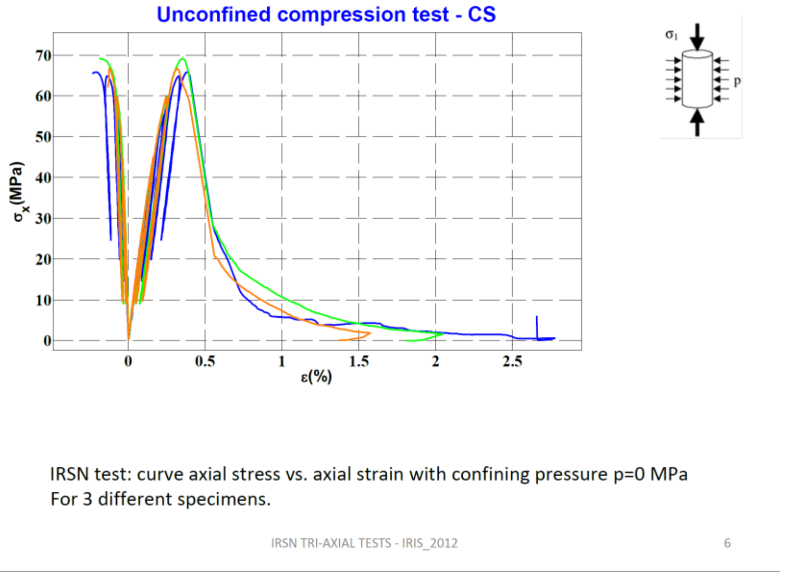

IRSN test: curve axial stress vs. axial strain with confining pressure p=0 MPa
For 3 different specimens.

IRSN TRI-AXIAL TESTS - IRIS_2012 6

Figure 2-20: IRSN 2012 Unconfined Compression Test on Standard Concrete Cylinder.

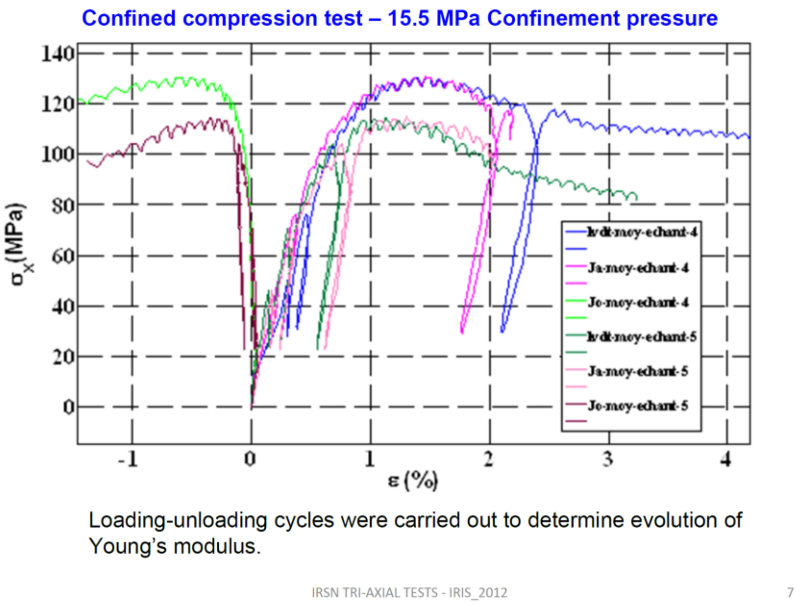

Confined compression test – 15.5 MPa Confinement pressure

Loading-unloading cycles were carried out to determine evolution of Young’s modulus.

IRSN TRI-AXIAL TESTS - IRIS_2012 7

Figure 2-21: IRSN 2012 Triaxial Compression Test on Standard Concrete Cylinder with 15.5 MPa Confinement.

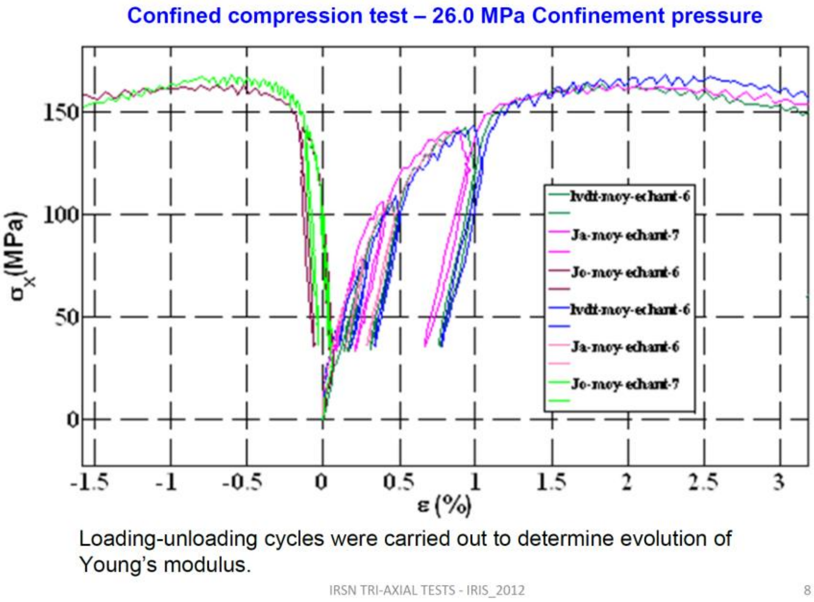

Confined compression test – 26.0 MPa Confinement pressure

Loading-unloading cycles were carried out to determine evolution of Young’s modulus.

IRSN TRI-AXIAL TESTS - IRIS_2012 8

Figure 2-22: IRSN 2012 Triaxial Compression Test on Standard Concrete Cylinder with 26.0 MPa Confinement.

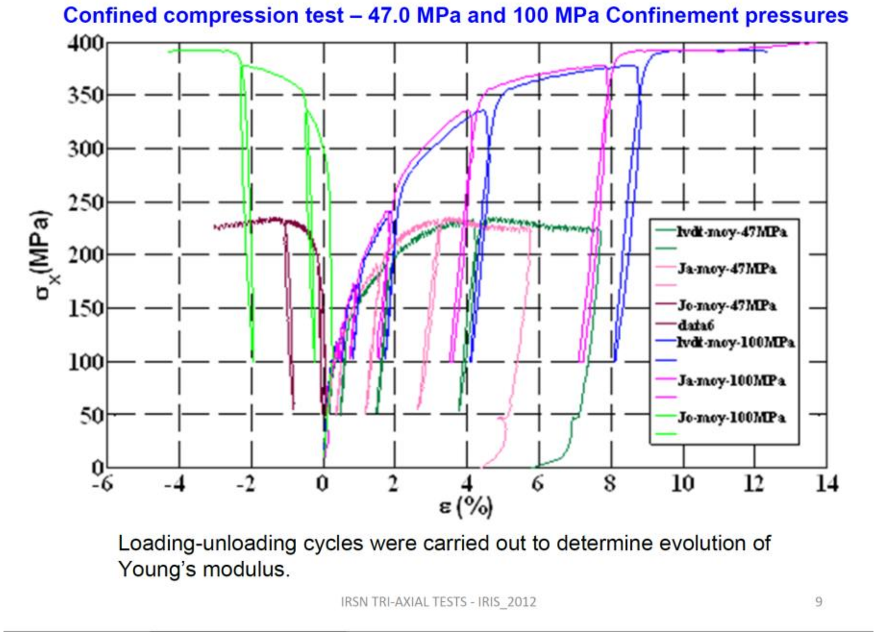

Confined compression test – 47.0 MPa and 100 MPa Confinement pressures

Loading-unloading cycles were carried out to determine evolution of Young's modulus.

IRSN TRI-AXIAL TESTS - IRIS_2012 9

Figure 2-23: IRSN 2012 Triaxial Compression Test on Standard Concrete Cylinder with 47.0 and 100.0 MPa Confinement.

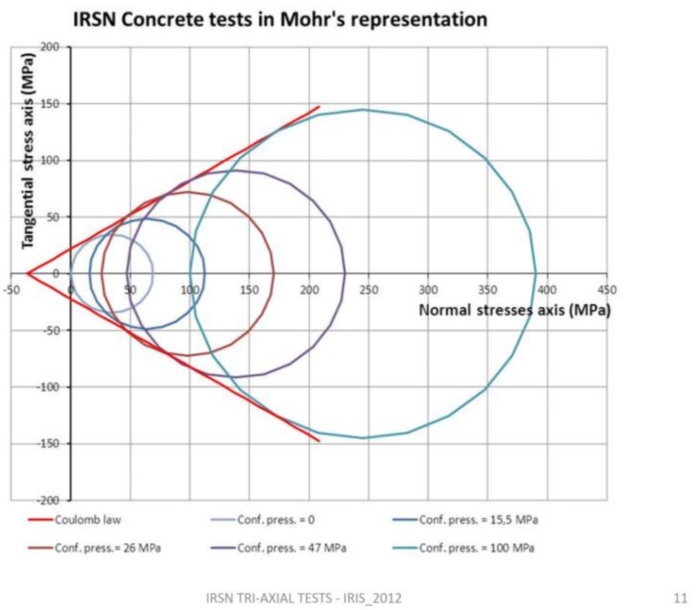

IRSN Concrete tests in Mohr's representation

IRSN TRI-AXIAL TESTS - IRIS_2012 11

Figure 2-24: IRSN 2012 Mohr's Circle Response for All Standard Concrete Cylinder Tests.

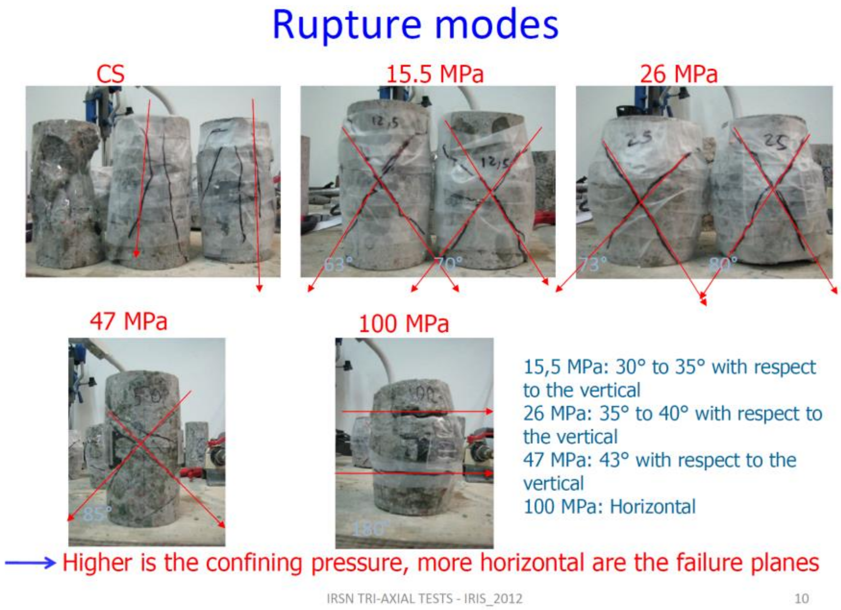

Rupture modes

CS

15.5 MPa

26 MPa

47 MPa

100 MPa

15,5 MPa: 30° to 35° with respect to the vertical
26 MPa: 35° to 40° with respect to the vertical
47 MPa: 43° with respect to the vertical
100 MPa: Horizontal

→ Higher is the confining pressure, more horizontal are the failure planes

IRSN TRI-AXIAL TESTS - IRIS_2012 10

Figure 2-25: IRSN 2012 Final Deformed Shapes of All Standard Concrete Cylinder Tests.

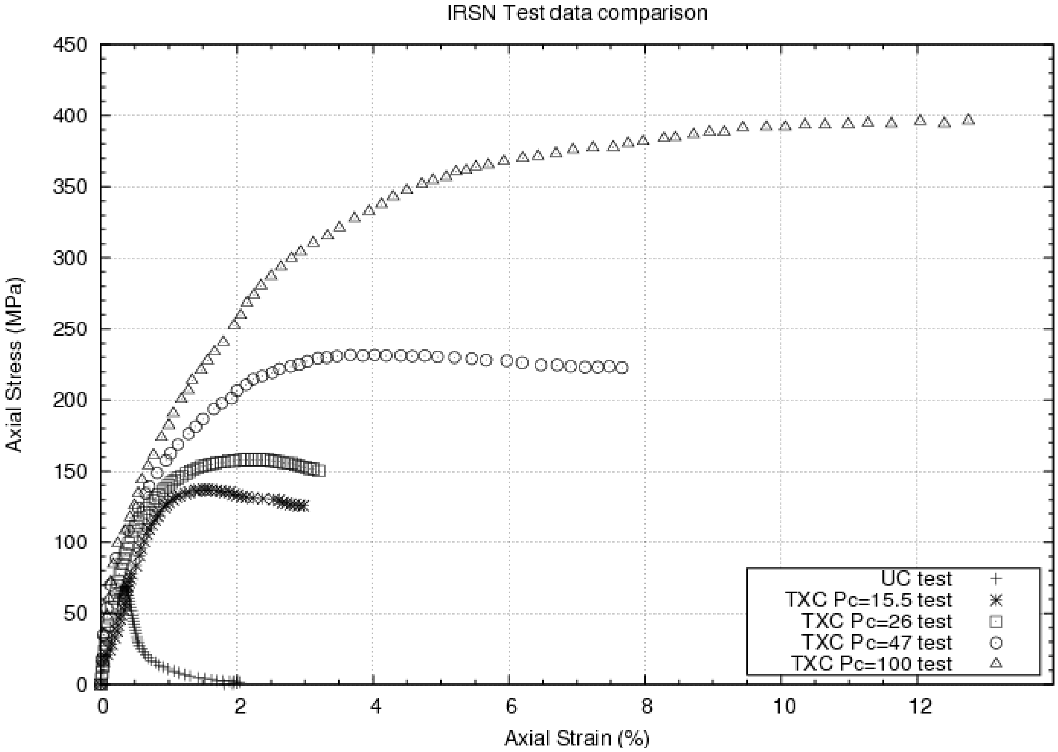

Figure 2-26: 2012 IRSN Standard Concrete Cylinder Test Unconfined (UC) and Triaxial Compression (TXC) Axial Stress vs. Axial Strain Response.

2.2.2 Reinforcing Steel Data

The reinforcing steel data for the Meppen test was provided with a limited subset of strain rate dependence information and is shown in Figure 2-27.

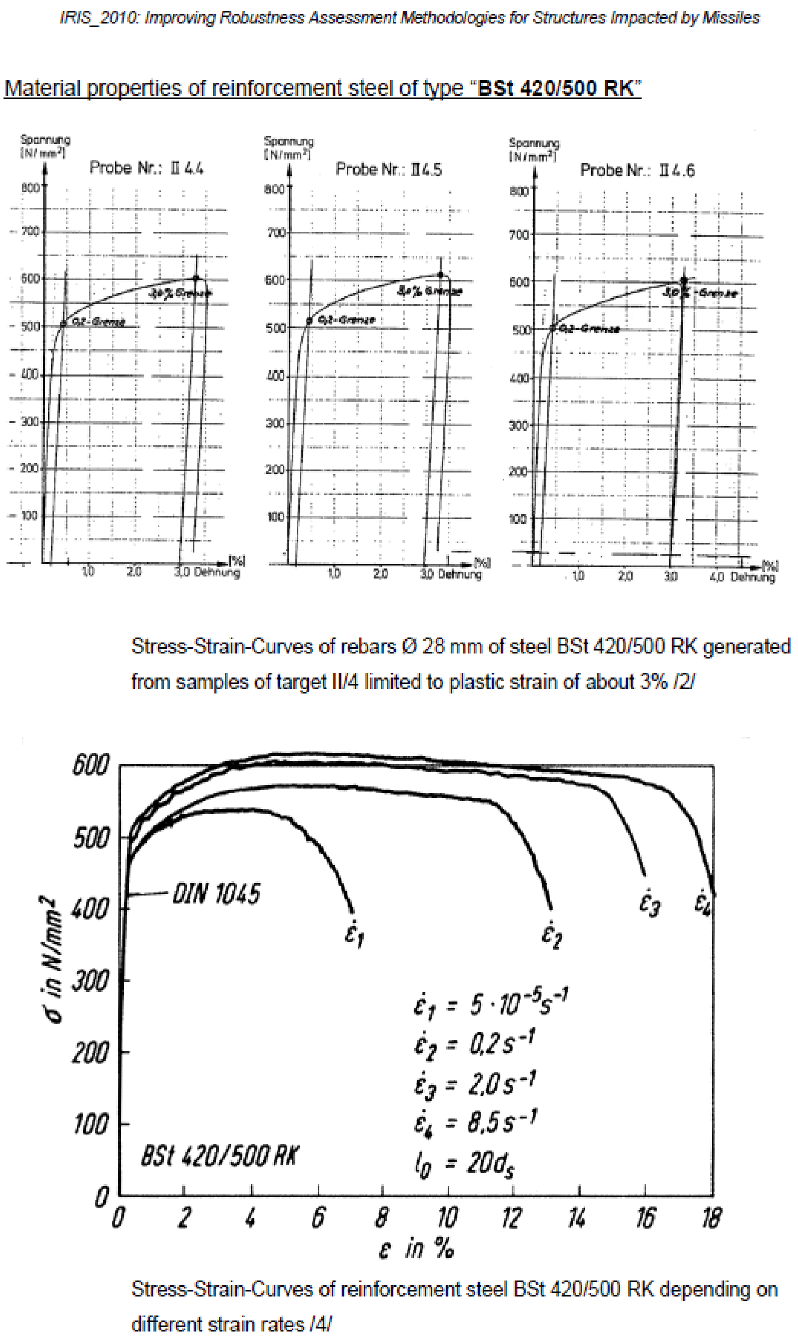

IRIS_2010: Improving Robustness Assessment Methodologies for Structures Impacted by Missiles

Material properties of reinforcement steel of type "**BSt 420/500 RK**"

Stress-Strain-Curves of rebars Ø 28 mm of steel BSt 420/500 RK generated from samples of target II/4 limited to plastic strain of about 3% /2/

Stress-Strain-Curves of reinforcement steel BSt 420/500 RK depending on different strain rates /4/

Figure 2-27: Meppen II-4 Test Reinforcing Steel Stress and Strain Rate Behavior.

The reinforcing steel data for the flexural and punching test are given below in Table 2-1, Figure 2-28, and Figure 2-29. No information regarding strain-rate dependence with respect to the steel strength was provided for either the flexural test reinforcing steel bars (6 mm outside diameter) or the punching test reinforcing steel bars (10 mm outside diameter). Although Figure 2-28 shows response only out to 2.5 to 4.5% strain, however, as mentioned in the reference (Vepsä 2010a), the requirement was to have a failure strain of 12%.

Table 2-1: Flexural Test Reinforcing Steel Bar Strength Requirements.

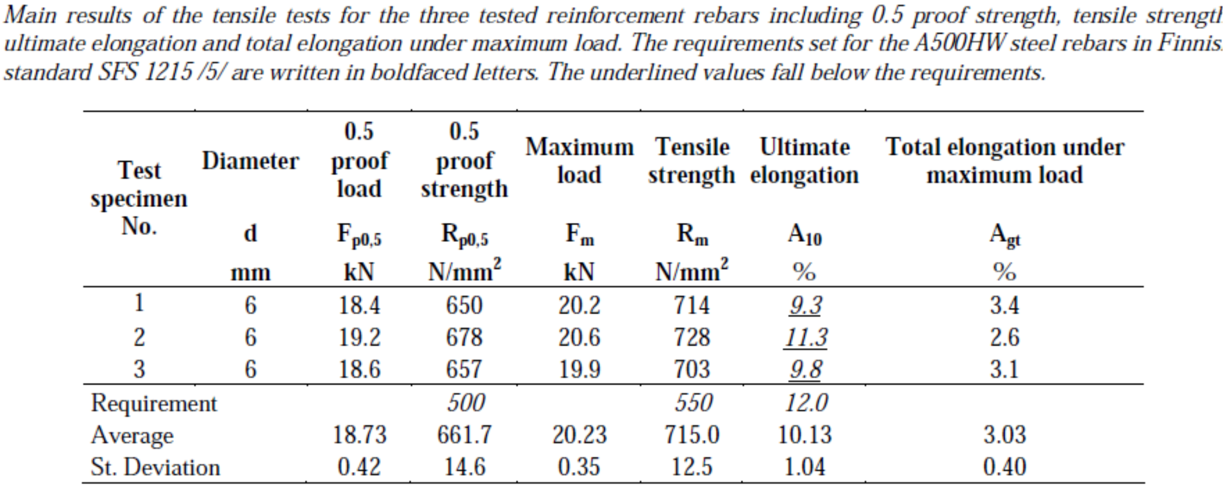

Main results of the tensile tests for the three tested reinforcement rebars including 0.5 proof strength, tensile strengt ultimate elongation and total elongation under maximum load. The requirements set for the A500HW steel rebars in Finnis standard SFS 1215 /5/ are written in boldfaced letters. The underlined values fall below the requirements.

Test specimen No.	Diameter	0.5 proof load	0.5 proof strength	Maximum load	Tensile strength	Ultimate elongation	Total elongation under maximum load
	d	$F_{p0,5}$	$R_{p0,5}$	F_m	R_m	A_{10}	A_{gt}
	mm	kN	N/mm^2	kN	N/mm^2	%	%
1	6	18.4	650	20.2	714	9.3	3.4
2	6	19.2	678	20.6	728	11.3	2.6
3	6	18.6	657	19.9	703	9.8	3.1
Requirement			*500*		*550*	*12.0*	
Average		18.73	661.7	20.23	715.0	10.13	3.03
St. Deviation		0.42	14.6	0.35	12.5	1.04	0.40

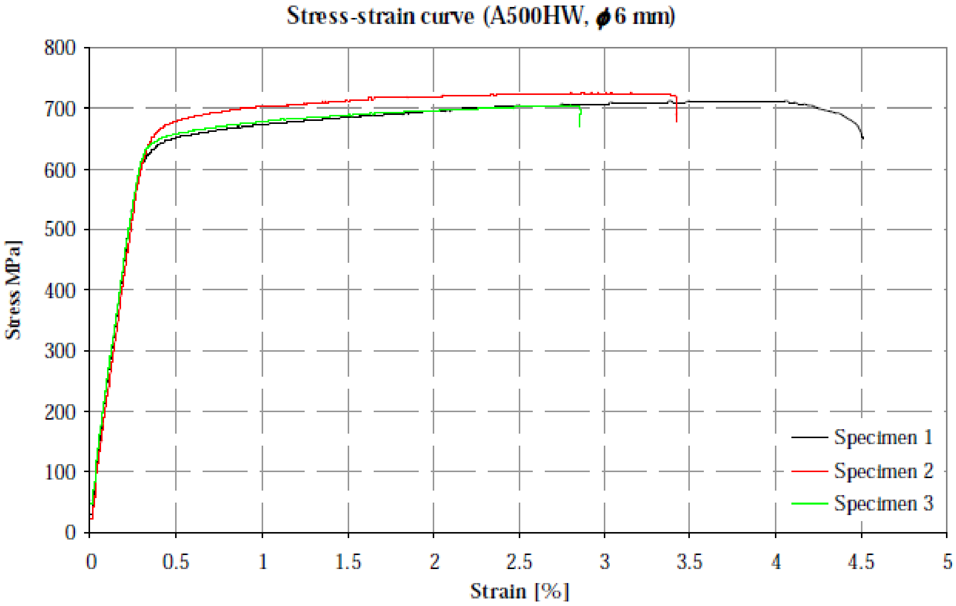

Figure 2-28: Flexural Test Reinforcing Steel Bar Strength.

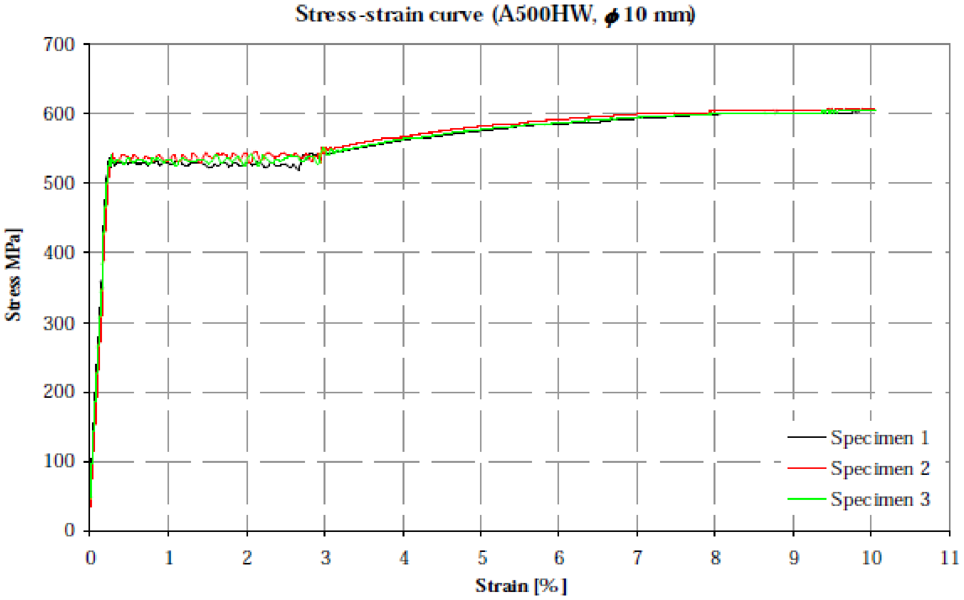

Figure 2-29: Punching Test Reinforcing Steel Bar Strength.

2.2.3 Missile Steel Data

The missile steel data for the Meppen test is presented in Figure 2-30. As seen in the Figure 2-30, the missile steel has an approximate failure strain of 25% and a peak stress of 400 MPa.

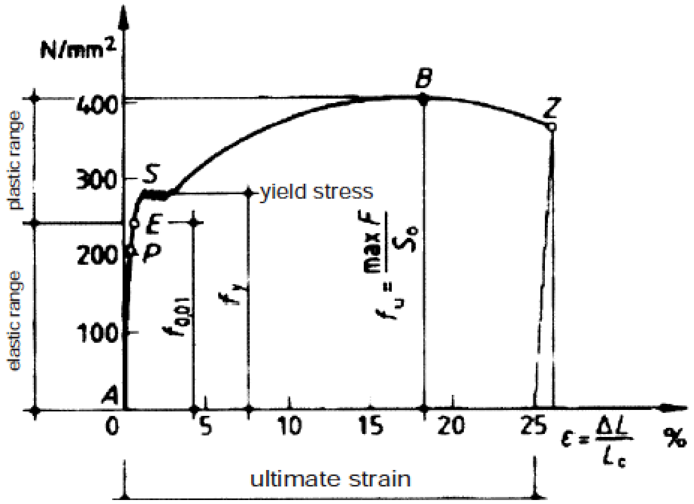

E = 210000 MPa
Poisson's ratio ν = 0.3

Figure 2-30: Meppen II-4 Test Missile Steel Strength.

Shown in Table 2-2 and Figure 2-31 is the data provided for the flexural test missile steel strength.

Table 2-2: Flexural Test Missile Steel Strength Requirements.

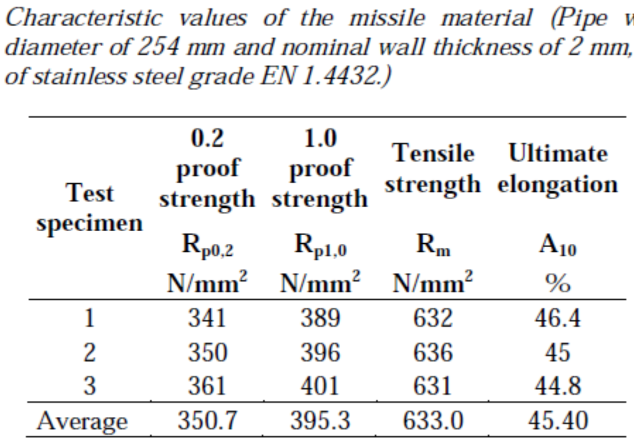

Characteristic values of the missile material (Pipe with outer diameter of 254 mm and nominal wall thickness of 2 mm, made out of stainless steel grade EN 1.4432.)

Test specimen	0.2 proof strength $R_{p0,2}$ N/mm²	1.0 proof strength $R_{p1,0}$ N/mm²	Tensile strength R_m N/mm²	Ultimate elongation A_{10} %
1	341	389	632	46.4
2	350	396	636	45
3	361	401	631	44.8
Average	350.7	395.3	633.0	45.40

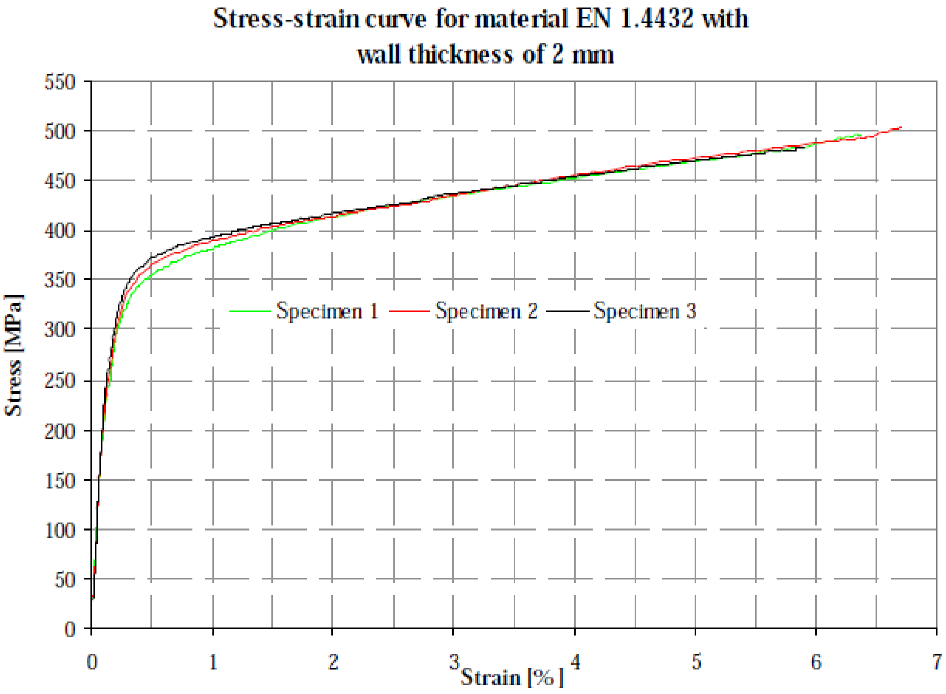

Figure 2-31: Flexural Test Missile Steel Strength.

2.2.4 Data Not Provided

There was a great amount of data that was either not available or unknown for all three impact tests. Shown in Table 2-3 is a summary of data missing for the three impact tests; an X represents missing data.

Table 2-3: Summary of Missing and/or Unavailable Test Data.

Test	Target Concrete Strain Rate Dependence	Missile Steel Strain Rate Dependence	Reinforcing Steel Bar Strain Rate Dependence	Missile Steel Thick Component Properties	Missile Concrete Fill Properties
Phase I and Phase II					
Meppen II-4	X	X			N/A
Flexural	X	X	X	X	N/A
Punching	X	X	X	X	X
Phase III					
Soft Missile	X	X	X	X	N/A

2.3 Phase I Finite Element Model Description

In this section the numerical model components representing the mesh, boundary conditions, and material models are discussed for Phase I.

2.3.1 LS-DYNA Numerical Models

All LS-DYNA finite element models (FEMs) were constructed using the SNL meshing tool, Cubit (Cubit, 2010). There was no FEM representation of the missile, since that was treated using the Riera method. The concrete target material was represented using standard 8-node hexagonal brick elements. The reinforcing steel bars (a.k.a. rebar) were modeled using 3-noded beam elements; whereby a third node is used only to reference the orientation of the two primary beam element nodes. The contact between rebar elements (beams) and concrete elements (hex8 bricks) was assumed to be rigid, thus not permitting any rebar slippage or pull-out behavior around the concrete material.

2.3.1.1 Treatment of Reinforcing Steel in Finite Element Models

All LS-DYNA simulations used a FEM whereby the mesh connected 2-noded bar elements (representing the reinforcing steel) to nodes of 8-noded hexagonal brick elements (that representing the concrete). The capability of matching rebar grid-work density resides in the concrete element mesh resolution, since rebar beam elements are connected to (coincident) nodes of the concrete hexagonal 8-noded brick elements. Due to this constraint, there is no representation of rebar that is spliced or overlapped, which is common in structures, etc. All rebar grids or mats consist of regular lines, represented as beam elements, connected to nodes. This simple realization results a two-dimensional grid whereby the steel is connected as a frame in vertical and horizontal directions. For example, several IRIS benchmark FEM rebar grids consisted of two-dimensional grids in the xy-plane representing longitudinal rebar layout schemes. Other two-dimensional grids comprised of beam elements vertically aligned in the z-direction were constructed to represent transverse (a.k.a*.,* stirrups) rebar layout schemes. These rebar meshes will be discussed and depicted in the next section.

2.3.1.2 Concrete Target Meshes

The IRIS 2010 Meppen II/4 simulation target mesh was constructed using 1/4 model symmetry; contrary to the punching and flexural mode simulation concrete target meshes which used full symmetry. The three IRIS 2010 simulation concrete target FEM meshes are shown in Figure 2-32, Figure 2-33, and Figure 2-34, respectively. Shown in each of these figures are the nodes associated with the Riera loading function (shown in aqua).

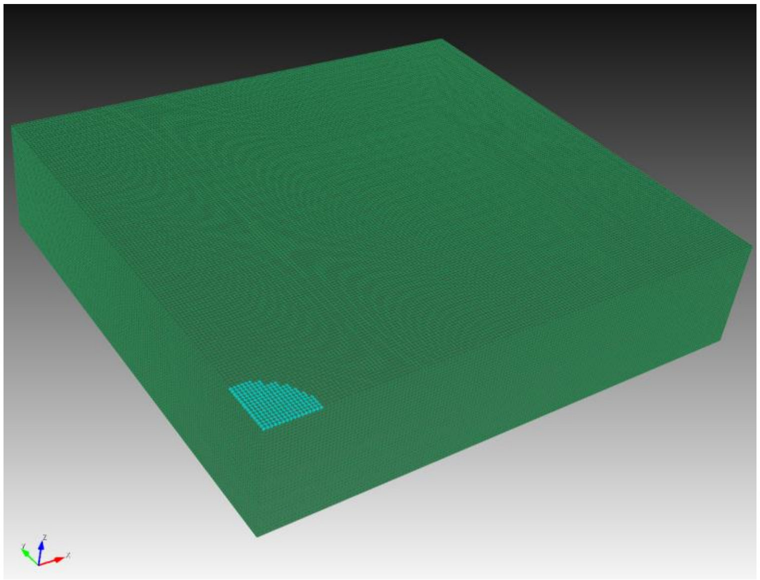

Figure 2-32: LS-DYNA Meppen II/4 Test Simulation Concrete Target Mesh, using 1/4 model symmetry, showing impact area for Riera load curve.

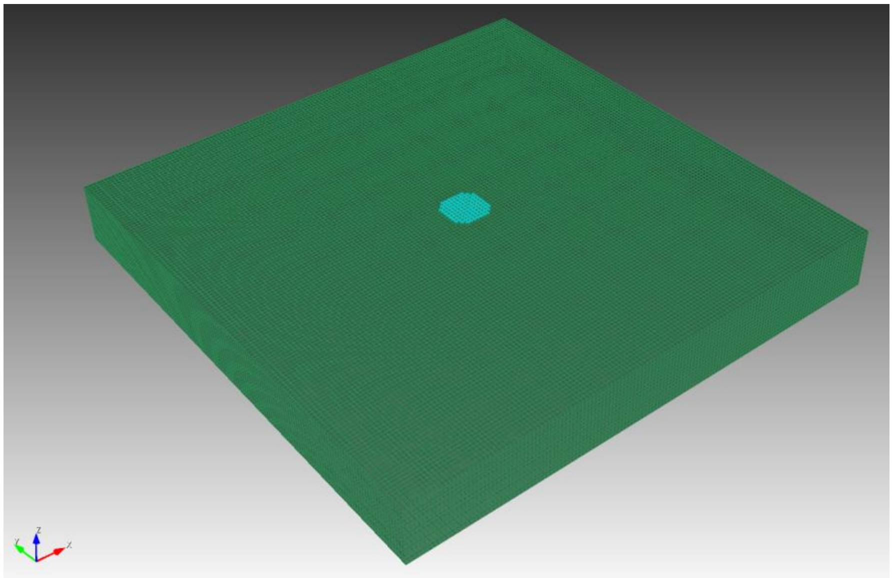

Figure 2-33: LS-DYNA Punching Mode Test Simulation Concrete Target Mesh, using full symmetry, showing impact area for Riera load curve

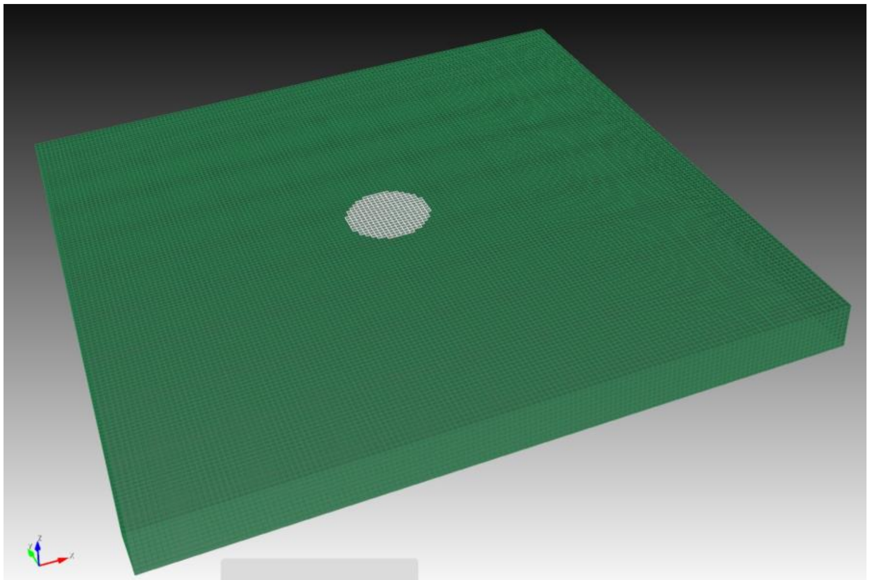

Figure 2-34: LS-DYNA Flexural Mode Test Concrete Target Mesh, using full symmetry, showing impact area for Riera load curve.

The discretization of the FEM concrete target meshes are shown below in Table 2-4.

Table 2-4: LS-DYNA Simulation Concrete Target Mesh Element Sizes.

Simulation	Nominal hexagonal 8-noded brick element characteristic length (mm)
Meppen II/4 Test	20
Punching Mode test	15.625
Flexural Mode Test	15.15

2.3.1.3 Steel Reinforcing Bar Meshes

Using the rebar-beam/concrete-brick coincident meshing technique, both the rebar area per unit length (longitudinal rebar elements) and rebar area per concrete area (transverse or stirrup rebar elements) density requirements, as specified for each benchmark exercise, were maintained.

The spacing of the steel reinforcing bars was limited by the concrete hex8 element discretization. Shown in Table 2-5 are the reinforcing steel bar grid dimensions (i.e., number of bars) for each of the three reinforced concrete targets.

Table 2-5: Reinforcing Steel Bar Grid Layout for each Target.

Simulation	Width or X-direction (m)	Length or Y-direction (m)	Number of bars along X direction	Number of bars along Y direction	Number of bars along Z direction
Meppen II/4*	6.0	6.5	52	56	728
Punching Mode	2.1	2.1	23	23	N/A
Flexural Mode	2.1	2.1	37	37	324

*Note that simulation #1 used ¼-model symmetry; these values correspond to a full model

In order to satisfy the steel density of the target specifications, the following two formulas were used to solve for the reinforcing steel bar diameters:

Equation 1

$$d_{Bar,L} = \sqrt{\frac{A_L * L_{SPAN} * 4}{N_{BAR} * \pi}}$$

Equation 2

$$d_{Bar,L} = \sqrt{\frac{A_L * L_x * L_y * 4}{N_{BAR} * \pi}}$$

where

$d_{BAR,L}$ = Diameter of Reinforcing Steel Bar (Longitudinal),
$d_{BAR,T}$ = Diameter of Reinforcing Steel Bar (Transverse),
A_L = Longitudinal Linear Density (cm/m^2),
A_T = Transverse Areal Density (m^2/m^2),
L_{SPAN} = Length of target in direction rebar is laid (m),
L_X = Width of Target along x-direction (m),

L_Y = Length of Target along y-direction (m), and
N_{BAR} = Number of reinforcing bars.

Solving Equation 1 and Equation 2, Table 2-6 shows the final reinforcing bar diameters that satisfy the longitudinal and transverse reinforcing steel bar densities.

Table 2-6: Calculated Reinforcing Steel Bar Diameters from Density Specifications.

Simulation	Specified Longitudinal Steel Reinforcing Bar Density (cm^2/m)	Specified Transverse Steel Reinforcing Bar Density (m^2/m^2)	Computed Reinforcing Steel Longitudinal Bar Diameter (mm)	Computed Reinforcing Steel Transverse Bar Diameter (mm
Meppen II/4 (Front Face, X-direction)	27.30	N/A	20.03	N/A
Meppen II/4 (Front Face, Y-direction)	27.30	N/A	20.01	N/A
Meppen II/4 (Rear Face, X-direction)	53.60	N/A	28.06	N/A
Meppen II./4 (Rear Face, Y-direction)	53.60	N/A	28.14	N/A
Meppen II/4 (Transverse)	N/A	50.2	N/A	18.65
Punching Mode (Front or Rear Face, X- or Y-direction)	8.70	N/A	10.06	N/A
Flexural Mode (Front or Rear Face; X- or Y-direction)	5.00	N/A	6.011	N/A
Flexural Mode (Transverse)	N/A	50.00	N/A	9.309

Figure 2-35, Figure 2-36, and Figure 2-37 show the reinforcing bar grid layout for each of the IRIS benchmark simulations.

All LS-DYNA simulations used the Hughes-Liu Beam element with a rectangular cross-section type. All rebar cross-sections were assumed to be square-box shaped, with the side length of the cross-section equal to the particular reinforcing steel bar outer diameter. All beam elements used the default LS-DYNA integration scheme, 2 x 2, or four integration points. A circular shaped cross-section beam element was not used due to problems encountered with added complexity and material model compatibility.

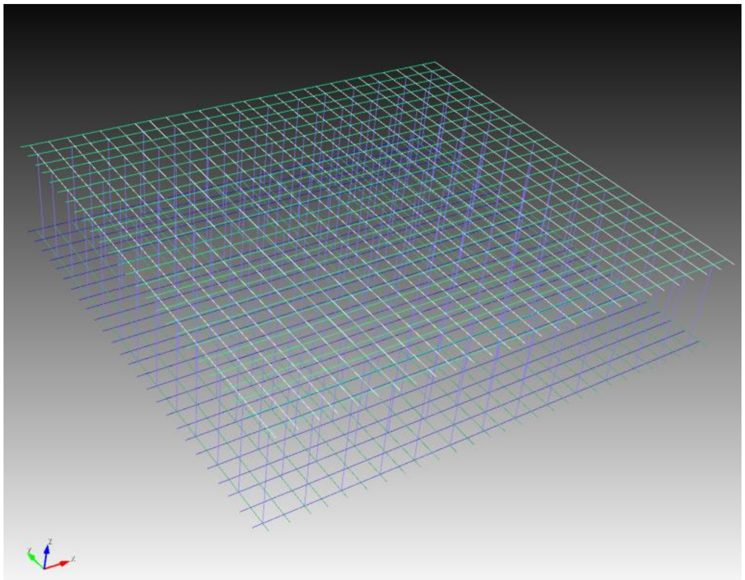

Figure 2-35: LS-DYNA Meppen II/4 Test Simulation Rebar Grid.

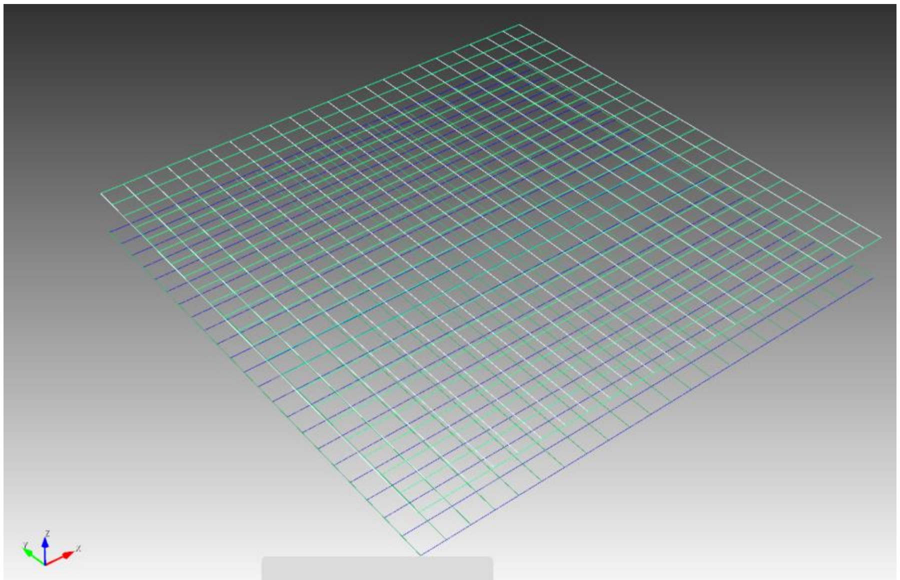

Figure 2-36: LS-DYNA Punching Mode Test Simulation Rebar Grid.

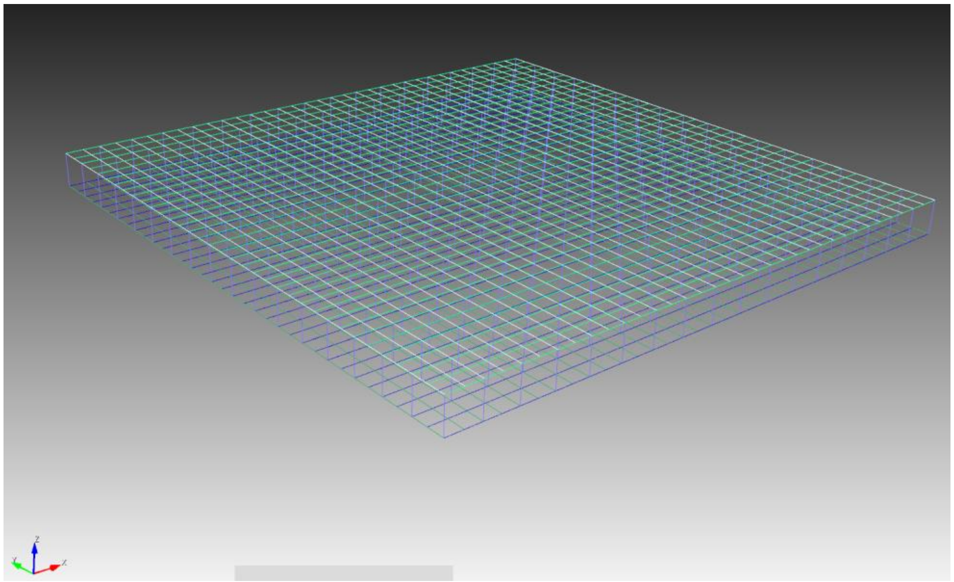

Figure 2-37: LS-DYNA Flexural Mode Test Simulation Rebar Grid.

2.3.1.4 Concrete Data Sets

Table 2-7 summarizes the final concrete target properties used in all the LS-DYNA simulations. As shown in Table 2-7, the Poisson ratio used in the numerical simulation is 0.25, which is rather high (typical values for the Poisson ratio of concrete are in the range 0.18 to 0.20).

Table 2-7: Concrete Strength Properties used in the LS-DYNA Simulations.

Simulation	Density (kg/mm^3)	Compressive Strength (MPa)	Tensile Strength (MPa)	Poisson Ratio	Elastic Modulus (GPa)
Meppen II/4 Test	2.25×10^{-6}	46.00	4.70	0.25	39.80
Punching Mode	2.30×10^{-6}	74.60	4.04	0.25	29.43
Flexural Mode	2.30×10^{-6}	76.00	3.71	0.25	26.92

2.3.1.5 Reinforcing Bar Data Sets

The IRIS 2010 project committee supplied reinforcing steel test data for the all three tests. Strain-rate data for the Type RK BSt 420/500 steel was supplied for the Meppen II/4 test. The other tests, both punching mode and flexural mode, used a different type of reinforcing steel, known in the European community as A500 HW. There was no strain-rate data provided for the A500 HW steel reinforcing bar material. The A500 HW steel is similar to ASTM A706 grade 60 steel, based on initial yield and ultimate strength. Table 2-8 summarizes the reinforcing steel properties used in the LS-DYNA simulations.

Table 2-8: Reinforcing Steel Strength Properties used in the LS-DYNA Simulations.

Simulation	Density (kg/mm^3)	Poisson Ratio	Yield Strength (MPa)	Ultimate Strength (MPa)	Ultimate or Failure Strain (%)	Strain-rate data provided?
Meppen II/4 Test	7.84 x 10^{-6}	0.30	500	620	5^{+}	Yes
Punching Mode	7.84 x 10^{-6}	0.30	595	669	15^{++}	No
Flexural Mode	7.84 x 10^{-6}	0.30	595	669	15^{++}	No

$^{+}$Meppen II/4 Test Simulation steel material odel is based on strain rate data provided (constant failure strain is not used by the LS-DYNA MAT_PIECEWISE_LINEAR_PLASTICITY model with connected strain rate functions)
$^{++}$Punching and Flexural Mode Test Simulations used 15% ultimate failure strain (average ultimate failure elongation)

2.3.1.6 Material Models

All three of the numerical simulations used the LS-DYNA material model MAT_CONCRETE_72REL3 to simulate the response of the concrete target. This material model is the Karagozian and Case (K&C) Concrete Model Release III (Malvar, Crawford, & Morrill, 2000)

The Meppen II/4 test simulation used the LS-DYNA strain-rate plasticity material model (MAT_PIECEWISE_LINEAR_PLASTICITY) to simulate the response of the steel reinforcing bars, since strain-rate data was provided by the IRIS 2010 project committee. The punching mode and flexural mode simulations used the LS-DYNA kinematic plasticity material model (MAT_PLASTIC_KINEMATIC) to predict the behavior of the steel reinforcing bars. For the second and third simulations, no strain-rates data was provided, so a simpler elastic-plastic material model was chosen.

2.3.1.7 Concrete Model

The K&C concrete model decouples the shear and volumetric responses, and is based on a three-invariant model which uses three shear failure surfaces, and includes both damage and strain-rate effects (Magallanes, Wu, Malvar, & Crawford, 2010). Due to the inherent three-invariant formulation to construct the yield surface, the model is capable of distinguishing triaxial extension and triaxial compression load paths in stress space. The K&C model use stress differences to describe the yield surface, the limit surface, and the residual surface. The model monitors the current state of the stress difference relative to these three failure surfaces. During the initial loading or reloading, the stresses are elastic until an initial yield surface is reached. The initial yield surface hardens to the limit surface or softens to the residual surface, depending on the loading or the material state.

The K&C concrete model employs an equation of state (EOS) to control the volumetric response, *i.e.*, the pressure, $\boldsymbol{P}$, versus volumetric strain, $\boldsymbol{\varepsilon_v}$. The K&C concrete model's EOS prescribes a tabulated set of pressure and unloading bulk modulus as a function of volumetric strain.

All simulations used the LS-DYNA K&C automatic material model generation method by supplying the unconfined compressive strength of the concrete.

2.3.1.8 Rebar Model

The LS-DYNA strain-rate plasticity model, MAT_PIECEWISE_LINEAR_PLASTICITY, employs a load curve to describe the yield strength, σ_0, as a function of effective strain rate, $\dot{e}_{eff}$, where

Equation 3

$$\dot{e}_{eff} = \sqrt{\frac{2}{3} * \varepsilon_{ij}^{\prime} \varepsilon_{ij}^{\prime}}$$

where,

$\dot{\varepsilon}_{ij}$ = indicial notation of deviatoric strain rate tensor components.

The yield stress, σ_Y, is defined as

Equation 4

$$\sigma_y = \sigma_0 * \dot{e}_{eff} + H * \varepsilon_{eff,p}$$

where,

$\varepsilon_{eff,p}$ = Effective plastic strain, and
H = Hardening Modulus

Equation 5

$$H = \frac{E * E_{TAN}}{E - E_{TAN}}$$

where,

E = Elastic modulus, and
E_{TAN} = Tangent modulus.

The LS-DYNA MAT_PIECEWISE_LINEAR_PLASTICITY model allows a simple mechanism to incorporate material failure. This option is activated by specifying a load curve ID defining the effective stress at failure as a function of strain rate.

The LS-DYNA plasticity model, MAT_PLASTIC_KINEMATIC, allows kinematic hardening and is compatible with the Hughes-Liu beam element. Through use of a user-define parameter, β, either kinematic, isotropic, or a combination kinematic and isotropic hardening may be obtained. The punching mode and flexural mode simulations used a prescribed value of $\beta = 0$ to implement full kinematic hardening behavior.

2.3.1.9 Boundary Conditions

The boundary conditions were applied to all of the benchmark simulations using nodal point constraints to prescribe a zero displacement condition normal to the impact surface at the rear surface of the reinforced concrete target. This direction is the *z*-component, and is consistent for all three LS-DYNA simulations, where the target resides in the x-y direction, with the impact surface being equal to (positive) half of the target thickness (*i.e.,* at coordinate $z = \frac{1}{2}$ target thickness). All of the LS-DYNA simulation used the single point constraint method to invoke no z-displacement boundary conditions. Since the Meppen II/4 Test (simulation #1), used ¼ model symmetry, a no *x*-displacement and no *y*-displacement boundary conditions were imposed on the symmetry faces (left *yz*-plane, and bottom *xz*-plane, respectively; see Figure 2-39)

The IRIS 2010 committee supplied a diagram displaying the 48 support points holding the Meppen II/4 test target in place, shown in Figure 2-38. Shown in Figure 2-39 is the FEM of the Meppen II/4 Test target ¼ model support points. For the full model, 48 equally spaced points are used to constrain the target during the impact. Thus, for the ¼ model representation of the Meppen II/4 test, 12 equally spaced points are used to impose a no z-displacement condition on the rear surface of the target in the *z*-direction.

Both the punching mode and flexural mode test targets were constrained as described in the schematic supplied by the IRIS 2010 committee, shown in Figure 2-40 and Figure 2-41, respectively. The proper orientation in Figure 2-40 or Figure 2-41 is that the positive z-direction is vertically upward. In order to accommodate this particular front and rear target surface clamp condition, both punching and flexural mode simulations used the LS-DYNA boundary single point constraint condition at defined node sets as shown in the FEM of Figure 2-42. Thus, nodeset 3 is the boundary condition to clamp the front and back faces of the target along the x-direction; whereby a no z-displacement constraint is applied and rotations about the x-direction are allowed (displacements in both the x-direction and y-direction are allowed, and no rotation about the either the y-direction or the z-direction is allowed). Likewise, nodeset 4 is the boundary condition used to enforce clamping on the front and back faces of the target along the y-direction; whereby a no z-displacement constraint is applied is and rotations about the y-direction are allowed (displacements in both the x-direction and y-direction are allowed, and no rotation about either the x-direction or the z-direction is allowed).

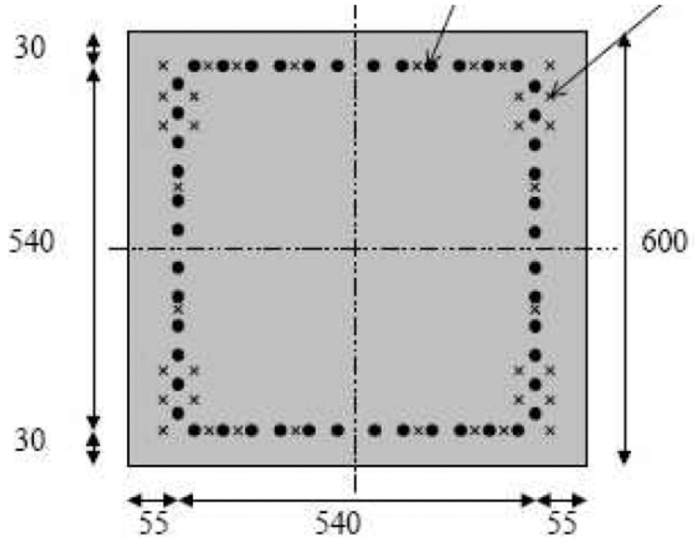

Figure 2-38: Meppen II/4 Test Support Points (black dots) on rear of target, z = -0.35 m.

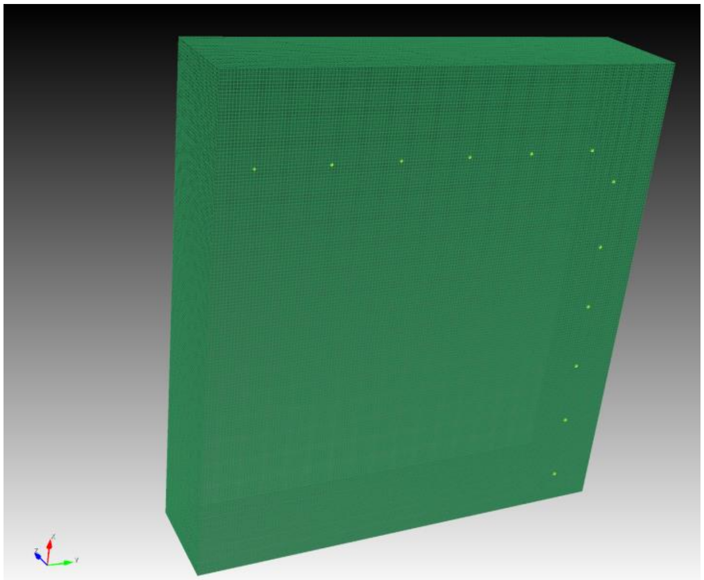

Figure 2-39: LS-DYNA Meppen II/4 Test Simulation Model no z-displacement boundary condition constraint.

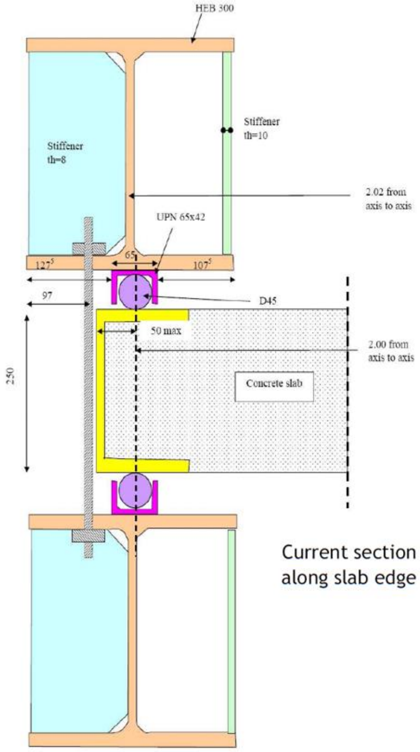

Figure 2-40: LS-DYNA Punching Mode Test Target constraint schematic (purple circles contact target to constrain motion).

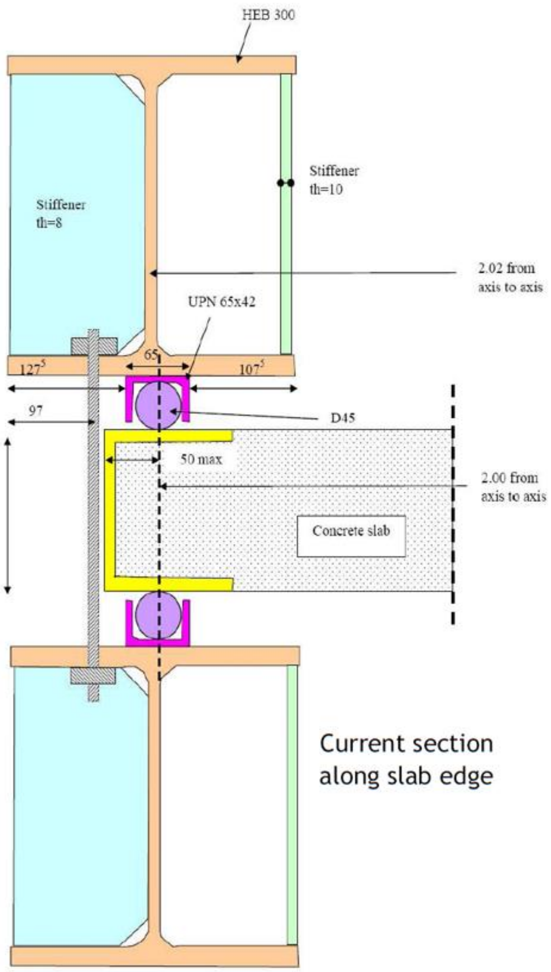

Figure 2-41: LS-DYNA Flexural Mode Test Target constraint schematic (purple circles contact target to constrain motion).

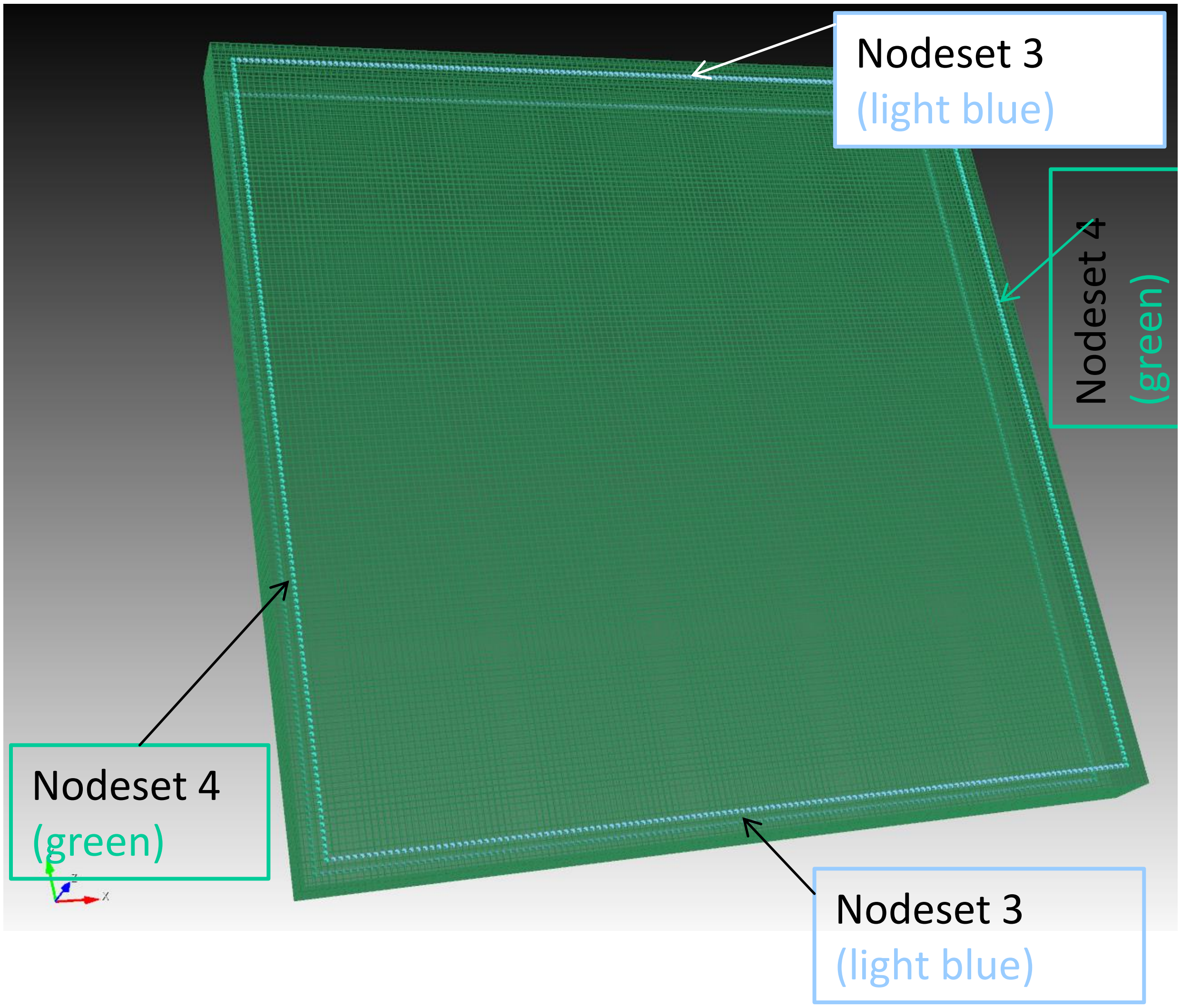

Figure 2-42: LS-DYNA Punching Mode and Flexural Mode Test Simulation Model of Target with no z-displacement nodes (highlighted in turquoise) on both front and rear of target.

2.3.1.10 Miscellaneous Conditions for Reinforced Concrete FEM models

All of the LS-DYNA simulations modeled the steel reinforcement bars explicitly using beam elements. In order to share nodes with the hexagonal 8-noded brick concrete elements, although meshes were already constructed using coincident nodes, these beam elements were coupled to the concrete material elements using the LS-DYNA method, *CONSTRAINED_LAGRANGE_IN_SOLID technique.

2.3.2 EMU Numerical Models

The EMU peridynamic microplastic material model was used for all components in the EMU simulations (*i.e.,* steel projectile, concrete target, and steel reinforcing bars). The microplastic model enforces the condition that peridynamic bonds respond independently of each other and permit permanent strain within the bond. The bond interactions can be thought of as nonlinear springs with history dependence. In all EMU simulations, the bond parameters were determined from the material properties listed in Table 2-9. For example, the stiffness of bonds in the elastic region, prior to yielding, was calibrated to the Young's modulus.

The interface bonds between concrete and rebar were treated as having the same properties as the concrete. Alternative assumptions were investigated but did not improve the agreement in the Meppen II/4 calculation with the available test results.

In all three EMU calculations, the numerical grid was set up using an external grid generator, rather than through code input. Each grid generator was a separate computer program that determines the initial positions of each numerical node. The grid generators created the EMU grids for all components in the models, including the projectile and target. The geometric spacing and layout of the steel reinforcing bars was determined from the data available (IRIS-Meppen, 2010),(IRIS-Punching, 2010), (IRIS-Flexural, 2010), although in some cases the arrangement had to be computed indirectly.

A nonzero angle of attack was assumed in all three calculations because of the practical difficulty of achieving ideal normal impact. It is not clear what controls or measurements were in place in the tests for angle of attack. Since no information was available, it was necessary to make some assumption about angle of attack. A value of 3 degrees was found to reproduce, to a reasonable extent, the kink angle that seems to be present in the post-impact image of the Meppen II/4 projectile given in (IRIS-Meppen, 2010), although this image is not very clear.

The model parameters for the three EMU simulations are listed below in Table 2-9.

Table 2-9: Parameters used in all three EMU calculations.

Parameter	Units	Meppen II/4	Flexural Test	Punching Test
Panel geometry				
Width (x)	m	6.5	2.1	2.1
Height (y)	m	6.0	2.1	2.1
Thickness (z)	m	0.7	0.15	0.25
Concrete				
Young's modulus	GPa	29	30	30
Poisson ratio		0.25	0.25	0.25
Flow stress	MPa	37	50	50
Failure strain		5.0E-4	2.5E-4	2.5E-4
Density	kg/m^3	2200	2200	2200
Reinforcement				
Front rebar diameter	mm	20	6	10
Front rebar spacing	mm	115	57	90
Number of rebars, front		53 + 57	37 + 37	23 + 23
Rear rebar diameter	mm	28	6	10
Rear rebar spacing	mm	115	57	90
Number of rebars, rear		53 + 57	37 + 37	23 + 23
Transverse rebar diameter	mm	20	9	none
Number of rebars, transverse		748	361	none
Young's modulus	GPa	210	210	210
Flow stress	MPa	500	600	600
Density	kg/m^3	7850	7850	7850
Failure strain		0.08	0.08	0.8
Projectile				
Length	m	6.0	2.1	0.64
Diameter	m	0.6	0.254	0.168
Mass	kg	1016	50	47.7
Density	kg/m^3	7245	7840	7400
Young's modulus	GPa	194	210	198 (case) 22 (fill)
Flow stress	MPa	400	400	600 (case) 60 (fill)
Failure strain		0.5	0.5	0.5 (case) 2.50E-4 (fill)
Impact velocity	m/s	247.7	110	136
Angle of impact	deg	0	0	0

Parameter	Units	Meppen II/4	Flexural Test	Punching Test
Angle of attack	deg	3	3	1
Numerical				
Node spacing	mm	40	15	15
Peridynamic horizon	mm	110	45	45
Total number of nodes		470,531	254,065	356,143
Number of processors (NNSA Redsky computer)		32	32	32
Time simulated	ms	100	30	30
Time step size (typical)	μs	1.8	0.49	1.0
Cpu time (each processor)	hr	11.0	15.3	9.5

2.3.2.1 EMU Peridynamic Model of the Meppen II/4 Test

The flow stress in the concrete was assumed to equal the unconfined compressive stress. This is the simplest assumption about reinforced concrete ductile response. Concrete alone is a brittle material, yet when concrete is reinforced with steel, the composite material becomes ductile. The flow stress depends on the confining hydrostatic pressure and other variables such as strain rate and damage. The critical bond strain for tensile failure was found from $2.5f_t/E$, where f_t is the tensile strength, E is the Young's modulus, and the factor of 2.5 accounts for the increase in strength due to dynamic, as opposed to static, loading.

Metal components, including the reinforcing bars and the projectile, were also treated as microplastic, with model parameters as shown in Table 2-9. Although the projectile was constructed with multiple components with varying thickness, the model contained just one node through the shell radially. The varying thickness of the projectile wall was accounted for in the model by assigning node volumes appropriate to actual thickness at each location.

The load cells were modeled explicitly according to the positions given by the IRIS 2010 project committee (IRIS-Meppen, 2010). They were assumed to be weakly coupled to the panel in tension. Although this assumption is not perfect, it was found by trial and error that strong coupling gave worse agreement with the test data for the structural response of the panel.

Shown in Figure 2-43 and Figure 2-44 are the view of the target panel and projectile at the time of impact, and a close-up view of the rebar pattern in the target, respectively. Note that each dot in these figures represents an EMU peridynamic numerical node.

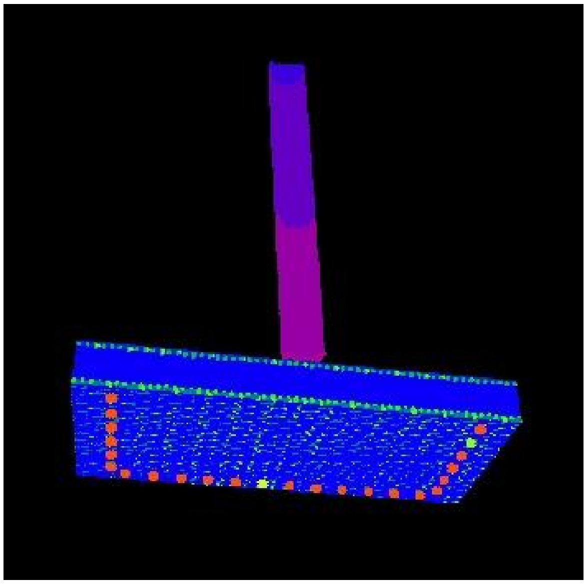

Figure 2-43: Initial EMU Meppen II/4 Test Simulation Grid.

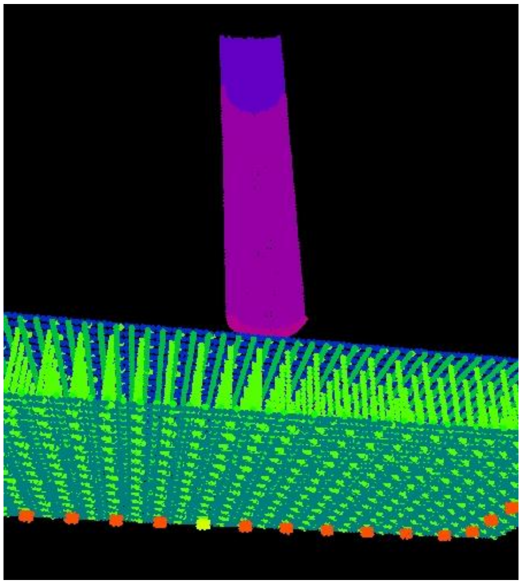

Figure 2-44: Reinforcement in the EMU Meppen II/4 Test Simulation Grid.

2.3.2.2 EMU Peridynamic Model of the Punching Mode Test

The EMU numerical model geometry and test conditions were similar to a smaller-scale version of the Meppen II/4 test. One significant difference was that instead of load cells, the panel edges were held in place by rollers that approximate a simply supported boundary condition. These rollers were modeled explicitly in the numerical model, making some simplifying assumptions. In particular, the supporting frame structure was not modeled. Instead, the roller positions were assumed to be fixed. The importance of the frame response was not investigated; this could be a source of error in the calculation. The EMU punching model of the target panel was similar to the flexural mode panel, but has with greater thickness and contains no transverse reinforcement.

The specifications for the punching mode test (IRIS-Punching, 2010) reported an unusually high value of unconfined compressive strength for the concrete, about 60 MPa. For purposes of assigning a plastic flow stress in the model, this value was reduced somewhat arbitrarily to 50 MPa. This reduction was made because, based on previous experience using EMU and peridynamic models.

The tensile failure strain in the rebar was also reduced to 0.08 instead of the reported value of 0.12. This change was based on experience (using peridynamics and EMU) that has shown failure of rebar in the presence of impact loads in concrete, particularly if the rebar undergoes bending, can occur at significantly lower strains than are measured in a uniaxial tension test.

Shown in Figure 2-45 is the initial EMU punching mode grid viewed on a vertical cross-section. The fill and case materials in the steel projectile are modeled explicitly, but the net effect is that the projectile acts like a rigid cylinder. Shown in Figure 2-46 is a close-up view of the EMU punching model target reinforcement.

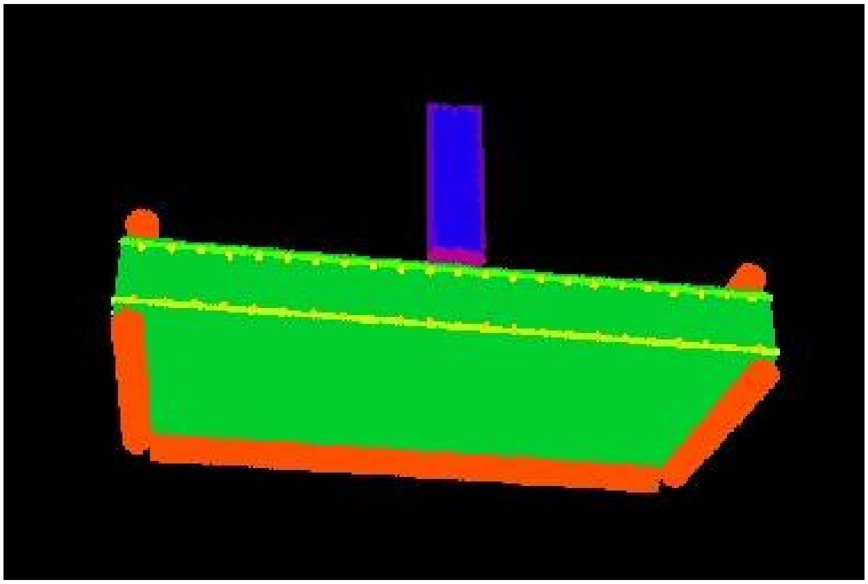

Figure 2-45: Initial EMU Punching Mode Simulation Grid. Rollers (red) provide boundary conditions at the edges of the panel.

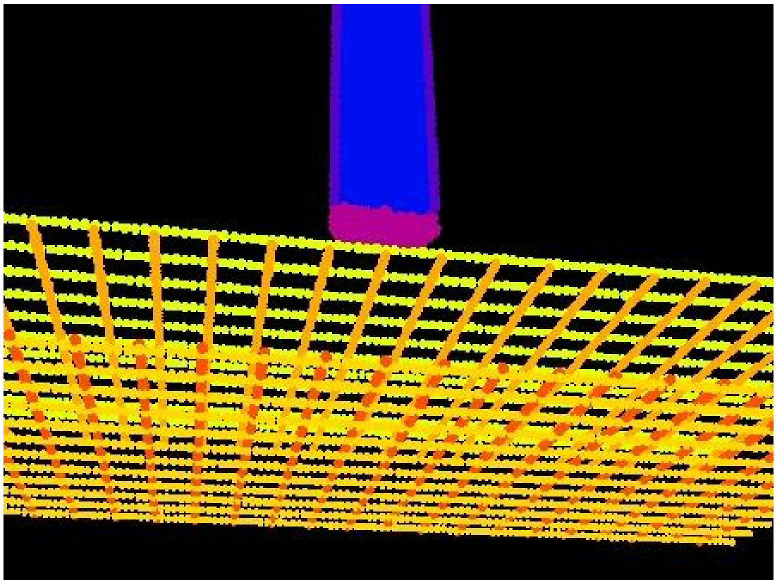

Figure 2-46: Reinforcement in the EMU Punching Mode Test Simulation Model.

2.3.2.3 EMU Peridynamic Model of the Flexural Mode Test

The EMU target boundary conditions and material properties were the same as for the Punching Mode Test (Section 2.3.2.1). The model for the projectile was defined using techniques similar to the Meppen II/4 model (Section 2.3.2.2).

Shown in Figure 2-47 is the initial EMU flexural mode grid along a vertical cross-section, including the rollers that support the edges of the panel. Shown in Figure 2-48 is a close-up view of the EMU flexural model target rebar grid.

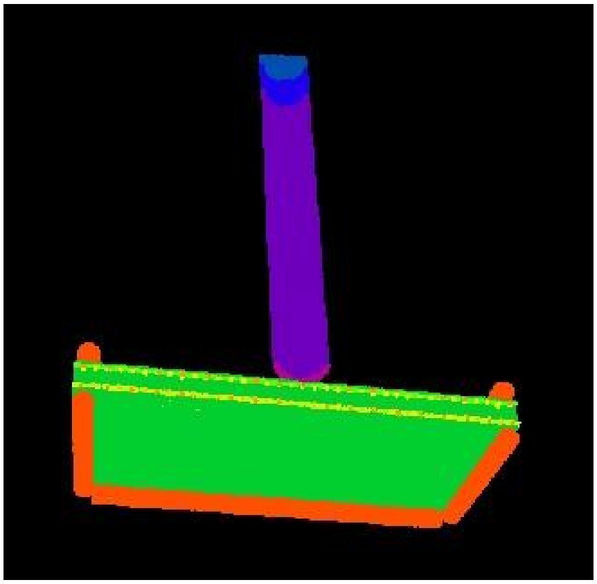

Figure 2-47: Initial EMU Flexural Mode Simulation Grid. Rollers (red) provide the boundary conditions on the panel.

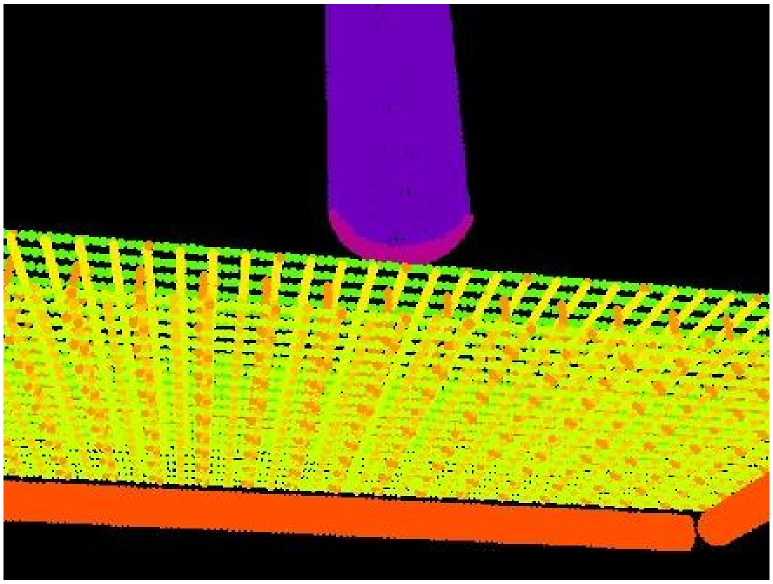

Figure 2-48: Reinforcement in the EMU Flexural Mode Test Simulation Model.

2.4 Phase I Results and Summaries

2.4.1 LS-DYNA Finite Element Method Advantages and Limitations

The major advantages versus consequences and drawbacks of the LS-DYNA Riera load function approach are compared below in Table 2-10.

Table 2-10: Advantages and Drawbacks of LS-DYNA Riera Load Function Approach.

Advantages	Consequences and Drawbacks
Riera Load Function approach is simple: avoids contact models and alleviates constructing an additional finite element model of missile.	Crushing Strength and Mass Distribution of missile is challenging for simplified Riera Loading approach. Visual penetration of target from a missile not possible (*e.g.,* plugging type target response presents extra challenges)
Karazogian and Case (K&C) concrete material model input requires only two parameters	K&C concrete material model does not provide a crack pattern visualization
Reinforcing Steel Bar material model based on yield strength (Flexural and Punching tests) without strain rate dependence.	Dynamic Increase Factors are well known attributes of steel reinforcing bar used in concrete structure response; they are strain rate dependent.
Coincident nodes for concrete material (hexagonal 8-noded brick elements) and reinforcing steel (pseudo 3-noded beam elements) permit orthogonal steel grid and concrete material geometric distribution.	(1) Steel Reinforcing Bar is not allowed to slip or exhibit pullout behavior – a more sophisticated contact model is needed to adequately address behavior between concrete and steel reinforcing bar. Finite Element Models may not have capability to include both coincident nodes and slippage/pullout response type behavior. (2) Steel Reinforcing Bar density (length steel/area concrete) may not always be preserved. (Caveat was to change diameter of steel bar to enforce density specifications.)
Meppen II/4 Simulations using ¼ Model Symmetry reduces computational resources	Unable to adequately include angle of attack and/or angle of impact; Forced symmetry may not replicate response of test target behavior (*e.g.*, radial crack pattern, measured load response at force transducers, etc.)

2.4.2 LS-DYNA Finite Element Method Improvements for Future Simulations

Use greater computational resources to include fully discretized finite element model of missile.

Investigate the influence of typical concrete Poisson's ratios (0.18 - 0.20).

Include steel penetrator (missile) and concrete material contact model + steel penetrator and steel reinforcing contact model.

Include erosion effects (LS-DYNA terminology) to replicate scabbing and spall behavior of concrete material (Other computational methods involving material deletion are sometimes denoted as "element death" or "discarded cells/material", etc.).

Explore different concrete material model (*e.g.*, LS-DYNA Winfrith Concrete model) to exploit fracture/crack patterns for visualization.

2.4.3 EMU Peridynamics Method Advantages and Limitations

In this exercise, the EMU peridynamics code did not exhibit any surprising sensitivities or pathological behavior, such as numerical instability. Although many calculations were required to reproduce the Meppen II/4 test results with reasonable fidelity, this repetition was mainly to correct input errors.

The authors consider the following to be the most likely sources of uncertainty in the predictive modeling of the Flexural Mode Test and the Punching Mode Test:

- Concrete penetration is widely thought to involve a strong size scale effect, in which small scale targets act differently (usually appearing stronger) than large targets. This effect, which is difficult to quantify and whose origin is controversial, was not considered in the EMU analysis.
- The unconfined compressive strength of concrete is an important but incomplete measure of the material response under large stress and high deformation.
- Rate effects in material response were not included explicitly in the EMU material model. These are generally measured with split Hopkinson bar tests, but these tests do not take into account confining pressure and do not relate directly to deformations with high rates of shear.

Strengths of the EMU peridynamics code for this application include the following:

- EMU utilizes a meshless Lagrangian formulation which avoids complex mesh generation requirements and problems with mesh tangling or distortion.
- It provides treatment of fracture without supplemental relations or special numerical techniques needed with finite elements.
- Its formulation inherently allows large strains and nonlinearity.
- The method lends itself to massively parallel computation.
- The contact algorithm is simple and fairly robust.
- EMU allows incorporation of any material model that can be used with finite elements (although this capability was not used in the results presented here).
- Because the formulation is nonlocal and explicitly involves a material length scale, it could potentially take into account the effect of aggregate size in localizations such as those predicted to occur on the surface of the plug in the Punching Mode Test.

Some of the EMU peridynamics code weaknesses include:

- EMU does not allow large variations in grid spacing within a model.
- It runs slower than traditional finite element method codes.
- It does not represent the bending rigidity of rebar.
- It does not treat friction at sliding interfaces.

3 PHASE II: IMPACT OF LARGER STRUCTURES

3.1 Phase II Test Overview

The portions pertaining to Phase II describe analyses and numerical results obtained from simulations of a steel missile impacting a concrete target reinforced with steel bars using two different computer codes: LS-DYNA and EMU. Phase II of the IRIS program was implemented to continue the activity developed in Phase I. The objectives were as follows:

- To give the opportunity to IRIS 2010 participants (plus newcomers) to update and improve the simulations with the knowledge of the test results and with the experience gained by one's own 1st computation and by others' computations using a single set of material properties;
- To give the opportunity to each participant to develop, test, and share the means and tools for alternative approaches ("simplified models");
- To gather all the results from the new simulations and all the proposals of simplified models and to issue a new set of recommendations.

This section introduces the two different numerical analyses, define the three test conditions, compare and contrast several numerical code simulation results of the three tests, and discuss the advantages and limitation of each computational approach. In order to maintain clarity, many detailed component schematics and test material data sets, etc. are listed in other publications.

3.1.1 LS-DYNA Finite Element Modeling Approach

The LS-DYNA finite element code was used to analyze the three impact experiments. First the Meppen II/4 test was analyzed and used to develop the appropriate modeling procedures and techniques including the material models, boundary conditions, and loading schemes. After completing the benchmarking of the Meppen II/4 test, the two pretest analyses were conducted: punching and flexural mode. All three of the LS-DYNA simulations used a force-time history, or Riera load function, to represent the impact of the missile onto the reinforced concrete panel. This simplification eliminates issues with material-interface contact algorithms and reduces the size of the numerical model which decreases simulation run times. This method of alternative loading is frequently used for finite element simulations involving impact and/or dynamic force conditions.

The LS-DYNA code is a three-dimensional transient dynamics finite element code well suited for complex engineering analysis of various impact scenarios. All LS-DYNA calculations were performed using explicit time integration with code version mpp971d R5.0, revision 59419. All of the LS-DYNA simulations were conducted on the Common Engineering Environment cee-compute003 (formerly known as ceesmp3) computer system located at Sandia National Laboratories in Albuquerque, NM.

3.1.2 EMU Peridynamic Modeling Approach

Similar to the LS-DYNA simulations, the Sandia-developed EMU peridynamics code was used to predict the response of three impact experiments. Again, first the Meppen II/4 test was analyzed and used to develop the appropriate modeling procedures and techniques including the material models, boundary conditions, and loading conditions. After completing the benchmarking of the Meppen II/4 test, the remaining two pretest analyses were conducted on the punching and flexural mode tests. Unlike the LS-DYNA simulations, all three of the EMU simulations used an explicit representation of the missile impacting the reinforced concrete panel.

The EMU code provides numerical solutions to the equations of the peridynamic theory of continuum mechanics (Silling & Askari, 2005). EMU is three-dimensional code and operates without a computational mesh (note that finite element meshes are comprised of connected nodes and elements). Explicit time integration was used in the application discussed in this report. All EMU simulations were completed using code version 2.6.32. All of the calculations were performed on the National Nuclear Safety Administration Redsky computer system located at Sandia National Laboratories in Albuquerque, NM.

The peridynamic theory is an extension of the conventional theory of solid mechanics that allows greater generality and flexibility in treatment of damage and fracture. In the peridynamic model, cracking is treated without the need for supplemental relations that in standard methods would be required to prescribe the nucleation and growth of cracks. Therefore, the peridynamic approach offers advantages for modeling of problems involving the spontaneous growth and mutual interaction of multiple dynamic fractures in complex geometries. The theory has been under development for 11 years.

3.1.3 IRIS 2010 Tests

As mentioned earlier, the three tests involve a steel projectile, or a missile, impacting a heavily reinforced concrete panel, or target. Descriptions of each IRIS 2010 test's steel missile and corresponding target are provided in prior sections.

3.2 Phase II Test Data and Material Properties

Phase II was a continuation of Phase I, so all test data and material properties given for Phase I apply to Phase II.

3.3 Phase II Finite Element Model Description

In this section the numerical model components representing the mesh, boundary conditions, and material models are discussed for the 2012 standard concrete cylinder tests and for the three missile impact models for Phase II. In addition several test cases for each finite element model are presented.

3.3.1 Standard Concrete Cylinder Tests Model

The standard concrete cylinder test model was assembled to address calibrating existing material models using the newly obtained concrete data from the committee (CSNI 2012). In the following sub-sections, the finite element model mesh, boundary conditions, material models, and the unconfined and triaxial compression stress path tests are presented.

3.3.1.1 Mesh

The standard concrete cylinder test finite element model employed quarter symmetry about the x-z and y-z planes and was constructed with 1536 8-noded hexahedral single point under-integrated elements. The finite element mesh had a total of 2013 nodes and used only a single material (or block) to represent the entire cylindrical specimen. The average element volume was 87 mm^3, and the aspect ratio of the 8-noded brick elements (*i.e.,* hex8 type elements) varied from 1.03 to 1.56. The 1/4 symmetry finite element model representing the standard concrete cylindrical specimen is shown below in Figure 3-1. As seen in Figure 3-1 there are 32 elements along the axial direction (z-direction) and eight (8) elements along each symmetry plane's radial dimension (x-direction or y-direction). The finite element model had a length equal to that of the standard concrete cylinder test (140 mm) and had an equivalent radial dimension (represented in quarter symmetry) equal to the test specimen's diameter (70 mm).

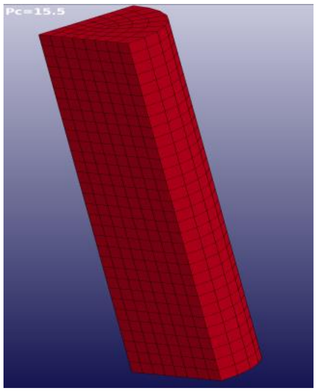

Figure 3-1: ¼ Symmetry Finite Element Model Representing the Standard Concrete Cylinder Test.

3.3.1.2 Boundary Conditions

The major boundary conditions imposed on the quarter symmetry finite element model displacement controls on the x-z symmetry plane (*e.g.,* no x-displacement) and the y-z symmetry plane. The minor boundary conditions imposed on the finite element mesh are in regards to the loading surfaces. To accomplish axial loading, the upper and lower x-y plane surfaces (at z=0 and z=140 mm), were constrained to move only in the z-direction.

3.3.1.3 Material Models

A material model capable of capturing concrete response behavior was chosen as the LS-DYNA *MAT_072R3 (MAT_CONCRETE _DAMAGE_REL3), or the Karagozian and Case concrete material model (LSTC, LS-DYNA Keyword User's Manual Volume 1 and Volume 2 2010). The Karagozian & Case (K&C) Concrete Model is a three-invariant model, uses three shear failure surfaces (i.e., yield, maximum, and residual), includes damage and strain-rate effects, and has its constitutive model origins based on the Pseudo-Tensor model (MAT_016). Although the model has an automatic parameter generation capability based on the unconfined compressive strength (f_c'), this material model was calibrated or "fit" (*i.e.* all of its parameters were defined individually) to the recently available 2012 IRSN concrete data (CSNI 2012). Shown in Figure 3-2, Figure 3-3, and Figure 3-4 are the preliminary shear failure surface models (*i.e.,* maximum, yield, and residual, respectively) using the *MAT_072R3 model calibrated ("fit") to the data provided. After judiciously applying some experience and adjustments, the final shear failure surfaces, plotted in the Meridional plane (or Stress difference vs. Mean Pressure), of the IRSN 2012 standard concrete cylinder model are shown in Figure 3-5.

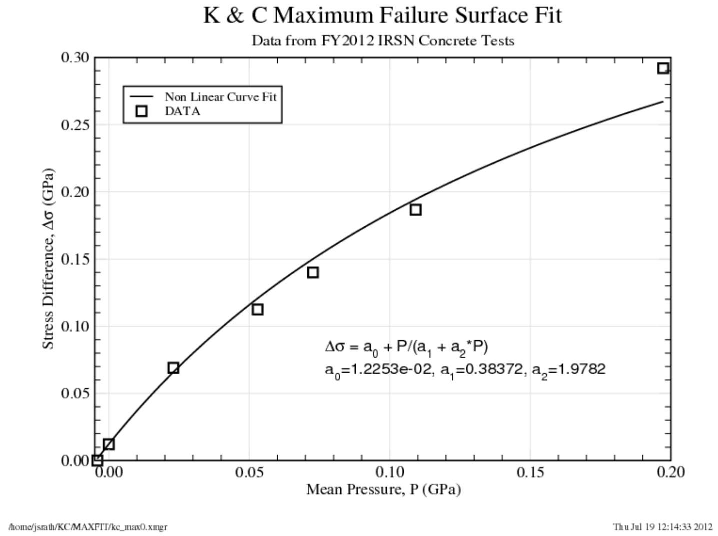

Figure 3-2: Preliminary 2012 IRSN Standard Concrete Cylinder Model *MAT_072R3 Maximum Surface.

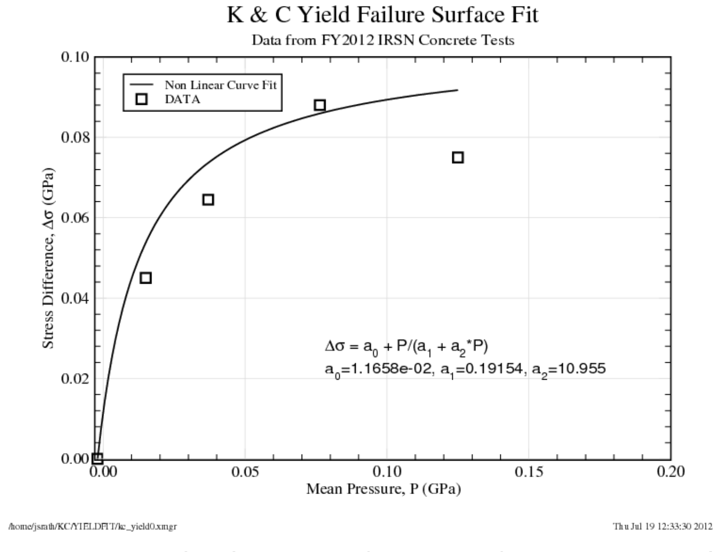

Figure 3-3: Preliminary 2012 IRSN Standard Concrete Cylinder Model *MAT_072R3Yield Surface.

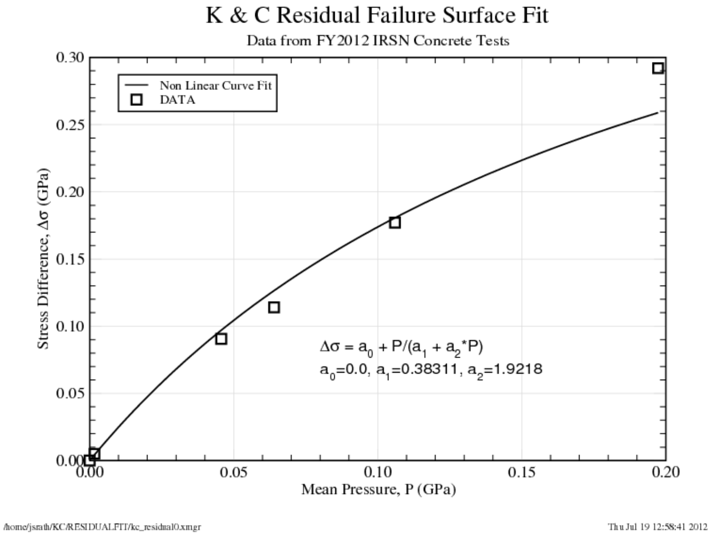

Figure 3-4: Preliminary 2012 IRSN Standard Concrete Cylinder Model *MAT_072R3 Failure Surface.

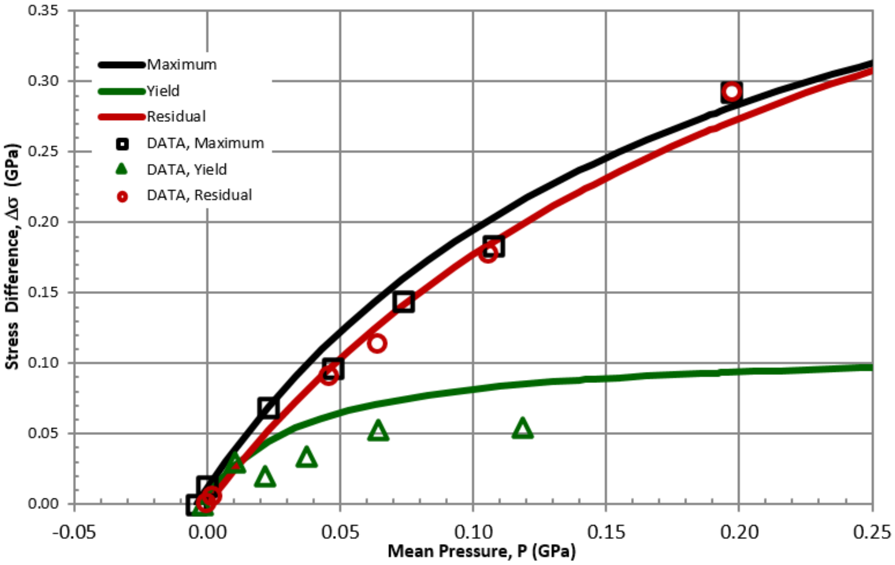

Figure 3-5: Karagozian and Case (*MAT_072R3) Concrete Material Model Failure Surfaces.

3.3.1.4 Test Cases

A schematic displaying the loading conditions for the standard concrete cylinder test is shown in Figure 3-6. An unconfined compression test can be represented as a triaxial compression test with zero confining pressure (P_C). The standard concrete cylinder tests were modeled for the case of unconfined compression (*i.e.,* $P_C = 0$) and four triaxial compression tests (*i.e.,* P_C = 15.5, 26.0, 47.0, and 100.0 MPa).

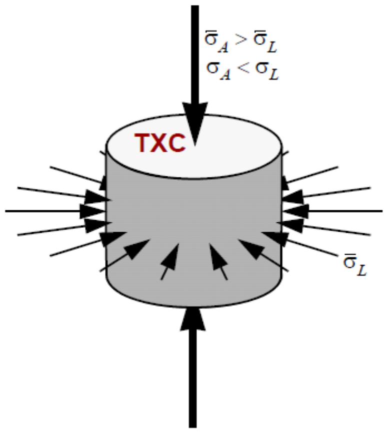

Triaxial Compression (**TXC**)
Typical Concrete Cylinder specimen:
Specimen Diameter = D
Length, L = 2*D
L/D = 2
σ_L = Confinement Pressure = P_C
$\sigma_A = \sigma_L$ and then increase σ_A

Figure 3-6: Triaxial and Unconfined Compression Test Schematic.

3.3.2 Missile Impact Test Models

The first and second impact scenarios (Meppen II-4 test and VTT Flexural test) incorporated a soft missile comprised mostly of 4-noded Belytschko-Tsay shell elements with 5 integration points through the thickness. The third impact scenario missile component (VTT Punching test) was constructed entirely with under-integrated 8-noded hexahedral elements (*i.e.,* one integration point) to represent both the missile's concrete fill and the missile's steel case. All three LS-DYNA impact scenario simulations used two or more contact models to permit: a concertina-mode folding of the thin soft missile (e.g., the soft missile and subsequent bending response for the Meppen and Flexural scenarios); and/or erosion of the reinforced concrete target (*e.g.*, the hard missile and resulting penetration type response for the Punching scenario). The reinforcing steel component for each impact scenario target assembly was realized using Hughes-Liu beam elements with a 2 x 2 Gauss quadrature scheme, and a circular cross-section. These scenario target geometrically unique reinforcing steel grids were included into the global finite element model using the LS-DYNA keyword *CONSTRAINED_LAGRANGE_IN_SOLID and inherent fluid structure interaction methodology. Three different concrete material models were used to predict and simulate the response of the concrete target: Karagozian & Case (*MAT_072R3), Winfrith without strain-rate effects (*MAT_085), and the Continuous Surface Cap Model (*MAT_159), since sufficient and/or necessary triaxial compression, triaxial extension, triaxial torsion, and/or hydrostatic compression test data was not available or known.

The LS-DYNA finite element code provided a wealth of computational models necessary to simulate three different impact scenarios. Each of the three impact scenario simulations assembled/combined three minor finite element meshes (or sub-components: missile, concrete target, and reinforcing steel bars) into a global system. The use of the LS-DYNA Constrained Lagrange in Solid method was used to alleviate the constraint of coincident nodes for the concrete target mesh and the reinforcing steel bar grid. This method allowed the reinforcing steel bar density to be accurately represented, and easily constructed in a computational sense. In addition, a three dimensional (3D) ¼-symmetric model was used throughout (*i.e.,* applying symmetry to both x- and y-directions) which reduced simulation run times and used less computational resources. The use of ¼ symmetry may reduce predicting high-fidelity target response (more important for a non-zero angle of attack and/or a non-zero angle of incidence), however with the amount of material data uncertainty (*e.g.*, limited concrete test data, unknown strain rate response on reinforcing steel and missile steel, etc.) this was assumed to be a valid approximation. All finite element meshes were constructed using the mesh generation tool Cubit (Cubit, A Finite Element Method Meshing Tool 2011).

3.3.2.1 Mesh

Using quarter symmetry each impact scenario target concrete component was built using under integrated, single point integration 8-noded hexahedral elements. In order to avoid problems using the under integrated element, the Flanagan-Belytschko stiffness form was used employed for both the Meppen II-4 and VTT flexural mode impact scenario models. Similarly, the Flanagan-Belytschko viscous form with exact volume integration was used for the VTT punching mode impact scenario target model. These type of hourglass controls for use with single point integration 8-noded hexahedral elements has been recommended for LS-DYNA simulations involving severe deformation (Schwer, et al. 2005). The reinforcing steel bars were constructed using beam elements and were not connected to the target concrete with common nodes. The reinforcement beam elements shared nodes at intersecting x- and y-direction junctions and did not consider over/under bar alignment. Each impact scenario target model connected the reinforcing steel beam elements to the concrete hexagonal solid elements interaction through a series of automatically generated nodal constraints through the use of the LS-DYNA keyword *CONSTRAINED_LAGRANGIAN_IN_SOLID.

The Meppen II-4 impact scenario simulations modeled the target using 12 support points (i.e*.,* a full symmetry model results 48 support points) to enforce the test clamp mechanism, as shown in Figure 3-7. As seen in the figure below, each support point was surrounded by the nearest node to help reduce sharp displacement gradient effects. The finite element mesh was discretized using 16 elements through the z-direction thickness of 700 mm and a geometric ratio (limited to an aspect ratio of 2.0) was used to permit ideal element aspect ratios at the target center and increasing element aspect ratios away from the center of the grid.

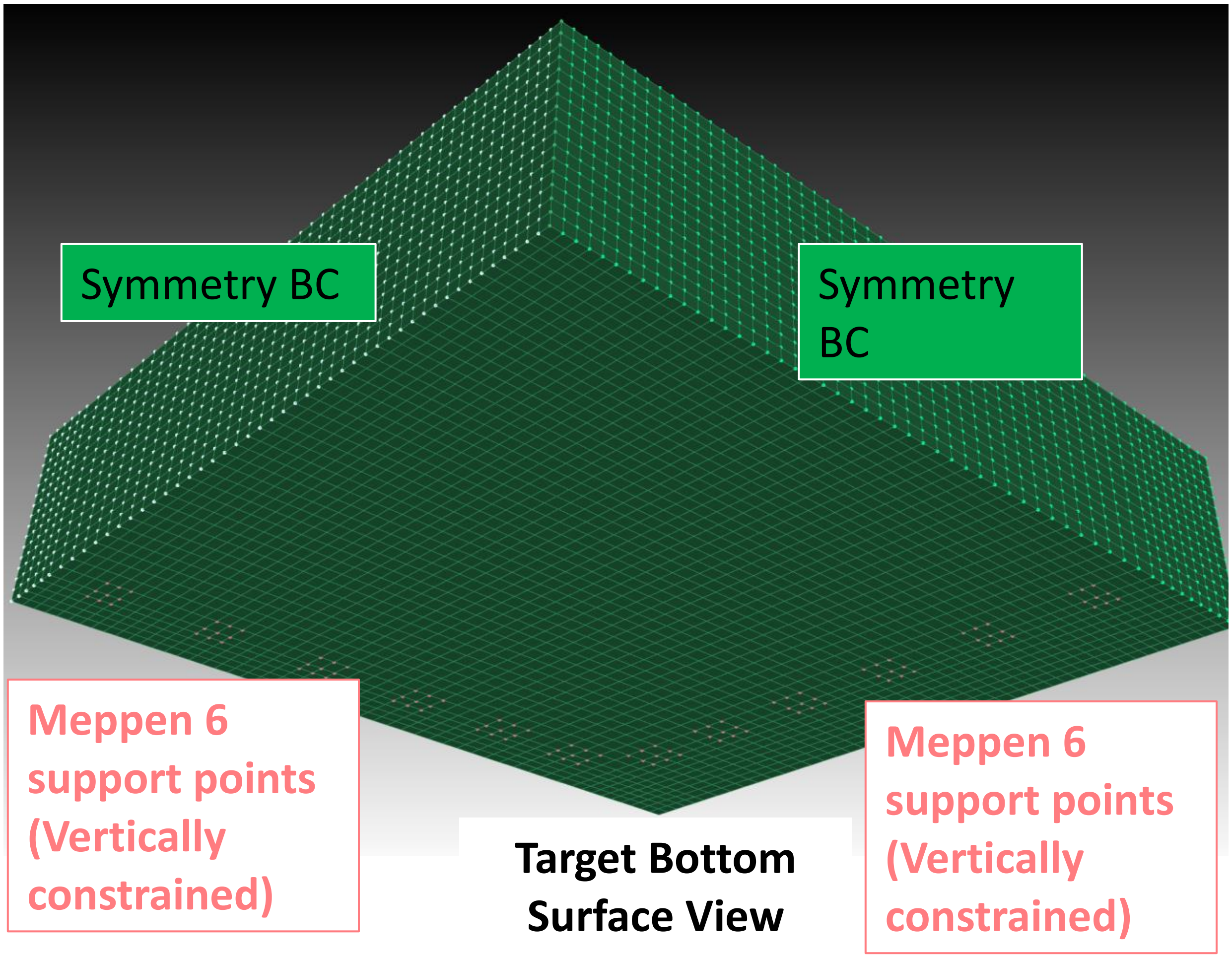

Figure 3-7: Quarter Symmetry Finite Element Model of the Target and Boundary Conditions For the Meppen II-4 Impact Scenario.

Unlike the Meppen II-4 impact scenario constraint conditions, both the VTT flexural mode and VTT punching mode impact scenario meshes were constrained using a patch of nodes near the outer extremes of the target on both top and bottom. The clamping mechanism of the VTT flexural mode and VTT punching mode test enforced a rigid constraint at the section of the target, as shown in Figure 3-8. Similar to the Meppen II-4 scenario target mesh, the VTT flexural mode grid was descritized using 17 elements through the z-direction thickness of 150 mm and a geometric ratio (limited to a aspect ratio of 2.2) was used to permit ideal element aspect ratios at the target center and increasing element aspect ratios away from the center of the grid. Shown in Figure 4-26 is the finite element mesh used for the VTT punching model whereby the grid was discretized using 33 elements through the z-direction thickness of 250 mm and similar to the VTT flexural model, the element aspect ratio was varied from ideal to a maximum of 2.2.

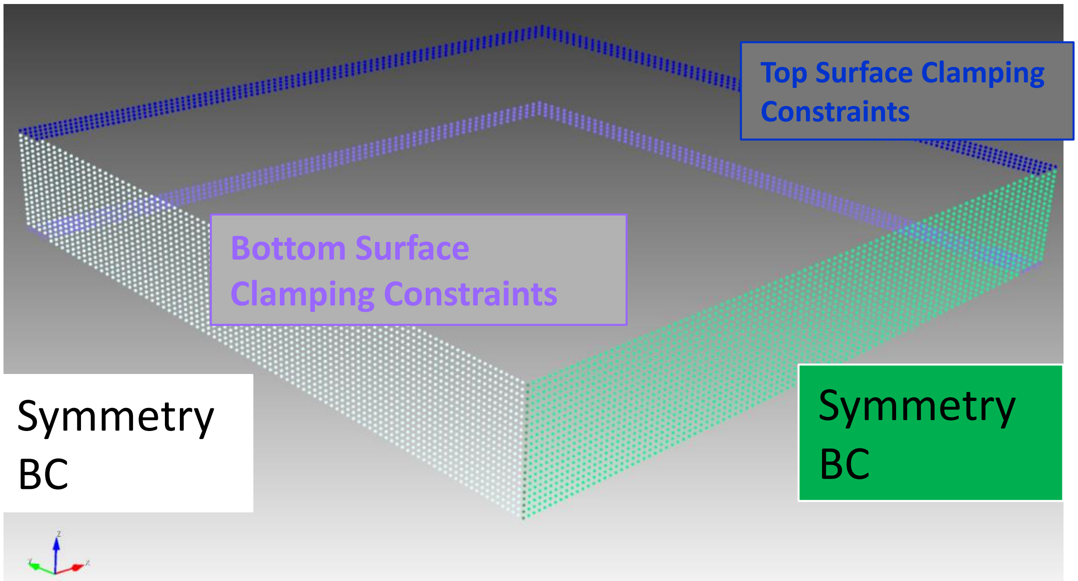

Figure 3-8: Quarter Symmetry Boundary Conditions Used to Enforce a Rigid Clamp Mechanism For Both the VTT Flexural and VTT Punching Models.

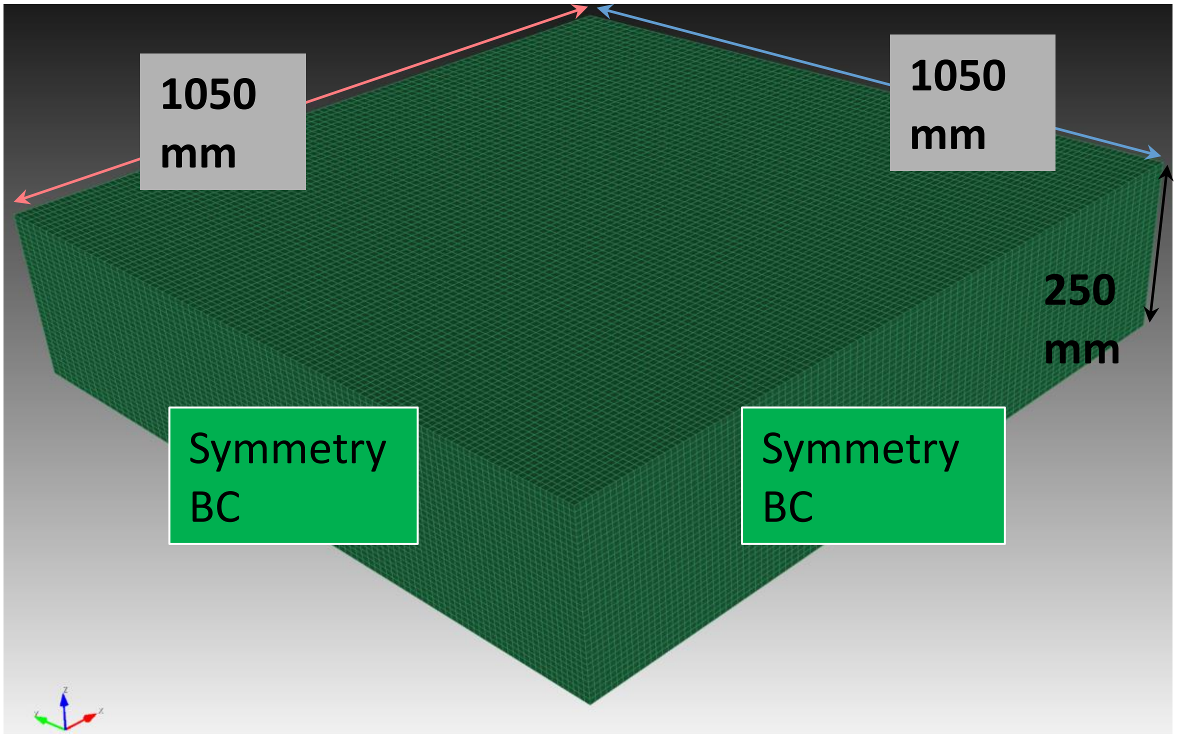

Figure 3-9: Quarter Symmetry Model Used for the VTT Punching Model.

Shown in Table 3-1 is a summary of the target concrete component hexahedral 8-noded finite element model for each impact scenario.

Table 3-1: Summary of the Target Concrete Component Finite Element Models

Attribute	Meppen II-4	VTT Flexural	VTT Punching
Characteristic Element Dimension (mm)	43.0	7.5	7.6
Best Element Aspect Ratio	1.0	1.0	1.0
Worst Element Aspect Ratio	2.0	2.2	2.2
Total Elements	39936	162000	267300
Total Nodes	44149	173901	281554

Shown in Figure 3-10 are the steel reinforcement grids used in the finite element model for each of the impact scenarios. The prescribed experimental reinforcing steel density and model reinforcing steel density for the rebar grids of each impact scenario are described in Table 3-2. Shown in Table 3-3 is a summary of the steel reinforcement beam-type finite element model for each impact scenario.

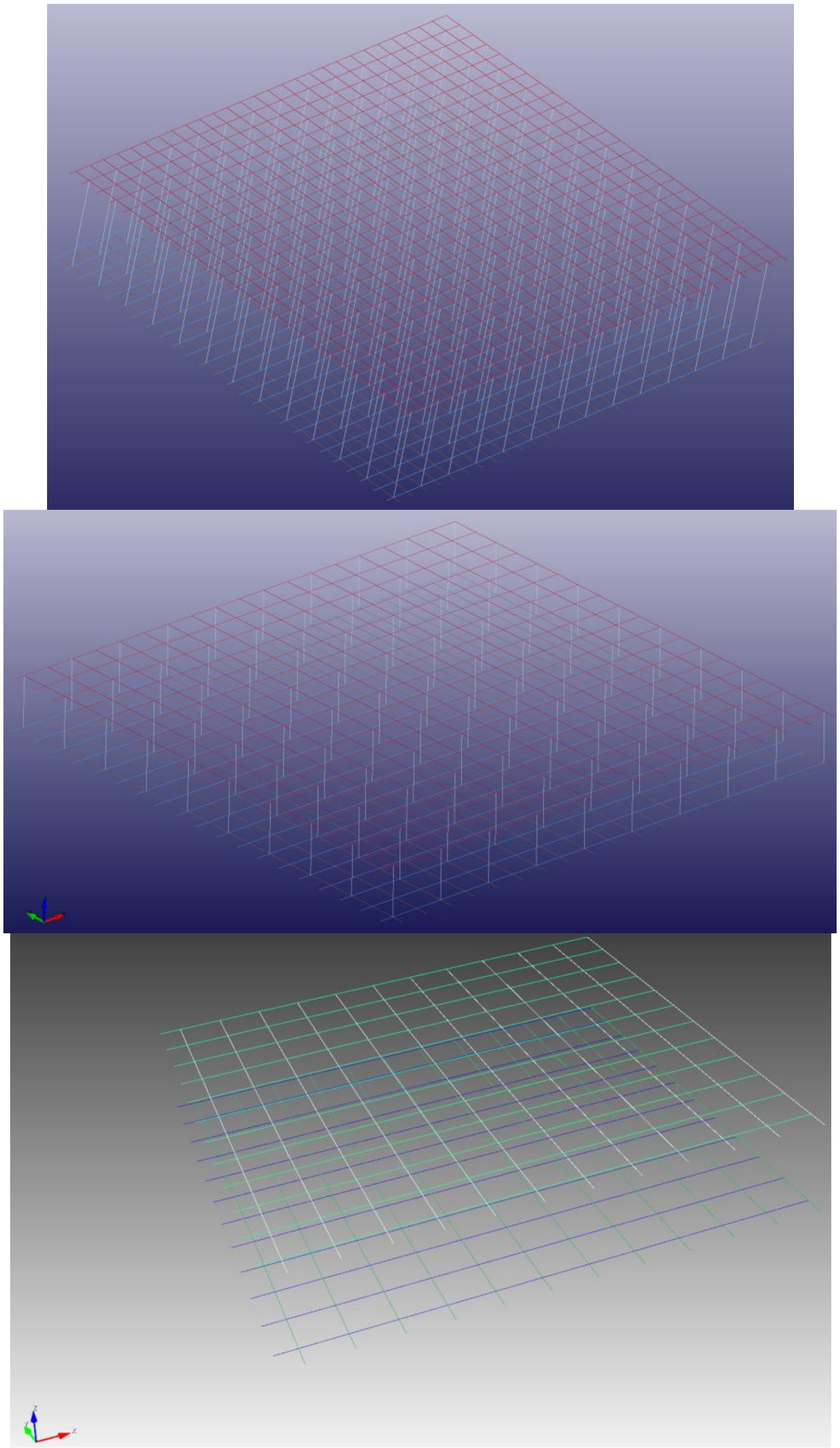

Figure 3-10: Reinforcement Steel Bar Grids used in LS-DYNA simulations (Top: Meppen II-4, Middle: VTT Flexural; Bottom: VTT Punching).

Table 3-2: Reinforcement Steel Grid Density Description.

Meppen II-4: BSt 420/500 RK Steel					
Part	**Diameter (mm)**	**Span (m)**	**Amount**	**Ratio Model (cm^2/m)**	**Ratio Test (cm^2/m)**
Front x-dir bar	19.93	5.94	52	27.0	27.3
Front y-dir bar	19.99	6.44	56	27.0	27.3
Back x-dir bar	27.92	5.94	52	53.6	53.6
Back y-dir bar	28.01	6.44	56	53.6	53.6
Part	Diameter (mm)	Span Area (m^2)	Amount	Ratio Model (cm^2/m^2)	Ratio Test (cm^2/m^2)
Transverse bar	18.29	38.25	728	50.0	50.0
VTT Flexural: A500HW Steel					
Part	**Diameter (mm)**	**Span (m)**	**Amount**	**Ratio Model (cm^2/m)**	**Ratio Test (cm^2/m)**
Front x-dir bar	5.87	2.06	38	5.0	5.0
Front y-dir bar	5.87	2.06	38	5.0	5.0
Back x-dir bar	5.87	2.06	38	5.0	5.0
Back y-dir bar	5.87	2.06	38	5.0	5.0
Part	Diameter (mm)	Span Area (m^2)	Amount	Ratio Model (cm^2/m^2)	Ratio Test (cm^2/m^2)
Transverse bar	8.22	4.24	400	50.0	50.0
VTT Punching: A500HW Steel					
Part	**Diameter (mm)**	**Span (m)**	**Amount**	**Ratio Model (cm^2/m)**	**Ratio Test (cm^2/m)**
Front x-dir bar	9.75	2.06	24	8.7	8.7
Front y-dir bar	9.75	2.06	24	8.7	8.7
Back x-dir bar	9.75	2.06	24	8.7	8.7
Back y-dir bar	9.75	2.06	24	8.7	8.7

Table 3-3: Summary of the Steel Reinforcement Bar Finite Element Models.

Attribute	Meppen II-4	VTT Flexural	VTT Punching
Rebar length (mm)	57.5	27.0	43.0
Transverse Rebar length (mm)	44.3	33.0	N/A
Total Elements [+]	7444	3112	1104
Total Nodes [++]	6734	2366	864

[+] 2-node beam elements were used to generate 3-noded beam elements whereby the third node is a LS-DYNA beam reference node

[++] This total node count is with respect to 2-noded beam elements which were generated using the Cubit mesh generation tool.

As previously mentioned, the finite element meshes of the steel reinforcing bar and the concrete which comprise the target, were constructed without enforcement of common or coincident nodes. In order to communicate forces from the steel reinforcement to the concrete material, the LS-DYNA *CONSTRAINED_LAGRANGE_IN_SOLID keyword and inherent fluid structure interaction methodology was used. This technique is considered to be a better way to embed reinforcement in concrete structures rather than sharing common nodes with the concrete Lagrange solid elements (L. Schwer 2010). The number of *CONSTRAINED_LAGRANGE_IN_SOLID coupling points (nquad x nquad) is a key parameter for effectively connecting the response of the reinforcing steel bar elements and the concrete solid elements. This parameter permits a distribution of nquad by nquad points along the surface of the Lagrangian segment. Typically 2 or 3 coupling points per each Eulerian element width is adequate (LSTC, LS-DYNA Keyword User's Manual Volume 1 and Volume 2 2010). All LS-DYNA impact scenario models accounted for this coupling parameter accordingly and the number of coupling points used is shown in Table 3-4.

Table 3-4: Constrained Lagrange in Solid Coupling Points Used in Impact Scenario Models.

Attribute	Meppen II-4	VTT Flexural	VTT Punching
xy-direction concrete hex8 element width (mm)	43.0	7.5	7.6
xy-direction steel reinforcing beam element length (mm)	57.5	27.0	43
xy-direction ratio rebar length to concrete width	1.3	3.6	5.6
xy-direction *nquad*^{2} parameter used	4	6	10
z-direction concrete hex8 element width (mm)	43	33	N/a
z-direction steel reinforcing beam element length (mm)	44.3	7.5	N/a
z-direction ratio rebar length to concrete width	0.99	4.4	N/a
z-direction *nquad*^{2} parameter used	4	8	N/A

All three impact scenario missile models were constructed using a combination of 4-noded shell elements and/or a combination of 8-noded hexahedral elements as appropriate. The Meppen impact scenario missile finite element model was built with shell element and hexahedral elements. The VTT flexural impact scenario missile finite element model was constructed primarily of shell elements, except for the tail section which used 8-noded hexahedral elements. All shell elements used the Belytschko-Tsay type formulation with 5 integration points through the thickness. The VTT punching scenario missile finite element model was assembled using solid 8-noded hexahedral elements that were under-integrated, using a 1-point integration scheme. The finite element model representing the VTT punching mode impact scenario missile did not include the aluminum pipe used for determining the residual velocity, as shown in Figure 2-12. This neglected detail of the model was justified based on the low aluminum pipe mass, virtual zero momentum addition, and that it could not properly be incorporated into the ¼ symmetry finite element model representation of the impact system. The three impact scenario finite element models are shown in Figure 3-11 and the finite element model discretization summary is provided in Table 3-5. Although the impact scenarios were build using quarter symmetry, Figure 3-11 shows a full symmetry visualization of the Meppen II-4 and VTT Flexural models and a half symmetry view of the VTT Impact model. The concrete tube encapsulated within the steel case of the VTT impact missile is distinguished by the tan colored elements.

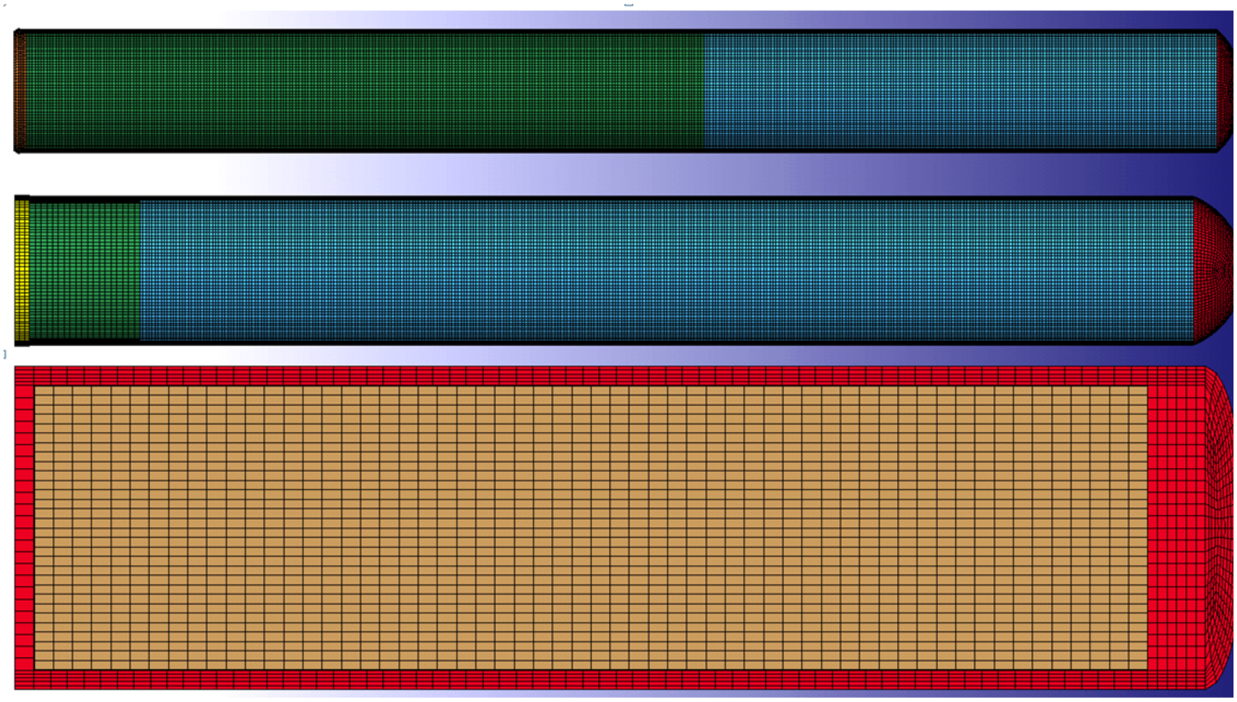

Figure 3-11: Missile Finite Element Models: Meppen II-4 (Top), VTT Flexural (Middle), and VTT Punching (Bottom); Note Missiles are not shown in the same scale.

Table 3-5: Impact Scenario Missile Finite Element Model Discretization Summary.

Attribute	Meppen II-4	VTT Flexural	VTT Punching
4-noded Shell Elements	15110	12256	N/A
8-noded Hexahedral Elements	2244	3264	21681
Total Elements	17354	15520	21681
Total Nodes	18406	17219	25844
Finite Element Model Mass^{+} (kg)	1017	50	47
Test Missile Mass (kg)	1016	50	47

$^{+}$¼ symmetry finite element representation of each missile was used (*i.e.,* a factor of 4 is included)

The size of the shell elements was chosen such that a minimum of four elements would exist in the half-fold length of the Meppen II-4 or VTT Flexural missile body when it collapses in a concertina fashion (Beltrán, Combescuscure and Rueda 2010). The size of the folds was estimated using an approximate formula (Aljawi 2002), (Alexander 1960)

$$H = 1.76 \cdot \texttt{sqrt}(Rt)/\texttt{sqrt}(2),$$
$$H^{*} = 0.86 - 0.568 \cdot \texttt{sqrt}(\cdot t/D), \text{ and}$$
$$H^{c} = H \cdot H^{*},$$

where D, R, t, H, H^{*}, H^{c} are the cylindrical tube diameter, cylindrical tube radius, cylindrical tube thickness, uncorrected half-fold length, fold correction factor, and corrected half-fold length, respectively. The size of the folds and resulting shell element size is summarized in Table 3-6 for the Meppen II-4 Missile and VTT Flexural Missile model.

Table 3-6: Computed Half-fold Size and Corresponding Shell Element Size.

Attribute	Meppen II-4		VTT Flexural
Mean Radius, R (mm)	300		127
Mean Diameter, D (mm)	600		254
Cylindrical Tube Thickness, t (mm)	5	10	2
Ratio D/t	120	60	127
Uncorrected Half-fold Length, H (mm)	68.2	96.4	28.0
Correction Factor, H^*	0.81	0.79	0.81
Corrected Half-fold Length, H^c (mm)	55.2	76.2	22.7
Characteristic Shell Element Length, $H^c/4$ (mm)	13.8	19.0	5.7
Typical Shell Element Length (Finite Element Models, mm)	15		6

3.3.2.2 Boundary Conditions

Boundary conditions to enforce displacement controls on the x-z symmetry plane (*e.g.,* no x-displacement) and the y-z symmetry plane were applied to all three impact scenario finite element models. The target clamping conditions used on the Meppen II-4 impact scenario model were shown previously, in Figure 3-7. Similarly, the target clamping conditions used on both the IRSN VTT Flexural and IRSN VTT Punching impact scenario model were shown in Figure 3-8. The missile component (or components, regarding the punching impact model, since it has both steel and concrete components) of each numerical impact model was given an initial velocity equal to the missile velocity specified for each test (*i.e.,* Meppen, missile initial velocity = 247.7 ms/sec; Flexural, missile initial velocity = 110.885 m/sec; and Punching, missile initial velocity = 135.0 ms/sec).

3.3.2.3 Material Models

The impact scenario target concrete, target reinforcing steel, and missile steel properties used in the calculations are listed in Table 3-7. The material property data used in the Meppen II-4 test impact scenario simulations was derived from values listed in the Meppen Test II-4 report provided by the IRIS 2010 project committee (Meppen 2010). Similarly, all material property data used in the Flexural test impact simulations was taken from the Technical Research Centre of Finland (VTT) Report VTT-R-05587-10 (Vepsä 2010a). Lastly, the material property values used in the Punching mode calculations were derived from the second Report VTT-R-05588-10 (Vespä 2010b). The Winfrith concrete material model (*MAT_085) required a specific fracture energy value necessary to construct a fracture aperture length to provide a linear strain softening response. A specific fracture energy value for each impact scenario target was linearly interpolated from a table based on cubic specimen, unconfined compressive strengths (Magallanes, et al. 2010).

Table 3-7: Impact Scenario Model Properties.

Target Concrete	**Meppen II-4**	**VTT Flexural**		**VTT Punching**	
Unconfined Compressive Stress, f'_c (MPa) [*cylindrical specimen*]	30.5	53.5		55.1	
Unconfined Compressive Stress, f'_c (MPa) [*cubic specimen*]	37.2	65.0		67.2	
Density, ρ [kg/m^3]	2250	2262		2300	
Poisson's Ratio, ν	0.2	0.20		0.19	
Unconfined Tensile Stress, f'_t (MPa)	4.8	3.7		4.04	
Young's Modulus$^+$, ***E*** (MPa)	26114	26915		29429	
Specific Fracture Energy, G_F (N/m)	62.0	91.6		95.1	
Target Reinforcing Steel					
Material Designation	BSt 420/500 RK	A500 HW		A500 HW	
Young's Modulus, ***E*** (MPa)	205000	219000		210000	
Density, ρ [kg/m^3]		7843		7843	
Poisson's Ratio, ν	0.29	0.29		0.29	
Yield Stress, σ_y (MPa)	444.3	600.0		535	
Ultimate True Stress, σ_{uts} (MPa)	526.0	747		666	
Failure Strain (%)	10	12		12	
Missile					
Material Designation	**RSt 37-2 Steel**	**Stainless Steel EN 1.4432**	**Carbon Steel S355J2H**	**Stainless Steel EN 1.4432**	**Lightweight Concrete Fill**
Young's Modulus, ***E*** (MPa)	210000	200000	200000	200000	10120
Density, ρ [kg/m^3]		7850	7738	7850	1514
Poisson's Ratio, ν	0.3	0.29	0.29	0.29	0.2
Yield Stress, σ_y (MPa)	280	302	500	302	N/A
Ultimate True Stress, σ_{uts} (MPa)	476.3	513	N/A	513	N/A

$^+$Young's Modulus, ***E***, was computed from the American Concrete Institute formula $E = 5.7\text{x}10^4 \cdot \texttt{sqrt}(f_c')$, where f_c' is the cylindrical specimen unconfined compressive strength specified in units of lb$_f$/in^2

The lightweight concrete filling in the punching mode impact missile was modeled using another LS-DYNA concrete constitutive model, *MAT_016 (a.k.a. *MAT_PSEUDO_TENSOR). This concrete constitutive law also utilizes a simplified input parameter construction based on the unconfined compressive cylindrical specimen strength which was assumed to be 20 MPa. A lightweight concrete density was selected such that the specified total missile mass was 47.0 kg (*i.e.,* density = 1514 kg/m^3, as shown in Table 4-13). Other unknown and guessed/assumed concrete property values included a Young's Modulus, ***E*** = 10120 MPa

The LS-DYNA MAT-024 (*MAT_PIECEWISE_LIENAR_PLASTICITY) material model was used in all impact scenario simulations to model the steel reinforcement behavior. A limited amount of data was provided permitting construction of a true stress vs. true strain (*i.e.,* effective plastic strain) curve from the engineering stress and strain data. Shown in Figure 3-12 are the reinforcing steel true stress vs. strain relations used in the LS-DYNA simulations.

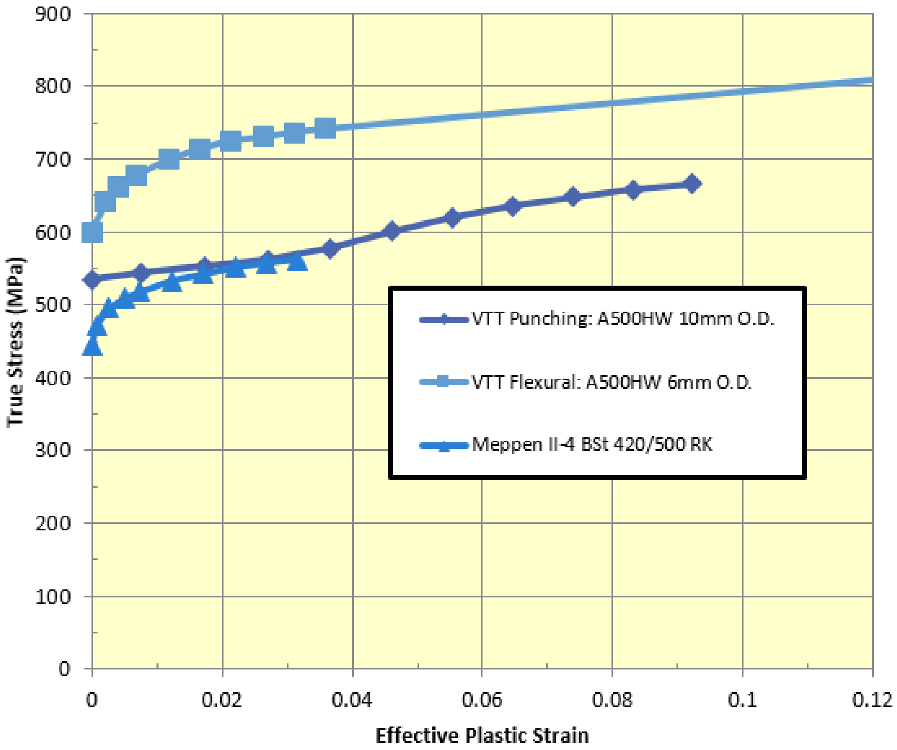

Figure 3-12: Reinforcing steel bar true stress vs. effective plastic strain curves used in the LS-DYNA simulations

This material model allows strain rate effects to be included through a Cowper-Symonds model as

$$\sigma_y^{dynamic}/\sigma_y^{static} = 1+[(\boldsymbol{d\varepsilon/dt})/\boldsymbol{C}]^{1/p},$$

where $\sigma_y^{dynamic}$, σ_y^{static} , $\boldsymbol{d\varepsilon/dt}$, $\boldsymbol{C}$, *and* $\boldsymbol{P}$ are the dynamic yield strength, static yield strength, strain rate, first Cowper-Symonds parameter, and $\boldsymbol{P}$ is the Cowper-Symonds parameter, respectively. The reinforcing steel strain-rate dependent model was used in both the Meppen II-4 and VTT Flexural scenario simulations, but not the in the VTT Punching scenario calculations.

The target concrete component was unequivocally the least well characterized material in the LS-DYNA simulations. Due to the limited amount of data provided (*e.g.,* unconfined compressive strength, unconfined tensile strength, Young's modulus, and density) only simple input concrete material models can be used (*e.g.,* *MAT_CONCRETE_DAMAGE_REL3, *MAT_WINFRITH_CONCRETE, *MAT_CSCM_CONCRETE) to automatically generate a complete concrete model parameter set. Thus it was reasoned that three different target concrete material models would be used in each of the impact scenario calculations and would at least provide a range of different responses regarding missile velocity during impact, target deflection, penetration, and/or missile exit velocity, etc. Shown in Figure 3-13 are the failure surface curves representative of the concrete targets for the Meppen II-4, VTT Flexural, and VTT Punching impact scenarios, respectively. As seen in these figures, each of the three concrete material models is quite different as viewed in the Meridonal plane (*i.e.,* Stress Difference vs. Mean Pressure). This figure clearly demonstrates that the continuous surface cap model (*MAT_159) is dramatically stronger, in the stress difference sense, than the Winfrith concrete model (*MAT _085) and the Karagozian and Case concrete model (*MAT_072R3) is the weakest. These

Meridonal plane responses were generated automatically from the LS-DYNA code using the simple input option requiring only a few parameters (*e.g.,* unconfined compressive stress, unconfined tensile stress, Young's modulus, Poisson's ratio, etc.). Figure 3-14 shows that the volumetric response for several LS-DYNA concrete material models are somewhat different, but not as varied as the shear response. Again, like the shear response, these pressure vs. volumetric strain curves were derived using the simple input methods of the concrete material models.

Both the Winfrith (*MAT_085 or *MAT_WINFRITH_CONCRETE) and the Continuous Surface Cap Model (*MAT_159 or *MAT_CSCM_CONCRETE) concrete constitutive laws were employed without strain-rate effects. However, the Karagozian and Case material model (*MAT_072R3 or *MAT_CONCRETE_DAMAGE_REL3) included a dynamic increase factor (DIF) function to permit strain-rate effects. A DIF function was chosen based on the unconfined compressive strength, $\boldsymbol{f_c'}$, which was similar to that shown in the LS-DYNA User's Guide (LSTC, LS-DYNA Keyword User's Manual Volume 1 and Volume 2 2010), but derived using the impact scenario's target concrete strength value (*e.g.,* Meppen II-4, $\boldsymbol{f_c'} = 30.5$ MPa). The DIF function was designed to allow:

1) A bilinear relationship with a change in slope near 30 x 10^{-3} 1/msec, when plotted in log(DIF) vs log($\boldsymbol{d\varepsilon/dt}$);
2) DIFs are greater for concrete with lower strength;
3) the DIFs are related to a strength measured at a specific *quasi-static* strain rate; and
4) Strength enhancement is different in tension than in compression (Attaway, et al. 2000)

Shown in Table 4-14 are the dynamic increase factors used with the *MAT_072R3 constitutive law based on unconfined compressive strength for each of the three impact scenarios.

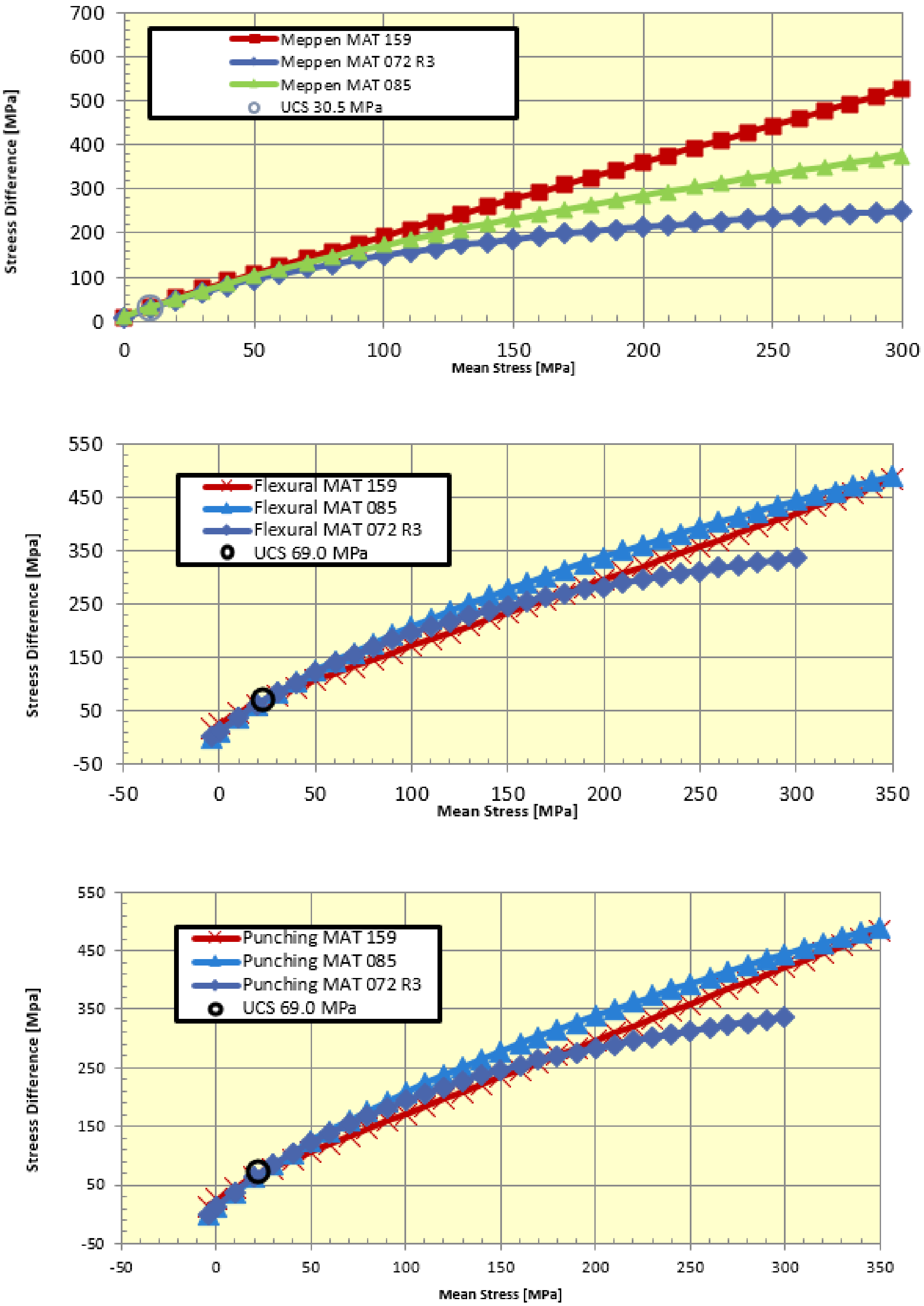

Figure 3-13: Comparison of triaxial compression surfaces in the Meridonal Plane using three LS-DYNA concrete models (Top: Meppen II-4;Middle: VTT Flexural; Bottom: VTT Punching).

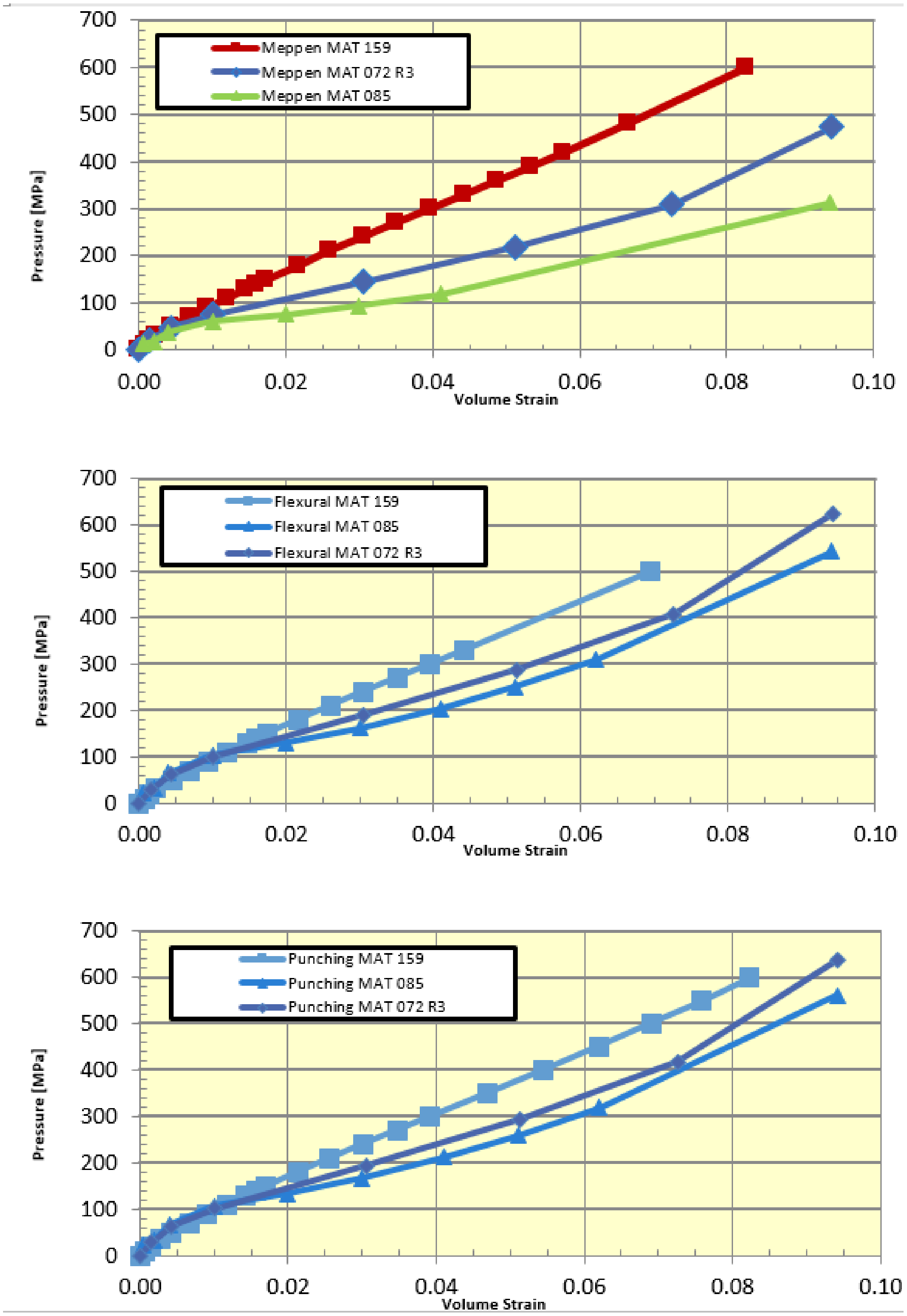

Figure 3-14: Comparison of Volumetric Response using three LS-DYNA concrete models (Top: Meppen II-4; Middle: VTT Flexural; Bottom: VTT Punching).

Table 3-8: Dynamic Increase Factors for Concrete Model *MAT_072R3.

Strain Rate (1/msec)	Dynamic Increase Factor		
	Meppen II-4	VTT Flexural	VTT Punching
-30	11.53	8.85593	8.85593
-0.3	11.53	8.8593	8.8593
-0.1	7.9942	5.9347	5.9347
-0.03	5.3516	3.9729	3.9729
-0.01	3.7106	2.7547	2.7547
-0.003	2.484	1.8441	1.8441
-0.001	1.7224	1.2787	1.2787
-0.0001	1.5732	1.2273	1.2273
-1.00E-05	1.4369	1.17818	1.17818
-1.00E-06	1.3124	1.1308	1.1308
-1.00E-07	1.1987	1.0854	1.0854
-1.00E-08	1.0949	1.0418	1.0418
0	1	1	1
3.00E-08	1	1	1
1.00E-07	1.0388	1.0186	1.0186
1.00E-06	1.1172	1.0551	1.0551
1.00E-05	1.2016	1.0929	1.0929
0.0001	1.2923	1.1321	1.1321
0.001	1.3898	1.1726	1.1726
0.003	1.4389	1.1925	1.1925
0.01	1.4947	1.2146	1.2146
0.03	1.5476	1.2352	1.2352
0.1	2.3116	1.8451	1.8451
0.3	3.3339	2.6611	2.6611
30	3.3339	2.6611	2.6611

All three impact scenario missile models were constructed using a combination of 4-noded shell Similar to the Target steel reinforcing bar, the missile steel material was modeled using the LS-DYNA piecewise-linear plasticity constitutive law MAT_024 (*MAT_PIECEWISE_LINEAR_PLASTICITY). This material model allowed a table of true stress versus true strain (*i.e.,* effective plastic strain) points to be input for each impact scenario missile steel material. Shown in Figure 3-15 are the missile steel true stress vs. strain relations used in the LS-DYNA simulations (note that both the VTT flexural and VTT punching missile steel properties were the same). The carbon steel S355J2H component of the VTT flexural mode impact scenario missile was modeled using the LS-DYNA *MAT_003 (*a.k.a.* *MAT_PLASTIC_KINEMATIC) constitutive law.

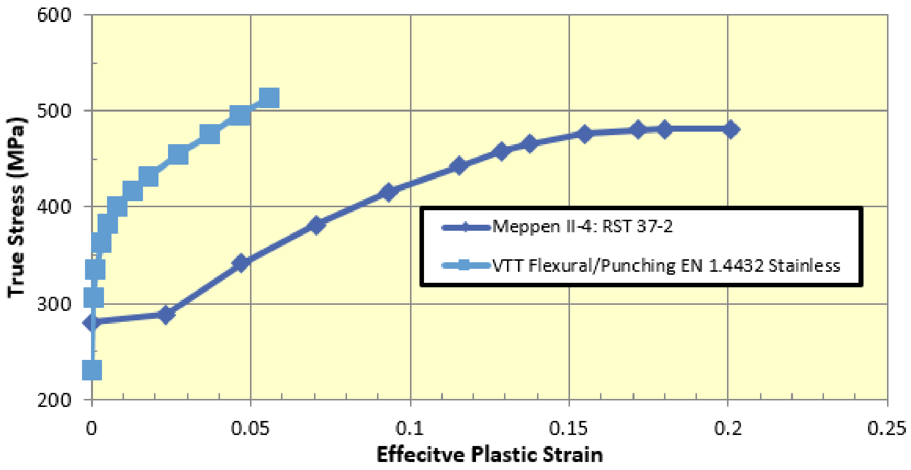

Figure 3-15: Missile Steel True stress vs. Effective plastic strain curves used in the LS-DYNA simulations.

Both missile steel material models (*MAT_003 and *MAT_024) allow strain rate effects to be activated through a Cowper-Symonds option (discussed earlier) and was included for each of the impact scenario missiles. Shown in Table 3-9 is a summary of the steel strain-rate parameters used in each impact scenario missile material model.

Table 3-9: Missile Finite Element Model Material Strain-Rate Parameters.

Missile	**Meppen II-4**	**VTT Flexural**		**VTT Punching**
Material Type	RSt 37-2 Steel	Stainless Steel EN 1.4432	Carbon Steel S355J2H	Stainless Steel EN 1.4432
Constitutive Law	*MAT_024	*MAT_024	*MAT_003	*MAT_024
Cowper-Symonds, ***C*** (1/msec)	4.04 x 10^{-2}	0.1	4.04 x 10^{-2}	0.1
Cowper-Symonds, ***P***	5	10	5	10

The Cowper-Symonds strain-rate parameters for the RSt 37-2 steel and carbon steel S355J2H were taken from values found in engineering literature based on common Young's Modulus (near 207 GPa), similar Poisson's ratio, and density (Peixinho and Pinho 2007). Likewise, the Cowper-Symonds strain-rate parameters used to model the stainless steel EN 1.4432 were obtained from an article providing data for a Austenitic grade AISI 304 and/or AISI 316 type steel (Nordbert 2004).

3.3.2.4 Contact Modeling

In order to adequately simulate the impact scenarios, several types of contact were invoked to provide necessary force transmission between various components. There is no one-size fits all when using contact methods with LS-DYNA, and the major contact methods used for each impact scenario is outline briefly in Table 3-10.

Table 3-10: Contact Methods Used in All Impact Scenarios.

Contact Method	Impact Scenario		
	Meppen II-4	**VTT Flexural**	**VTT Punching**
*CONTACT_ERODING_SURFACE_TO_SURFACE	Missile to Target Concrete (no erosion occurred)	Missile to Target Concrete (no erosion occurred)	Missile to Target Concrete (erosion occurred)
*CONTACT_AUTOMATIC_SINGLE_SURFACE	Missile Steel on Missile Steel (provides concertina type buckling)	Missile Steel on Missile Steel (provides concertina type buckling)	Missile Steel to Target Steel Reinforcement
*CONTACT_AUTOMATIC_SURFACE_TO_SURFACE	Not Used	Not Used	Missile Steel Case and Missile Concrete Fill

Common to all contact methods used was a specification of friction parameters. The *CONTACT_ERODING_SURFACE_TO_SURFACE method used equal values of static and dynamic friction coefficients, μ_s and μ_d, equal to 0.7 to represent a steel on concrete type friction interaction, and a computed exponential decay coefficient, based on the relative velocity of the surfaces in contact, $v_{rel} = 5 \times 10^{-4}$ (LSTC, LS-DYNA Keyword User's Manual Volume 1 and Volume 2 2010). The *CONTACT_AUTOMATIC_SINGLE_SURFACE method used $\mu_s = \mu_d = 0.2$ for the Meppen II-4 and VTT Flexural models to represent steel on steel type contact (method permits the concertina mode collapse behavior). The *CONTACT_AUTOMATIC_SINGLE_SURFACE type contact algorithm used with the VTT punching model simulations representing missile steel on reinforcing bar steel also used the same coefficient of friction values ($\mu_s = \mu_d = 0.2$). The *CONTACT_AUTOMATIC_SURFACE_TO_SURFACE method was used in the VTT punching mode impact scenario simulations to treat contact between the missile's steel case and the missile's internal tube of concrete. For this contact interface, friction values of $\mu_s = \mu_d = 0.7$ were employed (same values as the erosion type contact; steel on concrete friction interaction).

Another important aspect of contact definitions involves proper parameters regarding the soft constraint-based formulation when not using a penalty-based approach. For both the Meppen II-4 and VTT Flexural impact scenarios, a soft-constraint parameter value, ***SOFT*** = 2 was used which is well suited for shell element contact (LSTC-contact 2011). The VTT Punching impact scenarios are modeled entirely with 8-noded hexahedral solid elements; thus the contact definitions used a soft-constraint parameter of ***SOFT*** = 1.

3.3.2.5 Test Cases

As mentioned previously, all three impact scenario numerical calculations (i.e., Meppen, flexural, and punching) were conducted using three different target concrete material models: *MAT_072R3 (Karagozian & Case), *MAT_085 (Winfrith), and *MAT_159 (Continuous Surface Cap Model). Presented in Table 3-11, Table 3-12, and Table 3-13 are the baseline and sensitivity calculation matrix for all numerical impact simulations. At the beginning of the modeling effort during FY 2012, a sensitivity study for two of these impact scenarios, flexural and punching, using selected parameter variations of the three different target concrete material models, was realized as a means of identifying the target response sensitivity. A metric for evaluating flexural impact response was chosen as the deflection at gauge 1 on the target (not included in this report). A different metric for judging the response of the punching impact response was selected as the missile exit velocity. A brief punching response sensitivity comparison will presented in the results summary section.

Table 3-11: Meppen Impact Model Case Matrix (M for"Meppen").

Target Concrete Model *MAT_072R3 (K & C)	Target Concrete Erosion (epssh)	Target Concrete Dynamic Increase Factor (DIF)	Reinforcing Steel Bar Strain Rate Cowper-Symons	S-Lambda (Stretch Parameter on DIF of MAT_72R3, %)
Baseline M1	0.60	Strain Rate Dependent	ON	100
Target Concrete Model *MAT_085 (Winfrith)	**Target Concrete Erosion (epssh)**	**Reinforcing Steel Bar Strain Rate Cowper-Symonds**		
Baseline M2	0.60	ON	ON	
Target Concrete Model *MAT_159 (Continuous Surface Cap Model)	**Target Concrete Erosion (epssh)**	**Reinforcing Steel Bar Strain Rate Cowper-Symonds**		
Baseline M3	0.60	ON	ON	

Table 3-12: Flexural Impact Model Sensitivity Study Matrix (F for "Flexural").

Target Concrete Model *MAT_072R3 (K & C)	Target Concrete Erosion (epssh)	Target Concrete Dynamic Increase Factor (DIF)	Reinforcing Steel Bar Strain Rate Cowper-Symons	S-Lambda (Stretch Parameter on DIF of MAT_72R3, %)
Baseline F1	0.60	Strain Rate Dependent	ON	100
Sensitivity F1.1	0.60	1.0	OFF	N/A
Sensitivity F1.2	0.60	Strain Rate Dependent	ON	100
Sensitivity F1.3	0.60	Strain Rate Dependent	ON	110
Sensitivity F1.4	0.60	Strain Rate Dependent	ON	120
Target Concrete Model *MAT_085 (Winfrith)	Target Concrete Erosion (epssh)	Reinforcing Steel Bar Strain Rate Cowper-Symonds		
Baseline F2	0.60	ON		
Sensitivity F2.1	0.60	OFF		
Target Concrete Model *MAT_159 (Continuous Surface Cap Model)	Target Concrete Erosion (epssh)	Reinforcing Steel Bar Strain Rate Cowper-Symonds		
Baseline F3	0.60	ON		
Sensitivity F3.1	0.60	OFF		

Table 3-13: Punching Impact Model Sensitivity Study Matrix (P for "Punching").

Target Concrete Model *MAT_072R3 (K & C)	Target Concrete Erosion (epssh)	Target Concrete Dynamic Increase Factor (DIF)	Reinforcing Steel Bar Strain Rate Cowper-Symons	S-Lambda (Stretch Parameter on DIF of MAT_72R3, %)
Baseline P1	0.60	1.0	OFF	N/A
Sensitivity P1.1	0.60	Strain Rate Dependent	OFF	100
Sensitivity P1.2	0.60	Strain Rate Dependent	OFF	75
Sensitivity P1.3	0.60	Strain Rate Dependent	OFF	50
Sensitivity P1.4	0.60	1.0	ON	N/A
Sensitivity P1.5	0.61	1.0	OFF	N/A
Sensitivity P1.6	0.62	1.0	OFF	N/A
Target Concrete Model *MAT_085 (Winfrith)	Target Concrete Erosion (epssh)	Reinforcing Steel Bar Strain Rate Cowper-Symonds		
Baseline P2	0.565	ON		
Sensitivity P2.1	0.565	OFF		
Sensitivity P2.2	0.575	OFF		
Sensitivity P2.3	0.585	OFF		
Target Concrete Model *MAT_159 (Continuous Surface Cap Model)	Target Concrete Erosion (epssh)	Reinforcing Steel Bar Strain Rate Cowper-Symonds		
Baseline P3	0.60	OFF		
Sensitivity P3.1	0.60	ON		
Sensitivity P3.2	0.61	OFF		
Sensitivity P3.3	0.62	OFF		

3.4 Phase II Results and Summaries

3.4.1 Changes between Phase I and Phase II

Two approaches were investigated in Phase I: traditional finite element (LS-DYNA) and peridynamics (EMU). The Sandia team was never able to get contact between the missile and concrete working correctly with LS-DYNA, so Sandia employed a Riera method for the predictions. The peridynamic simulations included direct representations for the missiles impacting the targets. In Phase II, the peridynamic simulation approach was not pursued due to funding constraints. The LS-DYNA calculations were updated to include explicit representations of the missiles rather than the Riera approach. The concrete material model parameters were updated as well. Finally, shell elements were used in Phase II for various pieces of the simulations.

3.4.2 Standard Concrete Cylinder Tests

The standard concrete cylinder test numerical model originally used ten (10) elements located near the strain gauge locations to investigate the unconfined and triaxial compression response, as shown in Figure 3-16. However, in order to adequately capture the axial strain over the entire length of the test specimen, as was done in the test using a linear variable differential transformer (LVDT), the axial strain was computed as the integrated axial direction (*i.e.,* the z-direction) nodal force divided by the area of the end cap (x-y plane at z=0 or z=140 mm, top or bottom). This numerical approach to axial strain is the equivalent method of the LVDT axial strain. Thus to compute the radial or transverse direction strain, the x-direction strains at elements H772 and H724, and the y-direction strains at elements H804 and H756, shown in Figure 3-16, were averaged.

Results of the standard concrete cylinder test numerical calculations, axial stress vs. axial and transverse strain for the unconfined compression and the four triaxial compression stress paths are shown in Figure 3-17, Figure 3-18, Figure 3-19, Figure 3-20, and Figure 3-21, whereby the numerical results are labeled as "Num". Figure 3-23 shows both the test and numerical calculated axial stress vs. axial strain results together. Lastly, shown in Figure 3-22 are all of the numerical results of axial stress vs. axial strain. As seen in Figure 3-23, there are considerable numerical features that arise for lager confinement pressure triaxial compression numerical calculations. This may be due to in insufficient quasi-static strain rate applied to the axial loaded surfaces (1.0 x 10^{-4} 1/msec). Also, this behavior may indicate inertial effects are contributing to a noisy-like response. A possible work-around to alleviate this behavior is to decrease this quasi-static strain rate and use a velocity controlled approach using a slower speed (equivalent to strain rate of 1.0 x 10^{-6} 1/msec).

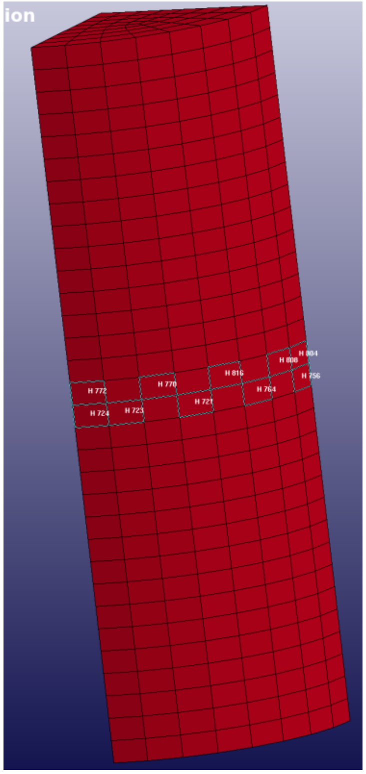

Figure 3-16: Standard Concrete Cylinder Test Finite Element Model Response Monitoring Element Locations.

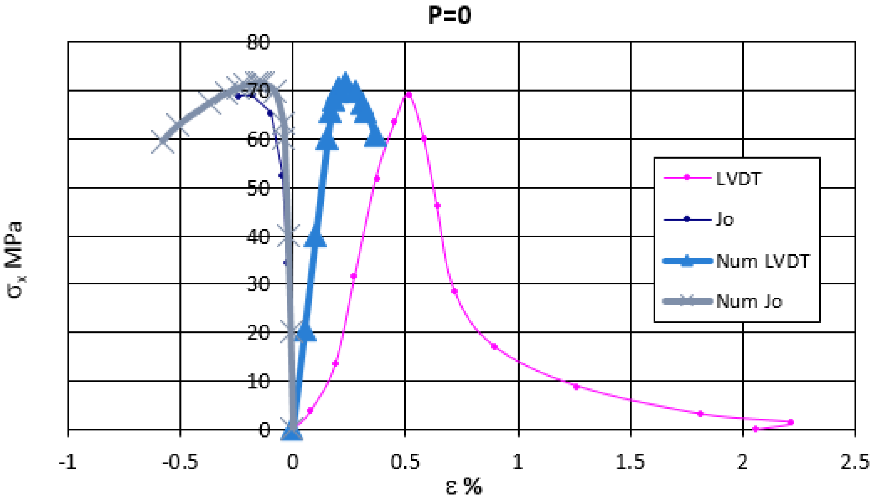

Figure 3-17: 2012 IRSN Standard Concrete Cylinder Test and Numerical Prediction for Unconfined Compression (P=0).

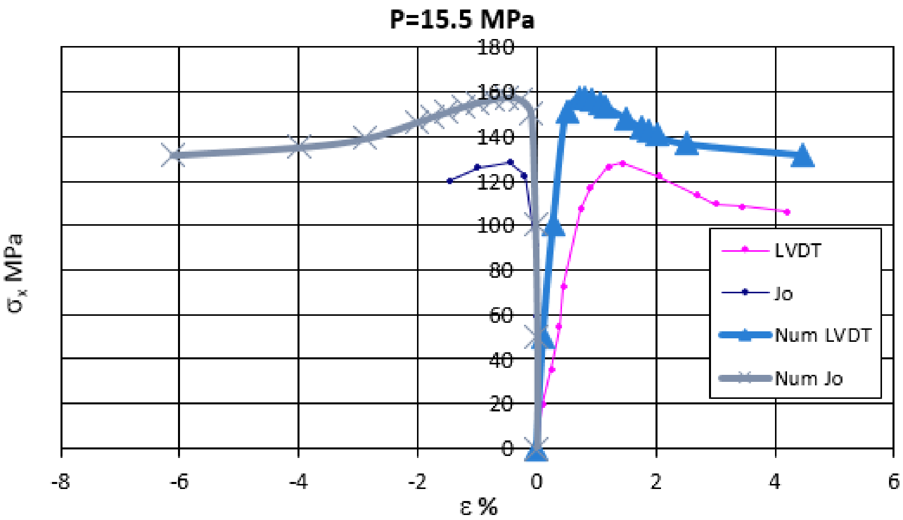

Figure 3-18: 2012 IRSN Standard Concrete Cylinder Test and Numerical Prediction for Triaxial Compression (P=15.5 MPa).

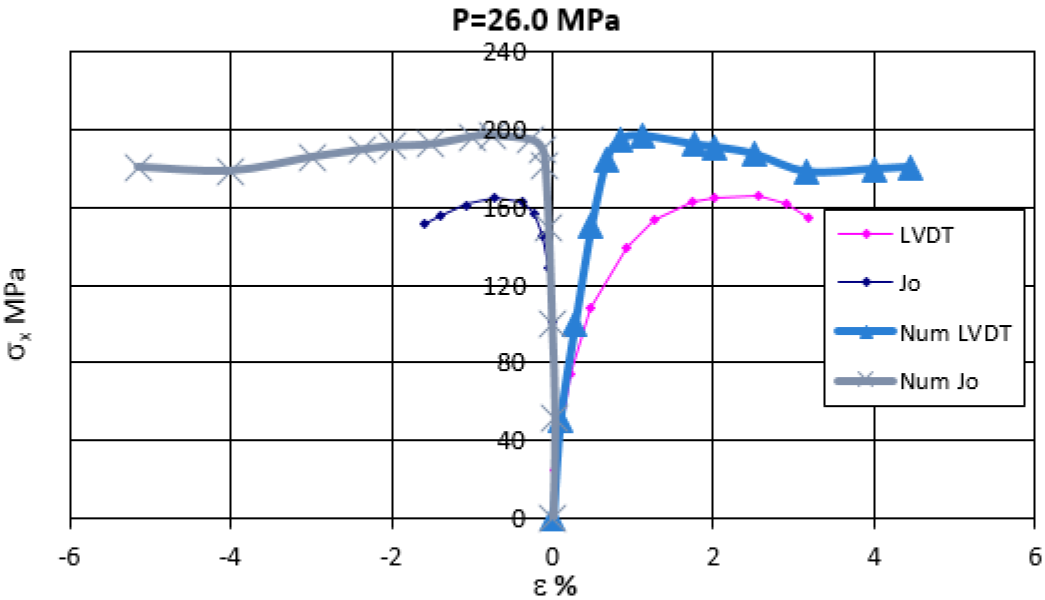

Figure 3-19: 2012 IRSN Standard Concrete Cylinder Test and Numerical Prediction for Triaxial Compression (P=26.0).

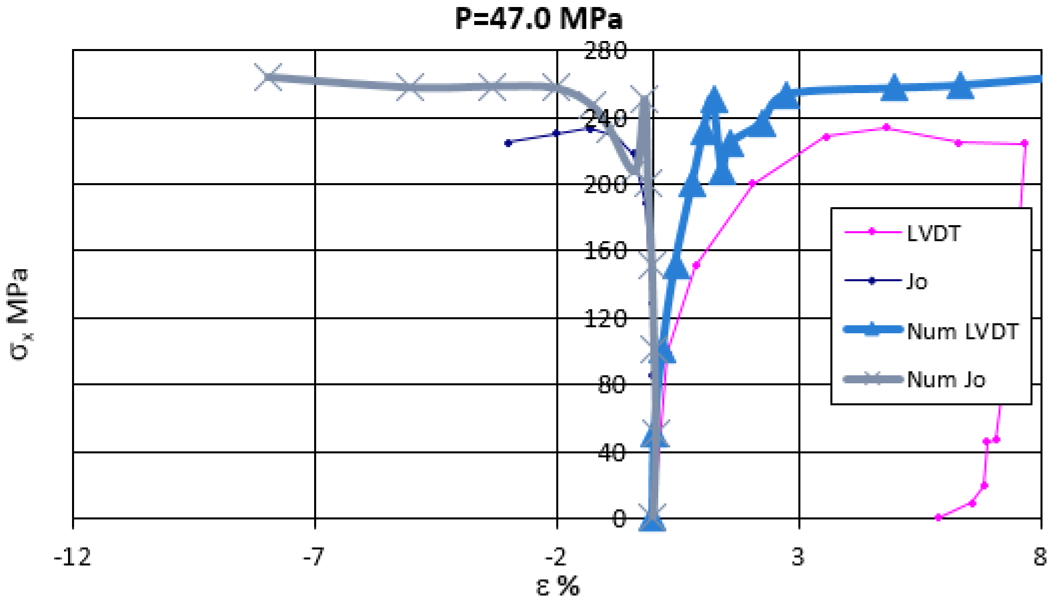

Figure 3-20: 2012 IRSN Standard Concrete Cylinder Test and Numerical Prediction for Triaxial Compression (P=47.0 MPa).

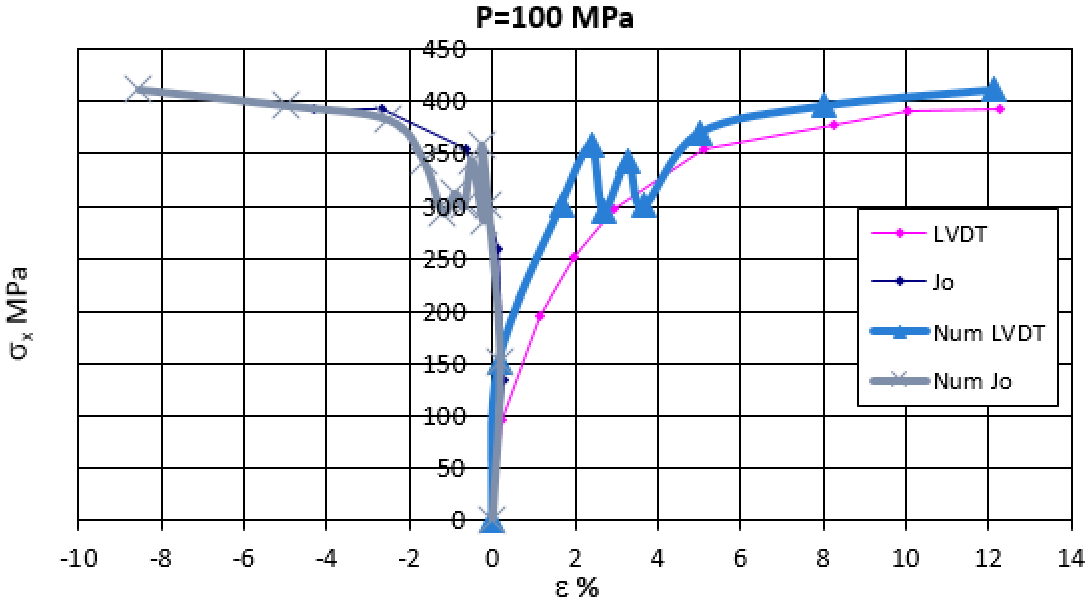

Figure 3-21: 2012 IRSN Standard Concrete Cylinder Test and Numerical Prediction for Triaxial Compression (P=100.0 MPa).

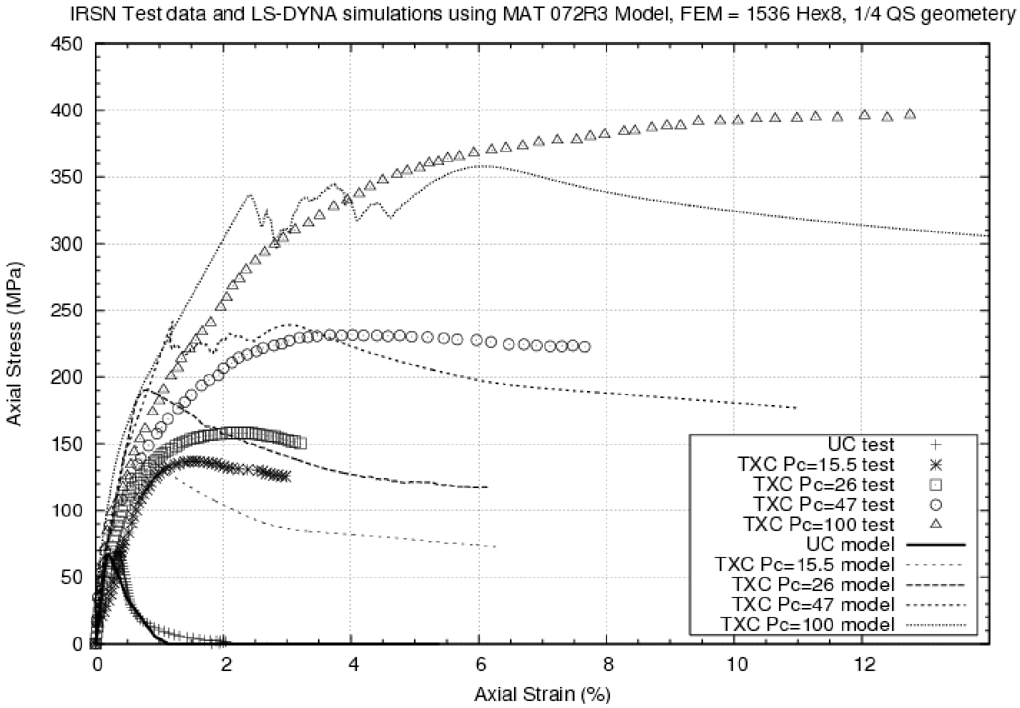

Figure 3-22: 2012 IRSN Standard Concrete Cylinder Test and Numerical Predictions of Axial Stress vs. Strain.

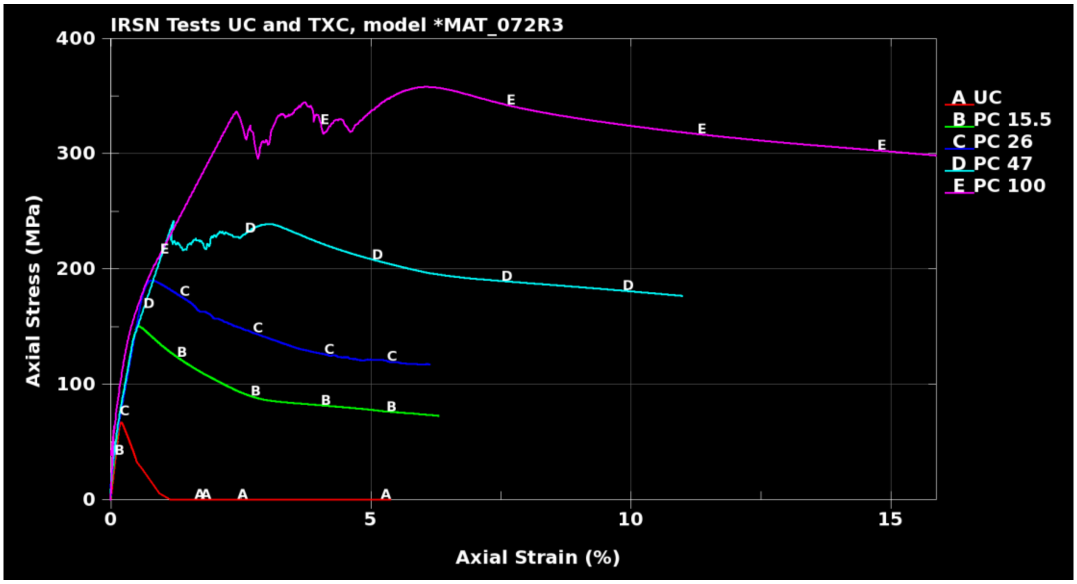

Figure 3-23: 2012 IRSN Standard Concrete Cylinder Test Numerical Prediction of Axial Stress vs. Axial Strain.

3.4.3 Meppen

As mentioned earlier, three different target concrete models were used to predict the response of the Meppen II-4 impact scenario (*i.e.,* *MAT_072R3, *MAT_085, and *MAT_159). Three baseline calculations (M1, M2, and M3, in accordance with Table 3-11) were completed to predict and compare with the Meppen impact test. All of the simulations assumed no strain-rate strength enhancement in the steel reinforcing bars. It was reasoned that the predicted bending mode response would not generate significant strain rates in the reinforcing steel and thus the effect of strain-rate enhanced strength was ignored. The Winfrith (*MAT_085) and the Continuous Surface Cap Model (CSCM or *MAT_159) concrete constitutive laws were also employed without strain-rate effects. However, the Karagozian and Case concrete material model (*MAT_072R3) used a dynamic increase function to permit strain-rate effects (shown in Table 3-8) based on the unconfined compressive cylindrical specimen strength, f_c' = 30.5 MPa. The stress-strain response using a one-element numerical model using each of these concrete constitutive laws was conducted for both a compressive and tensile loading to compare differences in observed behavior. Figure 3-24 displays a simplified representation of the compressive and tensile stress vs. strain behavior for each target concrete model (note that the one-element simulations using the *MAT_072R3 model did not include dynamic increase factors). As seen in Figure 3-24, both the *MAT_072R3 and *MAT_159 constitutive laws experience strain softening in compression, as opposed to the absence of any compressive strain softening witnessed in the *MAT_085 concrete model response. Also seen in this figure is the *MAT_085 model's use of an unconfined compressive cubic specimen strength, f_c' = 37.2 MPa.

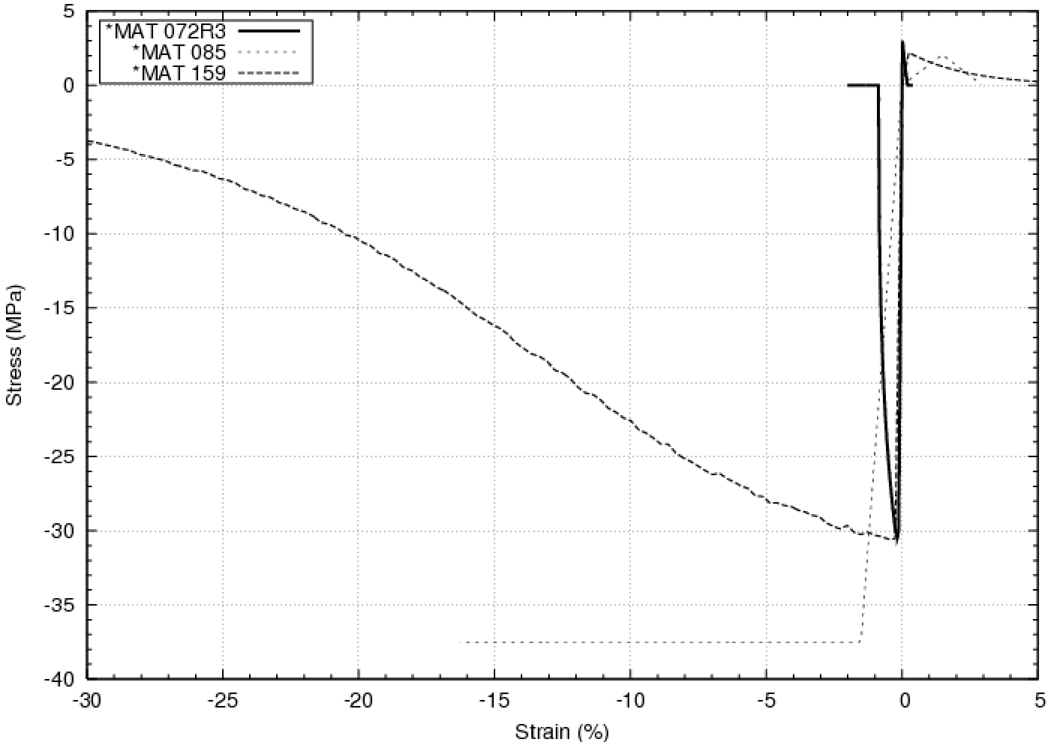

Figure 3-24: Meppen II-4 Target Concrete One-Element Stress vs. Strain Response of Several LS-DYNA Concrete Constitutive Laws.

Shown in Figure 3-25 is the schematic of the Meppen II-4 missile deformed shape at the post-shock time. Shown in Figure 3-26 are the deformed missile shapes from three numerical simulations of the Meppen II-4 impact scenario whereby the concrete target material model was varied. Shown in Table 3-14 are the key results from the Meppen II-4 impact scenario calculations compared with the Test data available. Shown in Figure 3-27, Figure 3-28, Figure 3-29, Figure 3-30, and Figure 3-31 are the results of numerical predictions compared to the Meppen II-4 test data for the missile tail displacement history, missile tail velocity history, Meppen II-4 test deflection monitor points, target deflection response at monitor location W1, and target deflection at monitor location W3, respectively. Since a ¼-symmetry finite element model was used, the recorded Meppen II-4 target displacements at all monitor locations are included for comparison.

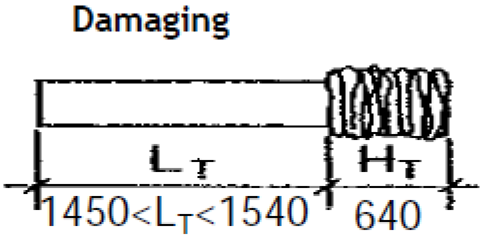

Figure 3-25: Schematic of Meppen II-4 Missile Post-Shock Deformed Shape (Meppen 2010).

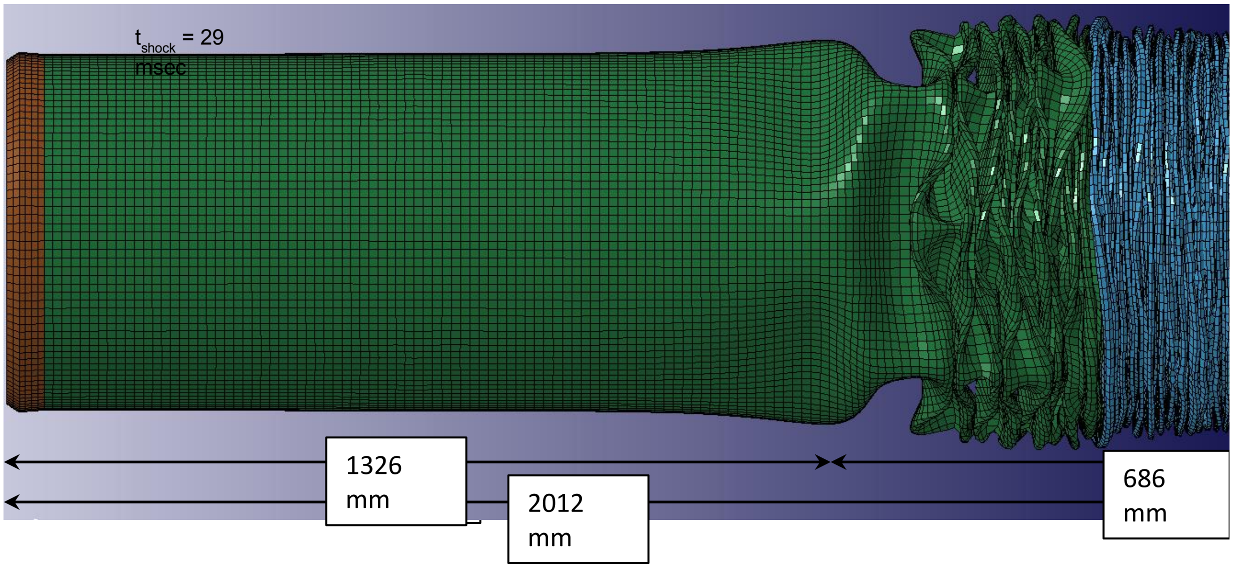

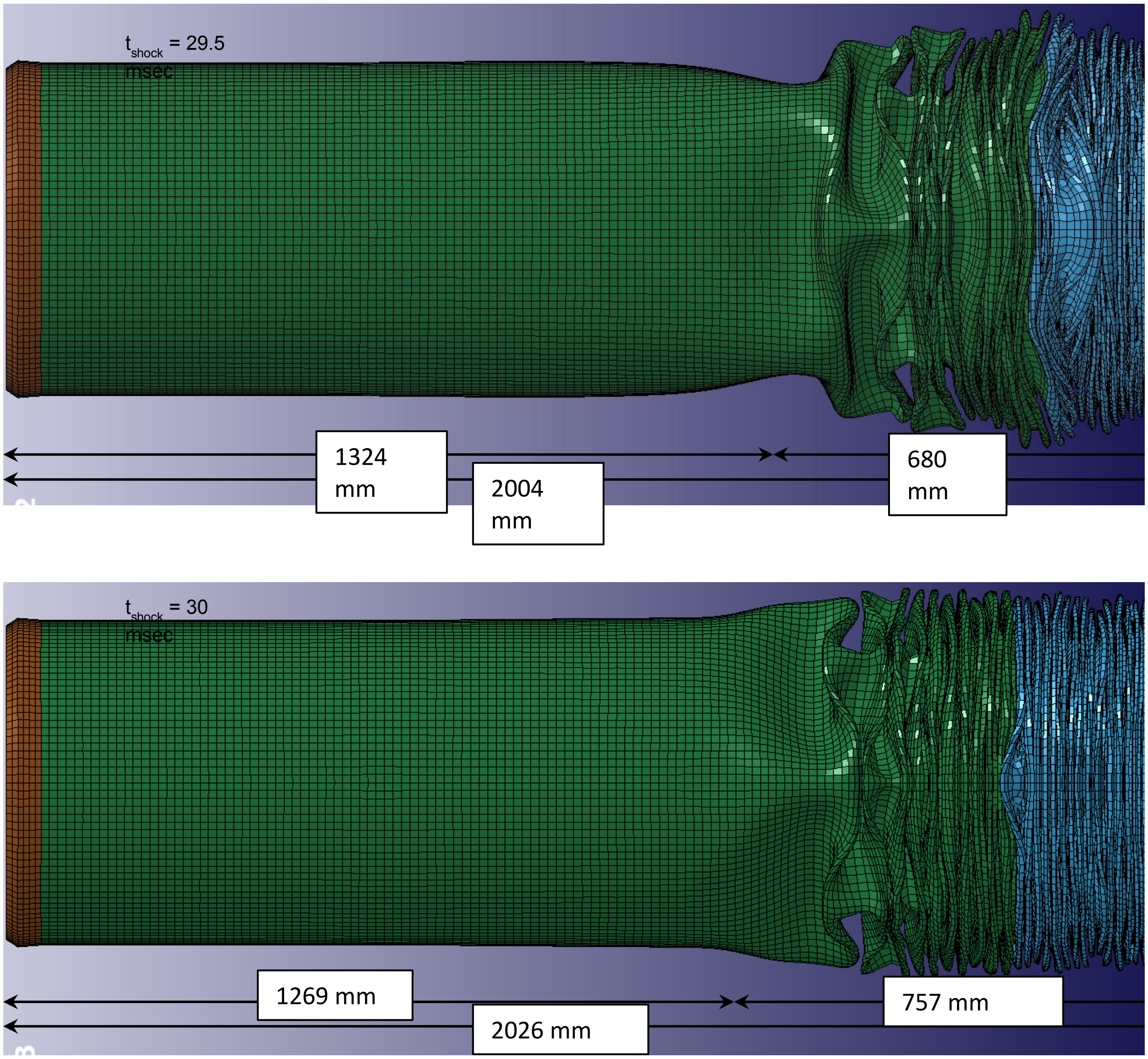

Figure 3-26: Meppen II-4 Impact Scenario Simulation Deformed Missile Shapes At End of Shock: *MAT_072R3 (First); *MAT_085 (Second); *MAT_159 (Last).

Table 3-14: Key Results of the Meppen II-4 Impact Scenario Simulations.

Response	Experiment	*MAT_072R3		*MAT_085		*MAT_159	
		Value	Error	Value	Error	Value	Error
Peak Load (MN)	13.1	12.5	-4.6 %	12.5	-4.6 %	12.5	-4.6%
Shock Duration (msec)	26	29	+11.5%	29.5	+11.9 %	30	+15.4 %
L_T of Missile (mm)	1450:1540	1326	-12.7 %	1324	-12.9 %	1269	-17.8 %
H_T of Missile (mm)	640	686	+7.8 %	680	+6.3 %	757	+18.3 %

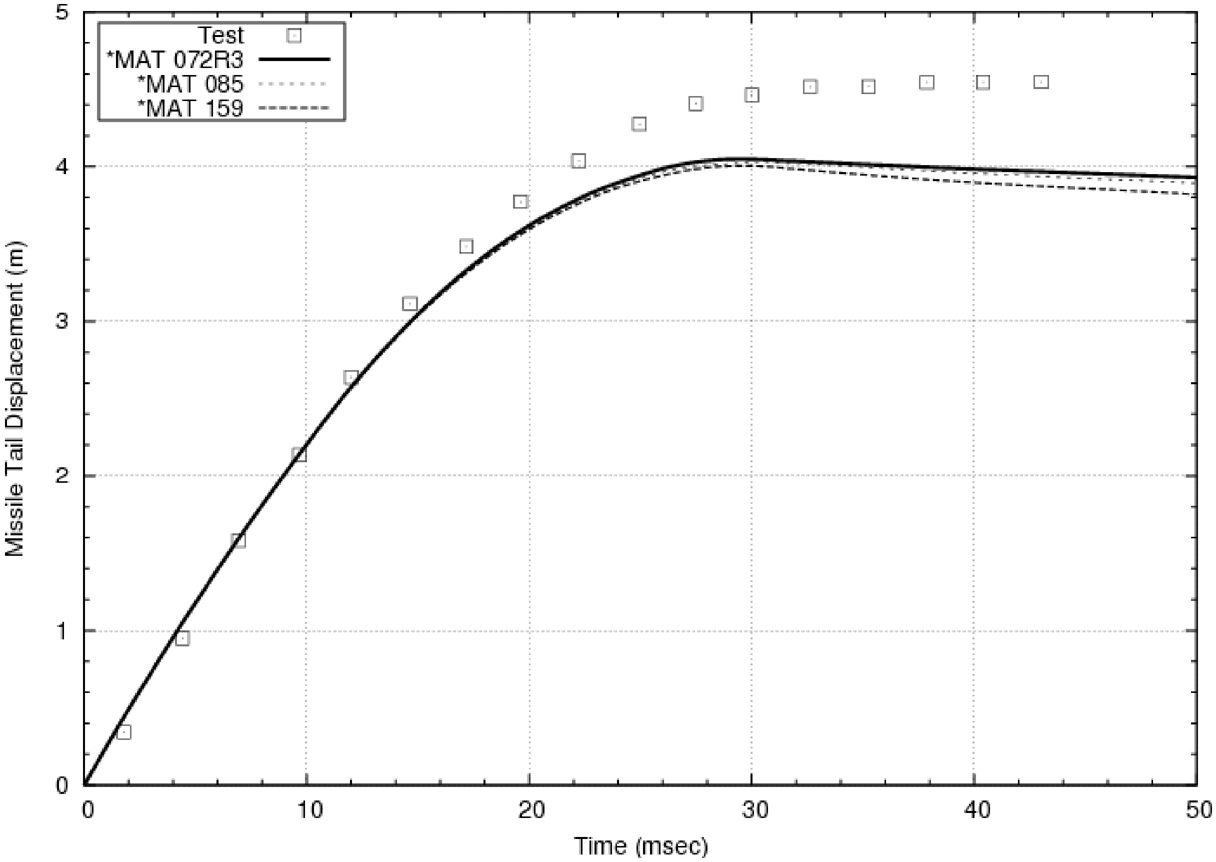

Figure 3-27: Meppen II-4 Test and Numerical Predictions of Missile Tail Displacement History.

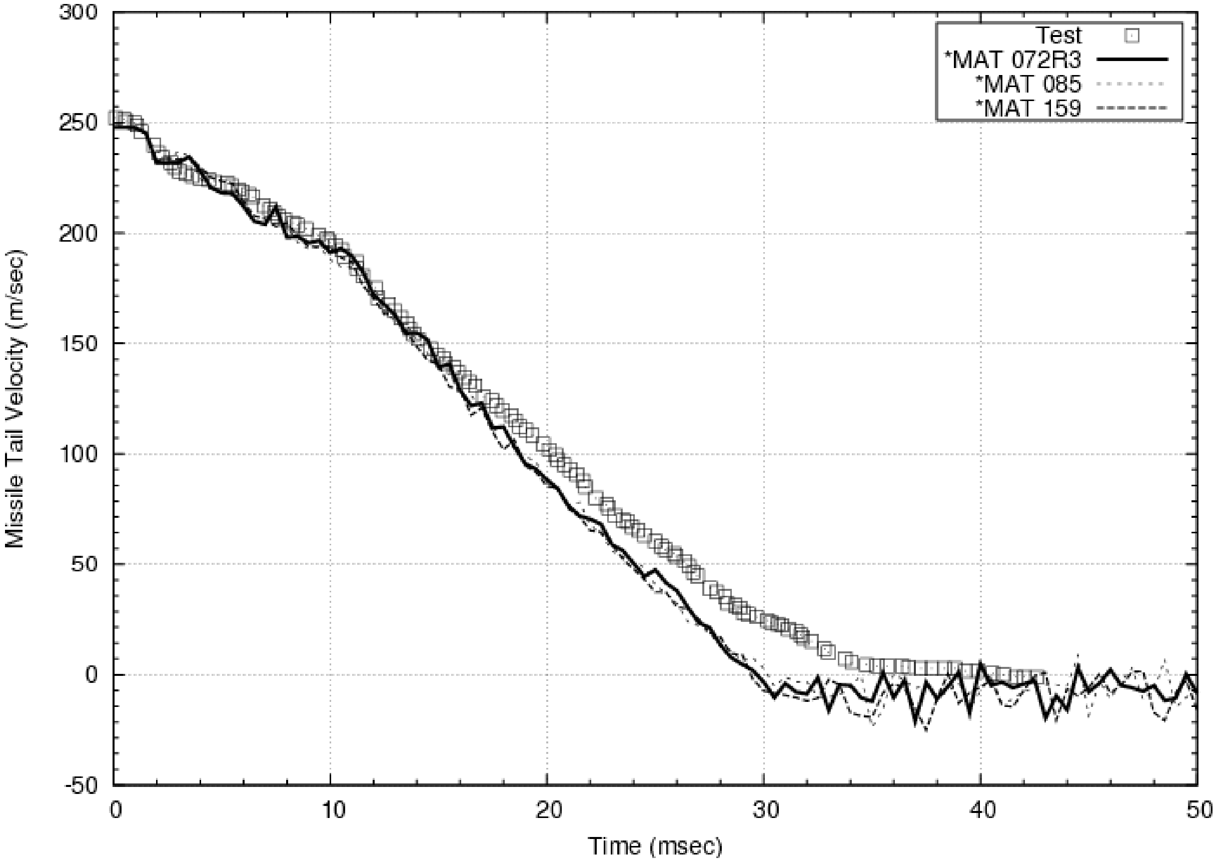

Figure 3-28: Meppen II-4 Test and Numerical Predictions of Missile Tail Velocity History.

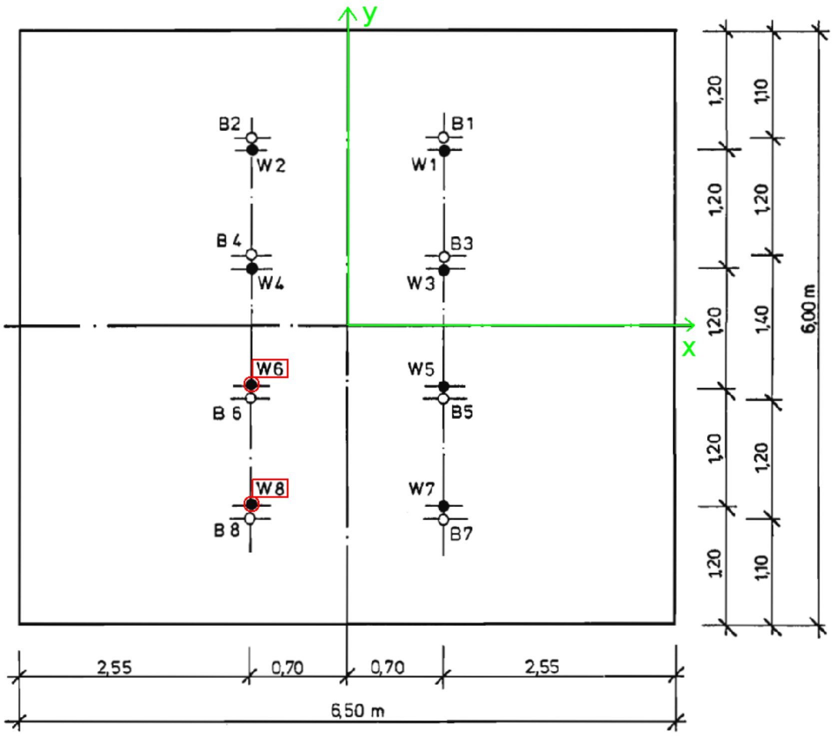

Figure 3-29: Meppen II-4 Target Deflection Monitoring Locations.

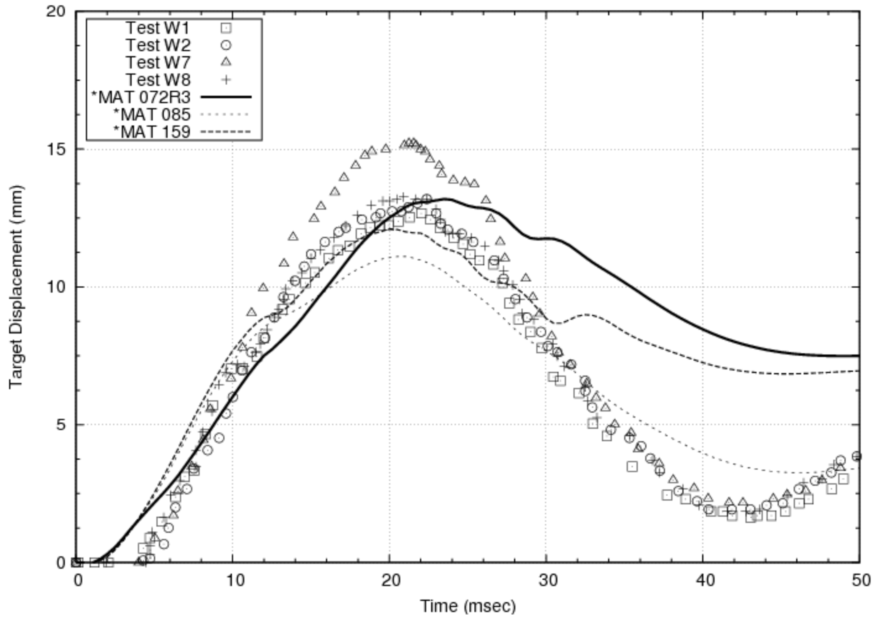

Figure 3-30: Meppen II-4 Test and Numerical Predictions of Target Displacement Near Monitoring Location W1.

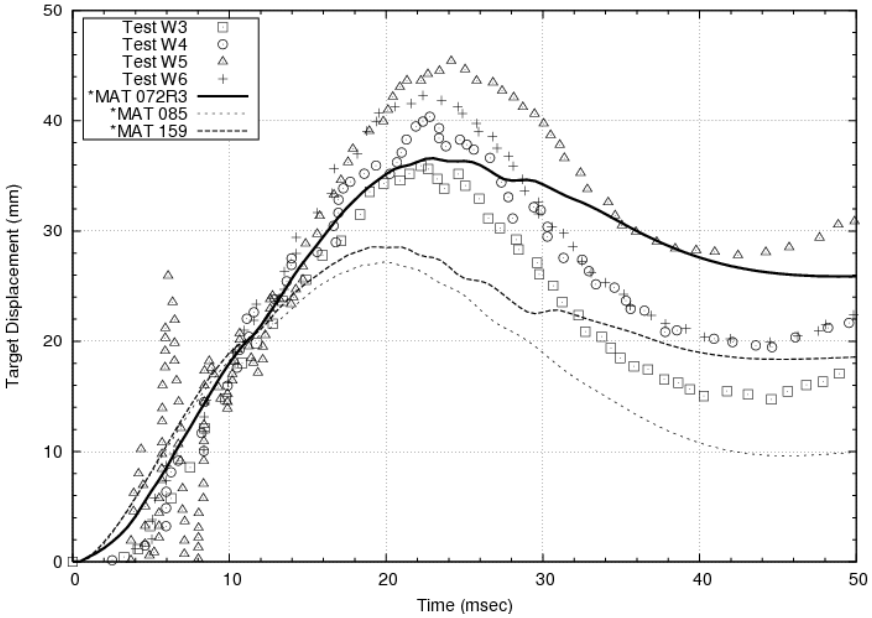

Figure 3-31: Meppen II-4 Test and Numerical Predictions of Target Displacement Near Monitoring Location W3.

As seen in Figure 3-30 and Figure 3-31 the simulated target displacements show that the simulations employing the *MAT_072R3 target concrete constitutive law are closer than either the *MAT_085 or *MAT_159 (i.e., Winfrith or CSCM) models at predicting target displacements. Also using a ¼-symmetric finite element model has predicted target displacements that are within the bounds of symmetric and skew-symmetric target monitoring points (*e.g.,* displacement monitor location W1 compared with W8, W7, and W2; and the W3 monitor location compared with W6, W5, and W4; shown in Figure 3-29).

Due to a bug in the LS-DYNA version mpp971d Dev, visualization of crack patterns was not possible from the *MAT_085 simulations of the Meppen II-4 impact scenario. Shown in Figure 3-32 is the deformed finite element model at 29 milliseconds. Shown in Figure 3-33 is the predicted damage (whereby a value of 2.0 represents a state of complete damage) of the concrete target at 29 milliseconds. As seen in Figure 3-33, a large portion of the front side of the target face has experienced a state of complete damage (i.e., the painted contour label "Effective Plastic Strain" is actually the damage; and damage = 2 denotes a state on the residual failure surface). The predicted reinforcing steel plastic strain response at 29 milliseconds is shown in Figure 3-34. As seen in this figure, the maximum plastic strain predicted in the transverse direction reinforcing steel bar is near 5 % and is far below the failure limit of 10 %.

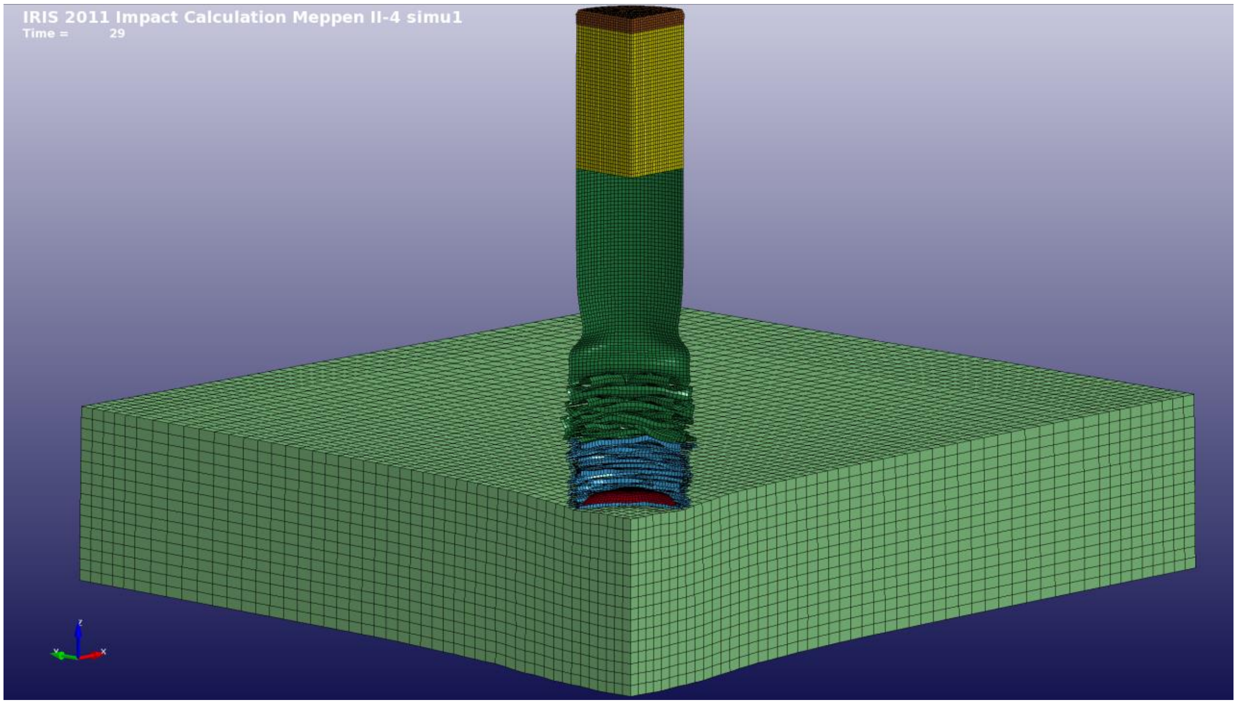

Figure 3-32: Deformed Finite Element Model for the Meppen II-4 Impact Scenario at 29 milliseconds (using target concrete model *MAT_072R3).

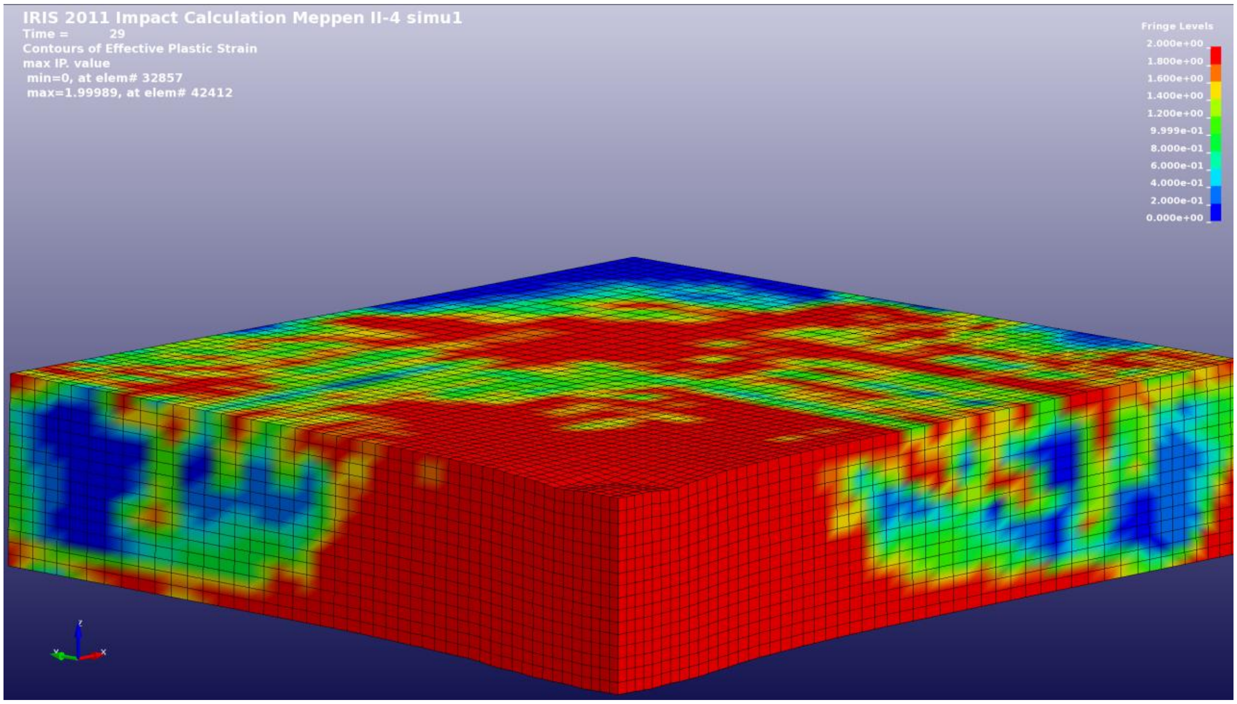

Figure 3-33: Predicted Damage of the Meppen II-4 Impact Scenario at 29 milliseconds (using target concrete constitutive law *MAT_072R3).

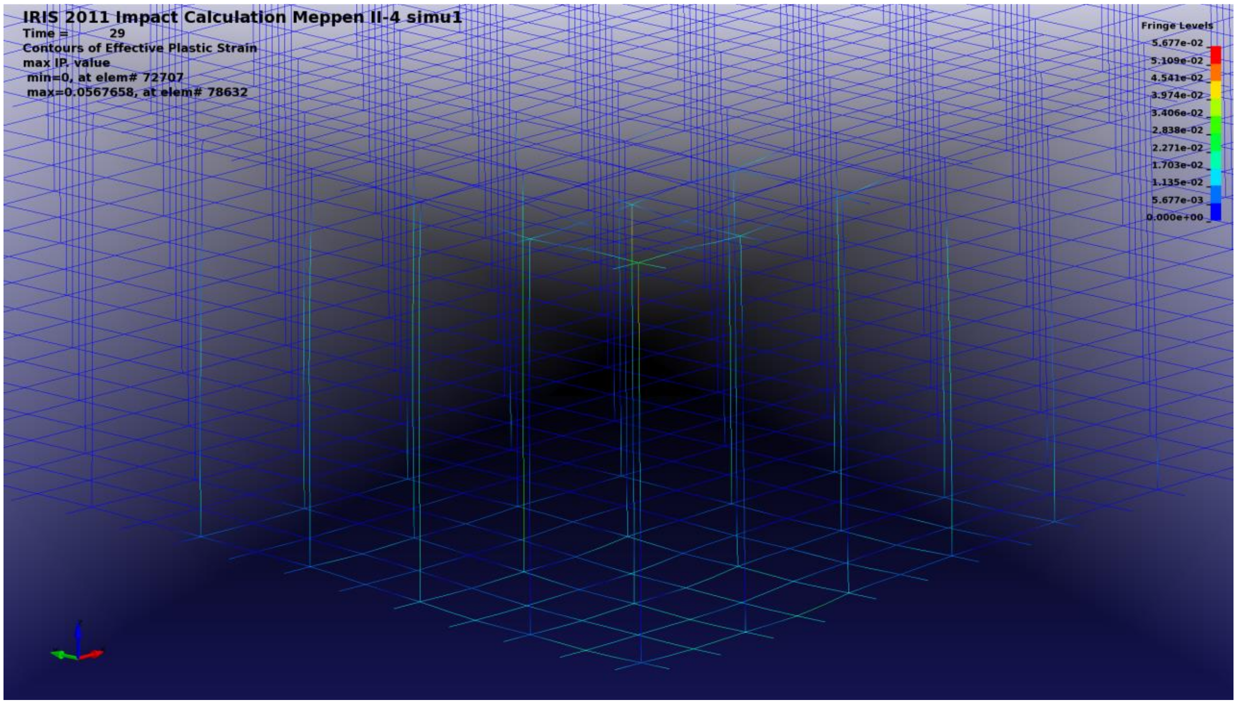

Figure 3-34: Predicted Plastic Stain in Reinforcing Steel Bars of the Meppen II-4 Impact Scenario (using target concrete model *MAT_072R3).

3.4.4 IRIS IRSN VTT Flexural

Similar to the Meppen II-4 impact scenario calculations, three different target concrete models were used to predict the response of the VTT flexural impact scenario (*i.e.,* *MAT_072R3, *MAT_085, and *MAT_159). Three baseline calculations (F1, F2, and F3, in accordance with Table 3-12) were completed to predict and compare with the flexural impact test. Unlike the Meppen II-4 impact scenario simulations, all of the simulations applied strain-rate strength enhancement in the steel reinforcement bars using the Cowper-Symonds option of *MAT_024, with $\boldsymbol{C}$ = 40.4 x 10^{-3} 1/msec and $\boldsymbol{P}$ = 5. Similar to the Meppen II-4 simulations, both the Winfrith (*MAT_085) and the Continuous Surface Cap Model (CSCM or *MAT_159) concrete constitutive laws were employed without strain-rate effects. All flexural impact calculations used a target concrete model based upon the 2012 IRSN standard concrete cylinder, shown previously in Figure 3-5, with an unconfined compressive strength, f_c' = 69 MPa.

Shown in Figure 3-35 are the deformed/post-impact missiles from VTT Flexural Mode Test B1 and B2, (Vepsä 2010a). Table 3-15 (where the baseline designation is cross-referenced to Table 4-18) and Figure 3-42 display key missile impact/deformation values and the computed finite element model missile shapes. Note that each missile deformed shape at the time = tshock, shown in Figure 3-35, are not drawn in the same scale. Comparing the test and numerical simulations of the deformed missile shapes after impact one can see that the resulting post-impact missile length of the numerical simulations is larger than those from the tests.

Figure 3-35: Deformed/Post-Impact VTT Flexural Mode Impact Missiles (Top: Test B1; Bottom: Test B2).

Table 3-15: Key Results from the VTT Flexural Impact Scenario Simulations.

Response	Experiment		*MAT_072R3 (Baseline F1)	*MAT_085 (Baseline F2)	*MAT_159 (Baseline F3)
	B1	B2			
Rebound Velocity (m/sec)	N/A	N/A	6.5	7.1	6.9
tshock = Bounce/Shock Duration (msec)	N/A	N/A	15.75	17.00	14.75
L_T of Missile (mm)	955	930	1122	1116	1286
H_T of Missile (mm)	185	190	191	190	225
$L_T + H_T$ (mm)	1140	1120	1313	1306	1511
Shortening of Missile (mm)	971	991	798	805	600

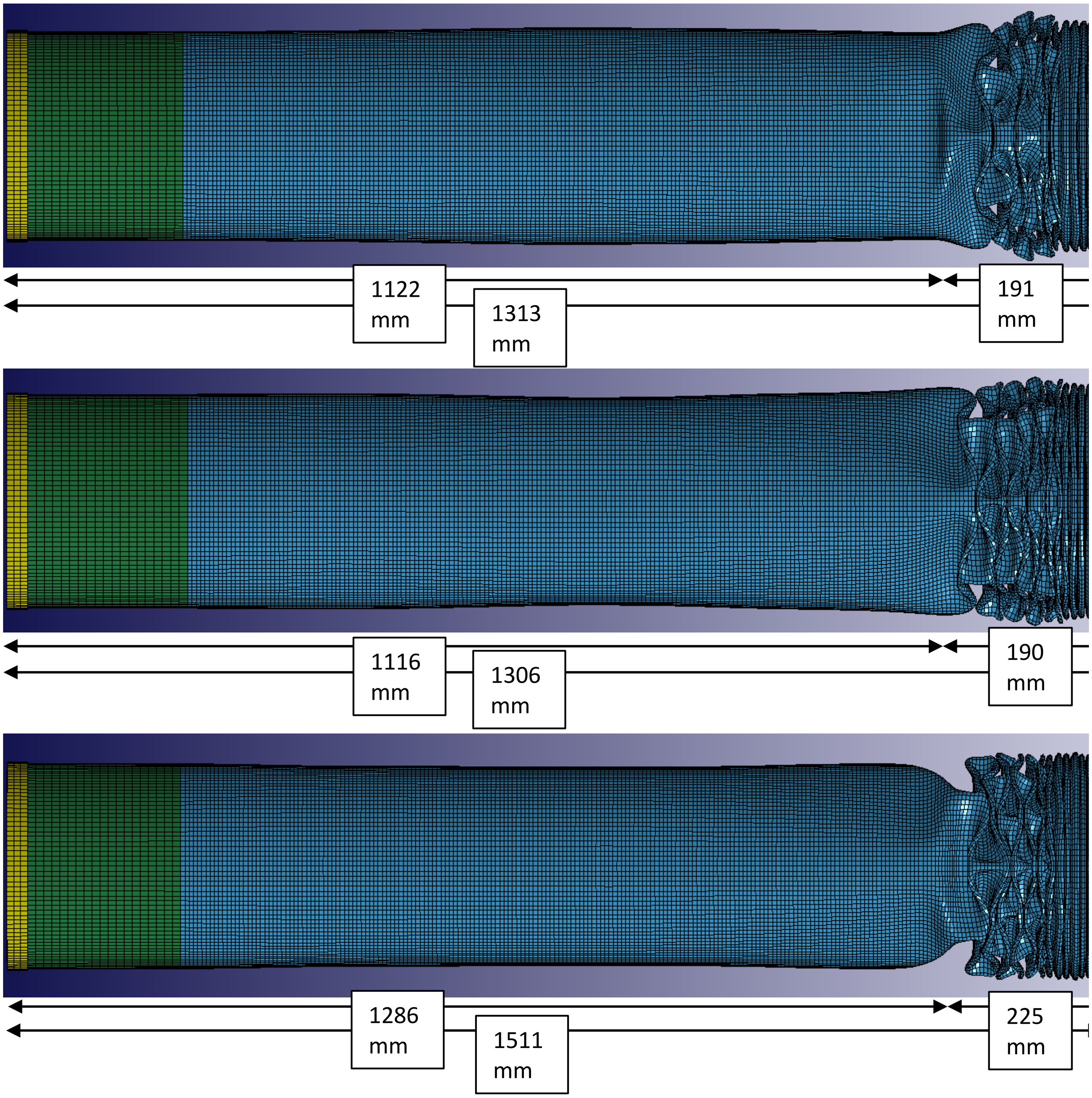

Figure 3-36: VTT Flexural Mode Impact Scenario Simulation Deformed Missile Shapes at time = tshock: *MAT_072R3 (Top); *MAT_085 (Middle); *MAT_159 (Bottom).

Shown in Figure 3-37, Figure 3-38, and Figure 3-39 are the VTT flexural impact scenario target displacement monitoring locations and the resulting numerical simulation's predictions of the target displacements compared with test data at locations W1, and W2, respectively. Comparing the displacement histories, again the *MAT_085 concrete model is consistently in less agreement with test data. Both *MAT_072R3 and *MAT_0159 LS-DYNA concrete constitutive material laws correctly capture the bending phase, which both tests reveal a peak displacement is reached at about 11.5 msec. This agreement may be related to adequate beam element discretization in the *CONSTRAINED_LAGRANGE_IN_SOLID type of steel reinforcement bar (i.e., beam elements) coupling to the concrete elements (8-noded hexahedral elements), and improved concrete material model shear failure surface constructions.

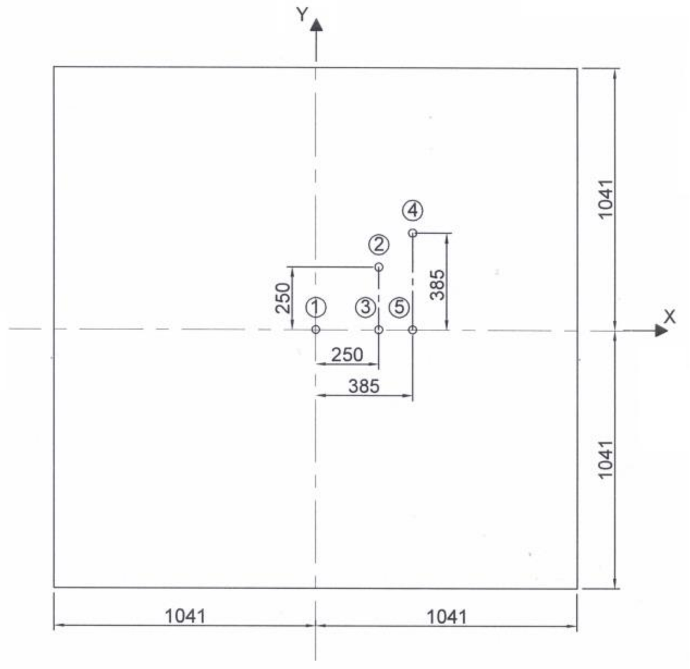

Figure 3-37: VTT Flexural Mode Impact Scenario Target Displacement Monitoring Locations.

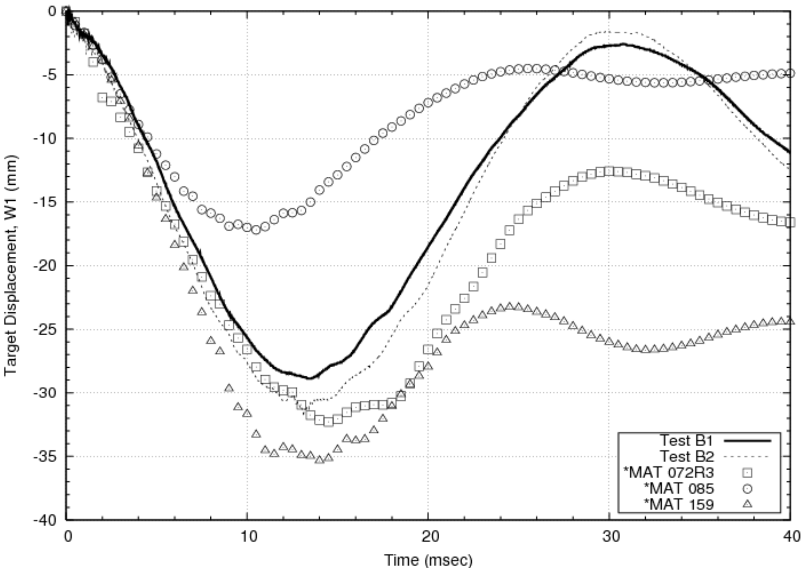

Figure 3-38: VTT Flexural Mode Impact Test and Numerical Predictions of Target Displacement at Monitor Location W1.

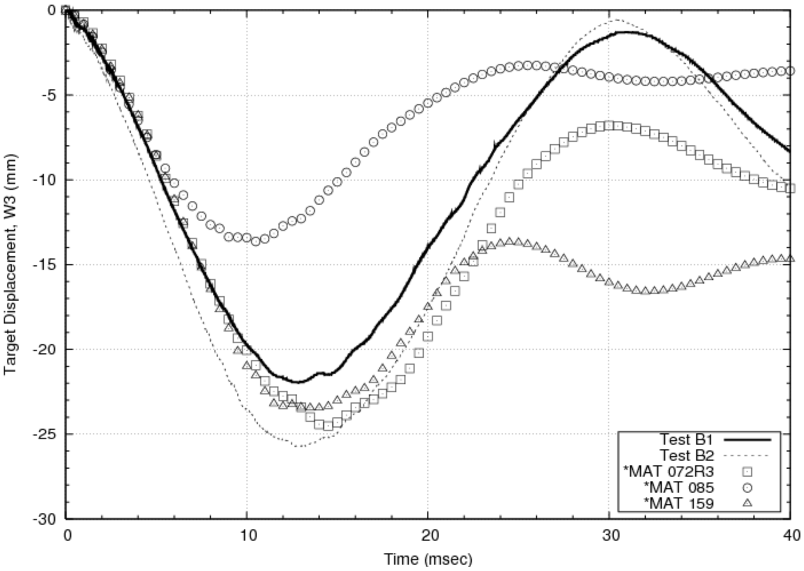

Figure 3-39: VTT Flexural Mode Impact Scenario Test Data and Numerical Predictions of Target Displacement at Monitor Location W3.

Shown in Figure 3-40 and Figure 3-41 is a schematic of the VTT flexural mode impact test target concrete strain gage locations and comparison plots of the test and numerical simulation strains, respectively. As seen in Figure 3-41, the computed predictions of strain magnitudes are nearly a factor of 3 different than the test data.

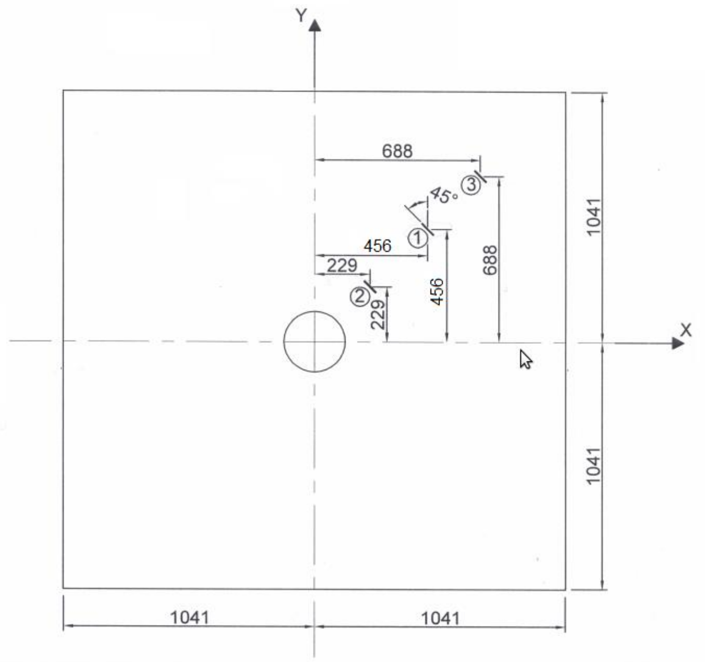

Figure 3-40: VTT Flexural Mode Impact Scenario Target Front Face Strain Gage Locations.

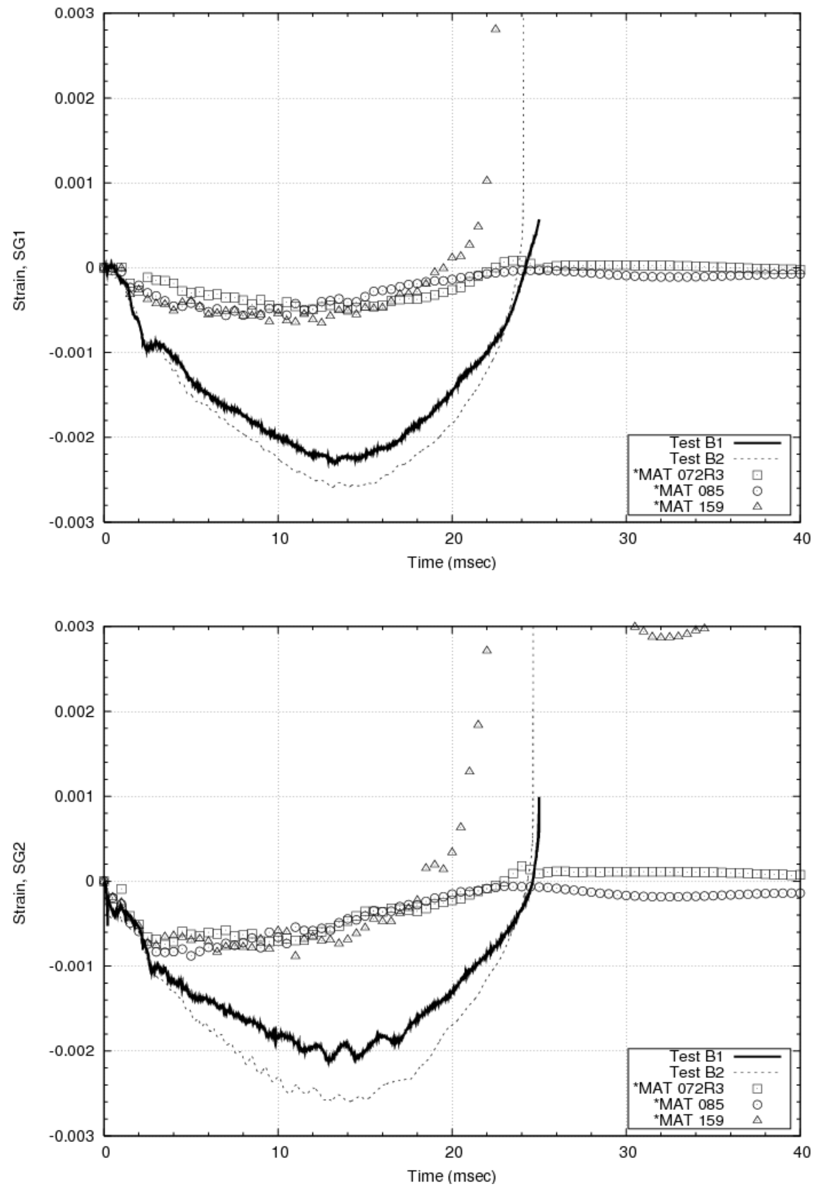

Figure 3-41: Comparison of VTT Flexural Mode Impact Scenario Test Data and Numerically Computed Target Concrete Strains (Top: Gage #1; Bottom: Gage #2).

Shown in Figure 3-42, Figure 3-43, Figure 3-44, and Figure 3-45 is a schematic of the VTT flexural mode impact test target reinforcing steel bar strain gage locations and comparison plots of the test data and numerically computed strains at gage locations 4, 10, and 15, respectively. As seen in Figure 3-43 and Figure 3-44 the numerically computed strains are nearly a third of the B1 test at gage locations 4 and 10.

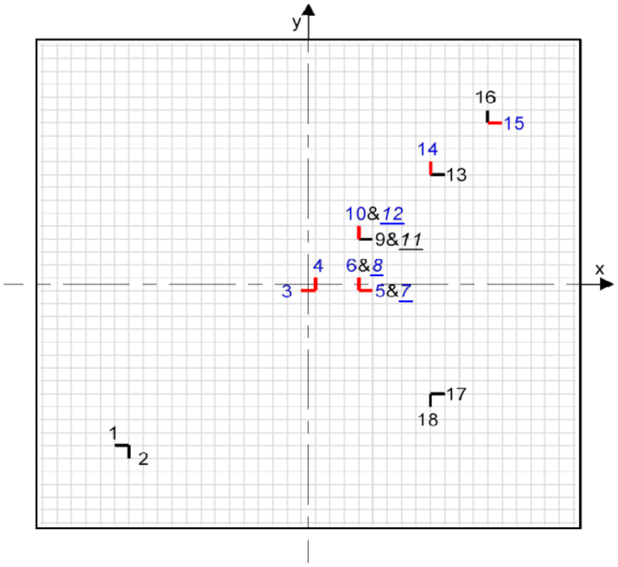

Figure 3-42: VTT Flexural Mode Impact Test Reinforcing Steel Bar Strain Gage Locations.

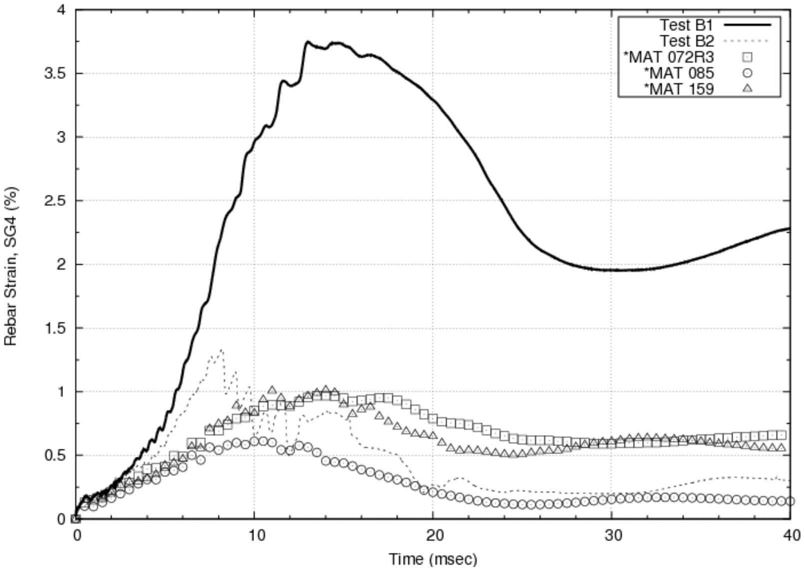

Figure 3-43: Comparison of VTT Flexural Mode Impact Test Data and Numerically Computed Steel Reinforcing Bar Strains at Gage #4.

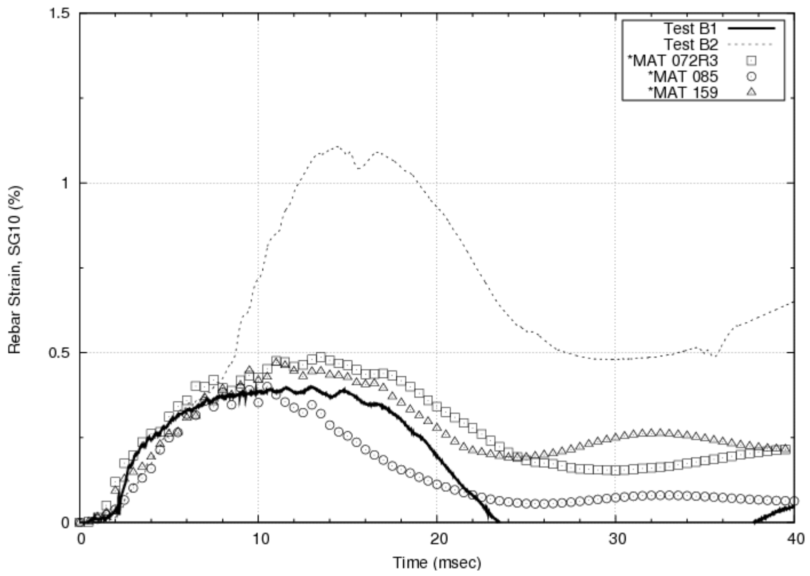

Figure 3-44: Comparison of VTT Flexural Mode Impact Test Data and Numerically Computed Steel Reinforcing Bar Strains at Gage #10.

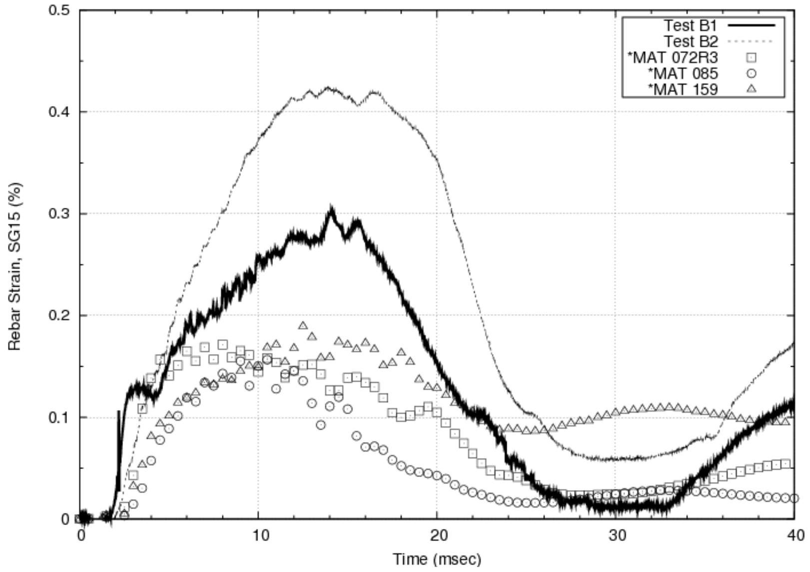

Figure 3-45: Comparison of VTT Flexural Mode Impact Test Data and Numerically Computed Steel Reinforcing Bar Strains at Gage #15.

Comparison of the test data and numerically computed strains at steel reinforcing bar strain gage location #15 of Figure 3-45 shows some agreement on the period of peak strain from the *MAT_072R3 concrete constitutive law, with approximately 50% error at the peak strain value. Several factors may account for this discrepancy between test data and numerically computed results: insufficient coupling of reinforcing bar (beam elements) with the concrete (solid 8-noded hexahedral elements), subsequent feature/outcome of the *CONSTRAINED_LAGRANGE_IN_SOLID methodology, discretization of the beam element grid representing the steel reinforcing bar, and/or material property characterization due to unknown strain rate behavior in the A500HW 6 millimeter outside diameter type reinforcing steel bar.

Due to a bug in the LS-DYNA version mpp971d Dev, visualizations of crack patterns were not possible from the *MAT_085 simulations for the VTT flexural mode impact scenario. However, a variable representing the crack state was able to be visualized and is shown later to assess some degree of damage for the *MAT_085 target concrete constitutive law. The crack variable, crack1, of the LS-DYNA *MAT_085 concrete material is defined in Table 3-16 (Day 2011).

Table 3-16: *MAT_085 Crack Variable States and Brief Definitions.

crack1 value	Definition
0	Uncracked state
1	The first crack is forming, but is still on the descending branch of the stress-displacement curve (*i.e.,*, not yet fully open)
2	The crack has started to form but has unloaded (or is reloading) from the descending branch.
3	The crack is fully open, or has been fully open in the past

The next three images are taken from the VTT flexural mode impact scenario simulations using each of the three different target concrete constitutive laws (i.e., *MAT_072R3, *MAT_085, and *MAT_0159) at 16 milliseconds. Shown in Figure 3-46, are plots of the damage state variable (i.e., the painted contour label "Effective Plastic Strain" is damage) from the VTT flexural mode impact scenario simulations using the *MAT_072R3 concrete constitutive law representing the target. Similarly, shown in Figure 3-47 are plots of the crack1 state variable (as defined in Table 3-16 above) for the target concrete constitutive law, *MAT_085 (*a.k.a.* Winfrith model without strain rate effects). Lastly, Figure 3-48 displays plots of a damage variable from the VTT flexural mode impact scenario whereby the target concrete is represented using the *MAT_159 model and the painted contour label "Effective Plastic Strain" is damage. Unlike the *MAT_072R3 damage variable, this damage variable ranges from 0 to 1. The overall response of the VTT flexural mode impact scenario simulations tends to abide with the target concrete's Meridonal plane strength curves, shown earlier in Figure 3-13, whereby the *MAT_072R3 target concrete is the weakest, and the *MAT_085 target concrete is stronger, and the *MAT_159 target concrete is the strongest; if the response is based purely on damage or crack1 state variables.

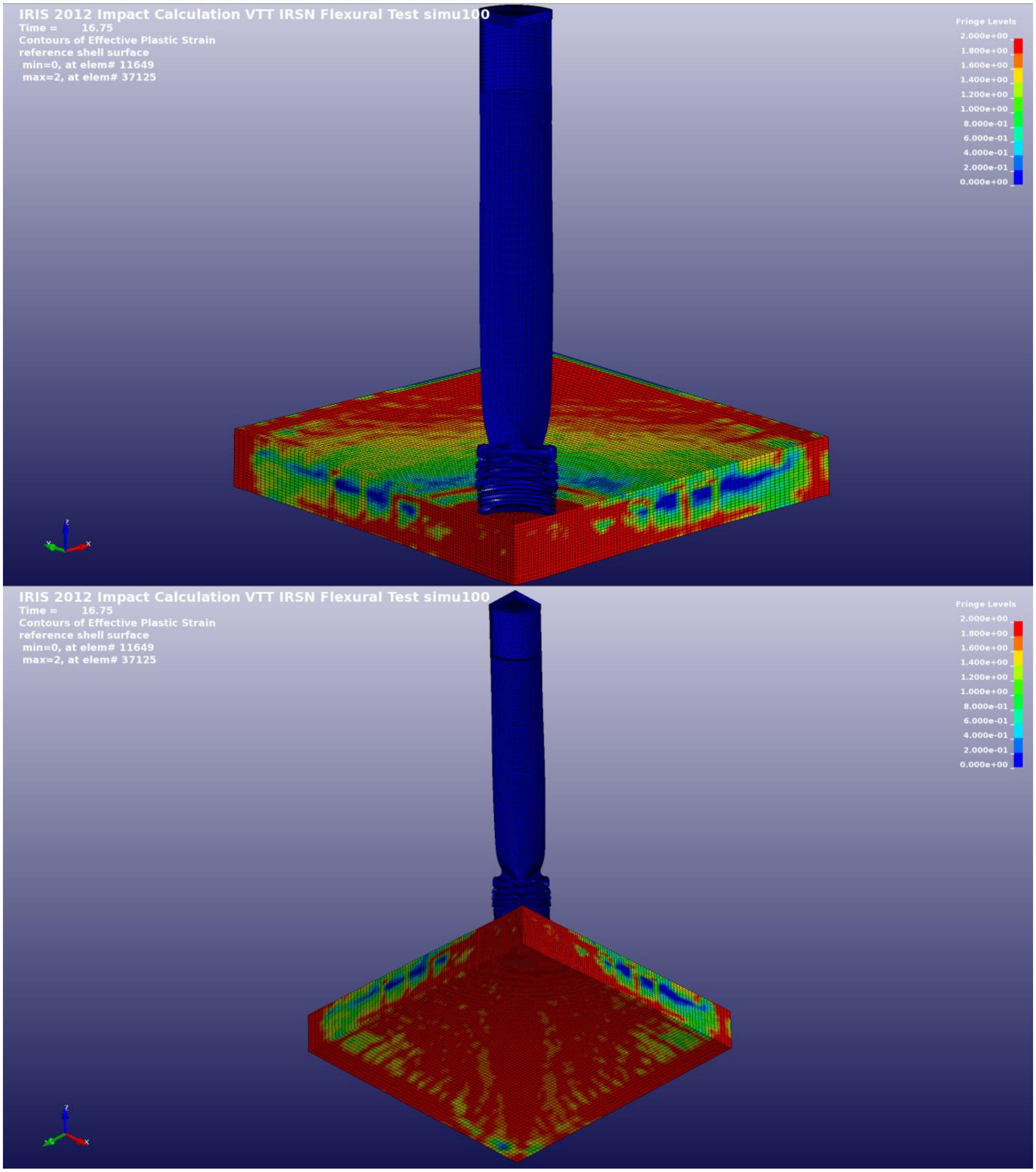

Figure 3-46: Damage State Variable Paint Plots From the VTT Flexural Mode Impact Scenario Simulations at t=16.75 msec Using the *MAT_072R3 Concrete Material Model Representing the Target Concrete (Top: Top Target Surface View; Bottom: Bottom Target Surface View).

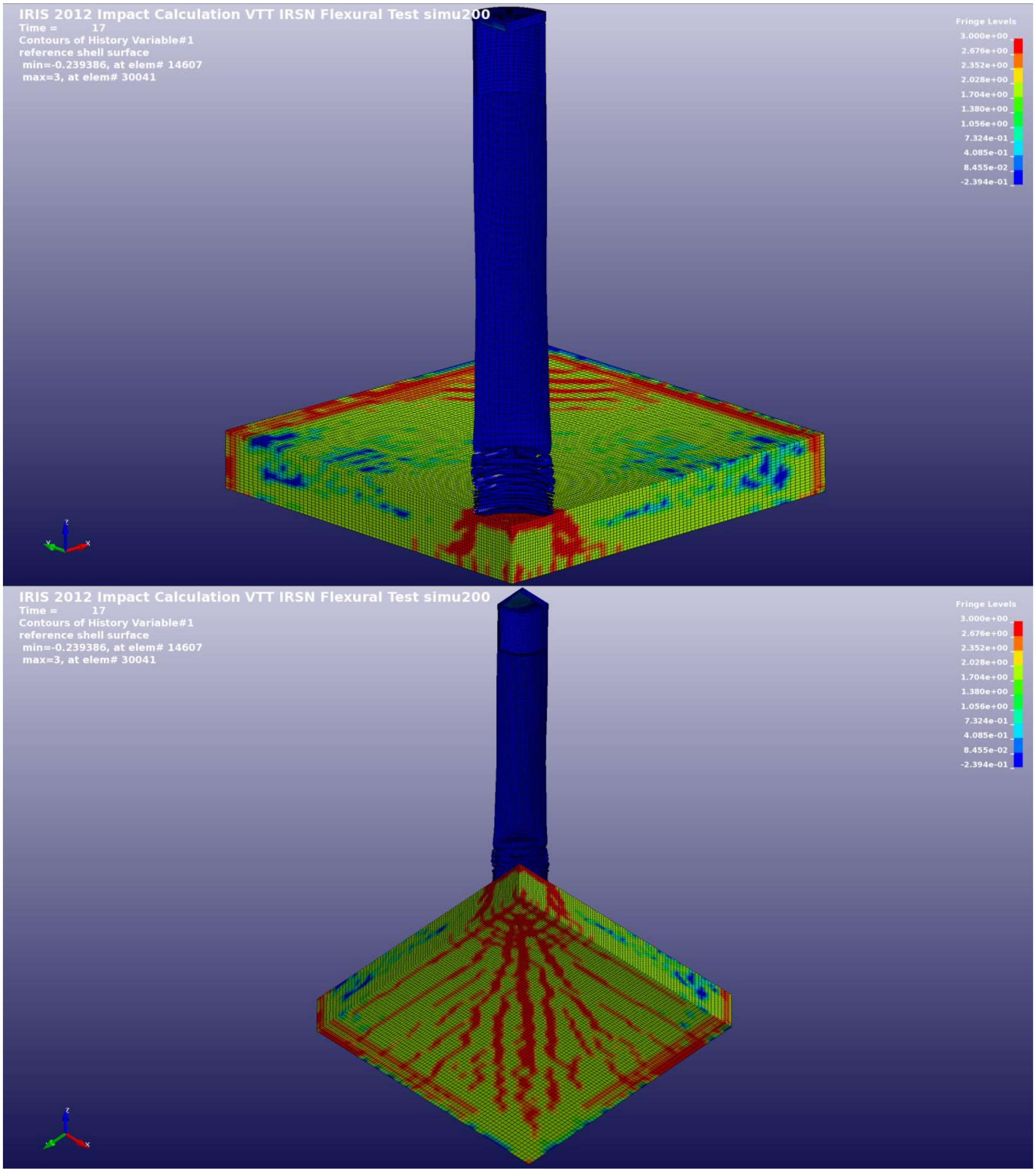

Figure 3-47: Crack1 State Variable Paint Plots From the VTT Flexural Mode Impact Scenario Simulations at t=17 msec Using the *MAT_085 Concrete Material Model Representing the Target Concrete (Top: Top Target Surface View; Bottom: Bottom Target Surface View).

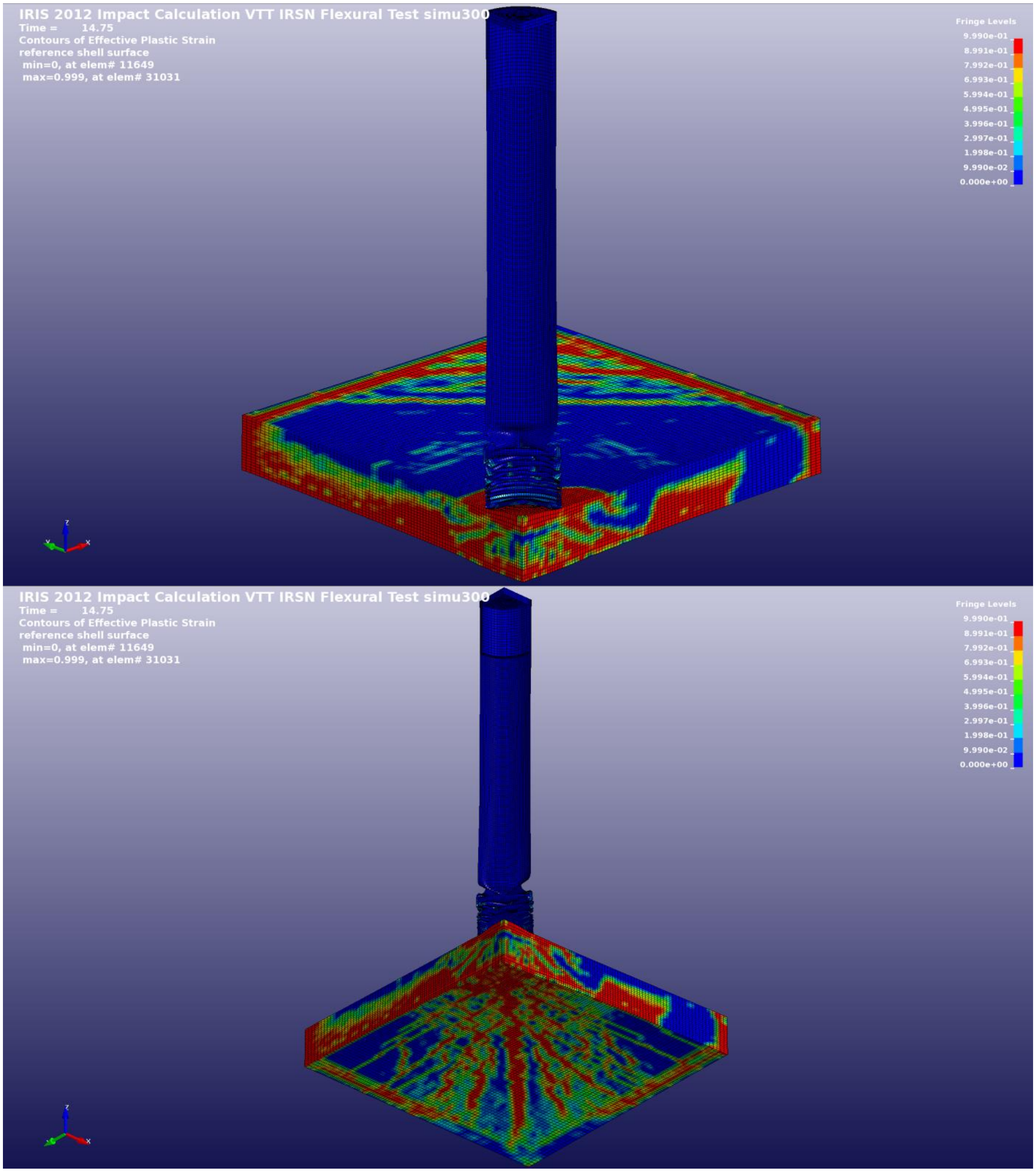

Figure 3-48: Damage State Variable Paint Plots From the VTT Flexural Mode Impact Scenario Simulations at t=14.75 msec Using the *MAT_159 Concrete Material Model Representing the Target Concrete (Top: Top Target Surface View; Bottom: Bottom Target Surface View).

3.4.5 IRIS IRSN VTT Punching

Again, similar to the two previous impact scenario calculations, three different target concrete models were used to predict the response of the VTT punching mode impact scenario (*i.e.,* *MAT_072R3, *MAT_085, and *MAT_159). Three baseline calculations (P1, P2, and P3, in accordance with Table 3-13) were completed to predict and compare with the punching impact test. Unlike to the Meppen II-4 impact scenario simulations, the VTT punching mode impact scenario simulations used no strain-rate strength enhancement in the steel reinforcement bars with the *MAT_024 only when using the *MAT_072R3 target concrete model. Several preliminary punching mode impact calculations were attempted with strain-rate strength enhancement in the steel reinforcement bars, whereby missile either bounced off the target after some penetration or became stuck in the target after impact when using the *MAT_072R3 target concrete model. In addition, the discovery and witnessed behavior using a lower-fidelity single point integration 8-noded hexahedral element (*e.g.,* Standard LS-DYNA viscous form, hourglass form ***ihq*** = 1) motivated the analyses to invoke a more robust 8-noded hexahedral element type. Using this knowledge, all of the punching mode impact simulations employed the LS-DYNA Flanagan-Belytschko viscous formulation with exact volume integration, 8-noded hexahedral element (Schwer, et al. 2005), whereby the hourglass parameter ***ihq*** = 3. Again, like the VTT flexural mode impact simulations, both the Winfrith (*MAT_085) and the Continuous Surface Cap Model (CSCM or *MAT_159) concrete constitutive laws were employed without strain-rate effects to treat the target concrete component. However, the Karagozian and Case material model (*MAT_072R3) included a dynamic increase function to permit strain-rate effects (shown in Table 4-14) based on the unconfined compressive cylindrical specimen strength, f_c' = 69 MPa. All punching impact calculations used a target concrete model based upon the 2012 IRSN standard concrete cylinder, shown previously in Figure 3-5, with an unconfined compressive strength fc' = 69 MPa.

The primary distinction of this scenario from the two previous simulations is the impact response resulting in penetration of the target comprised of both concrete and steel. Two of the target concrete constitutive laws (*MAT_072R3 and *MAT_085) do not permit implicit erosion control. The *MAT_159 material model has several means of controlling erosion. In order to equilibrate in some fashion this control between the three different target concrete constitutive models, the LS-DYNA control, *MAT_ADD_ERROSION was used. This method allows over thirteen different criteria, or any combination of, to invoke erosion of the 8-noded hexahedral elements representing the target concrete component. The punching mode scenario simulations using *MAT_072R3 and *MAT_159 used erosion controls based on the maximum shear strain, ***epssh*** = 0.6 (*i.e.,* 60 %). However, the punching mode impact simulations using the *MAT_085 constitutive law used a value of 0.5 (a value of ***epssh*** = 0.6 caused massive element erosion, and deleting the entire target concrete and steel reinforcing bar mesh). Another unique aspect of the VTT punching mode impact scenario is the hard type of missile - a relatively thick cylindrical vessel filled with concrete. In order to accurately capture the energy transfer of the composite missile (steel and concrete) perfect bonding between the steel and concrete components was not assumed. Thus a contact definition between the missile steel and the lightweight concrete was used (*e.g.,* *CONTACT_AUTOMATIC_SURFACE_TO_SURFACE).

Shown in Figure 3-49 is the deformed/post-impact missile from VTT punching mode test P1 (Vespä 2010b). As seen in the figure the missile remained intact and experienced some bulging in the nose section. Shown in Table 3-17, Figure 3-50, and Figure 3-51 are the missile impact/deformation statistics from the numerical simulations, the predicted punching mode impact missile velocity histories (only to 10 milliseconds), and the computed finite element model missile shapes after impact, respectively. Comparing the test and numerical simulations of the deformed missile shapes after impact reveals the target concrete *MAT_085 constitutive law calculation precludes any missile node bulging. This behavior is clearly in disagreement with both observed experiments (see Figure 5-34) and with the other two simulations (*i.e.,* those using the target concrete models: *MAT_072R3 and *MAT_159).

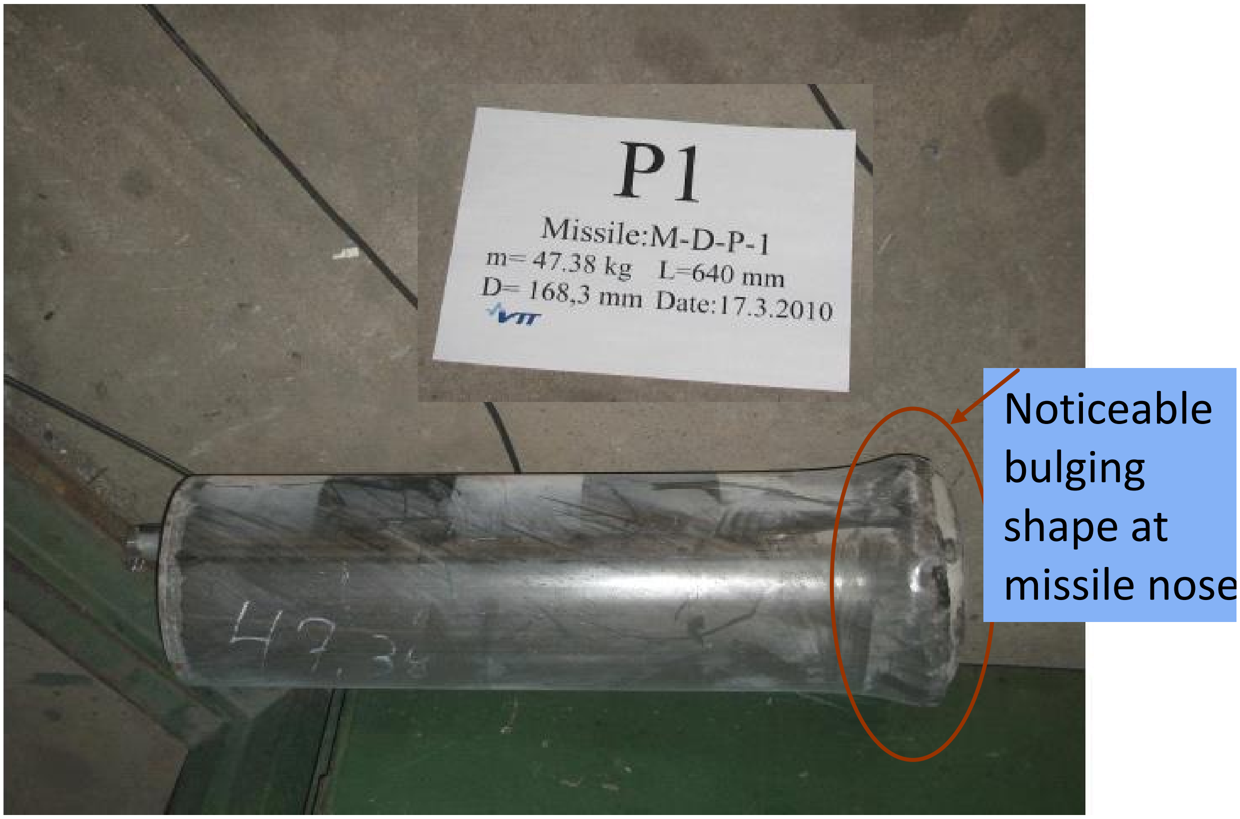

Figure 3-49: VTT Punching Mode Test P1 Missile After Impact (Vespä 2010b).

Table 3-17: Key Results From the VTT Punching Mode Impact Scenario Simulations.

Response	Experiment			Simulations		
	P1	P2	P3	*MAT_072R3 (Baseline P1)	*MAT_085 (Baseline P2)	*MAT_159 (Baseline P3)
Exit Velocity (m/sec)	33.8	45.3	35.3	52	41	45
Missile Nose Bulging	YES	YES	YES	YES	NO	YES

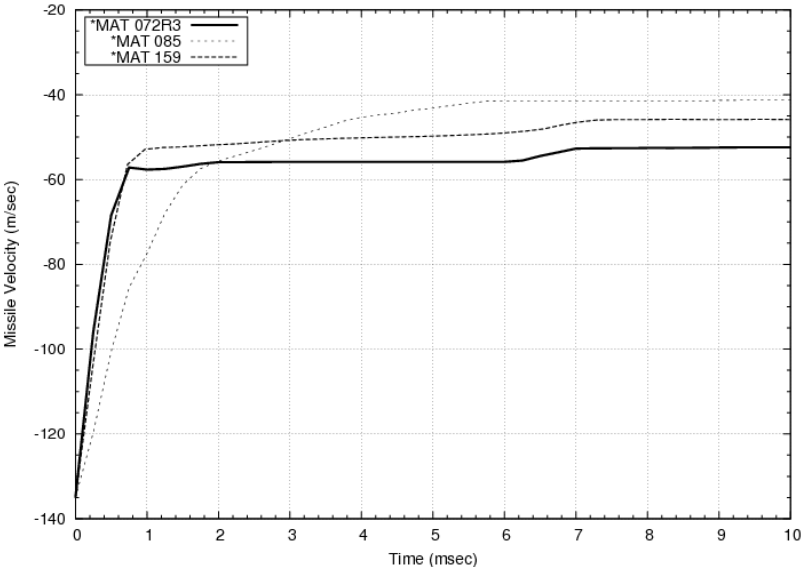

Figure 3-50: Predicted Missile Velocity Histories of the VTT Punching Mode Impact Scenario (From Numerical Simulations).

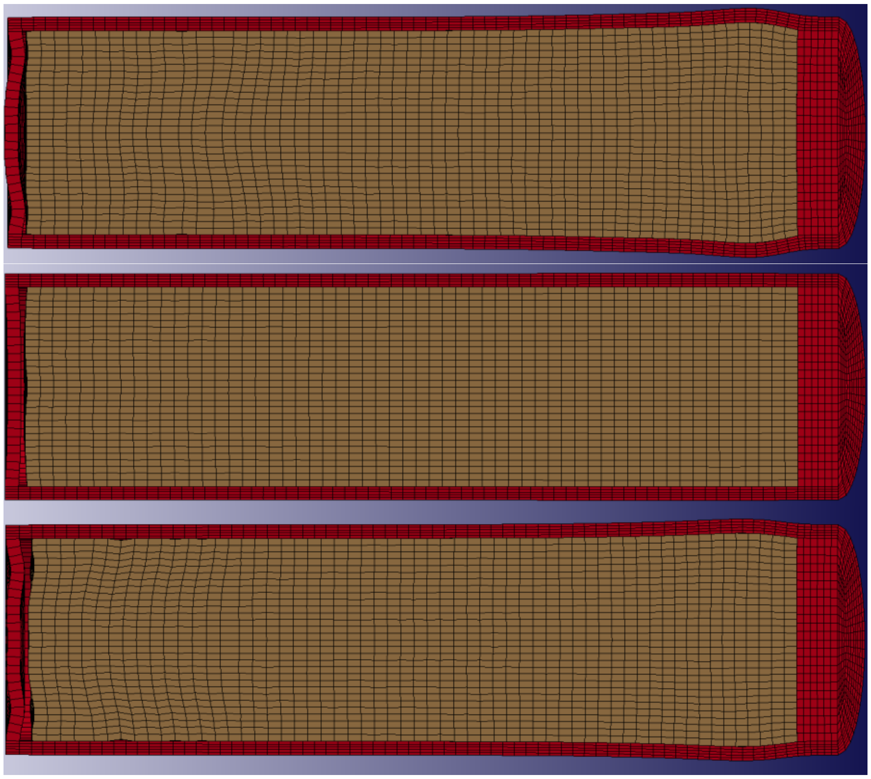

Figure 3-51: Predicted Deformed Half-Missile Shapes after 10 milliseconds From Numerical Simulations of the VTT Punching Mode Impact Scenario (Top: Using Target Concrete Model *MAT_072R3 model; Middle: Using Target Concrete Model *MAT_085; Bottom: Using Target Concrete Model *MAT_159).

Shown in Figure 3-52, Figure 3-53, and Figure 3-54 are the VTT punching impact scenario target displacement sensor locations and the resulting numerical simulation's predictions of the target displacements compared with test data at sensor locations #2 and #3, respectively. The numerical models used in these two comparison plots, Figure 3-53 and Figure 3-54, are cross-referenced to the Baseline and Sensitivity calculations employing *MAT_072R3 from Table 3-13). Comparing the displacement histories, again the sensitivity calculations P1.1, P1.2, and P1.3 are the closest to the test data, but are over-predicting target displacement. However, the calculations P1, P1.4, P1.5, and P1.6 under-predict target displacement. This bounding numerical distribution is suggestive that further sensitivity studies may produce better displacement predictions.

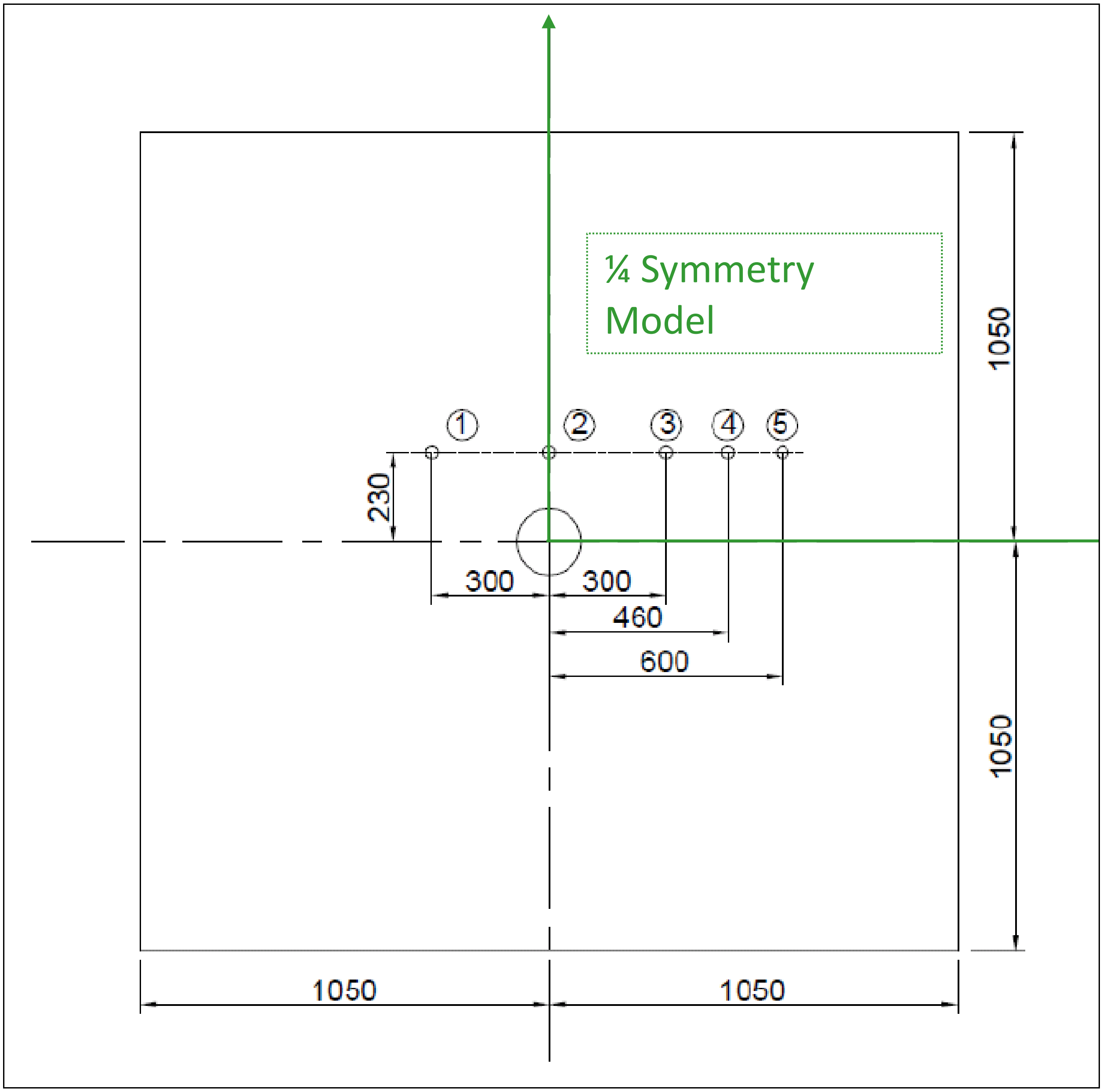

Figure 3-52: VTT Punching Mode Impact Scenario Displacement Sensor Locations at Front Side of Concrete Target (Vepsä 2010a) [Note: the 1/4 symmetric model used in the Numerical Simulations only computed target displacements at sensors #2 and #3].

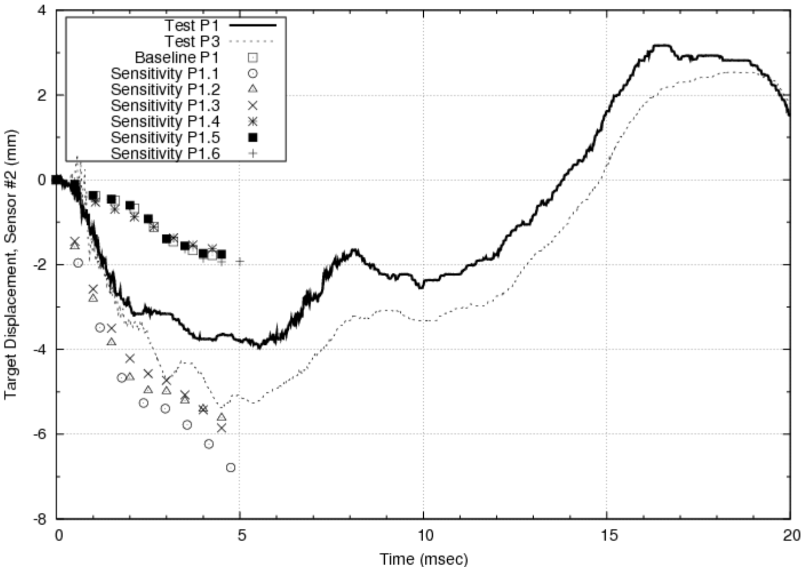

Figure 3-53: VTT Punching Mode Impact Test and Numerical Predictions of Target Displacement at Sensor Location #2.

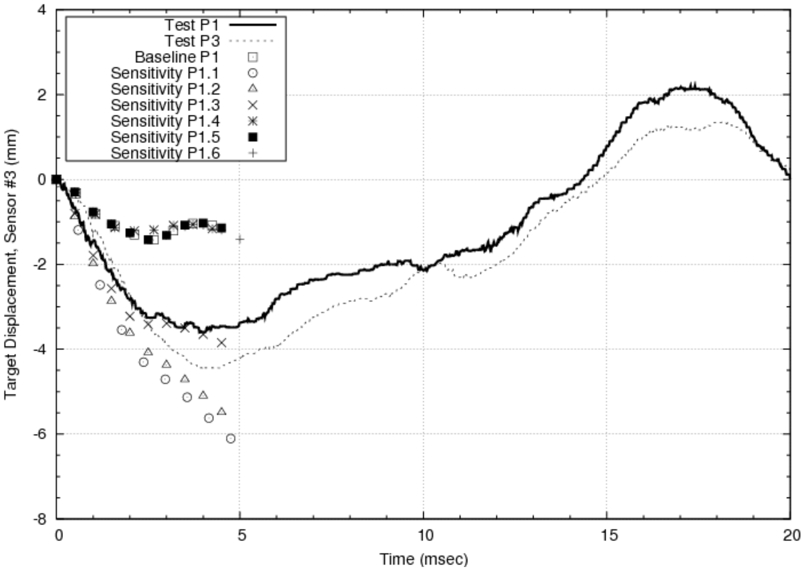

Figure 3-54: VTT Punching Mode Impact Test and Numerical Predictions of Target Displacement at Sensor Location #3.

Shown in Figure 3-55, Figure 3-56, Figure 3-57, and Figure 3-58 is a schematic of the VTT punching mode impact test target concrete strain gage locations, recorded strain histories for test P1 and P2, and numerically computed strains, respectively. As seen in Figure 3-56 and Figure 3-57 the tests P1 and P2 strains are nearly the same with peak strains at gage #1 equal to -2.3 x 10^{-03} (test P1) and -3.0 x 10^{-03} (test P2) and peak strains at gage #2 equal to -7.0 x 10^{-04} (both tests and P1 and P2). The numerically computed strains were written to the output database at 0.25 millisecond intervals, which is not frequent enough to capture the sharp initial strain response.

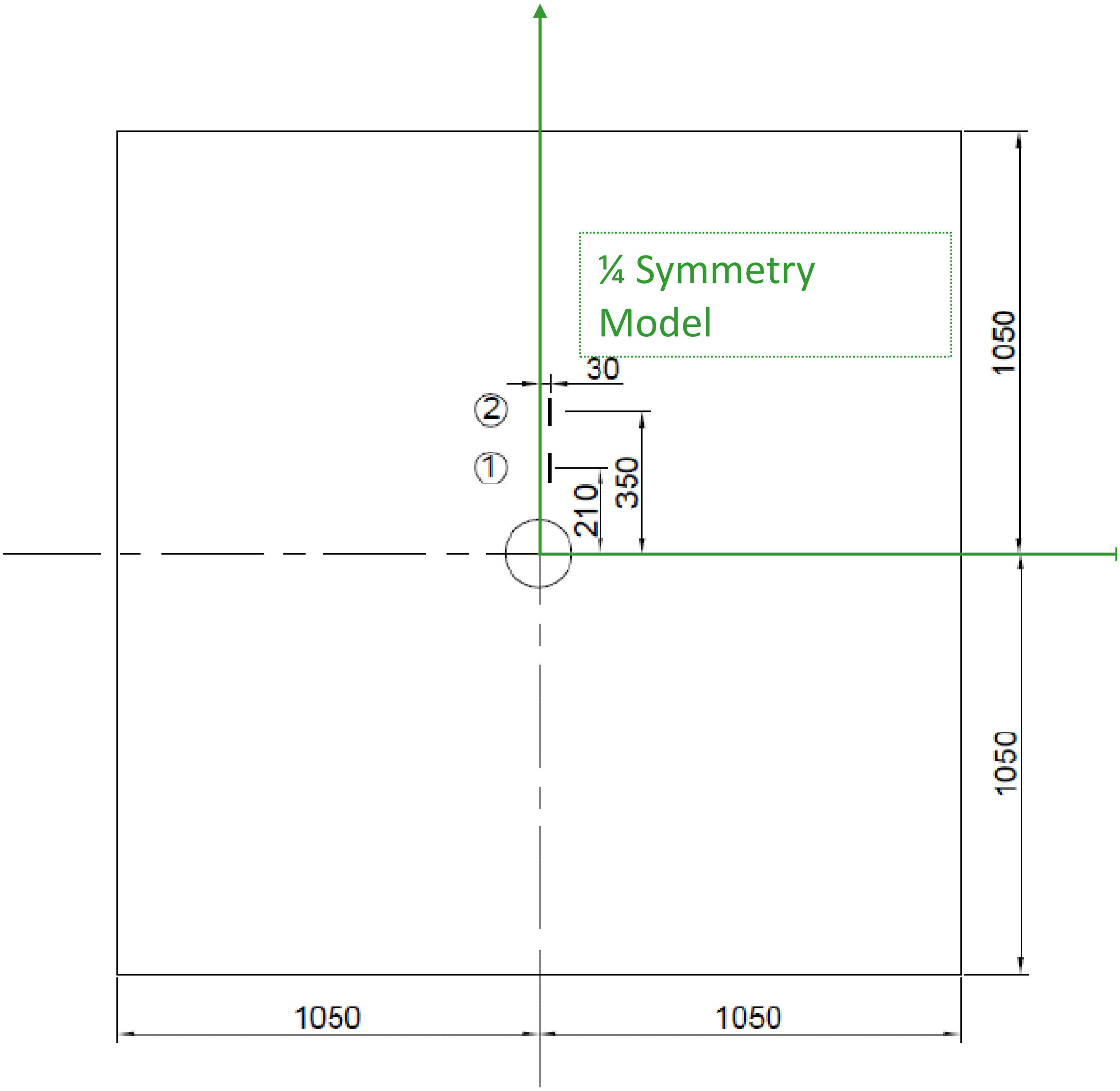

Figure 3-55: VTT Punching Mode Impact Test Strain Gage Locations at Front Side of Concrete Target (Vepsä 2010a).

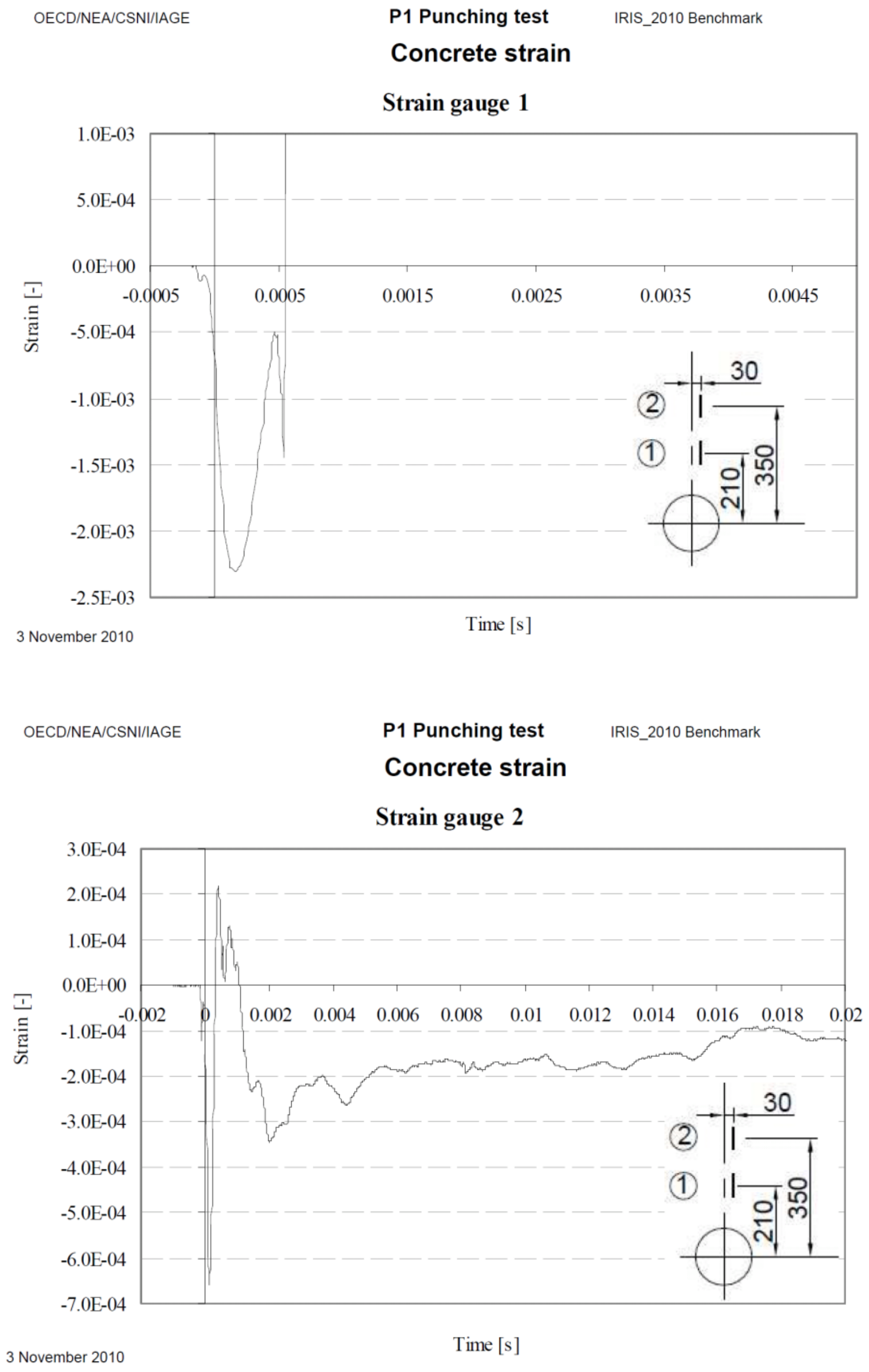

Figure 3-56: Target Concrete Strain Gage Histories from VTT Punching Mode Impact Test P1, (Nuclear_Energy_Agency 2010) [Top: Gage #1; Bottom: Gage #2].

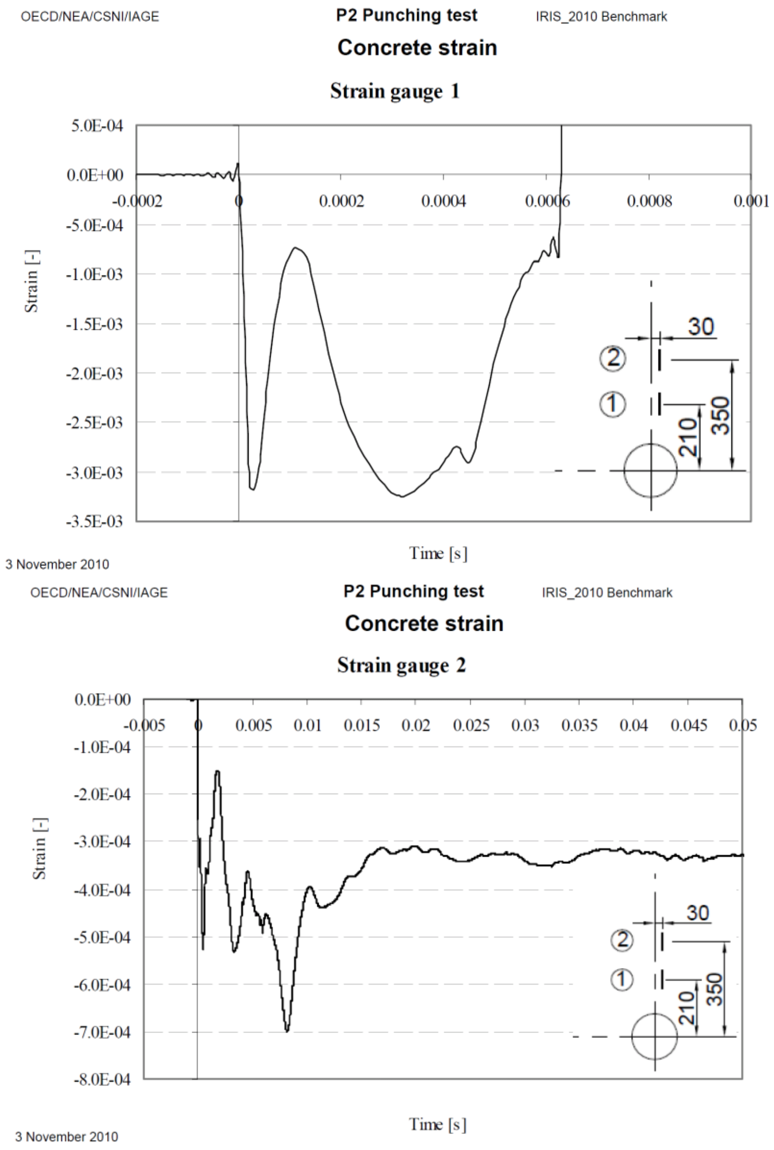

Figure 3-57: Target Concrete Strain Gage Histories from VTT Punching Mode Impact Test P2, (Nuclear_Energy_Agency 2010)[Top: Gage #1; Bottom: Gage #2].

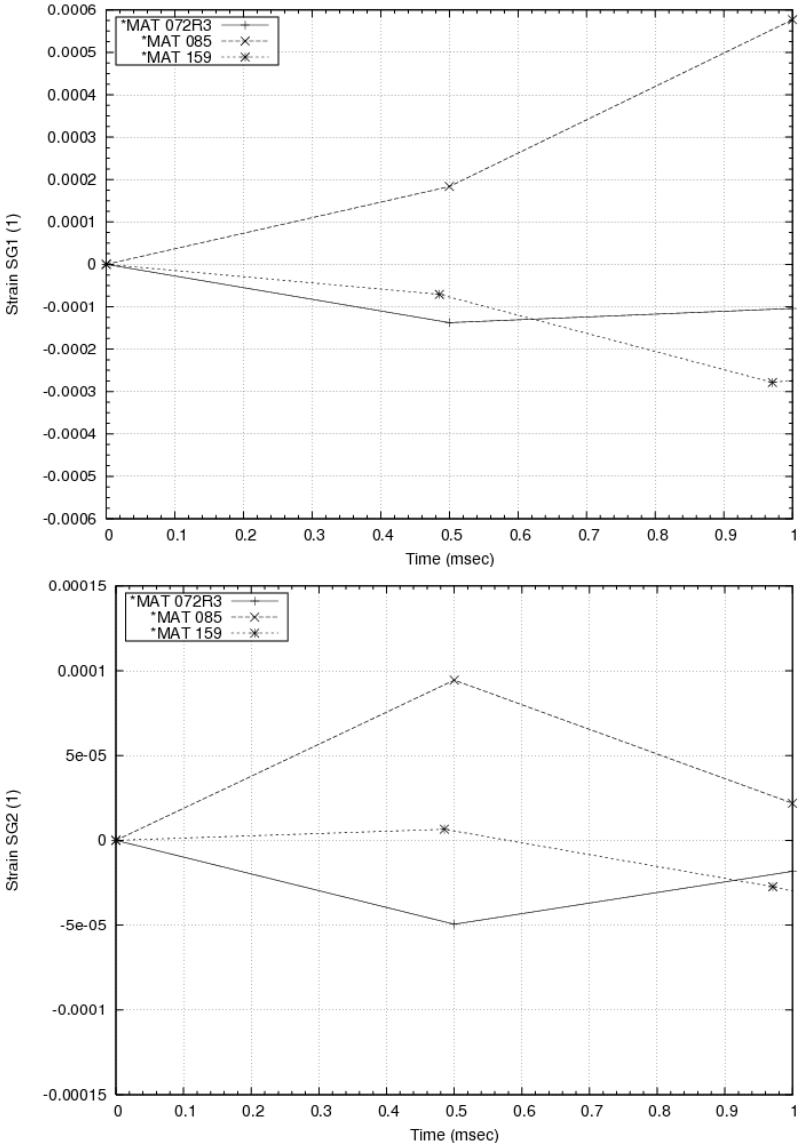

Figure 3-58: Comparison of VTT Punching Mode Impact Scenario Test Data and Numerically Computed Target Concrete Strains (Top: Gage #1; Bottom: Gage #2).

Shown in Figure 3-59 and Figure 3-60 is a schematic of the VTT punching mode impact test target reinforcing steel bar strain gage locations and comparison plots of the test data and numerically computed strains at gage locations #1, and #7, respectively. As seen in Figure 3-60 the numerically computed strains in the steel reinforcing bars do not capture the jump in strain behavior as witnessed in the test data. This lack of agreement in the numerically computed strains may be attributed to the method of embedding the reinforcing steel bar grid in the target concrete mesh using the LS-DYNA method *CONSTRAINED_LAGRANGE_IN_SOLID.

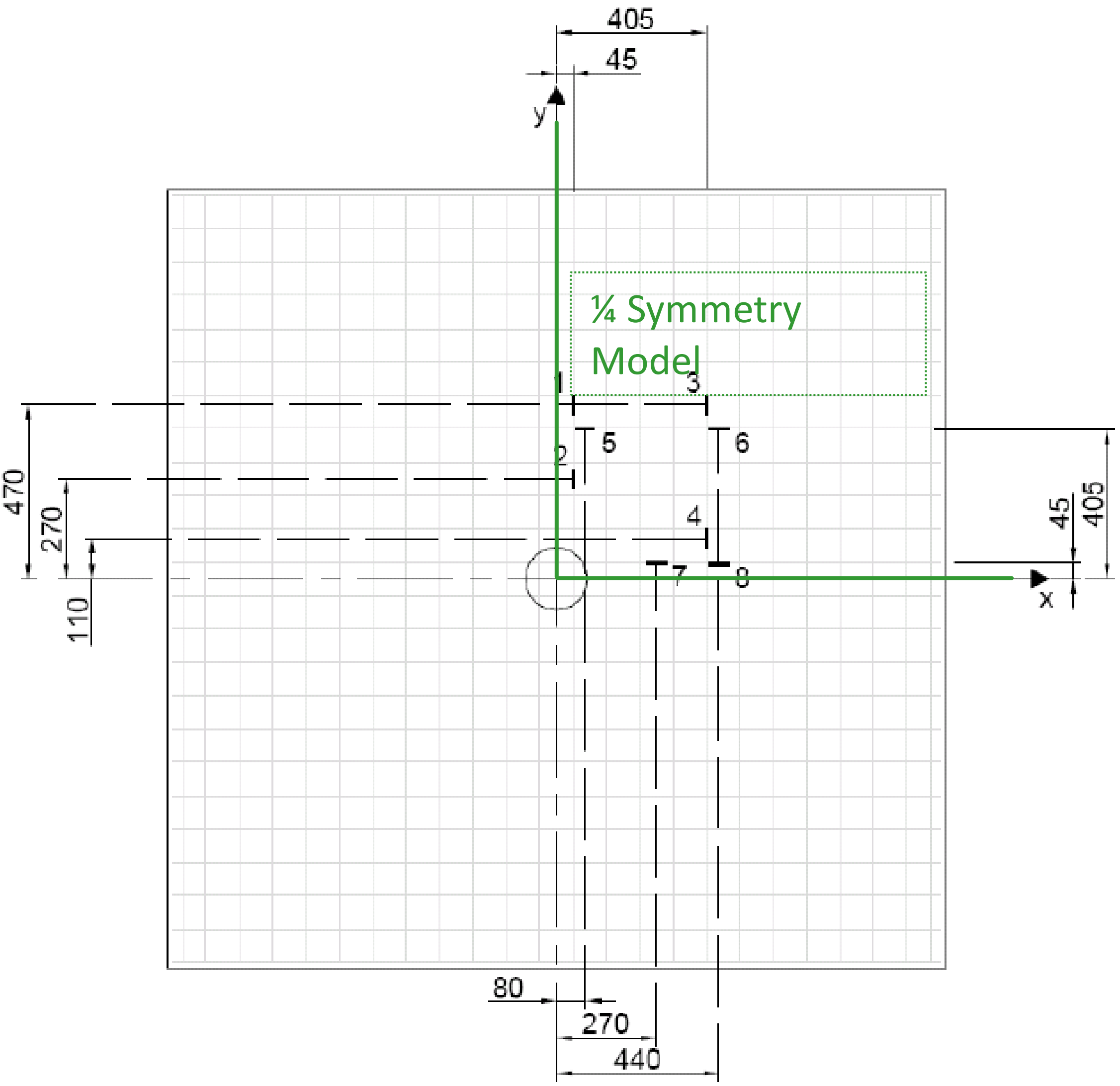

Figure 3-59: VTT Punching Mode Impact Test Reinforcing Steel Bar Strain Gage Locations, (Vepsä 2010a).

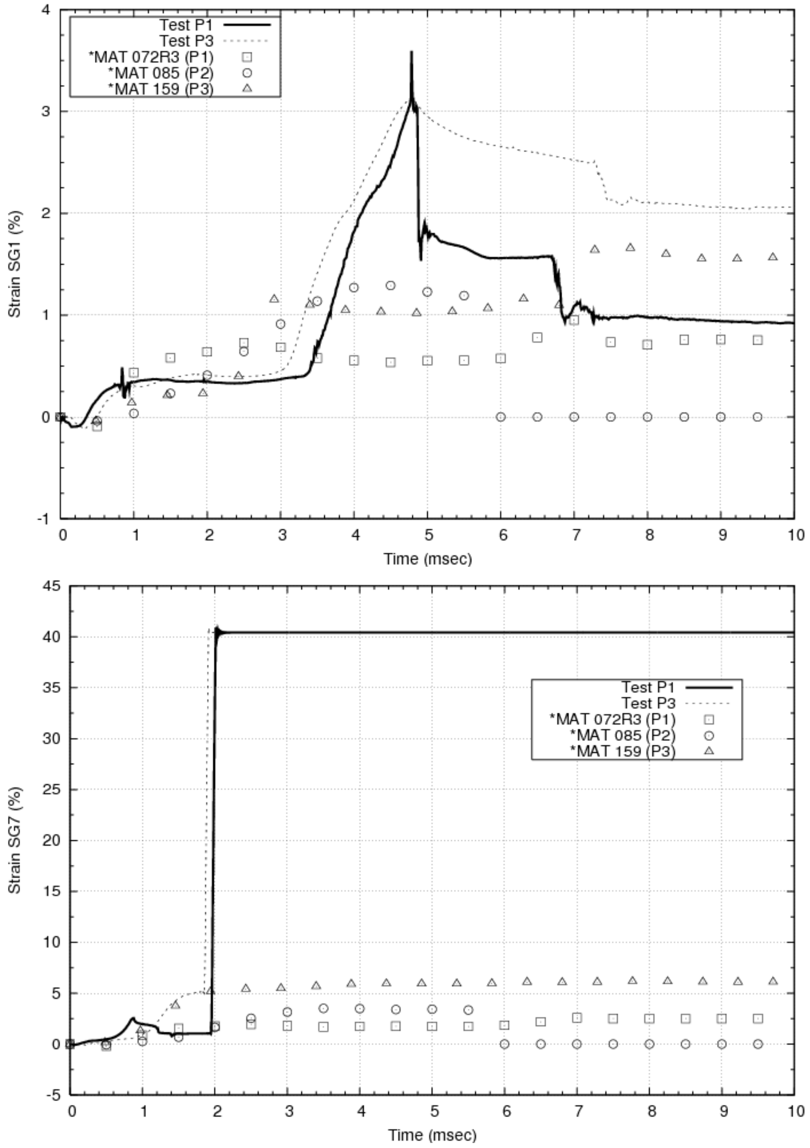

Figure 3-60: Comparison of VTT Punching Mode Impact Test Data and Numerically Computed Reinforcing Steel Bar Strains (Top: Gage #1; Bottom: Gage #7).

To further comprehend the numerically computed response of the steel reinforcing bars during impact, images of the steel bar grids after at 7.0 milliseconds for the punching simulations using *MAT_072R3 target concrete model (P1 cross-reference) using and *MAT_159 target concrete model (P3 cross-reference) and at 5.0 milliseconds for punching simulation using target concrete model *MAT_085 (P2 cross-reference), is shown in Figure 3-61, Figure 3-62, and Figure 3-63. As seen in the three images for the different target concrete models, the steel reinforcing bars near the missile impact zone (lower center of the snapshot) are experiencing axial strains up to 12 %, which was the strain failure limit. The punching mode impact simulations using any of the target concrete models, shown in Figure 3-61, Figure 3-62, and Figure 3-63, depict some reinforcing bars breaking off from the top x-y rebar grid and following the cone cracking type of plug and spall behavior as the missile penetrates through the target.

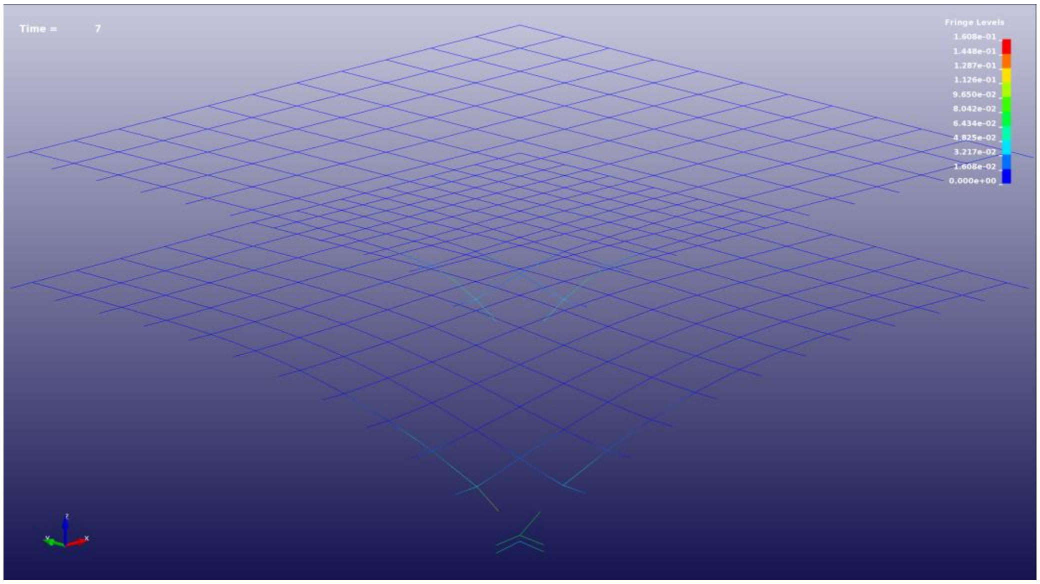

Figure 3-61: Numerically Computed Axial Strains in Reinforcing Steel Bars from VTT Punching Mode Impact Scenario Simulations at 7.0 milliseconds (Target Concrete Model *MAT_072R3, Punching Calculation P1 cross-reference).

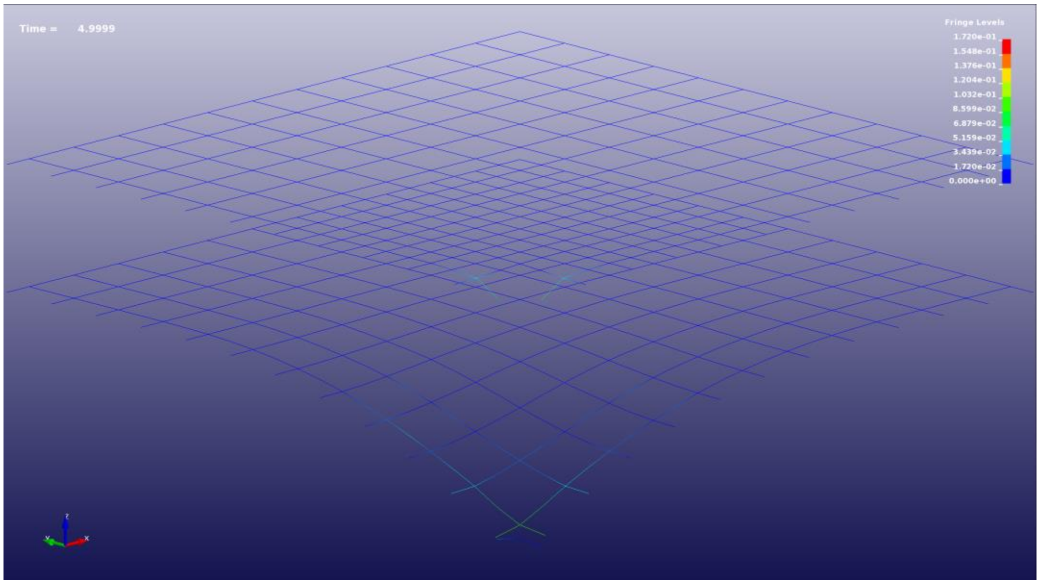

Figure 3-62: Numerically Computed Axial Strains in Reinforcing Steel Bars from VTT Punching Mode Impact Scenario Simulations at 5.0 milliseconds (Target Concrete Model *MAT_085, Punching Calculation P2 cross-reference).

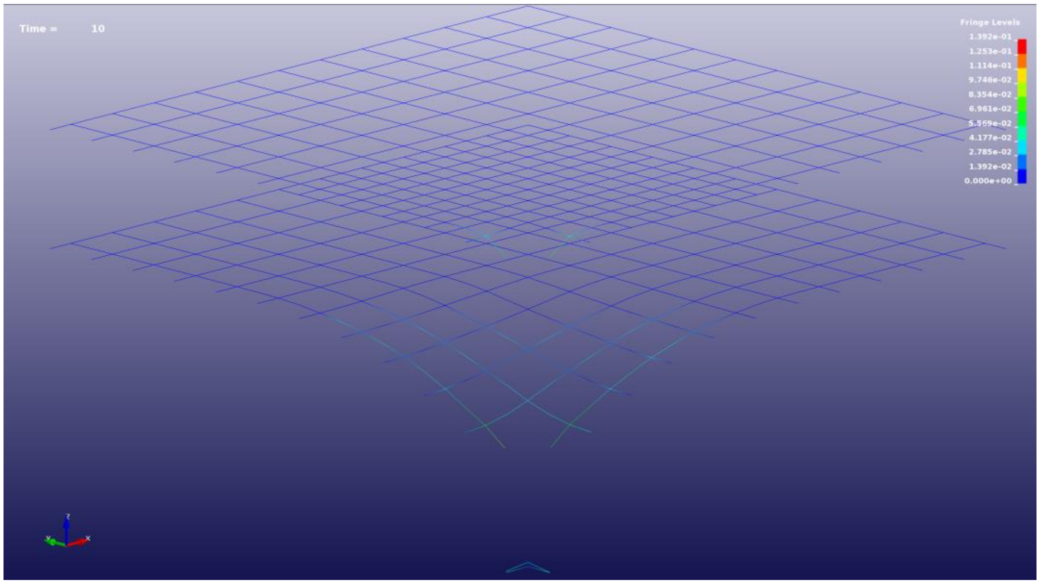

Figure 3-63: Numerically Computed Axial Strains in Reinforcing Steel Bars from VTT Punching Mode Impact Scenario Simulations at 7.0 milliseconds (Target Concrete Model *MAT_159, Calculation P3 cross-reference).

The next three images are taken from the VTT punching mode impact scenario simulations using each of the three different target concrete constitutive laws (i.e., *MAT_072R3, *MAT_085, and *MAT_0159, corresponding to P1, P2, and P3 cross-reference from Table 3-13) at 11 milliseconds. Shown in Figure 3-64, is a plot of the damage state variable (i.e., the painted contour label "Effective Plastic Strain" is damage) from the VTT punching mode impact scenario simulations using the *MAT_072R3 concrete constitutive law representing the target. Similarly, shown in Figure 3-65 is a plot of the crack1 state variable (as defined previously in Table 3-16) for the target concrete constitutive law, *MAT_085 (a.k.a. Winfrith concrete model without strain rate effects). Lastly, Figure 3-66 displays a painted plot of the damage variable from the punching mode simulations whereby the target concrete is represented using the *MAT_159 model and the painted contour label "Effective Plastic Strain" is damage. Unlike the *MAT_072R3 damage variable, this damage variable ranges from 0 to 1. Comparing the three simulations, the missile tail has penetrated approximately 1/3 of the target thickness for *MAT_085 target concrete models (Figure 3-65); the simulation employing the *MAT_072R3 target concrete model (Figure 3-64) the missile tail has only surpassed the target's top surface; and the calculation using the *MAT_159 target concrete model (Figure 3-66) the missile's length is positioned nearly centered with respect to the target's thickness. Viewing the three simulations, the model employing the target concrete *MAT_072R3 constitutive law (Figure 3-64) predicts a heavy spall type of response, contrary to the *MAT_159 target concrete model (Figure 3-66) which experiences more of a cone cracking and plug type of punching response. The overall response of the *MAT_085 target concrete model simulation depicts both spall and a plug type behavior (Figure 3-65).

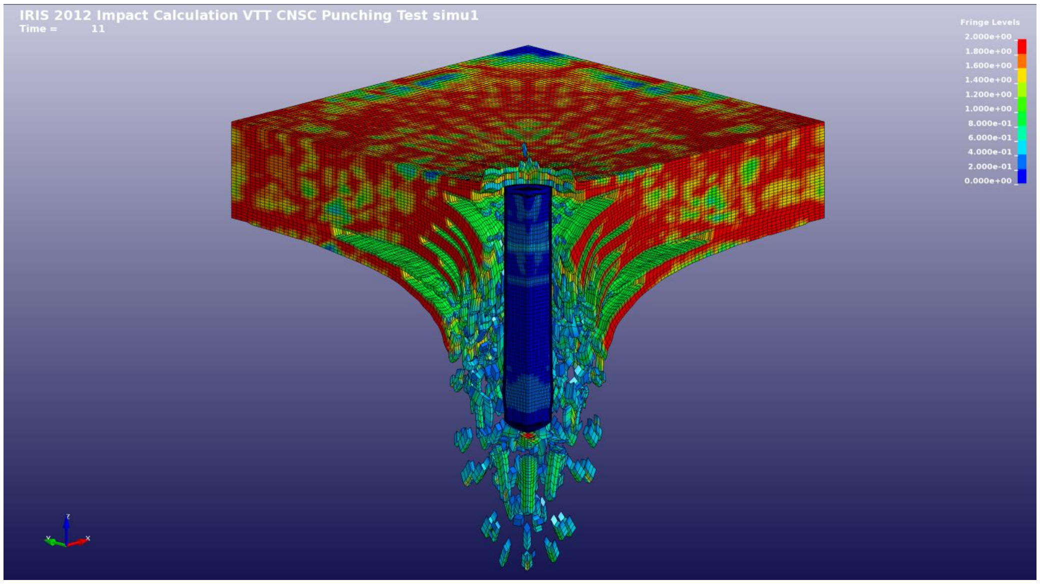

Figure 3-64: Damage State Variable Paint Plot From the VTT Punching Mode Impact Scenario Simulations Using the *MAT_072R3 Concrete Material Model Representing the Target Concrete (Calculation P1 cross-reference).

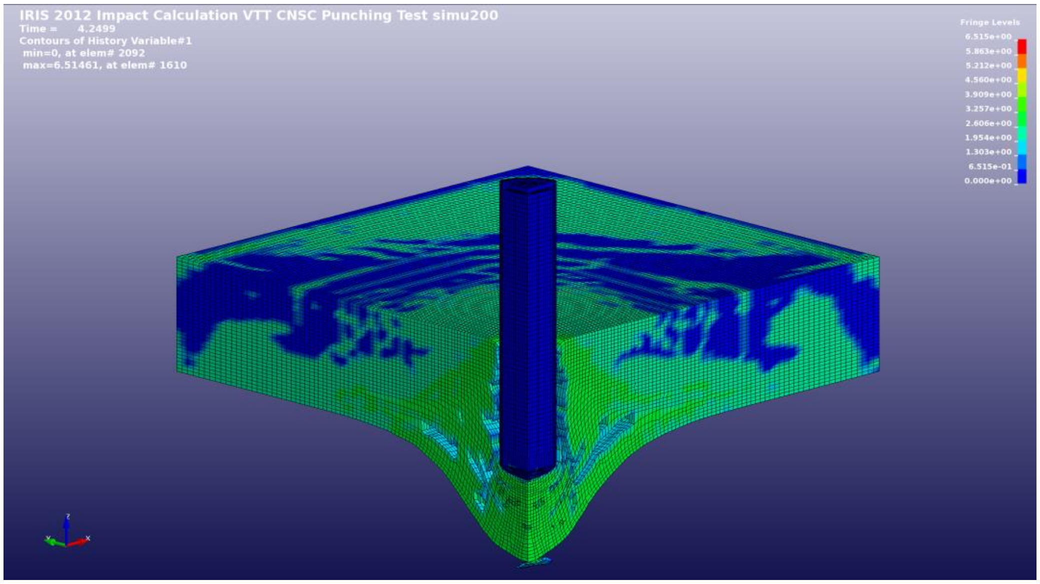

Figure 3-65: Crack1 State Variable Paint Plot From the VTT Punching Mode Impact Scenario Simulations Using the *MAT_085 Concrete Material Model Representing the Target Concrete (Calculation P2 cross-reference).

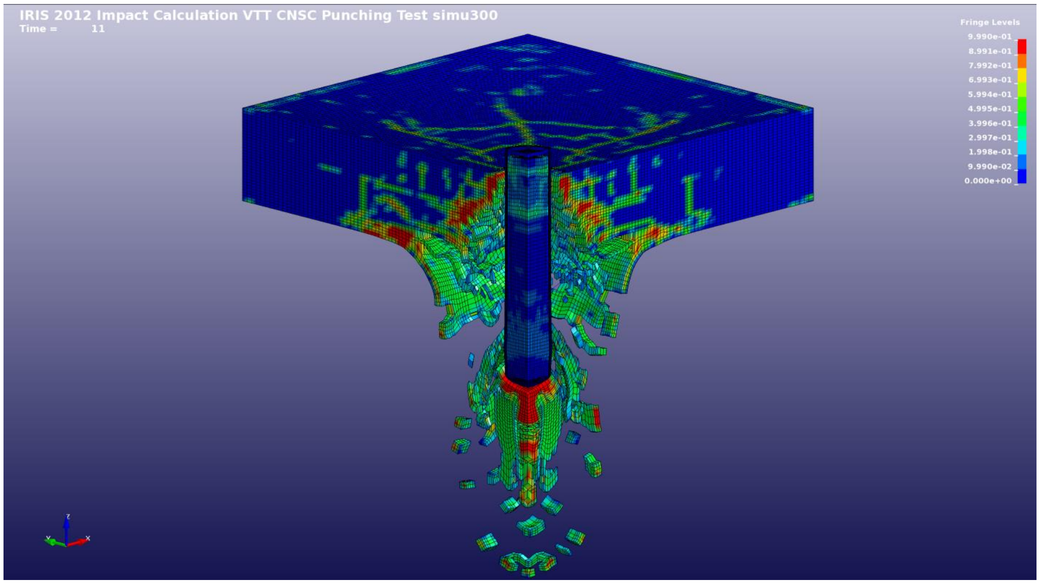

Figure 3-66: Damage State Variable Paint Plot From the VTT Punching Mode Impact Scenario Simulations Using the *MAT_159 Concrete Material Model Representing the Target Concrete (Calculation P3 cross-reference).

Lastly, shown in Figure 3-67, and Figure 3-68 are the concrete target and steel reinforcing bar mesh plots (depicted in half-model symmetry to enhance visualization) from the punching mode impact simulations near 59 milliseconds. As mentioned earlier, the simulation using the *MAT_159 concrete model representing the target concrete predicts a well-defined cone type cracking and plug punching response.

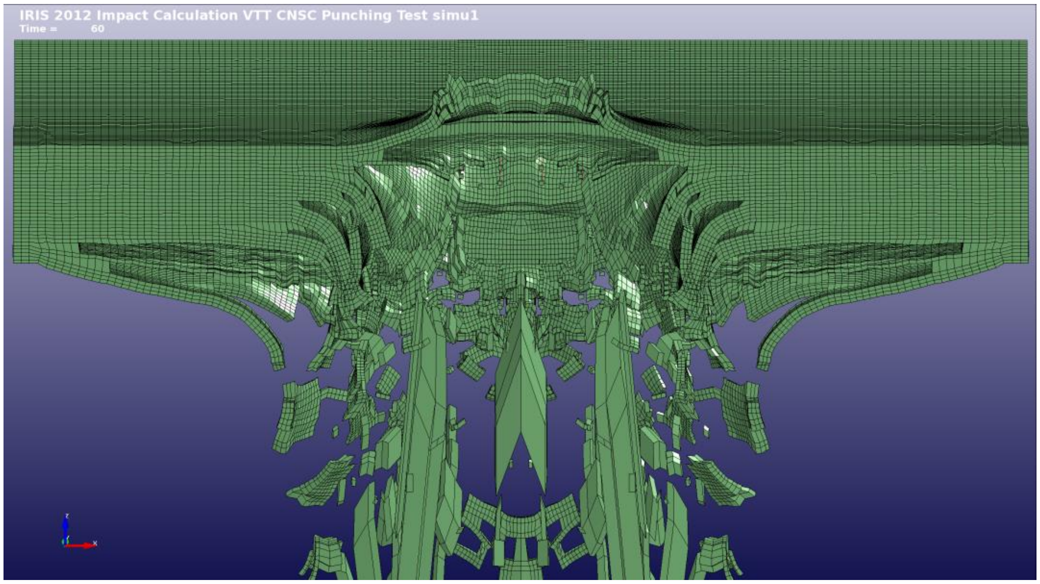

Figure 3-67: Concrete Target and Steel Reinforcing Bar Mesh Plot from the VTT Punching Mode Impact Scenario Simulations at 60 milliseconds Using the *MAT_072R3 Concrete Constitutive Law Representing the Target Concrete (Calculation P1 cross-reference).

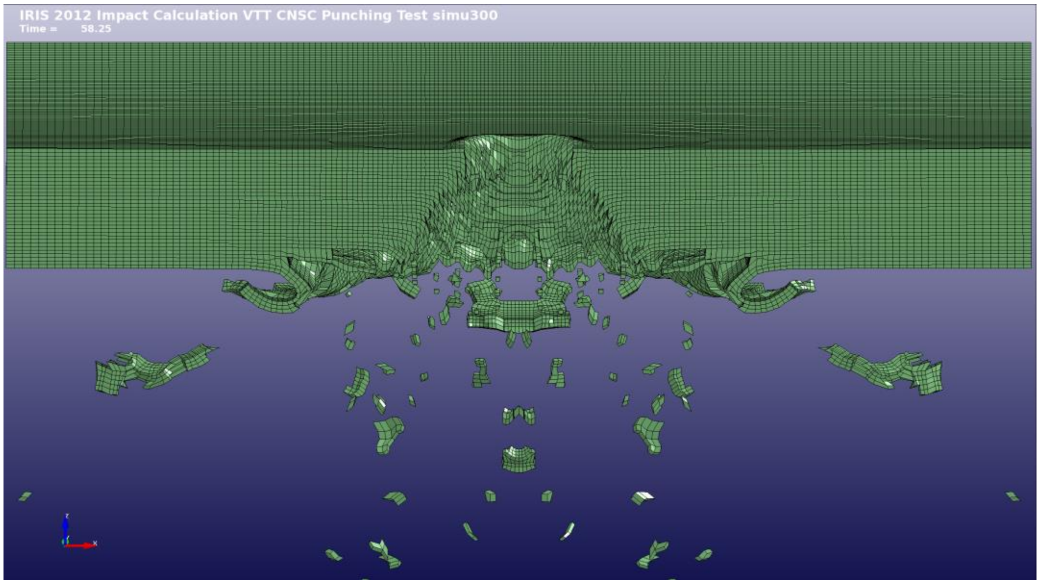

Figure 3-68: Concrete Target and Steel Reinforcing Bar Mesh Plot from the VTT Punching Mode Impact Scenario Simulations at 58.25 milliseconds Using the *MAT_159 Concrete Constitutive Law Representing the Target Concrete (Calculation P3 cross-reference).

Another investigation to decipher key differences in the impact response using the three different target concrete constitutive laws studied the impact force and energy absorbed by the concrete target. Shown in Figure 3-69 is the target concrete impact normal force history predicted by each concrete material model. As seen in Figure 3-69, both the *MAT_072R3 and *MAT_159 target concrete models predict a maximum peak force near 2.0 MN. Due to the coarse time step frequency to store computational data to numerical simulation database (i.e., Δt = 0.25 milliseconds), the peak force of the *MAT_085 target concrete model may have been truncated. The agreement of peak impact force in the other two target concrete model simulations does provide some degree of confidence that correct impact force was transferred from the missile to the target. Shown in Figure 3-70 are the *CONTACT_ERODING_SURFACE_TO_SURFACE master surface (i.e., the target concrete component) contact energy histories for each of the punching mode impact simulations. As seen in Figure 3-70 the energy absorbed using the *MAT_072R3 target concrete constitutive law is approximately 30% less than the simulations using the *MAT_159 target concrete models. This discrepancy may be one reason why the missile exit velocity from the *MAT_072R3 target concrete model simulation is greater than the other two simulations (see Table 3-17). This difference in energy absorbed may be indicative that the *CONTACT_ERODING_SURFACE_TO_SURFACE contact parameters (e.g., static and dynamic friction coefficients, μ_s and μ_d, equal to 0.7) in combination with the target concrete *MAT_072R3 material model may not be sufficient.

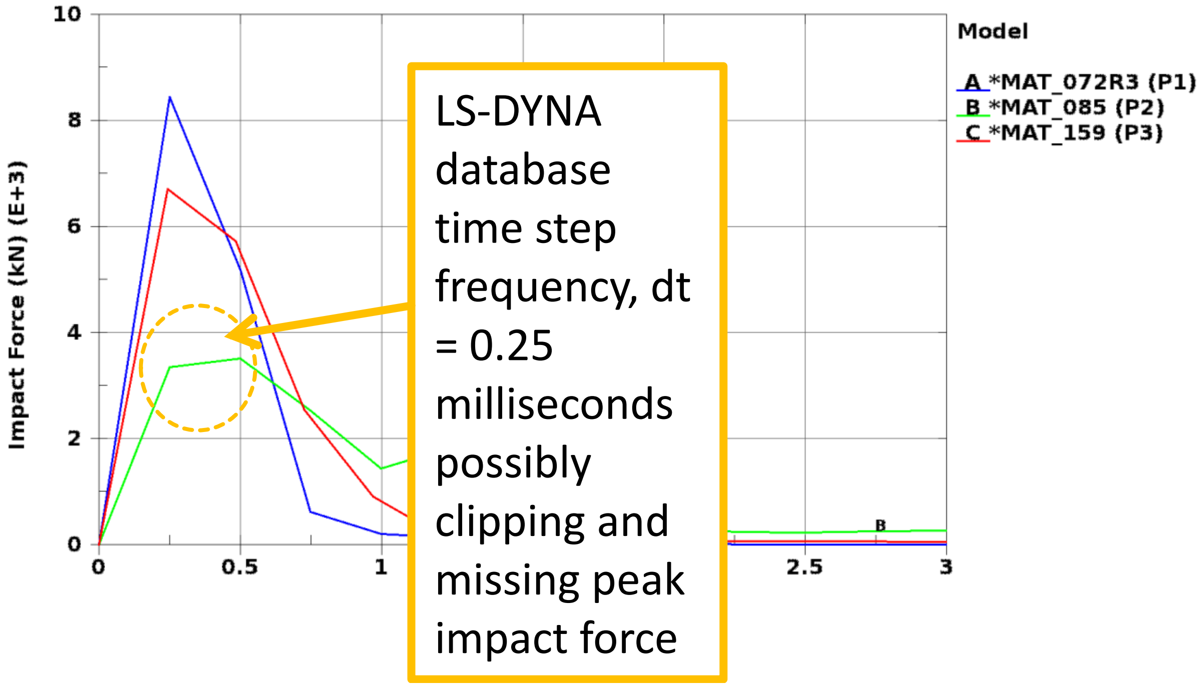

LS-DYNA database time step frequency, dt = 0.25 milliseconds possibly clipping and missing peak impact force

Figure 3-69: VTT Punching Mode Impact Scenario Numerical Predictions of Impact Force History Sustained by the Target Concrete Component.

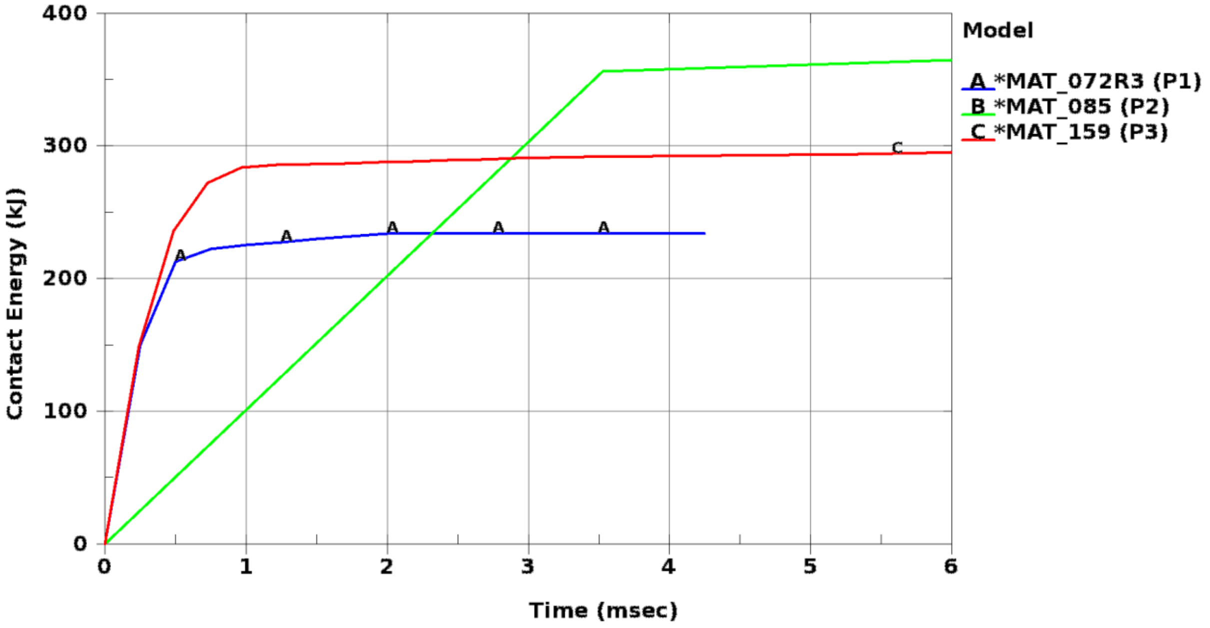

Figure 3-70: VTT Punching Mode Impact Scenario Numerical Predictions of Energy History Sustained by the Target Concrete Component.

3.4.6 IRIS IRSN Punching Sensitivity Study

A brief sensitivity study of the numerical punching model was completed using the 5 additional cases listed in Table 3-13 using the *MAT_072R3 target concrete material law (i.e., P1, P1.1, P1.2, P1.3, P1.4, and P1.5). Shown in Figure 3-71 is the exit missile velocity from the baseline calculation (P1) and the five other sensitivity cases (i.e., P1.1, P1.5). As seen in Figure 3-71 the exit velocity is bounded between 42 and 58 m/sec, and the punching test missile exit velocity ranged from 35 to 42 m/sec (see Table 3-17).

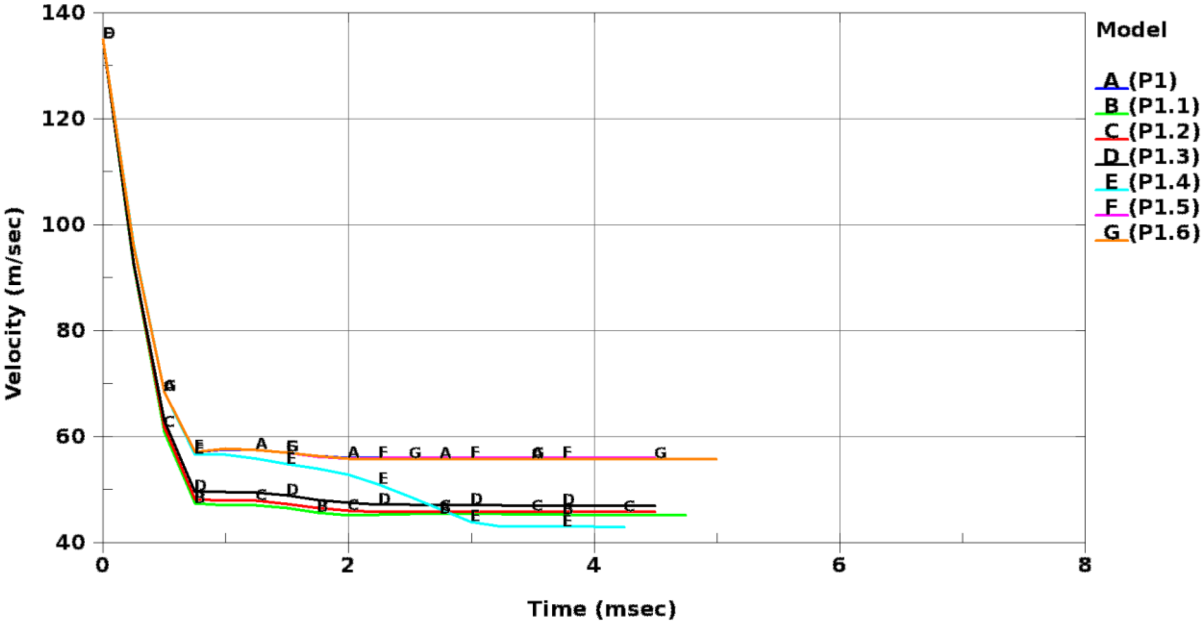

Figure 3-71: Sensitivity Study of Punching Impact Scenario Numerical Predictions of Missile Exit Velocity (using target concrete material model *MAT_072R3).

4 PHASE III: TRANSMISSION OF SHOCK AND VIBRATION TO INTERNAL COMPONENTS

4.1 Phase III Test Overview

The portions pertaining to Phase III describe analyses and numerical results obtained from simulations of a hollow steel missile impacting a concrete target reinforced with steel bars. Phase III was divided into two major portions: Part A1 and Part A2/B. A different structure was impacted in each Part. Phase III was completed using the finite element analysis code SIERRA. Various material models were tested in the simulation including pure elastic, Holmquist-Johnson-Cook concrete model (Holmquist, Johnson and Cook 1993), and Karagozian & Case concrete model (Malvar, et al. 1997). Sandia National Laboratories did not participate in Phase III Part A1. These results present the second iteration of effort resulting from the CSNI funding of the Phase III Part A2/B activities. Phase A2/B consisted of two benchmark workshops. The first benchmark workshop in June of 2017 analyzed blind submission results submitted by all teams. The second benchmark workshop in June 2018 analyzed re-calibrated submission results.

4.1.1 IRIS III Part A1: V1 Test

The concrete target in Phase III Part A1, also called the V1 test, consisted of an impact wall with side walls angling downwards towards the foundation; a cantilevered wall was located on the rear of the foundation. See Figure 4-1 for details. No further details will be discussed about Phase III Part A1 as Sandia National Laboratories did not participate in the round-robin analysis.

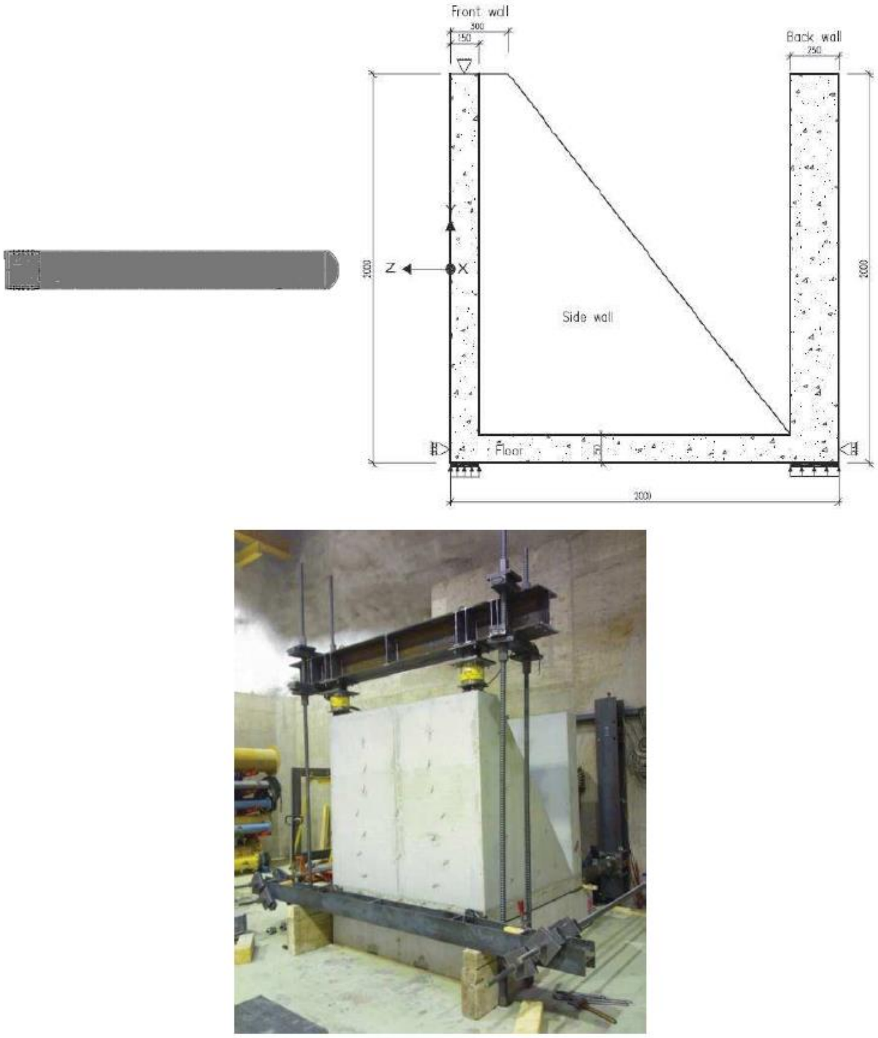

Figure 4-1: Schematic (top) and image (bottom) of Phase III Part A1 reinforced concrete impact structure.

4.1.2 IRIS III Part A2/B

IRIS III Part A2/B consisted of three impact tests of hollow missiles at medium to high velocity against a reinforced concrete structure. The project objectives of IRIS III Part A2/B were:

- To give the opportunity to each participant to use their means and tools for calculating the shock propagation and the associated floor response spectra.
- To gather all the results from a series of 3 impact tests.
- To assess the effect of the local damage caused by the impact on the induced vibrations: “mechanical effect”.
- To quantify structural damping in the areas which behave as a linear elastic material, and in the damaged areas.
- To assess or upgrade the usual approaches to implement the damping in the numerical calculations.
- To set up a shared basis of data related to the transmission of the shock inside the structure: “structural effect”.

- To draw on this basis a set of quantitative conclusions on the main parameters (dealing with material properties, boundary conditions, local damage, etc…) that have an influence onto the evolution of the shock inside the structure (in terms of magnitude, frequency domains and regarding different quantities of interest such as displacement, velocity and acceleration).
- To issue a set of recommendations considering the results of both the round robin calculations and the calibration calculations.

There was only one type of projectile with two different velocities that impacted the mock-up structure on the front wall as shown in Figure 4-2 and Figure 4-3. The projectile was “soft” hollow steel missile with a carbon steel endplate to add mass. Three missiles were launched at the mock-up: two missiles at 90 m/s and one missile at 170 m/s.

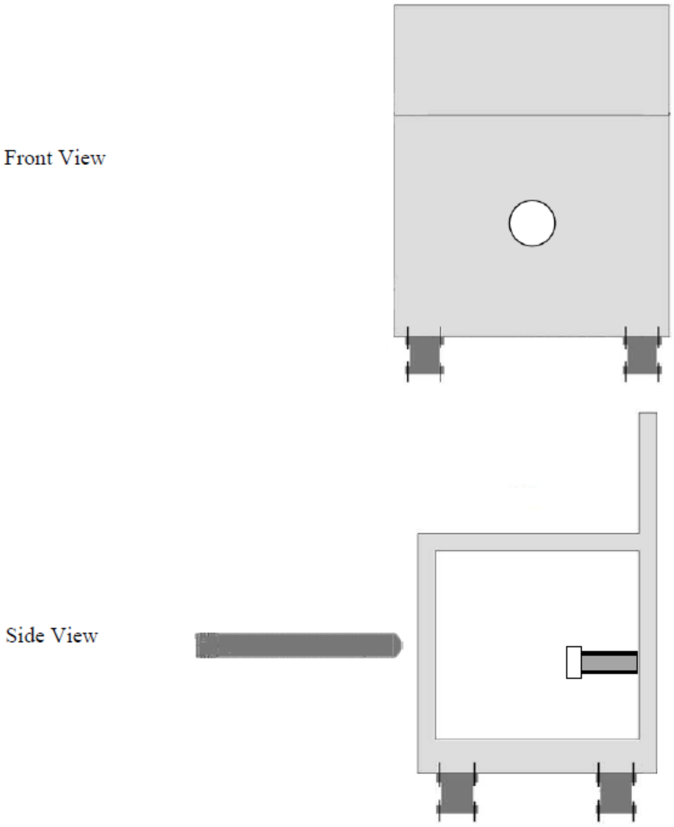

Figure 4-2: General schematic of mock-up structure and missile (front and side views).

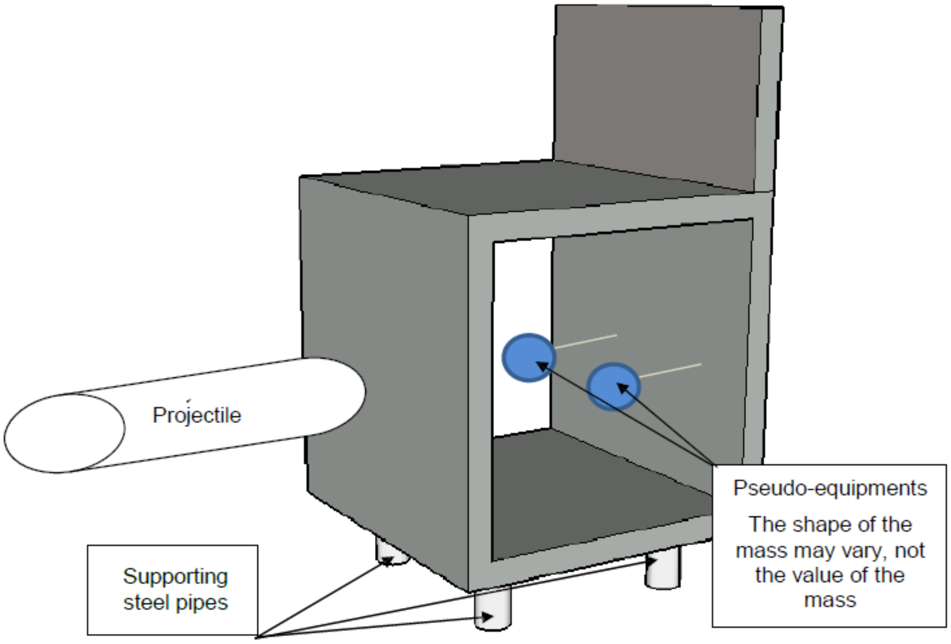

Figure 4-3: 3D schematic of the mock-up structure and missile.

The mock-up was installed at VTT laboratories in an underground cavern. The overall testing environment dedicated to the impact tests is shown in Figure 4-4.

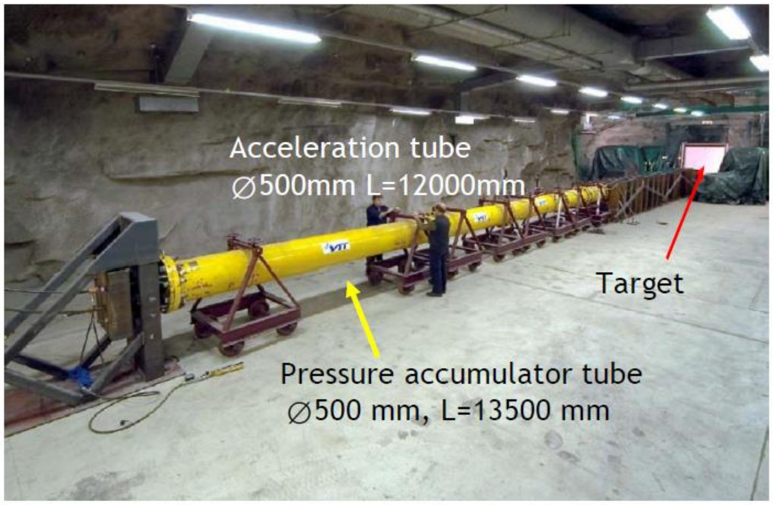

Figure 4-4: VTT launcher installed inside an underground cavern.

4.1.2.1 Description of the Mock-up

The mock-up is a 2.5 m wide structure made of reinforced concrete. It composed the following structural elements:

- Impacted wall: 2.5 m x 2 m x 15 cm
- Rear wall: 2.5 m x 2 m x 15 cm

- Lower floor: 2.5 m x 2 m x 40 cm
- Upper floor: 2.5 m x 2 m x 15 cm
- Cantilever wall: 2.5 m x 1 m x 15 cm

The mock-up was supported vertically on the ground of the cavern by means of four steel supports as shown in Figure 4-6. Each steel support consisted of a steel tube with flanges at 0°, 90°, 180°, and 270°. The tube/flanges structure was connected to steel plates on top and bottom. The top plate was embedded and anchored into the concrete. The bottom plate was bolted to the strongfloor. Two pseudo-equipments were attached to IPE 140 I-beams and monitored for their oscillation and accelerations. Each I-beam was connected by a different method to a steel plate that was embedded and anchored into the concrete. One I-beam was bolted to its connecting plate via angle steel; the other was welded to its connecting plate as depicted in Figure 4-5. Accelerometers and displacement transducers were placed throughout the mock-up as depicted in Figure 4-7, Figure 4-8, Figure 4-9, Figure 4-10, Figure 4-11, and Figure 4-12.

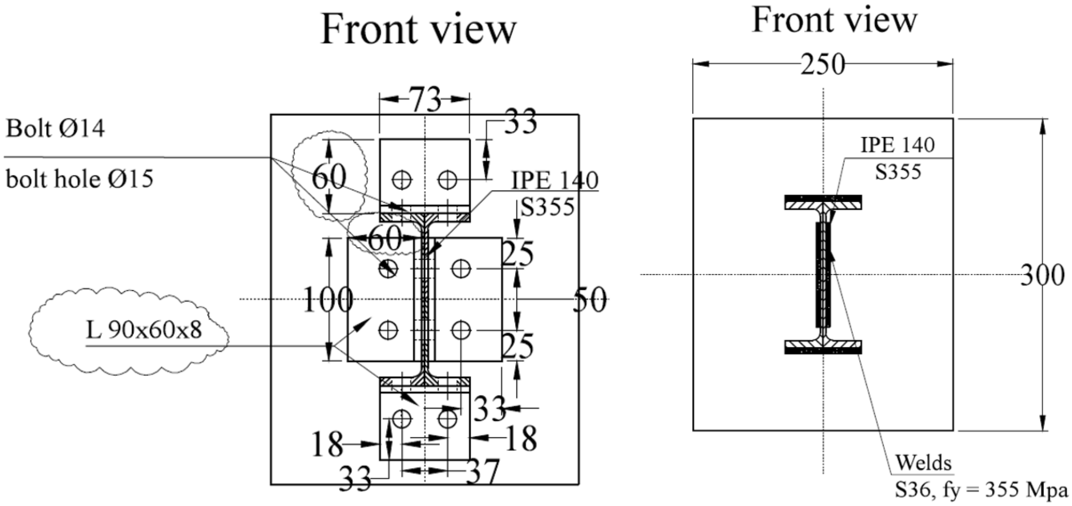

Figure 4-5: Bolted (left) and welded (right) I-beam connects to the support plate. Note that the images are different sizes, but the plates and I-beams are actually the same size for both.

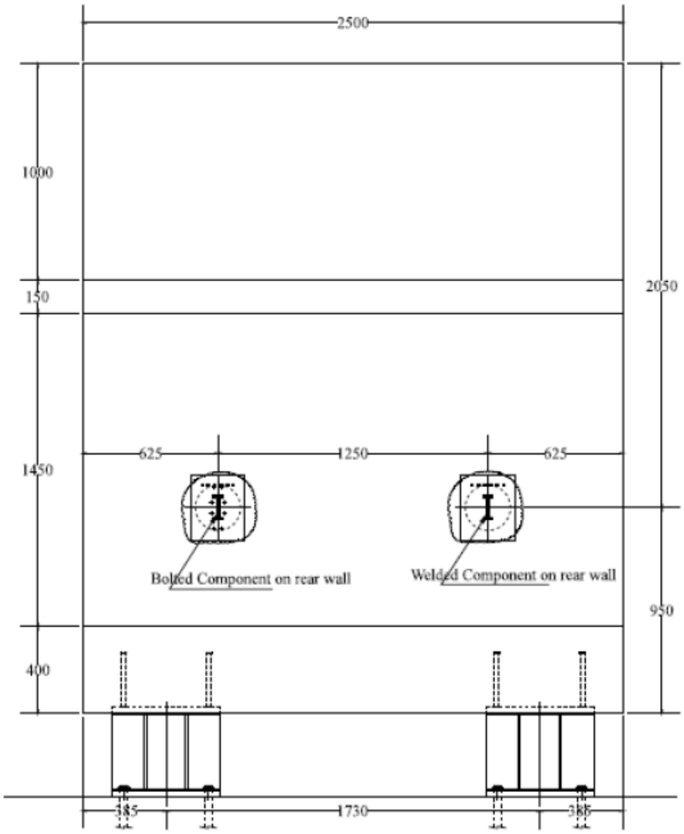

Figure 4-6: IRIS III Supporting System (front view, units are mm).

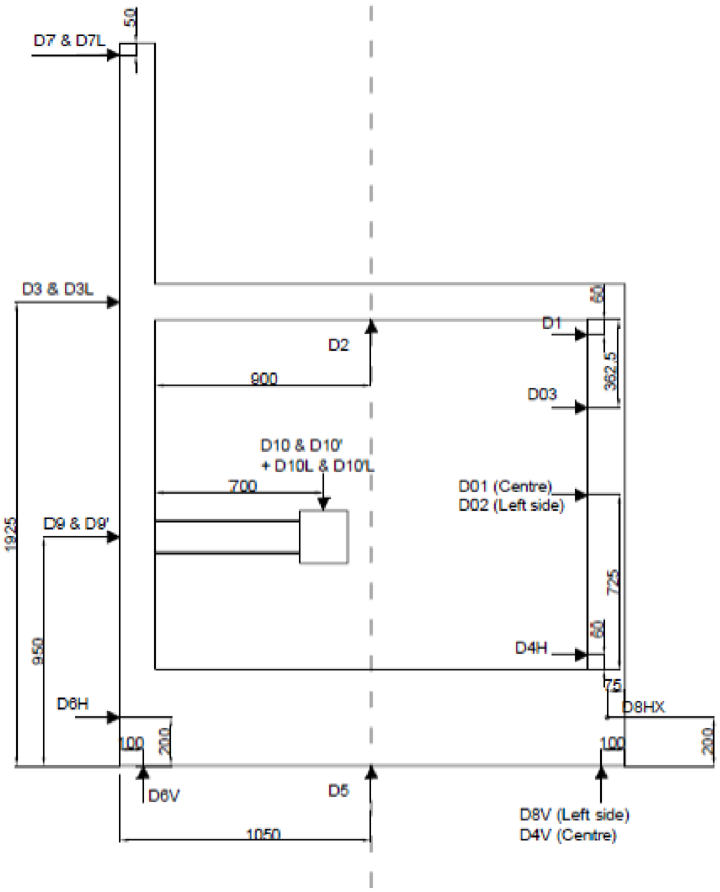

Figure 4-7: Displacement sensors in the mock-up symmetry plane (side view).

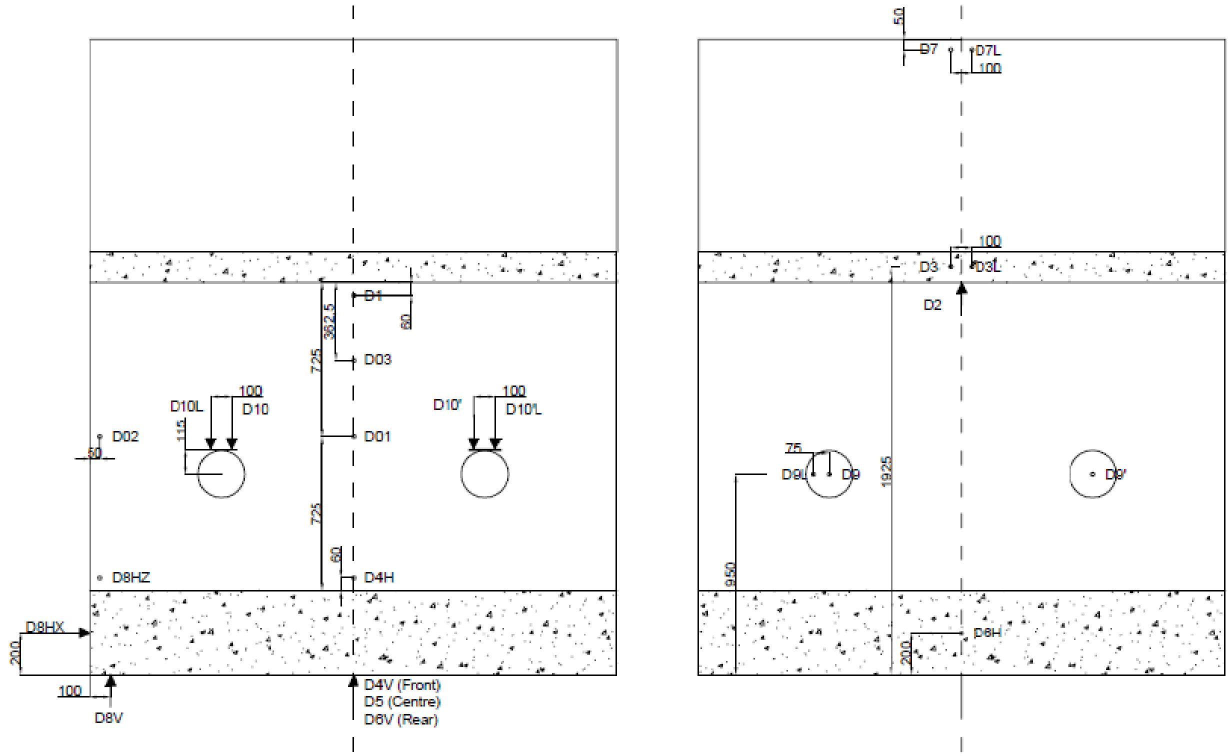

Front wall and equipments (front view)

Rear wall, floor and ceiling (front view)

Figure 4-8: Displacement sensors on the front and rear walls and on the equipments (front view).

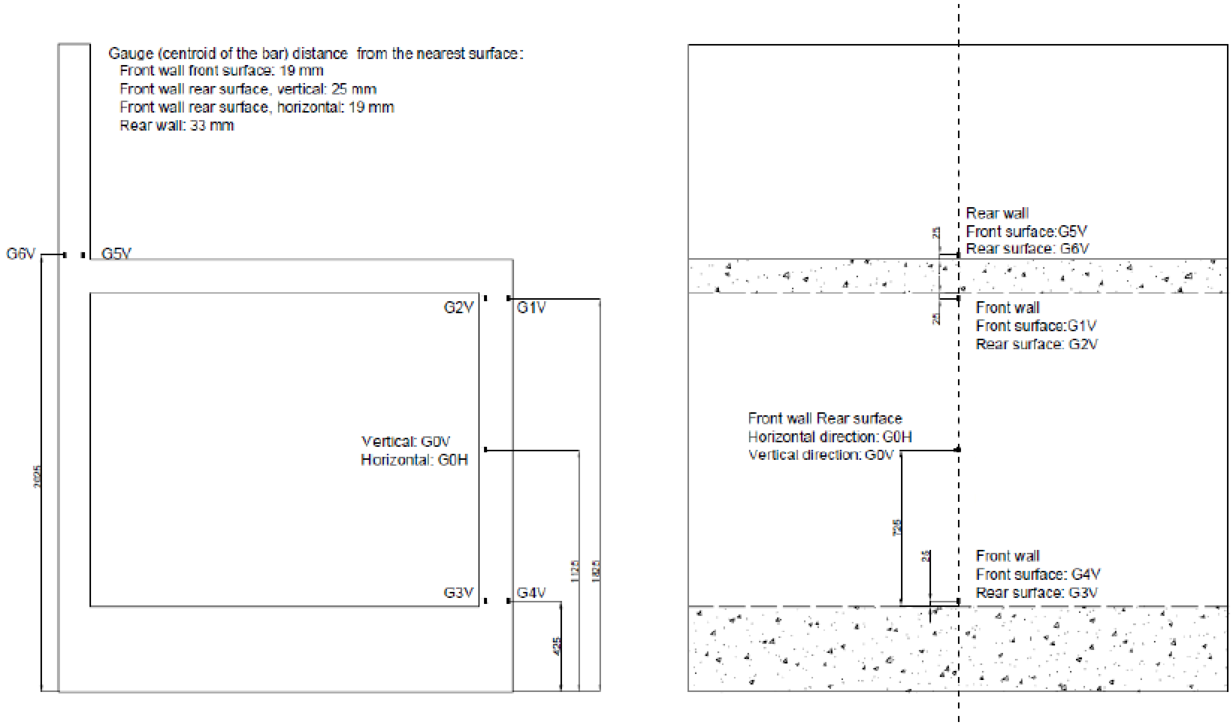

Figure 4-9: Rebar strain gauges (side view in the mock-up symmetry plane and front view).

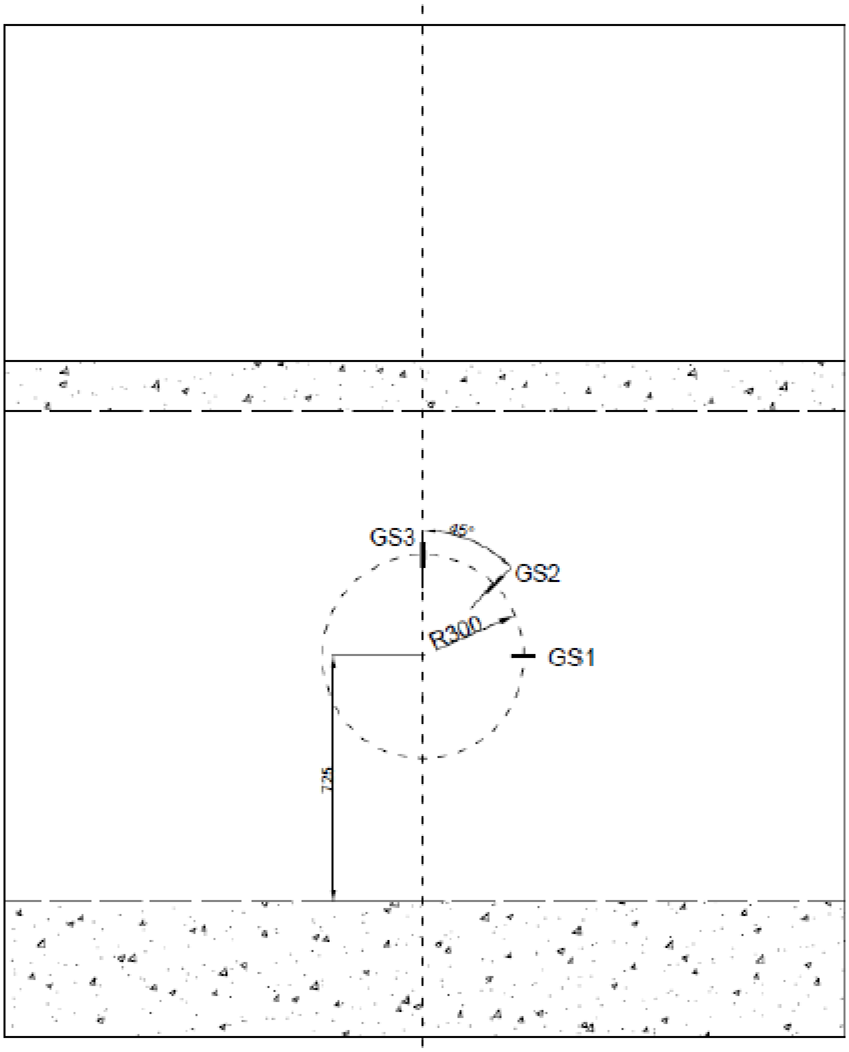

Figure 4-10: Concrete strain gauges on the front wall front surface (front view).

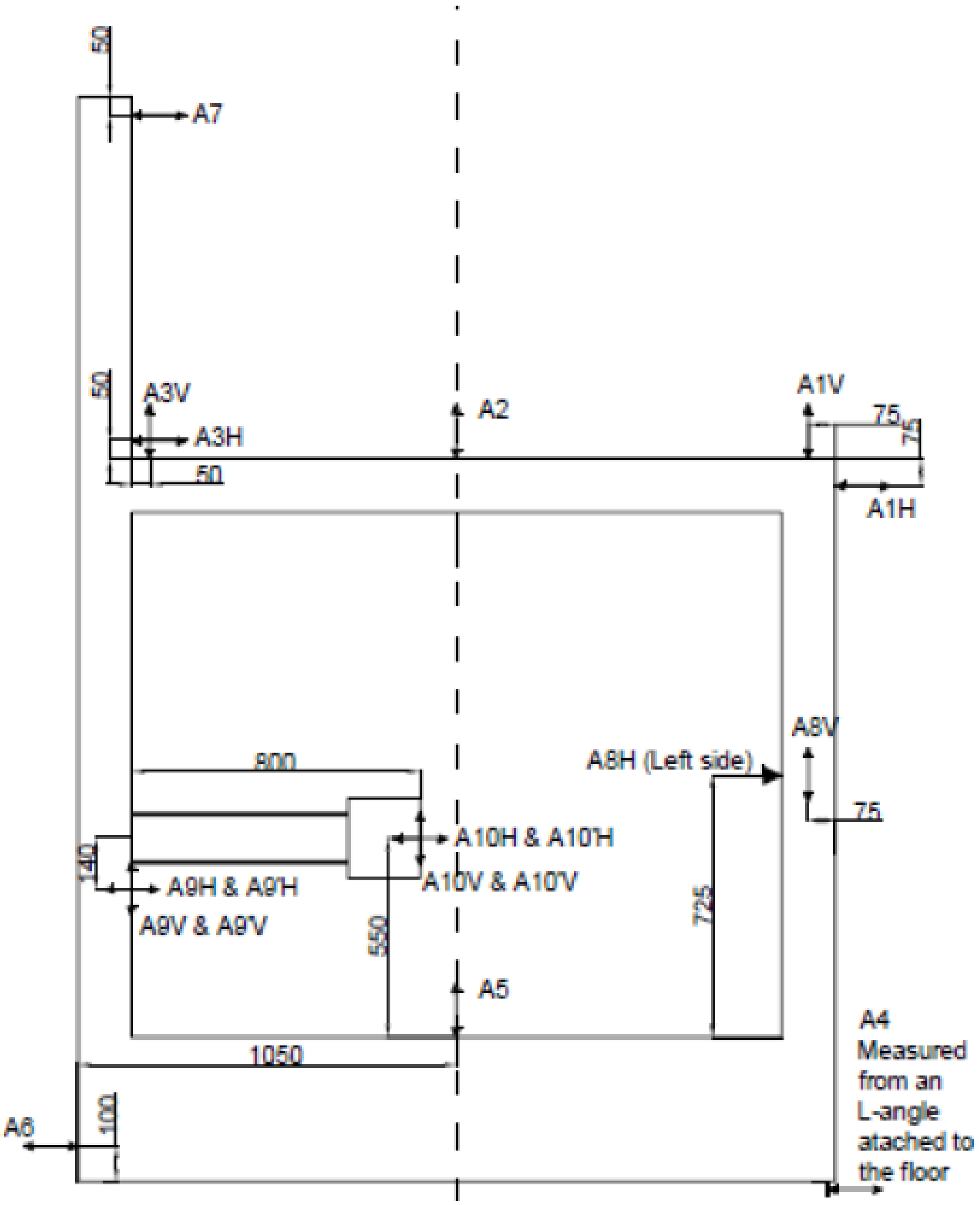

Figure 4-11: Acceleration sensors in the mock-up symmetry plane (side view).

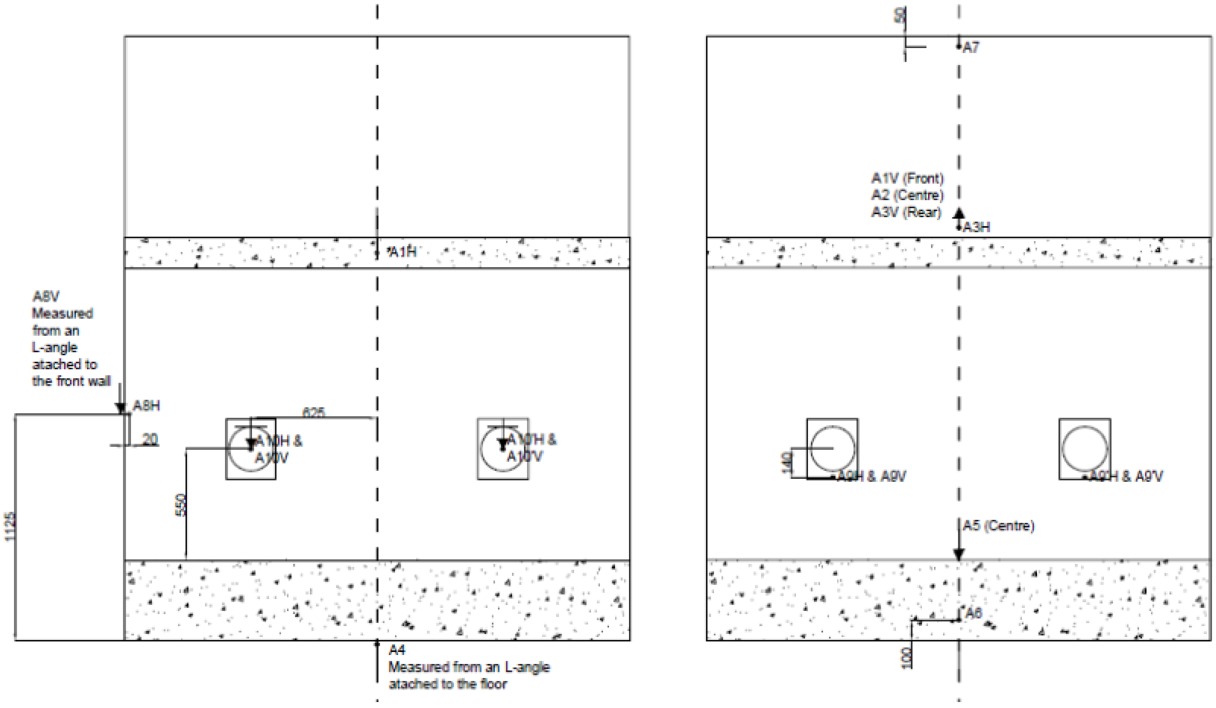

Front wall and equipments (front view) Rear wall, floor and ceiling (front view)

Figure 4-12: Acceleration sensors in the front and rear walls and on the equipments (front view).

4.1.2.2 Description of the Missile

Only one type of projectile (hollow, as opposed to solid) was used in three different impact tests, shown in Figure 4-13. The projectile mass was 50 kg. Two missiles were launched at 90 m/s, and the third and final missile was launched at 170 m/s. Typical dimensions for a missile with a length of 2.0 m are given in Table 4-1. The length of the stainless steel pipe was adjusted according to the projectile velocity to ensure proper folding of the projectile: 1500 mm for the 90 m/s tests and 2400 mm for the 170 m/s test. The carbon pipe was adjusted depending on the stainless pipe length such that the total mass of the projectile reached 50 kg. The mass and shape of this carbon pipe welded to the rear plate did not affect the projectile behavior.

Table 4-1: Main items constituting the projectile.

Item	Diameter (mm)	Thickness (mm)	Length (mm)	Mass (kg)
Stainless steel pipe	254.0	2.0	2000	23.64
Stainless steel end cap	256.0	3.0	86	2.11
Carbon steel pipe	244.5	12.5	190	14.16
Carbon steel plate	256.0	25.0	25	10.10

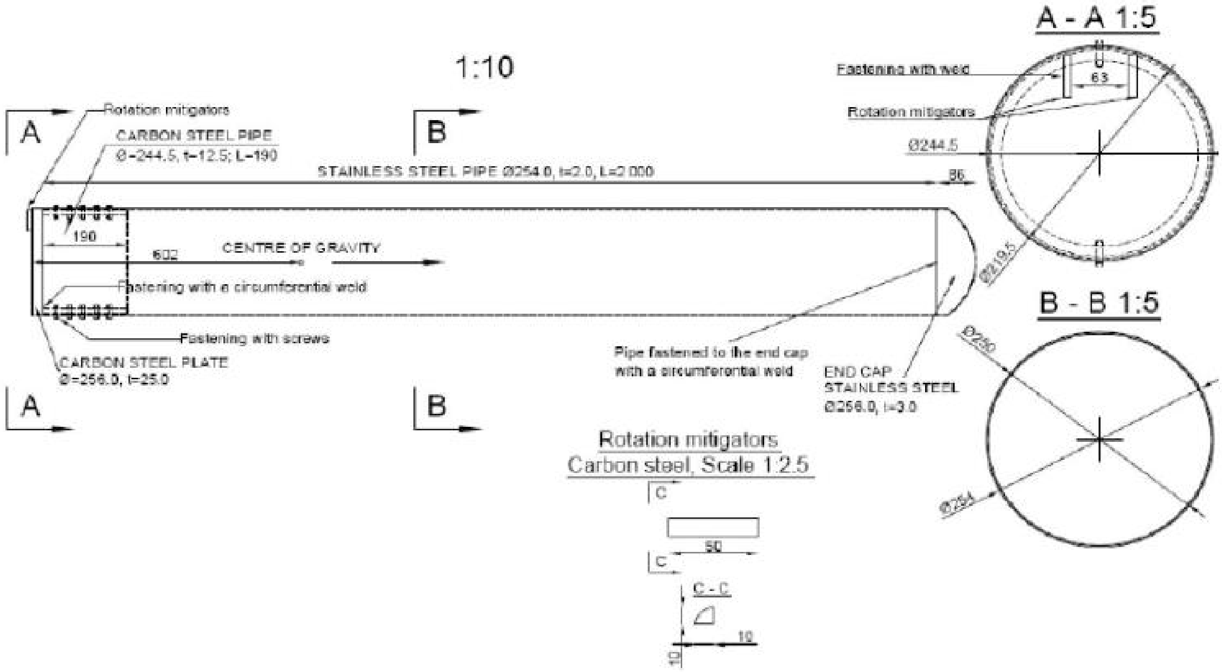

Figure 4-13: Projectile used for the tests.

4.2 Phase III Test Data and Material Properties

During Phase III, general concrete material data was provided, but no triaxial test data was supplied. Rebar and steel stress-strain curves were supplied by CSNI.

4.2.1 Concrete Test Data

The mock-up materials are described in Table 4-2. No information about the concrete was given outside of what is presented in Table 4-2. Compressive strength C40/50 indicates that the compressive strength was between 40 MPa and 50 MPa, and the maximum aggregate size was 8 mm.

Table 4-2: Main properties for reinforced concrete.

	Characteristics	Target value
Concrete	ρ (kg/m^3)	2500
	ν (unitless)	0.2
	Compressive strength	C40/50
	Aggregate size (mm)	8.0
Rebar	ρ (kg/m^3)	7850
	f_{yk} (MPa)	500
	E (MPa)	200,000
Supporting pipes	f_{yk} (MPa)	355

4.2.2 Reinforcing Steel Data

The stress-strain curves for the mock-up steel are shown in Figure 4-14, Figure 4-15, Figure 4-16, and Figure 4-17. The tensile tests were first performed on specimens taken form the batch delivered for the floor of the IRIS III mock-up. Therefore, they were performed for both 10 mm diameter bars and 6 mm diameter bars.

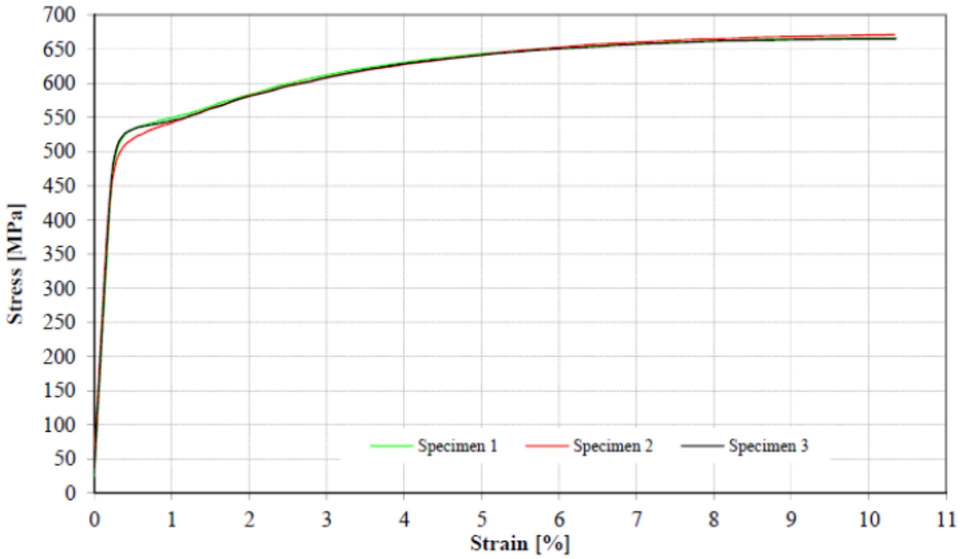

Figure 4-14: Stress-strain curve for B500B steel rebars (floor batch) with a diameter of 6 mm (L_0 = 200 mm).

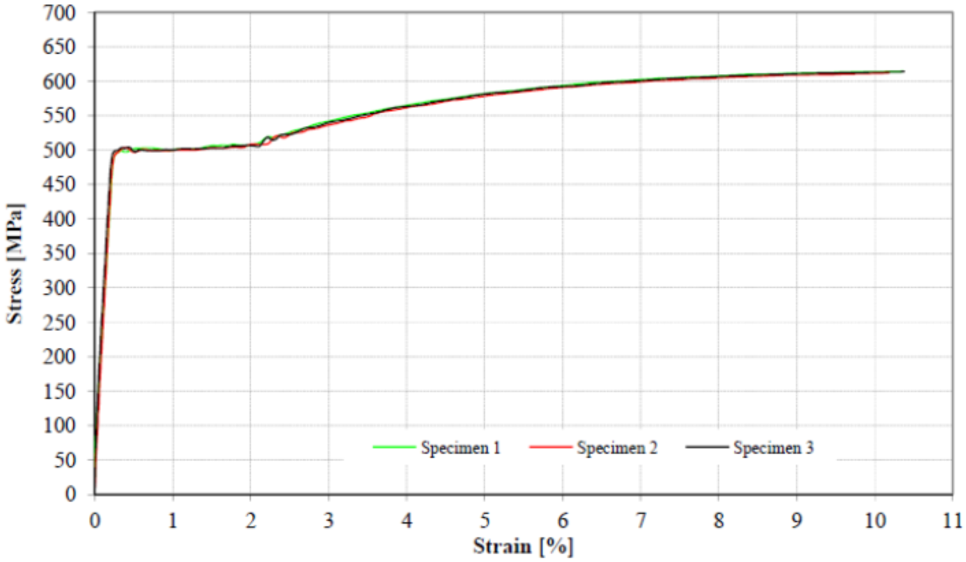

Figure 4-15: Stress-strain curve for B500B steel rebars (floor batch) with a diameter of 10 mm (L_0 = 200 mm).

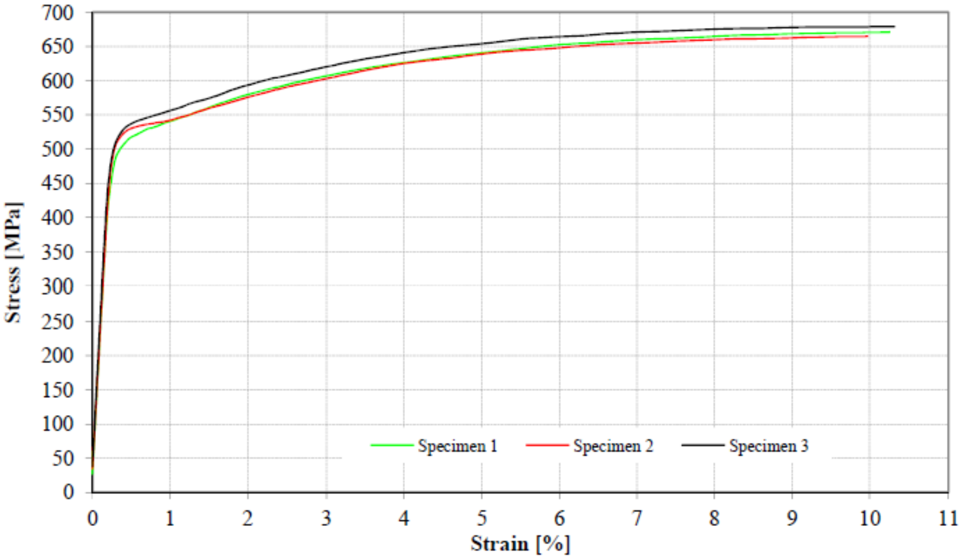

Figure 4-16: Stress-strain curve for B500B steel rebars (walls batch) with a diameter of 6 mm (L_0 = 200 mm).

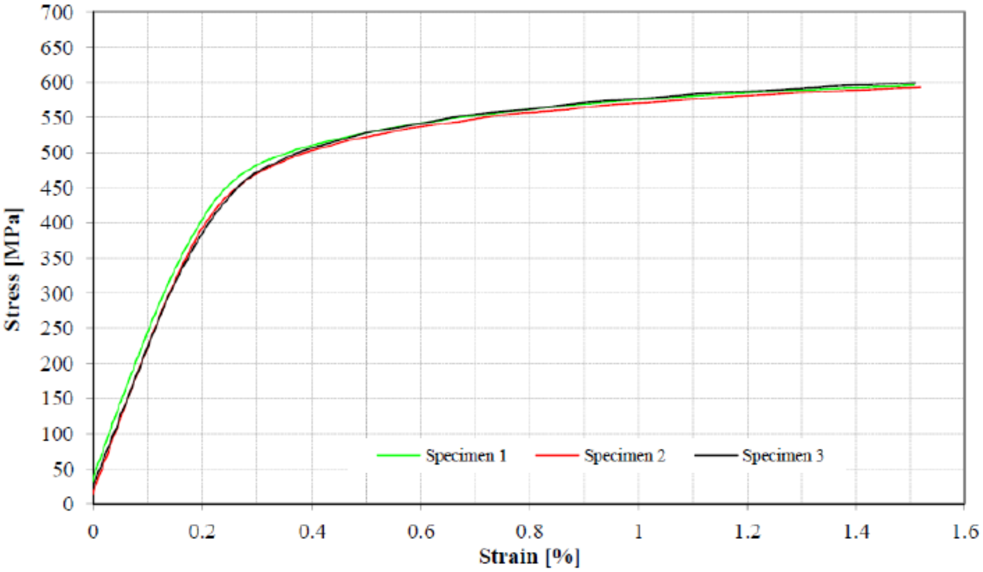

Figure 4-17: Stress-strain curve for S255 steel used for the support pipes (L_0 = 100 mm).

4.2.3 Missile Steel Data

The missile steel for Phase III was standard ASTM 316L stainless steel. Stress vs strain curves for three samples of the steel are shown in Figure 4-18. The material model used for the simulations was calibrated to an average of these three test curves.

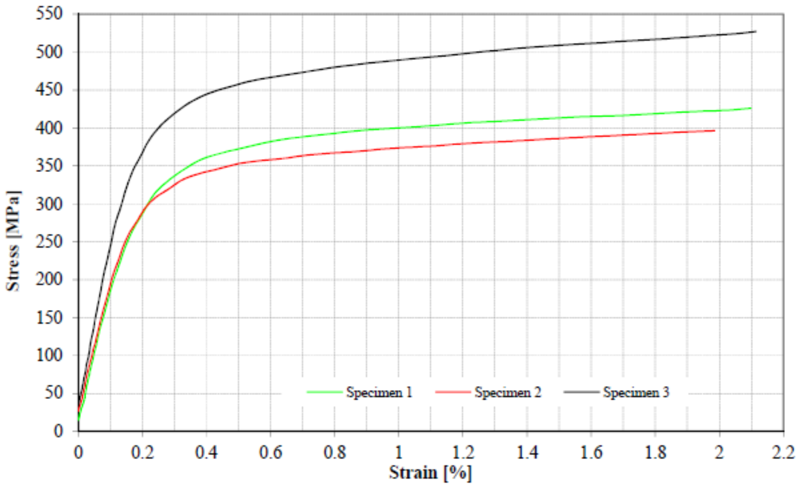

Figure 4-18: ASTM 316L Stainless Steel Stress vs Strain Curves.

4.2.4 Data Not Provided

In addition to the information reported missing in Table 2-3, Phase III concrete stress-strain data was not provided. The triaxial stress-strain data presented for Phase I and Phase II was scaled to match the compressive strength of Phase III.

4.3 Phase III Finite Element Model Description

In this section the numerical model components representing the mesh, boundary conditions, and material models are discussed for Phase III. All meshes for Phase III were created using the Sandia in-house meshing software Cubit (Cubit 2016). All finite element simulations were completed using the Sandia in-house finite element software SIERRA (SIERRA 2016). All simulations were solved utilizing explicit dynamics. The time step in each simulation was primarily dominated by the element size. No damping was used in any simulation since damping reduced the time step by two orders of magnitude.

4.3.1 Concrete Testing

4.3.1.1 Triaxial Testing Method

Triaxial testing as describe in Section 3.3.1.4 was performed on the concrete material to ensure relative agreement with the triaxial data presented in Phase II. ‘Relative’ agreement intends that the triaxial testing presented in Phase II has the same shape and general behavior as the material response in Phase III but scaled to the concrete strength for concrete in Phase III. The hydrostatic pressure in the simulation was gradually increased with the smoothstep function shown in Figure 4-19 and Equation 6 to prevent shock damage to the material.

Equation 6

$$Pressure = P_0 * \left(3 * \left(\frac{t}{t_0}\right)^2 - 2 * \left(\frac{t}{t_0}\right)^3\right)$$

P_0 is the hydrostatic pressure and t (time) ranges from 0 to t_0 seconds. The smoothstep equation eliminated shock effects during the simulation during high-pressure triaxial tests.

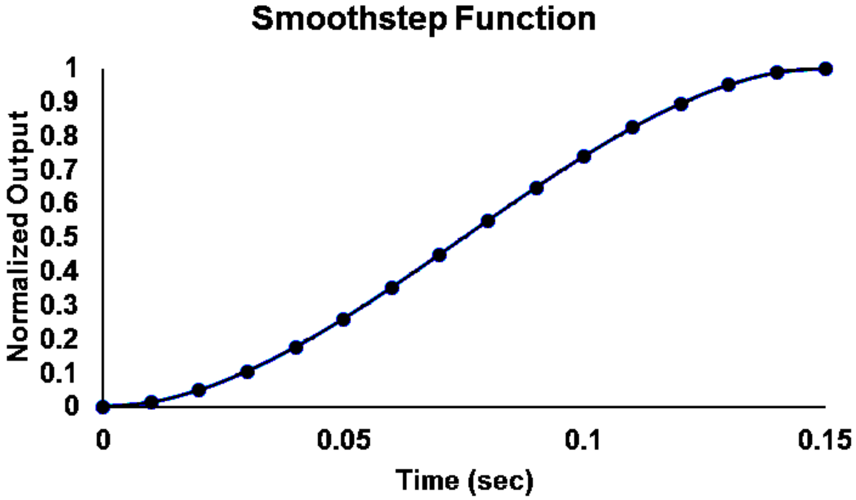

Figure 4-19: Normalized smoothstep function.

4.3.1.2 Single-element Concrete Testing

Initial material testing consisted of a single element (Figure 4-20) in either uniaxial or triaxial testing. The top and bottom faces of the element were given a constant displacement for a cumulative 1.0% strain/min. Force was summed on either the top or bottom face and divided by the area to attain the element stress. Element stress was also calculated directly by SIERRA and compared to the force/area computation for verification. Element strain was calculated from the given constant displacement. Stress vs strain curves were developed for the single-element tests to ensure that the concrete behaved as expected.

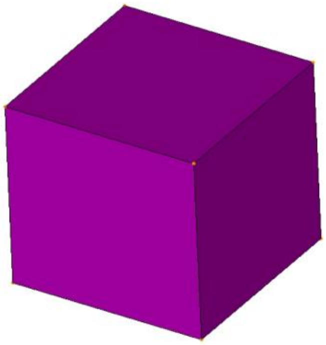

Figure 4-20: A single hexahedral element for material testing.

4.3.1.3 Concrete Cylinder Testing

After confirming that the single element tests were stable and agreed with expected material behavior, the constitutive model was applied to the concrete cylinder shown in Figure 4-21 for both uniaxial and triaxial compression testing. The model consisted of 435 hexahedral elements and 598 nodes. The top and bottom surfaces of the cylinder were given a constant displacement for a cumulative 1.0% strain/min. Force was summed on either the top or bottom face and divided by the area to attain the element stress. Element stress was also calculated directly by SIERRA and compared to the force/area computation for verification. Element strain was calculated from the given constant displacement. Stress vs strain curves were developed for the single-element tests to ensure that the concrete behaved as expected. The top and bottom nodes on the cylinder were constrained in both the x and y directions; only movement in the z direction was allowed. This restraint mimicked end effects in actual concrete cylinder testing and created failure patterns that are shown in Figure 2-25 for both uniaxial and triaxial testing. Damage accumulation in the cylinder revealed the failure pattern as shown in Figure 4-22.

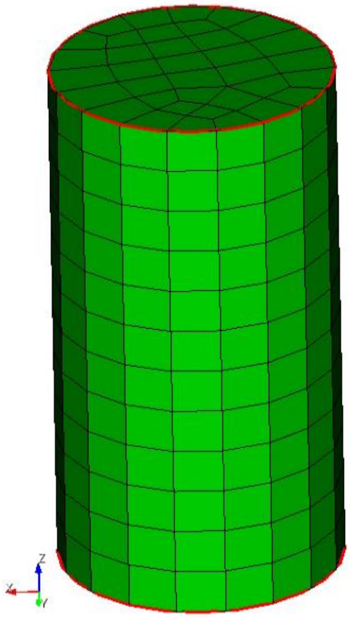

Figure 4-21: Concrete cylinder in Phase III.

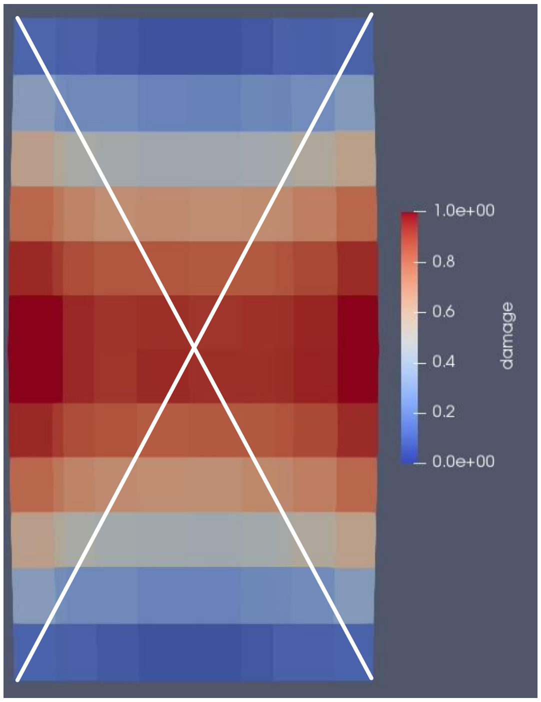

Figure 4-22: Damage in a concrete cylinder showing an X-pattern failure (marked with white lines).

Simulations were also performed on a Brazilian split-tensile concrete test (ASTM 2017). The split-tensile concrete test compresses a concrete cylinder on its side as shown in Figure 4-23. The top and bottom of the cylinder are subjected to high compressive stresses near the ends of the vertical diameter and a nearly uniform tensile stress acting over about the middle two-thirds of the specimen. Since the concrete is much weaker in tension than in compression, failure will be in splitting tension at a much lower load than would be required to crush the specimen in compression, thus permitting an estimate to be made of the tensile strength of the concrete. The element on the vertical diameter in Figure 4-23a is subjected to the stresses shown in Equation 7 and Equation 8.

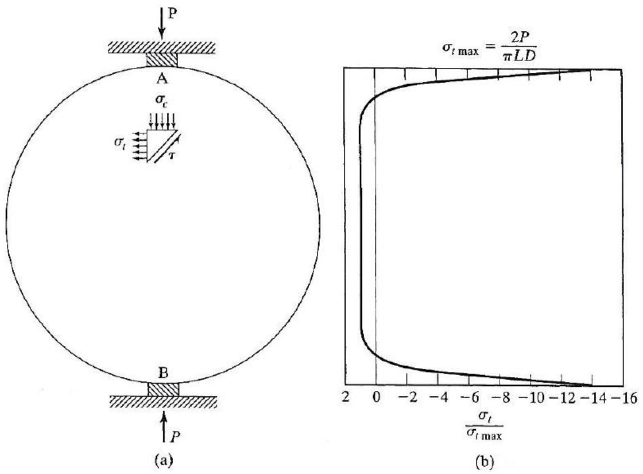

Figure 4-23: Brazilian split-cylinder concrete test (Sidney Mindess 2003). (a) Schematic of overall test configuration and load application. (b) Graph of stresses showing tensile stresses throughout most of the cylinder during the test.

Equation 7

$$\sigma_c = \frac{2P}{\pi LD}\left[\frac{D^2}{r(D-r)} - 1\right]$$

Equation 8

$$\sigma_t = \frac{2P}{\pi LD}$$

P is the applied compressive load, *L* is the cylinder length, *D* is the cylinder diameter, and *r* is the distance of the element from the top of the cylinder. The split-tensile simulation mesh is shown in Figure 4-24. Two steel platens are on top and bottom of the cylinder. The cylinder is composed of 37,582 hexahedral elements, and each platen is composed of 2030 hexahedral elements. The bottom nodes on the bottom platen are fixed in space, and the top nodes on the top platen are moved down at a fixed strain rate of 0.1%. The platens are curved where they contact the cylinder to ensure that the cylinder does not move laterally during testing.

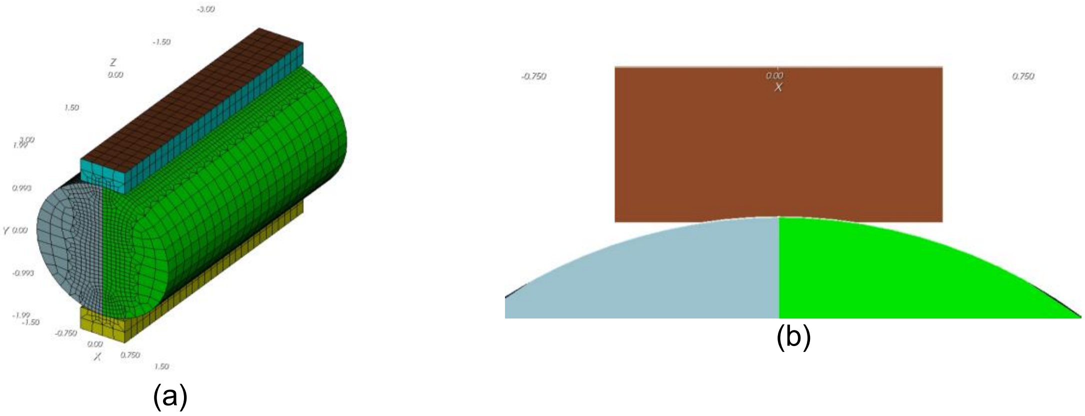

(b)

(a)

Figure 4-24: (a) Brazilian split-tensile simulation mesh. Cylinder height/diameter = 2:1 ratio. (b) Cut-view of the cylinder-platen contact showing the curved cut on the steel platen.

4.3.2 Steel Testing

All steel constitutive models were calibrated using an FE simulation consisting of a series of beam elements extruded to form beam elements of appropriate diameter. The beam elements were pulled in uniaxial tension at a constant deformation rate and the force required was recorded. Further information on steel material testing is given in Section 4.3.3.3 .

4.3.3 Mock-up Model

The mock-up dimensions are described in detail in Section 4.1.2.1 and is briefly described again here for convenience. The mock-up is a 2.5 m wide structure made of reinforced concrete. It composed the following structural elements:

- Impacted wall: 2.5 m x 2 m x 15 cm
- Rear wall: 2.5 m x 2 m x 15 cm
- Lower floor: 2.5 m x 2 m x 40 cm
- Upper floor: 2.5 m x 2 m x 15 cm
- Cantilever wall: 2.5 m x 1 m x 15 cm

The concrete was constructed entirely with 8-noded hexahedral elements. Rebar was constructed entirely with 2-noded beam elements embedded into the concrete and given the properties of the specified rebar diameter. The I-beams, the metal plates connecting the I-beams to the concrete, the angle steel on the “bolted” I-beam, and the metal plates connecting the supports to the concrete and the ground were constructed with 8-noded hexahedral elements. The supports and the missile were constructed with 4-noded shell elements extruded to the thickness specified in the drawings. Each piece of rebar was constructed as specified in the drawings and embedded in the concrete. 3D hexahedral elements were analyzed with a single integration point at the midpoint. 2D shell elements were integrated as a 5 point trapezoidal rule through the thickness. 1D beam elements extruded as a rod or cylinder were analyzed with 9 integration points.

4.3.3.1 Mesh

The overall mockup without the missile or mesh is shown in Figure 4-25. The number of elements and nodes for the mockup are listed in Table 4-3. The use of two different connection methods connecting the I-beams to the structure eliminated the possibility of simplifying the model with symmetry.

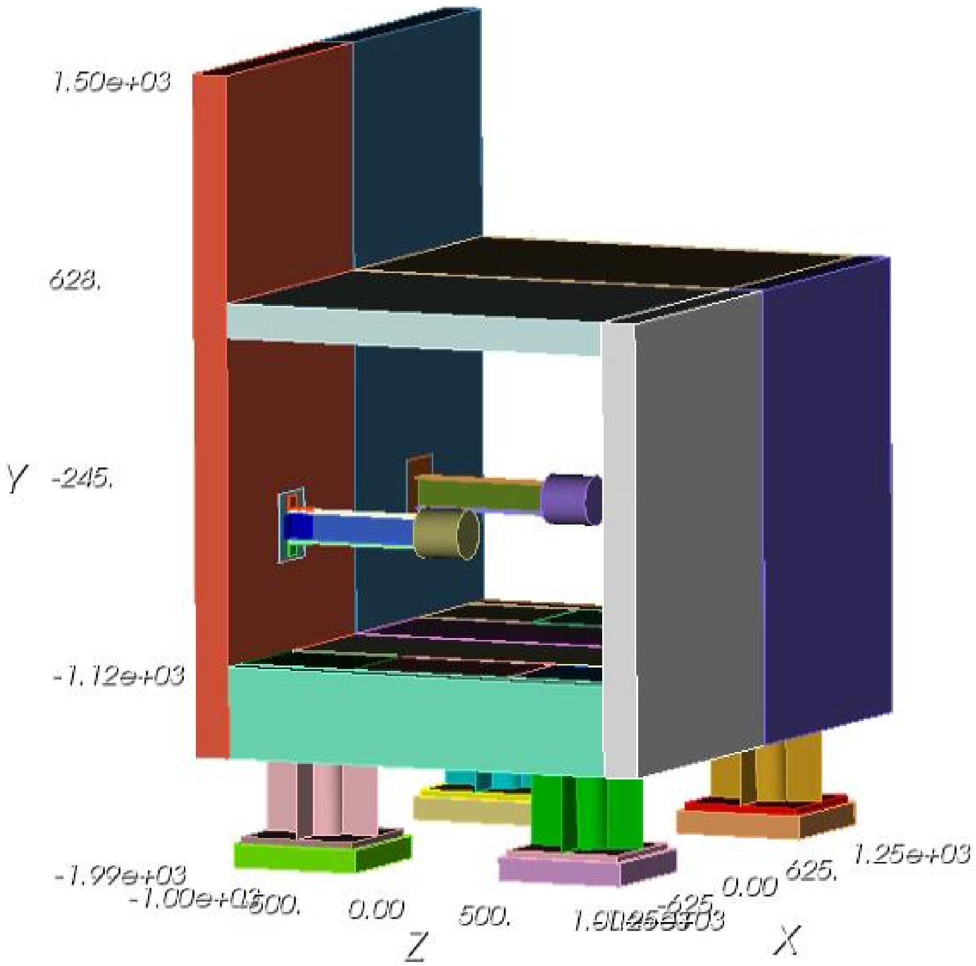

Figure 4-25: Overall mockup without mesh or missile. Units are in mm.

Table 4-3: Elements in the Mockup.

Element Type	No. of Elements
8-node hexahedral	2,051,928
4-node shell	2,464
2-node beam	154,644
Total	2,209,036

The mesh of the concrete is shown in Figure 4-26, Figure 4-27, and Figure 4-28. The mesh was refined on the impact face and around corners where moments would occur. Elements away from corners and the front face had approximately 62 mm edge lengths; elements near corners had approximately 21 mm edge lengths; elements on the front face had approximately 8.5 mm edge lengths. The mesh was doubly refined on the front face where the missile impacts the structure to fully capture damage propagation and to account for damage accrual in elements. As the missile impacts the front face, the concrete elements become damaged and lose strength per the material models used (see Section 4.3.3.3). If too few elements are used through the thickness, then the front faces loses more structural capacity compared to what actually happens in the test.

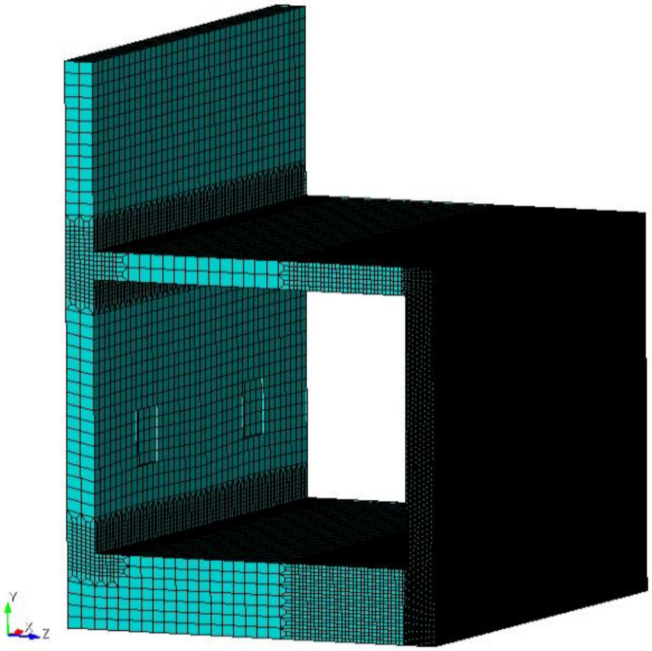

Figure 4-26: Overall concrete mesh.

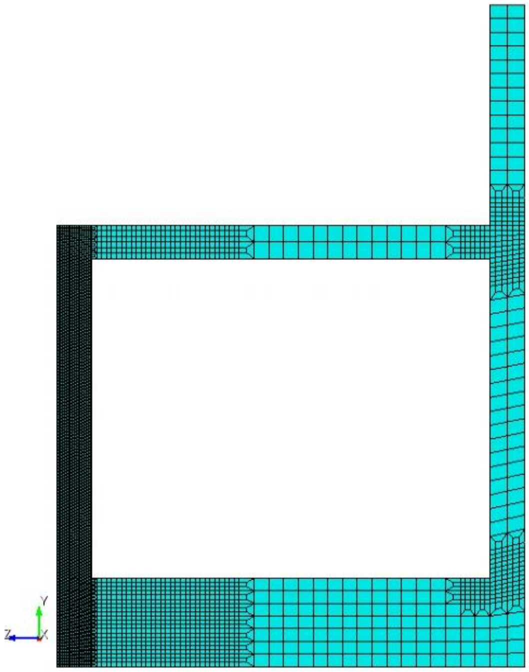

Figure 4-27: Concrete mesh side view.

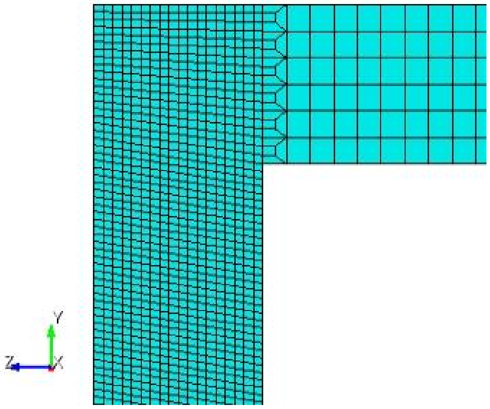

Figure 4-28: Refinement of the concrete front face.

Forces from the impact of the missile were obtained by summing the forces in the nodes on the impact face as shown in Figure 4-29 in the direction of missile impact (the z-direction).

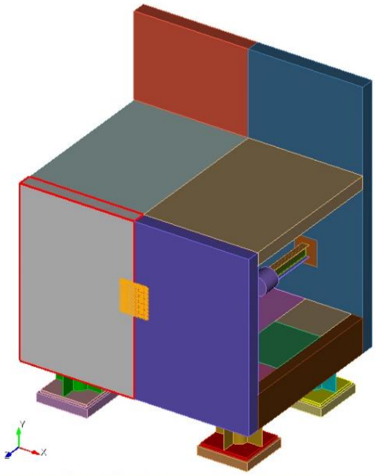

Figure 4-29: Highlighted nodes showing where missile impact forces are summed.

A supports of the mockup is shown in Figure 4-30. The column structure of the support is a cylinder with flanges welded at 0°, 90°, 180°, and 270°. The column structure of the support is constructed with shell elements. The top and bottom plates of the support are steel plates constructed with hexahedral elements. The column structure of the support is fixed to the steel plates, the top steel plate is fixed to the concrete structure, and the bottom steel plate is fixed to the concrete base shown in Figure 4-31. Figure 4-31 shows a mockup support sitting on a concrete base (hexahedral elements) with connecting rods protruding from the top of the support (beam elements). The connecting rods are fixed at one end (against both spatial and rotational movement) to the steel plate and are embedded into the concrete structure. There was a divot in the concrete structure to allow room for the steel plate. Elements in the supports had edge lengths between 25-30 mm. Reaction forces were summed in the Y-direction (vertical) through the base of the concrete supports shown in Figure 4-31.

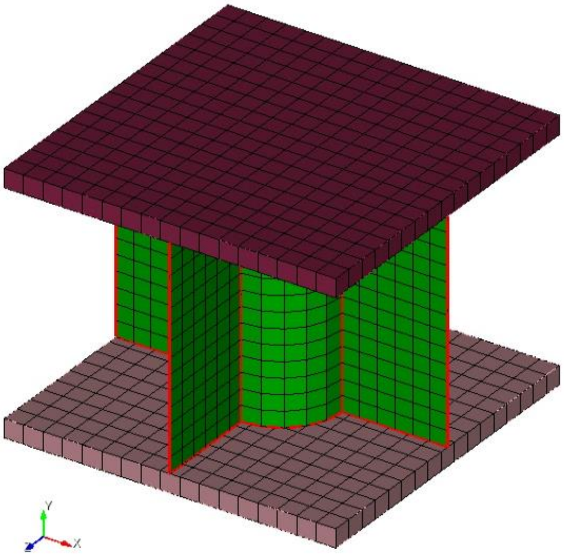

Figure 4-30: Mockup support with steel plates on top and bottom with a steel column structure between.

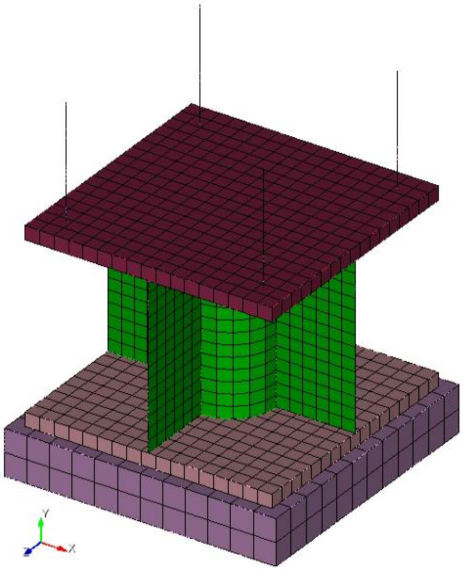

Figure 4-31: Mockup support sitting on concrete base with connecting rods protruding from the top.

The two I-beams are constructed from hexahedral elements and are identical. The welded I-beam (hexahedral elements) and its supporting plate (hexahedral elements) are shown in Figure 4-32. This I-beam is welded directly to the supporting plate in the experiment, and the simulated I-beam is connected directly to its supporting plate via the nodes highlighted in Figure 4-32. These nodes are directly coincident with where the welds exist in the experiment. The supporting plate was a steel plate fixed to the concrete. There was a divot in the concrete structure to allow room for the supporting plate. Elements in the I-beam had edge lengths that ranged from 24 mm across to 4.7 mm through the thickness.

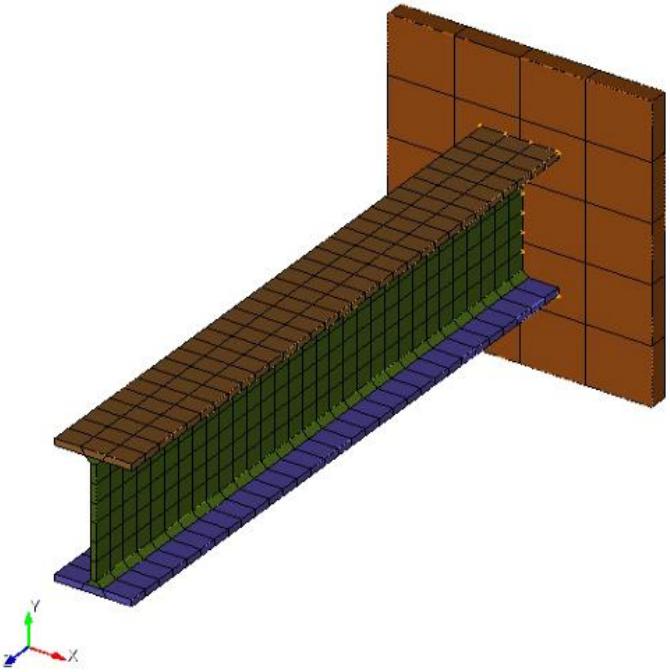

Figure 4-32: Welded I-beam, its supporting plate, and nodes fixed to the supporting plate (highlighted).

The bolted I-beam, its supporting plate, and the angle steel (hexahedral elements) connecting the two is shown in Figure 4-33. Elements in the angle steel had edge lengths of 8-12.5 mm. The nodes in the angle steel connected to the supporting plate are fixed to the supporting plate, and the nodes in the angle steel connected to the I-beam are fixed to the I-beam. While fixing so many nodes to the I-beam and supporting plate may not seem accurate, analyses with bolts, bolt holes, and various connecting methods involving bolts/bolt holes returned extremely large oscillations in the I-beam, much larger than the actual experiment or the welded I-beam. Other analyses with connecting the angle steel in Figure 4-33 to the I-beam and supporting plate included 1) fixing only nodes located in the vicinity of the bolts or 2) fixing only nodes at the far edges of the angle steel; both methods resulted in extremely large oscillations as well.

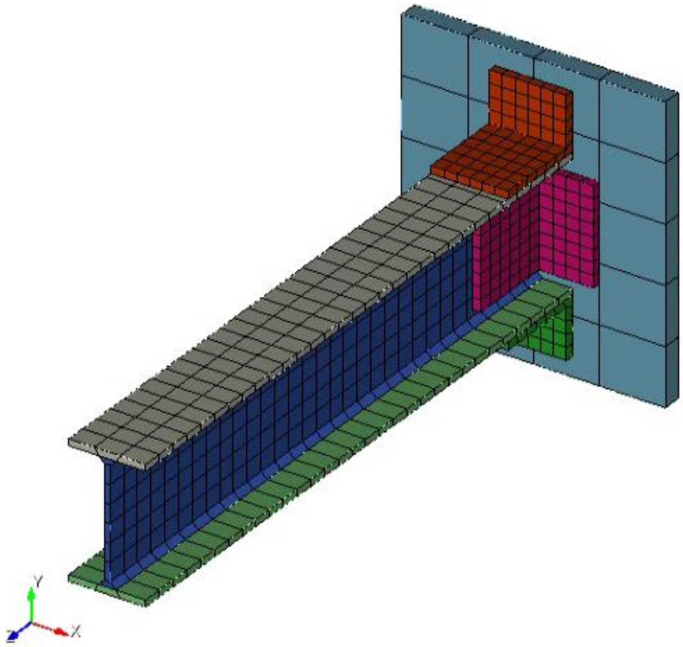

Figure 4-33: Bolted I-beam, its supporting plate, and angle steel connecting the two.

Figure 4-34 shows the bolted I-beam, its angle steel, and its attached pseudo-equipment. The pseudo-equipment was modeled as a circle extruded to a cylinder of appropriate size, mass, and density. The pseudo-equipment was completely fixed to the I-beam. Both pseudo-equipments were identical (on the welded and bolted I-beams).

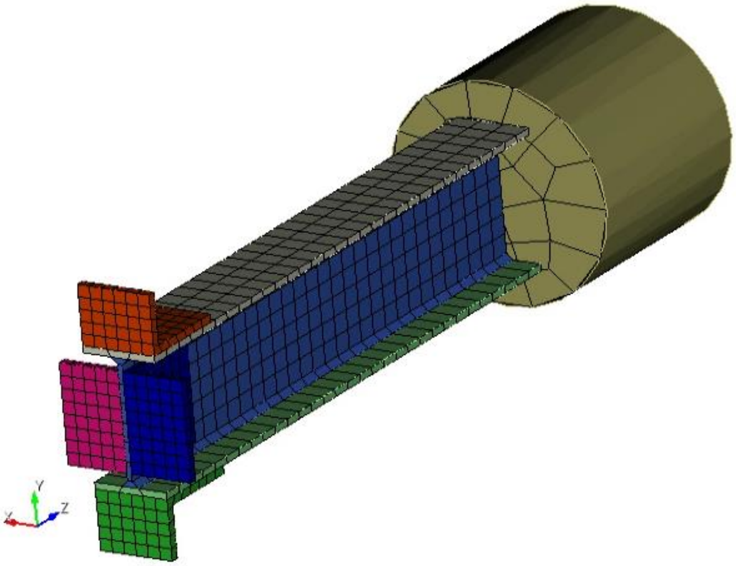

Figure 4-34: Bolted I-beam with its angle steel and attached pseudo-equipment.

Each piece of rebar inside the concrete was explicitly meshed with 2-noded 6-degree of freedom beam elements as shown in Figure 4-35and Figure 4-36. Elements were 15 mm in length except on the impact face wherein elements were 5 mm in length. Two layers of rebar, transverse and longitudinal, were included on every face of concrete. Concrete cover was as dictated in the drawings. Rebar ties that connected the two faces of rebar were modeled as shown in Figure 4-36. U-bars were placed at the top of the cantilever and at the top of the front impact face as shown in Figure 4-37. L-bars were placed in the bottom-front and bottom-rear of the mockup for both faces of rebar as shown in Figure 4-38. The impact face had extra rebar C-ties as shown in Figure 4-36 and Figure 4-39.

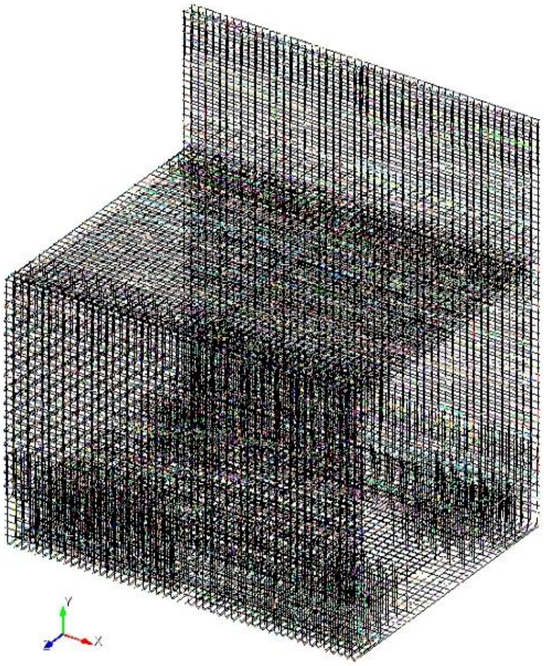

Figure 4-35: Isometric view of all rebar.

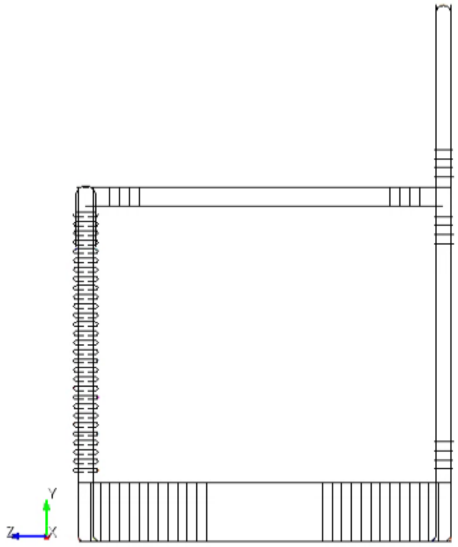

Figure 4-36: Side view of all rebar. Cross-rebar (into plane) can't be seen since it is only 2D.

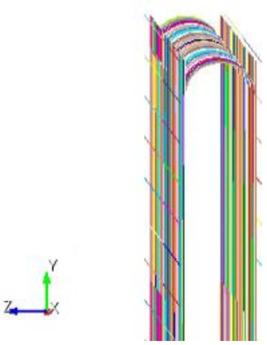

Figure 4-37: U-bars at the top of the cantilever.

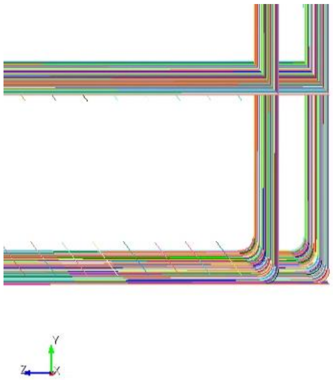

Figure 4-38: L-bars in the bottom-rear of the mockup.

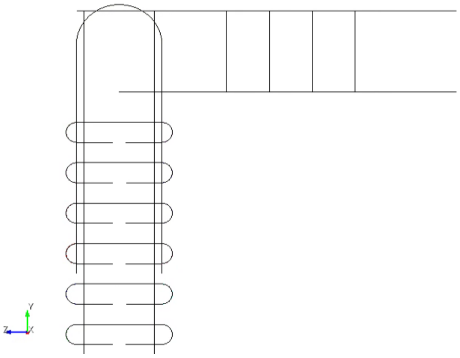

Figure 4-39: Impact face rebar showing U-bar, transverse and longitudinal rebar, straight ties, and C-ties.

4.3.3.2 Boundary Conditions

The mockup was fixed in space via the nodes on the base of the concrete supports highlighted in Figure 4-40. These nodes were fixed in space against translational and rotational motion. Gravity was not included in the model.

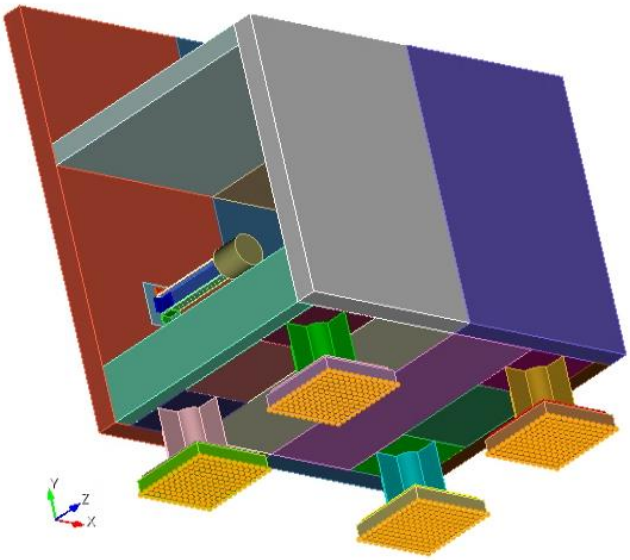

Figure 4-40: Fixed boundary condition.

4.3.3.3 Material Models

Several different material models were used throughout the mockup depending on the material in question and on expected deformation.

4.3.3.3.1 Steel Material Models

The rebar steel was modeled using a bilinear elastic-plastic model since beam line elements could not use a higher-order deformation model (such as multilinear elastic-plastic). Major deformation was not expected (or seen) in any rebar, so a bilinear elastic-plastic model functioned as needed for these simulations. Figure 4-41 and Figure 4-42 show the stress vs strain curves of experimental and elastic-plastic rebar.

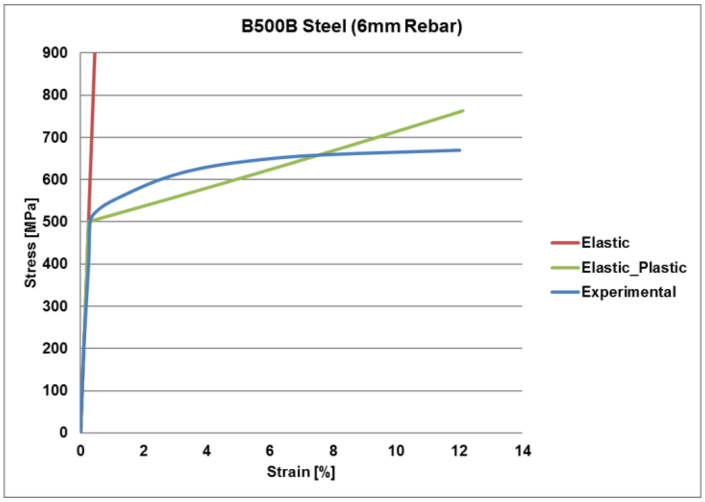

Figure 4-41: B500B Steel Elastic-Plastic Model for 6mm Rebar.

Figure 4-42: B500B Steel Elastic-Plastic Model for 10mm Rebar.

The S355 steel used for the supports was modeled using a higher-order failure mode model called multi-linear elastic-plastic with failure (ML_EP_FAIL) as shown in Figure 4-43. The shell elements used in the supports could use a higher-order constitutive model than the beam elements used for rebar. Similarly, the ASTM 316L stainless steel for the missile was modeled using shell elements and with ML_EP_FAIL as shown in Figure 4-44.

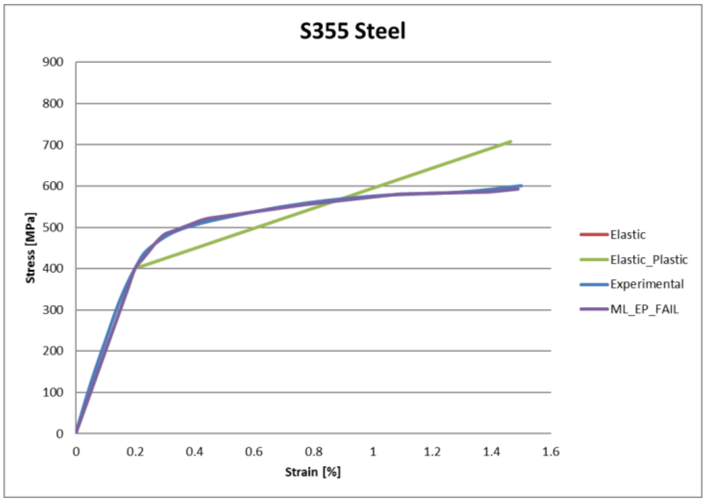

Figure 4-43: S355 Steel ML_EP_FAIL Model for Support Steel.

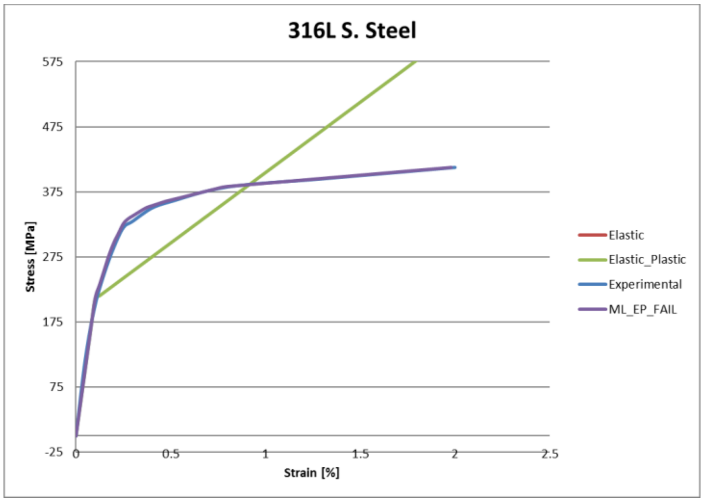

Figure 4-44: ASTM 316L Stainless Steel ML_EP_FAIL Model for Missile Steel.

The I-beams, the angle steel, and the supporting plates connecting the I-beams to the concrete were all modeled as elastic, requiring only Young's modulus and Poisson's ratio (200 GPa and 0.29, respectively). No deformation was expected in these materials, and no deformation was seen in the experiments.

4.3.3.3.2 Concrete Material Models

The concrete was modeled using two different models with three total sets of inputs to compare and contrast. The concrete model proposed by Holmquist, Johnson, and Cook (Holmquist, Johnson and Cook 1993), henceforth titled HJC, has many promising features for use in the IRIS program. The HJC model increases the compressive strength of the material with increasing confining pressure, and damage decreases the overall strength of the material. In addition, the damage parameter is stabilized such that damage requires a minimum strain to begin accruing, preventing unstable damage propagation through the material due to numerical artifacts or artificial material shock. Artificial material shock potentially occurs in finite element simulations when an element becomes damaged. The damaged element instantly transfers from the undamaged strength/strain to the damaged strength/strain, and the sudden change in strain can cause a shockwave through the simulation instantly damaging surrounding elements that would otherwise be undamaged. The other model used for the IRIS Phase III simulations is the Karagozian & Case concrete model, henceforth titled K&C, as described in detail in Section 3.3.1.3 . The K&C model also accrues damage and gains strength with confining pressure. The K&C model progresses from an 'undamaged' failure plane through a 'peak strength' plane to a final 'damaged' plane. More information is provided in Section 3.3.1.3 .

The HJC incorporates damage into the model based on hydrostatic pressure and excessive strains as shown in Equation 9.

Equation 9

$$Damage = \sum \frac{\Delta\varepsilon_p + \Delta\mu_p}{D_1(P^* + T^*)^{D2}}$$

In Equation 9, $\Delta\varepsilon_p$ and $\Delta\mu_p$ are the equivalent plastic strain and plastic volumetric strain, respectively; *D1* and *D2* are constants; and *P** and *T** are the pressure and hydrostatic tensile pressure normalized by f'_c. Hence, larger hydrostatic compressive pressures *P** can negate damage from hydrostatic tensile pressures *T**, and no damage accrues without plastic strain. The HJC also accounts for concrete crushing under large hydrostatic compressive pressures since concrete is porous as shown in Figure 4-45. Plastic volumetric strain increases linearly with pressure until reaching P_{crush} and μ_{crush}. Then the concrete crushes resulting in more volumetric strain per unit increase in pressure until reaching P_{lock}, after which all pores have been crushed and the concrete behaves as a solid without pores.

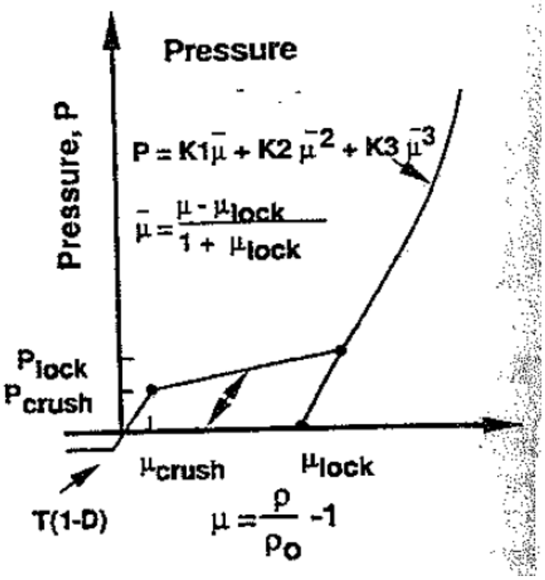

Figure 4-45: HJC pressure vs plastic volumetric strain crushing behavior.

The biggest drawback in using the HJC concrete model is its large list of variables: 21 in all. Young's modulus, Poisson's ratio, initial concrete density, compressive strength f'_c, two damage coefficients, initial shear modulus, a variable titled "maximum stress", maximum tensile pressure, minimum failure strain, P_{crush}, P_{lock}, μ_{crush}, μ_{lock}, three post-crushing behavior coefficients K_1, K_2, and K_3, a pressure hardening coefficient, a strain rate coefficient, and another maximum yield stress variable. Experiments can determine each variable, but many of the required experiments are rarely performed except in extremely specific scenarios (such as determining the pressure at which pore crushing begins and ends). Trial and error is required to hone the model to existing data. Several variables have significant impact on the material behavior that should be governed by other variables, making trial and error efforts difficult and time consuming. Attempts at fitting the HJC model to the existing triaxial data suggested multiple sets of variables that can match triaxial data.

Therefore, two different sets of input parameters for the HJC model were tested for use in the IRIS Phase III simulations. One set of input parameters was empirically modified to match existing triaxial compression testing data. The second set of input parameters was taken directly from the original documentation for the HJC model (Holmquist, Johnson and Cook 1993). The original documentation tested a concrete with f'_c = 7000 psi / 48.3 MPa including all experiments required to determine the 21 variables for the HJC model. The two models will be called by the following names in this report:

- Empirical HJC: HJC model using the empirically determined set of input parameters with results that resemble the behavior of typical concrete.
- Original HJC: HJC model using the input parameters taken directly from the original documentation for the HJC model.

Figure 4-46 shows the results of a single-element uniaxial compression test of Empirical HJC model concrete with a maximum strength of 49.2 MPa. The fall-off after peak strength is not representative of actual concrete behavior since the element retains strength, but the peak strength is representative of C40/50 concrete. Figure 4-47 shows the results of a single-element uniaxial tension test of Empirical HJC model concrete with a maximum strength of 4.9 MPa. Again, the fall-off after peak strength is not representative of actual concrete behavior since the element retains strength, but the peak strength is representative of C40/50 concrete.

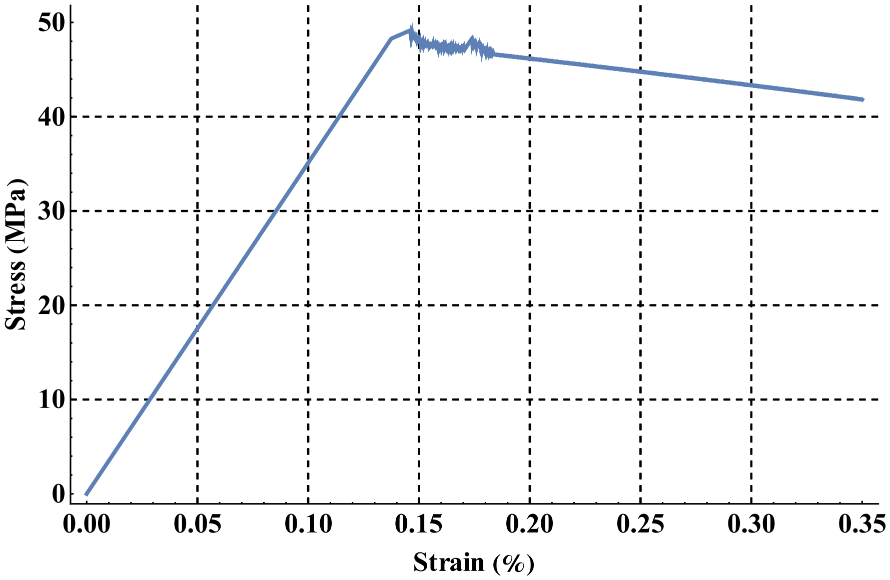

Figure 4-46: Single-element uniaxial compression test of Empirical HJC model concrete..

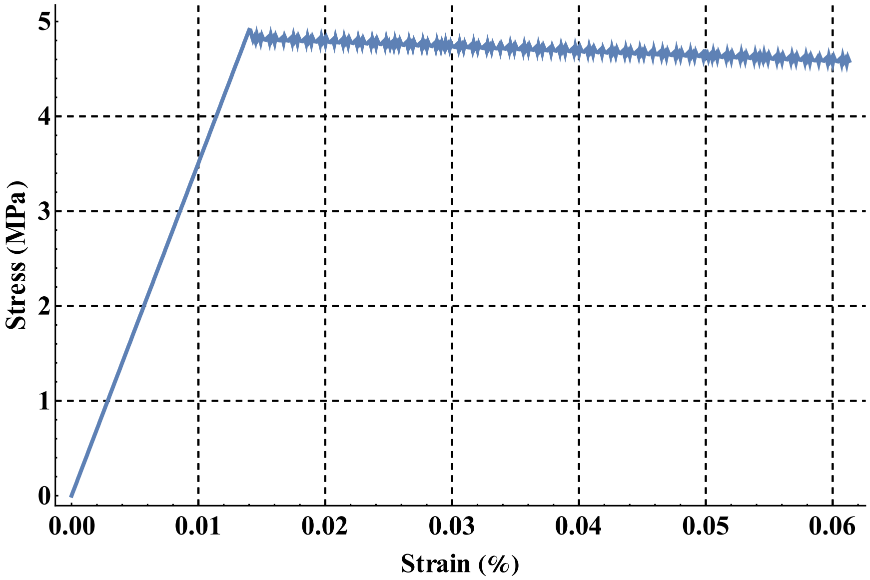

Figure 4-47: Single-element uniaxial tension test of Empirical HJC model concrete.

Triaxial compression testing for the Empirical HJC model on a concrete cylinder are shown in Figure 4-48. Peak strength of the unconfined uniaxial compression cylinder reached 48.6 MPa. These tests showed that increasing confining pressure resulted in increasing tri-linear stress vs strain behavior wherein the stress plateaus rather than decays after peak strength. Triaxial compression testing for the Original HJC model are shown in Figure 4-49; these triaxial tests did not agree with common concrete triaxial test behaviors. The unconfined uniaxial compressive test resulted in an ultimate concrete stress of 86.6 MPa, much higher than the assigned 48.3 MPa. In addition, subsequent triaxial tests with confining pressures predicted lower ultimate stresses than the triaxial experimental data presented in Figure 2-26.

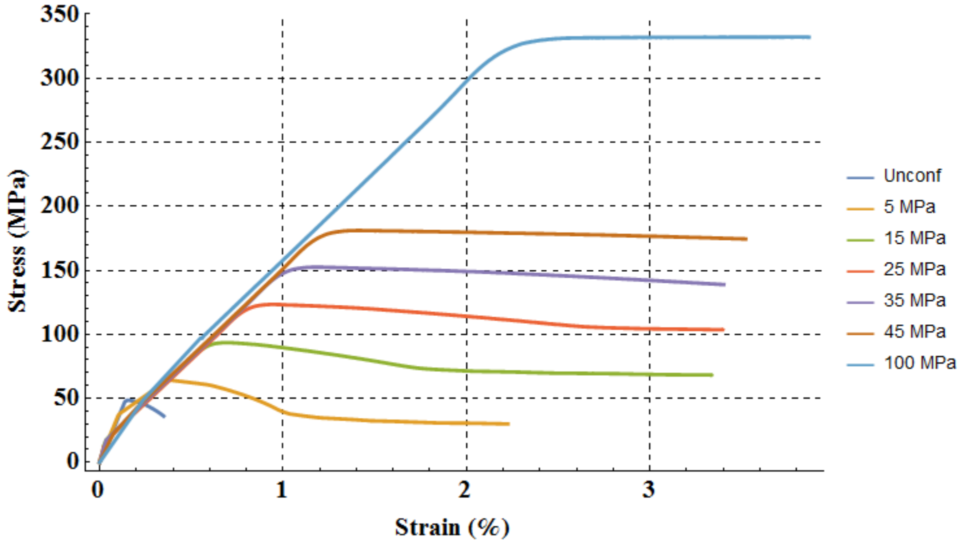

Figure 4-48: Triaxial testing of Empirical HJC model concrete cylinders.

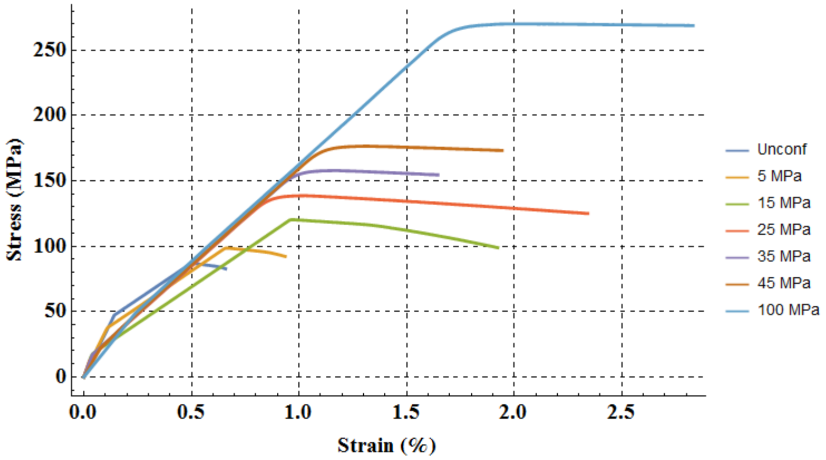

Figure 4-49: Triaxial testing of Original HJC model concrete cylinders.

Finally, the Brazilian split-cylinder test results for an Empirical HJC model concrete cylinder are shown in Figure 4-50. The peak strength of the cylinder was 10.2 MPa, over double the peak strength of the single-element uniaxial tension test simulation.

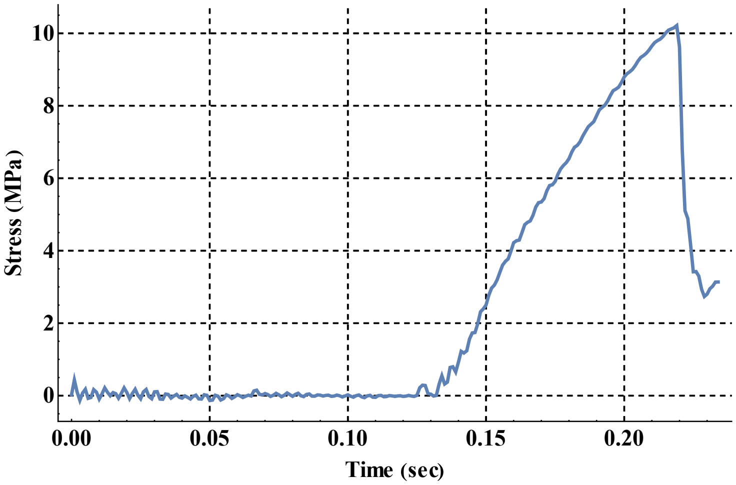

Figure 4-50: Brazilian split-cylinder stress vs time results for an Empirical HJC model concrete cylinder.

The fact that the triaxial cylinder tests do not resemble the behavior of triaxial concrete data presented in Figure 2-26 and that the single-element uniaxial tension test peak strength does not match the Brazilian split-cylinder test peak strength suggest that the HJC models do not accurately represent concrete behavior with the sets of inputs tested in this report.

The Karagozian & Case concrete model, described in detail in Section 3.3.1.3 , was used in the second attempt at Phase III simulations. The model parameters used in Section 3.3.1.3 were adjusted to match the Phase III concrete cylinder compressive strength of 50 MPa. The model also required hourglass stiffening to prevent instability. Figure 4-51 shows the uniaxial compression results of a single hexahedral element of Karagozian & Case concrete with a maximum compressive strength of 48.8 MPa. Figure 4-52 shows the uniaxial tension results of a single hexahedral element of Karagozian & Case concrete with a maximum tensile strength of 4.5 MPa. The behavior of the element was in good agreement with standard behaviors of concretes and agreed with the inputs of the K&C model. Figure 4-53 shows the triaxial test data for Karagozian & Case concrete cylinders. Increasing hydrostatic pressure increased the peak strength of the cylinder and allowed post-peak sustained loading as expected from typical triaxial concrete testing. Figure 4-54 shows the normalized peak strength of the concrete cylinder during triaxial testing versus the hydrostatic confining pressure. Figure 4-55 shows the Brazilian split-cylinder test results for the Karagozian & Case concrete cylinder. The split-cylinder test resulted in a tensile strength of 4.9 MPa, which is in good agreement with the uniaxial tensile strength of 4.5 MPa. Figure 4-56 shows the damage progression of the Brazilian split-tensile cylinder test for K&C concrete.

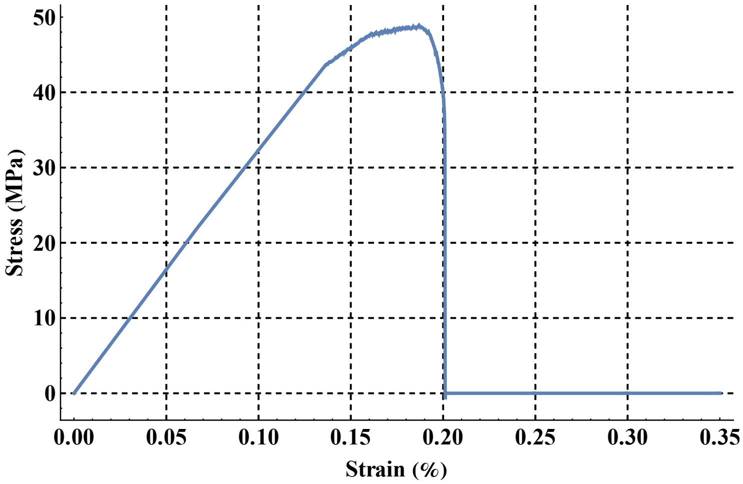

Figure 4-51: Single-element uniaxial compression test data for Karagozian & Case concrete.

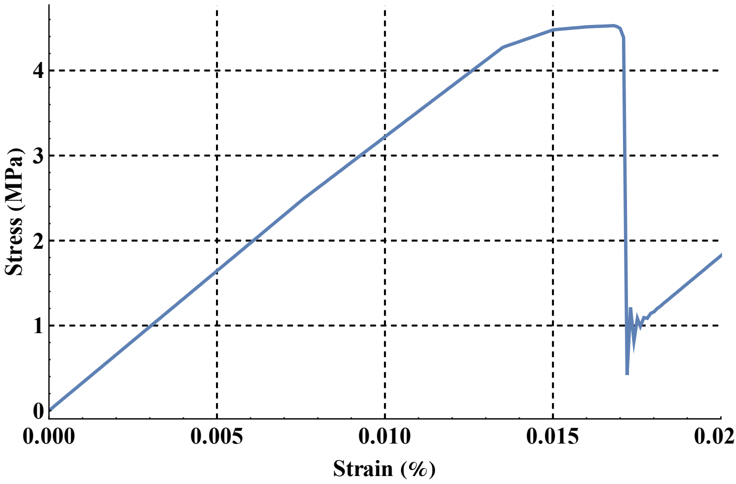

Figure 4-52: Single-element uniaxial tension test data for Karagozian & Case concrete.

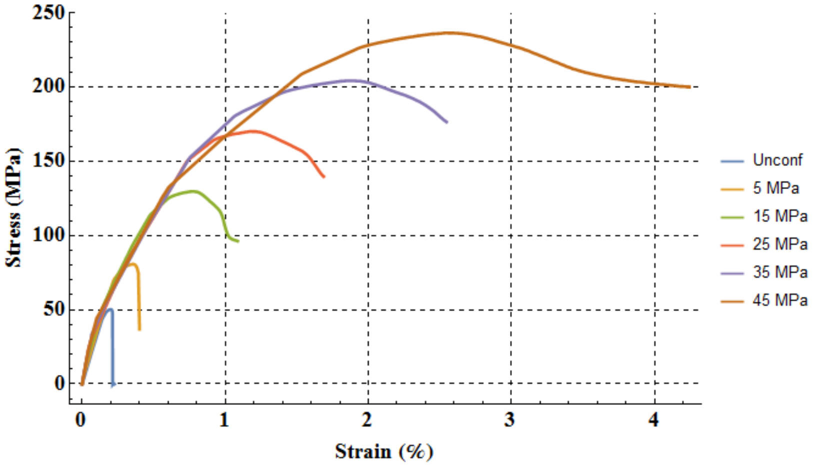

Figure 4-53: Concrete cylinder triaxial test data for Karagozian & Case concrete.

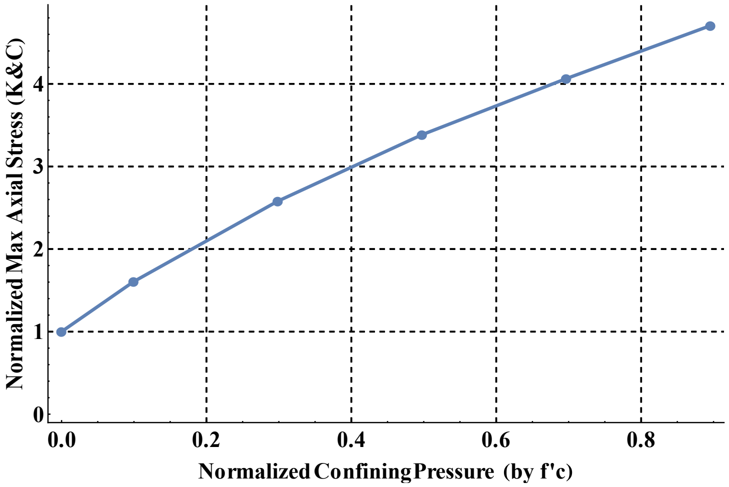

Figure 4-54: Normalized maximum axial stress vs normalized confining pressure for Karagozian & Case concrete.

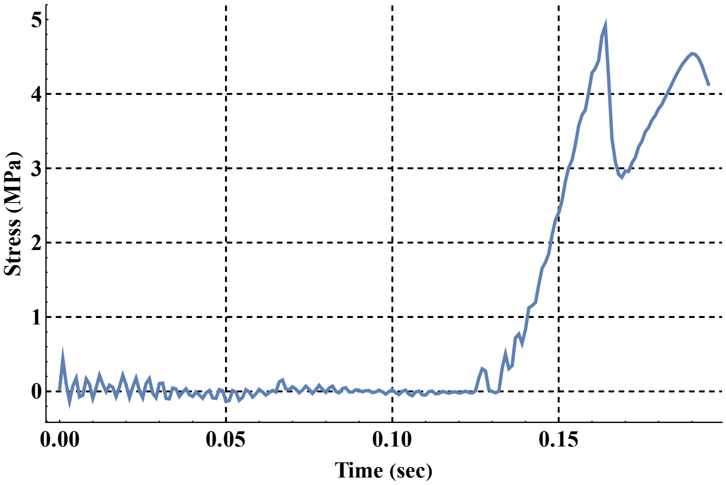

Figure 4-55: Brazilian split-tensile test of Karagozian & Case concrete.

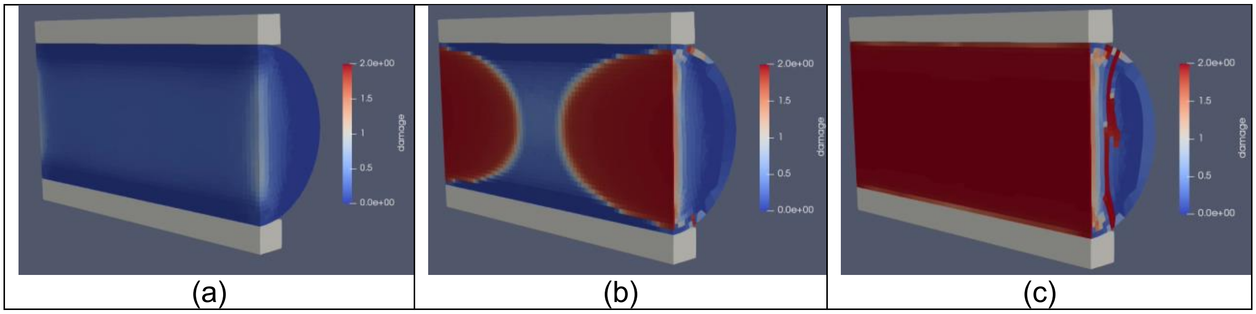

Figure 4-56: Cut view of Brazilian split-tensile test of Karagozian & Case concrete damage. (a) Damage initiation. (b) Damage propagation from outer edge through the center. (c) Failed.

4.3.3.4 Contact Modeling

Contact was explicitly effective in all pieces and materials of the mockup with the exception of rebar and reinforcing steel inside the concrete. Rebar and reinforcing steel were modeled as beam elements embedded inside the concrete and could not contact any material. Embedded reinforcement behaved as perfectly bonded with the concrete with no slip allowed. All other steel (steel plates, supports, the missile, etc.) included explicit contact.

4.3.4 Missile Model

4.3.4.1 Mesh

Different missiles were used for the 90 m/s test and the 170 m/s test. The mesh for the missiles are shown in Figure 4-57. The missiles were constructed as shell elements extruded to the proper thickness. Details of the missile meshes are given in Table 4-4. The missiles were two different lengths since the 170 m/s missile crushed significantly further than the 90 m/s missile. A carbon steel cylinder was embedded into the tail end of each missile; the total mass of each missile was 50.1 kg, made possible by altering the size of the carbon steel cylinder. The smallest elements in the missiles had edge lengths of approximately 8 mm; the mid-sized elements had edge lengths of 15-30 mm; the largest elements had edge lengths up to 65 mm. The elements on the tail end of the missile never impacted the concrete. The noses of the missiles were modeled as hemispheres.

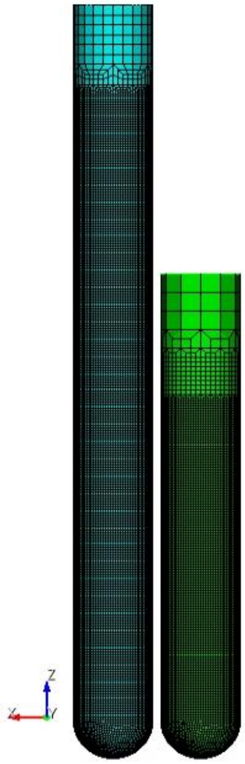

Figure 4-57: 170 m/s missile mesh (left) and 90 m/s missile mesh (right).

Table 4-4: Missile mesh details.

Missile Impact Velocity	Tube Length	Total Length	No. of Elements
90 m/s	1500 mm	1625 mm	15,976
170 m/s	2400 mm	2525 mm	26,848

4.3.4.2 Boundary Conditions

Each missile was modeled as a single merged surface. The carbon steel cylinder in the tail of the missile was fixed to the end of the missile and formed the rear face of the missile.

4.3.4.3 Material Models

The ASTM 316L stainless steel was modeled using a multi-linear elastic plastic model with failure (ML_EP_FAIL). The experimental and numerical model stress vs strain curves for ASTM 316L stainless steel are shown in Figure 4-58.

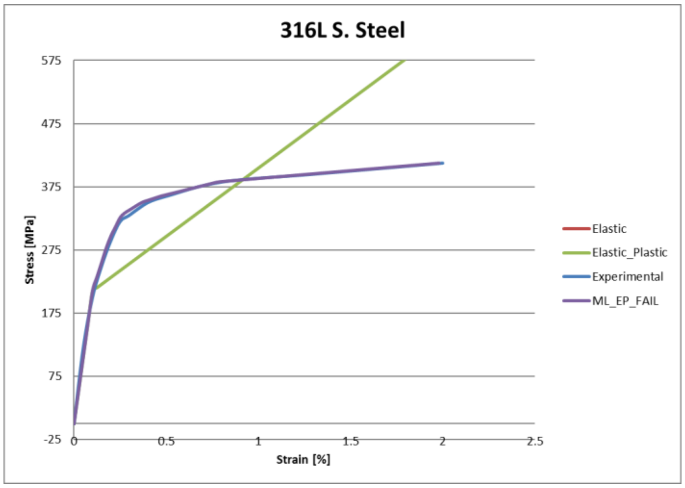

Figure 4-58: Materail model fit for ASTM 316L stainless steel

4.3.4.4 Contact Modeling

Contact was explicitly effective in all pieces and materials of the missile. The tail of the missile including the carbon steel mass did not impact the concrete.

4.4 Phase III Results and Summaries

4.4.1 Concrete Material Model Results

Sandia participated in two benchmark workshops for Phase III of the IRIS program. The first benchmark was a blind simulation in which the results of the missile impact on the mockup were not known. The second benchmark allowed the participants to calibrate their models to the experimental results. Section 4.3.3.3.2 discusses the different material models that were tested for the concrete:

- Karagozian & Case (K&C)
- Holmquist, Johnson, and Cook using empirical input parameters (Empirical HJC)
- Holmquist, Johnson, and Cook using input parameters taken directly from the original model documentation (Original HJC)

4.4.1.1 Phase III Benchmark I

The Empirical HJC model showed promise during the first benchmark since an exact fit was generated to the triaxial concrete cylinder tests. Simulations using the HJC model were submitted to and presented at the first benchmark workshop. Results from the missile impact experiments revealed that the HJC model accrued far too much damage in the simulation as seen by comparing Figure 4-59 to Figure 4-60. The simulation showed that the entire impact surface of the 170 m/s test should have been cracked, the rebar should have plastically deformed, and the missile should have penetrated up to 50 mm. The missile impact experiments revealed that the impact face was only slightly cracked with little permanent deformation. After the first benchmark, further simulations using the HJC model revealed that the set of parameters used to define the model and match the triaxial concrete testing data was not unique. At least two more sets of parameters were found that fit the triaxial concrete testing data, neither of which mimicked the same damage that occurred in the missile impact experiments.

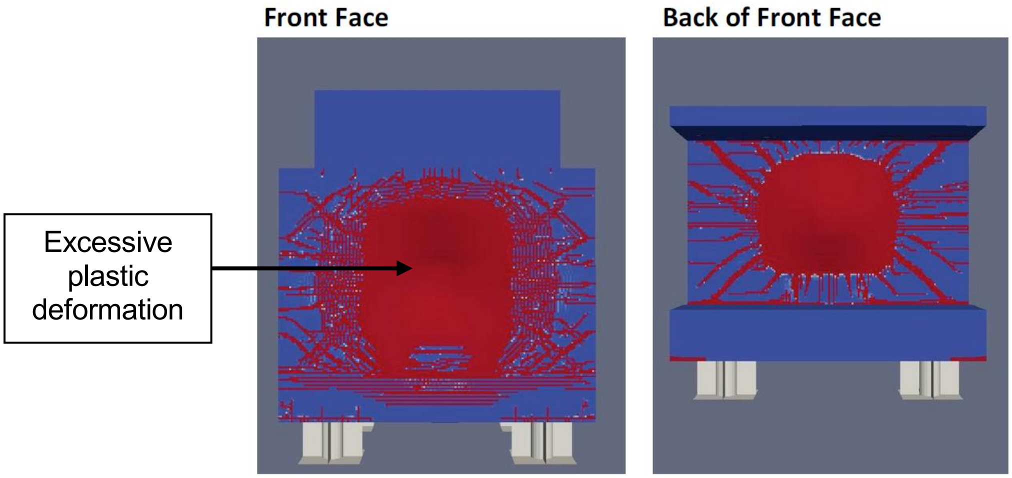

Figure 4-59: IRIS III mockup damage from the 170 m/s missile impact utilizing the HJC model showing too much damage accumulation. Fully damage concrete is red.

Figure 4-60: Experimental damage on the back face of the impact wall from the 170 m/s missile impact

4.4.1.2 Phase III Benchmark II

The goal of the IRIS program was to develop modeling tools and techniques so that future simulations will give precise results using material models developed without prior knowledge of experimental results. Therefore, the results of the IRIS simulations using the material models Karagozian & Case, Empirical HJC, and Original HJC are compared to the experimental in this section. Results are compared in selected few points on the mockup during the 170 m/s missile test to determine which models more closely represent the experimental results. Many of the figures present data filtered below 200 Hz to omit numerical noise; more information on post-processing techniques is presented in Section 4.4.3 .

Figure 4-61 shows the displacement of transducer D01 (immediately behind the missile impact point) for the 170 m/s missile test. The mockup experiment resulted in a peak displacement of 20 mm with a permanent displacement of ~12 mm. The Empirical HJC model predicted a peak displacement of ~95 mm with a permanent displacement of ~73 mm. The Original HJC model predicted a peak displacement of ~10 mm with a permanent displacement of ~1 mm. The K&C model predicted a peak displacement of ~10 mm with a permanent displacement of ~8 mm. Figure 4-62 shows the strain for strain gage GS3 (on the back of the impact face halfway between the missile impact point and the top of the front face). The mockup experiment resulted in a peak strain of 470 $\mu\varepsilon$ with a permanent strain of ~275 $\mu\varepsilon$. The Empirical HJC model predicted a peak strain of over 12,000 $\mu\varepsilon$ and a permanent strain of almost 2,000 $\mu\varepsilon$. Figure 4-63 shows the strain for strain gage GS3 excluding the Empirical HJC model. The K&C model predicted a peak strain of 467 $\mu\varepsilon$, almost identical to the peak strain value of the experiment. The Original HJC model predicted little strain for gage GS3 and predicted the opposite sign for the strain than what occurred in the experiment. Similarly for strain gages SG1 and SG2 shown in Figure 4-64 and Figure 4-65, the K&C model most accurately predicted the experimental results and the Empirical HJC model drastically over-estimated the peak and permanent strains.

From the comparisons presented in Figure 4-61 through Figure 4-65, the most accurate concrete model in terms of displacements and strains on the impact face of the concrete is the K&C model. Therefore, all subsequent information will be presented comparing the K&C model results with the experimental results, and the results from the HJC models will not be presented.

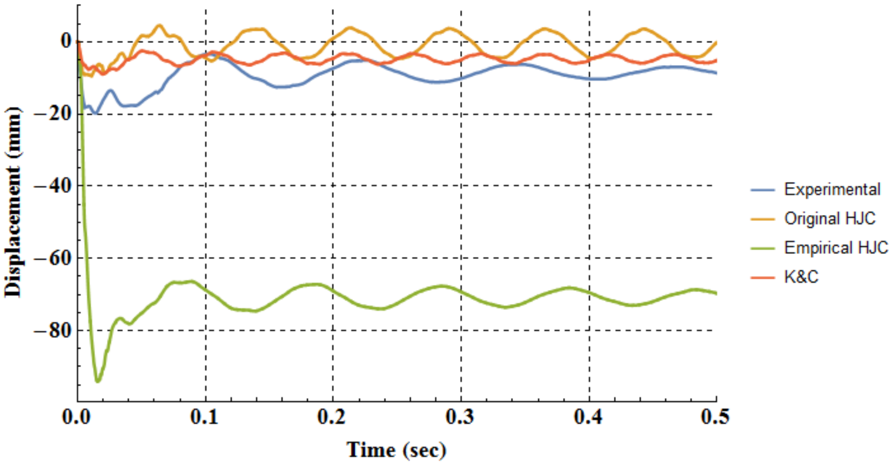

Figure 4-61: Displacement of transducer D01 (immediately behind the missile impact) for the 170 m/s missile test (sub 200 Hz).

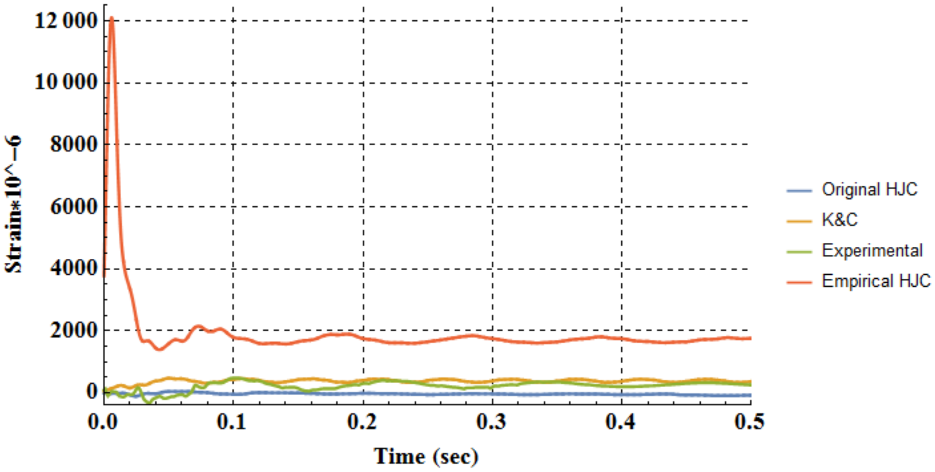

Figure 4-62: Strain gage GS3 (impact face of concrete halfway between the missile impact point and the top of the front face) for the 170 m/s missile test (sub 200 Hz).

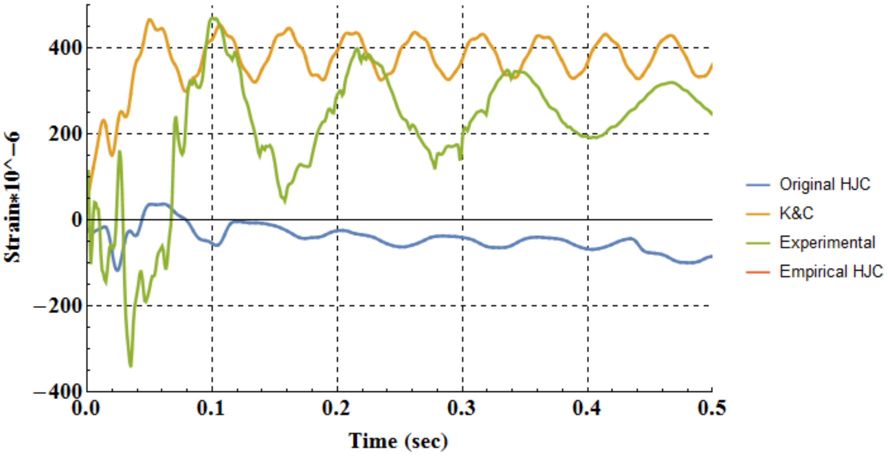

Figure 4-63: Strain gage GS3 for the 170 m/s missile test excluding Empirical HJC model (sub 200 Hz).

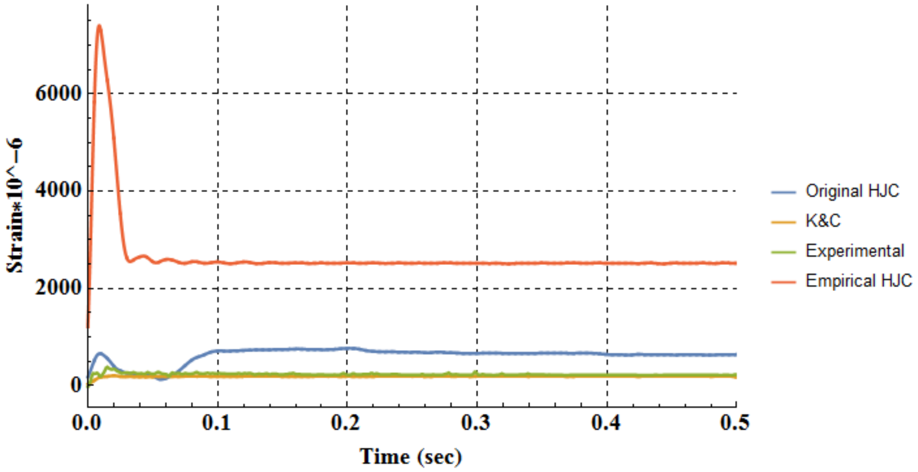

Figure 4-64: Strain gage GS1 for the 170 m/s missile test (sub 200 Hz).

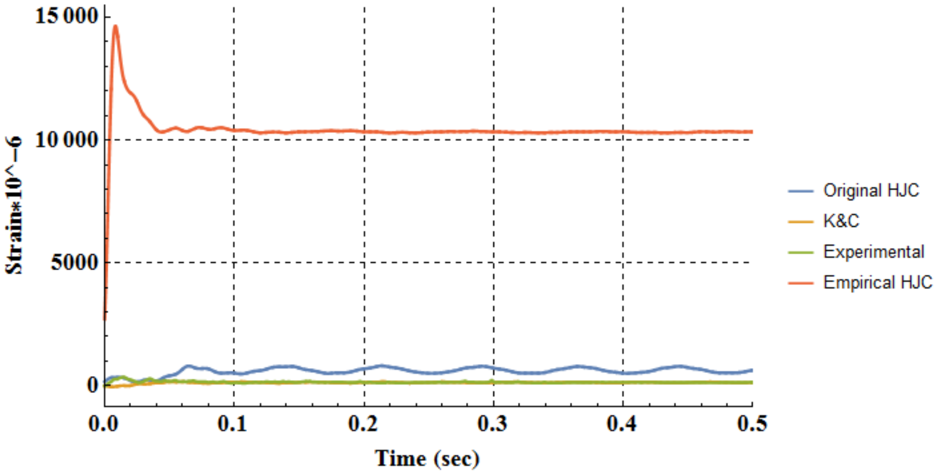

Figure 4-65: Strain gage GS2 for the 170 m/s missile test (sub 200 Hz).

4.4.2 Modal Analysis

A modal analysis of the Phase III mockup was performed and is presented in this section. The mesh was altered from a contiguous 6-noded 3D hexahedral and 4-noded 2D shell element mesh to a contiguous 4-noded 3D TETRA10 and 3-noded Tri6 shell element mesh. The new mesh based on tetrahedral and triangular elements is shown in Figure 4-66. The nodes on the base of the mockup were fixed in space as the only boundary condition. All materials were considered homogeneous, isotropic, and elastic for the modal analysis.

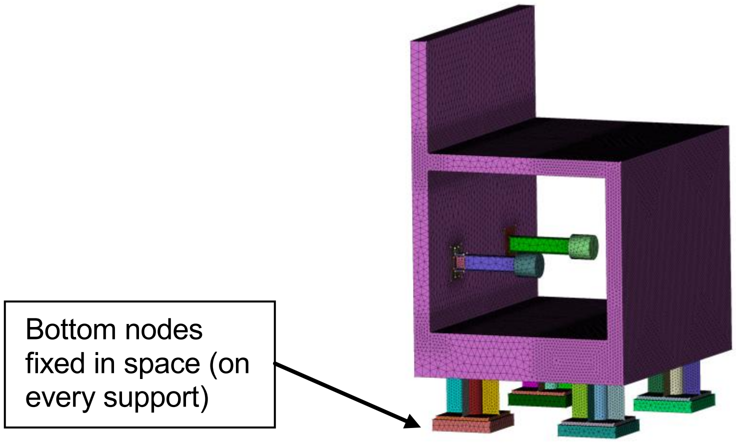

Figure 4-66: Phase III mockup based on tetrahedral 3D elements and triangular 2D shell elements.

The mode numbers and frequency of the modes are presented in Table 4-5. Images of the modal analysis are presented in Figure 4-67 through Figure 4-77.

Table 4-5: Modal analysis mode numbers and frequencies.

Mode Number	Frequency (Hz)	Mode Number	Frequency (Hz)
1	17.2	12	101.3
2	19.0	13	110.6
3	22.1	14	124.5
4	40.1	15	133.5
5	43.8	16	156.4
6	53.0	17	170.8
7	57.4	18	179.6
8	59.5	19	186.0
9	64.6	20	201.5
10	71.7	21	204.8
11	96.8	22	210.7

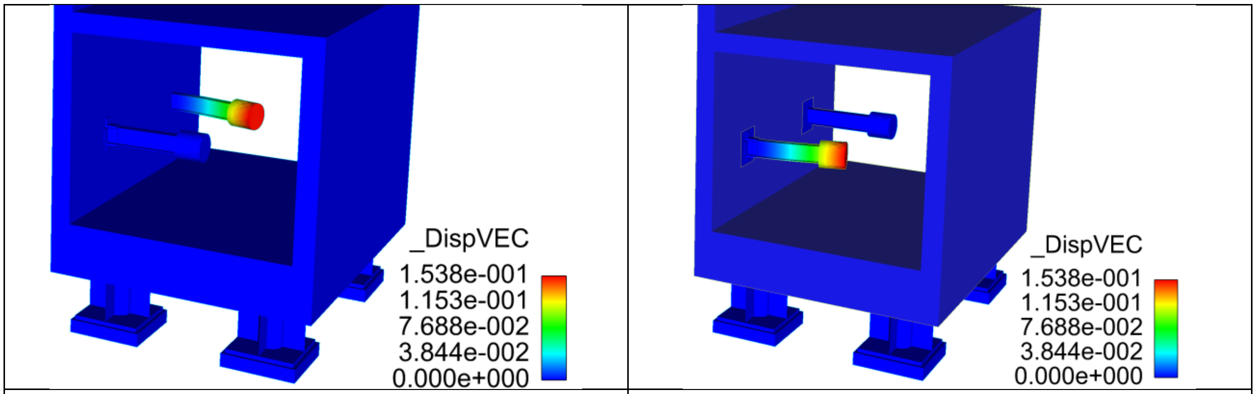

Visual displacement factor: 1000

Visual displacement factor: 1000

Figure 4-67: (Left) Mode 1: 17.2 Hz, first bending mode of second I-beam. (Right) Mode 2: 19.0 Hz, first bending mode of first I-beam.

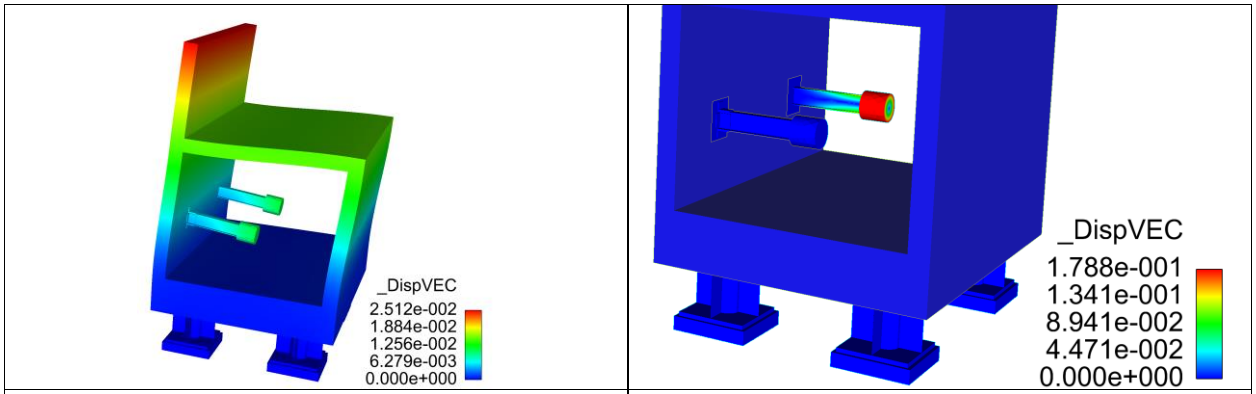

Visual displacement factor: 10000

Visual displacement factor: 100

Figure 4-68: (Left) Mode 3: 22.1 Hz, skewing mode of concrete box section. (Right) Mode 4: 40.1 Hz, first torsional mode of second I-beam.

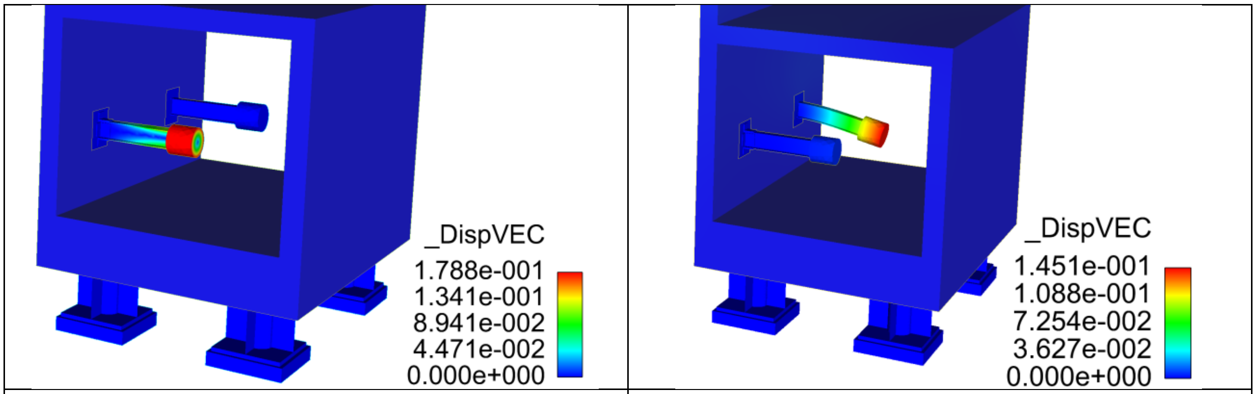

Visual displacement factor: 100	Visual displacement factor: 1000

Figure 4-69: (Left) Mode 5: 43.8 Hz, first torsional mode of first I-beam. (Right) Mode 6: 53.0 Hz, first bending mode in orthogonal direction of second I-beam.

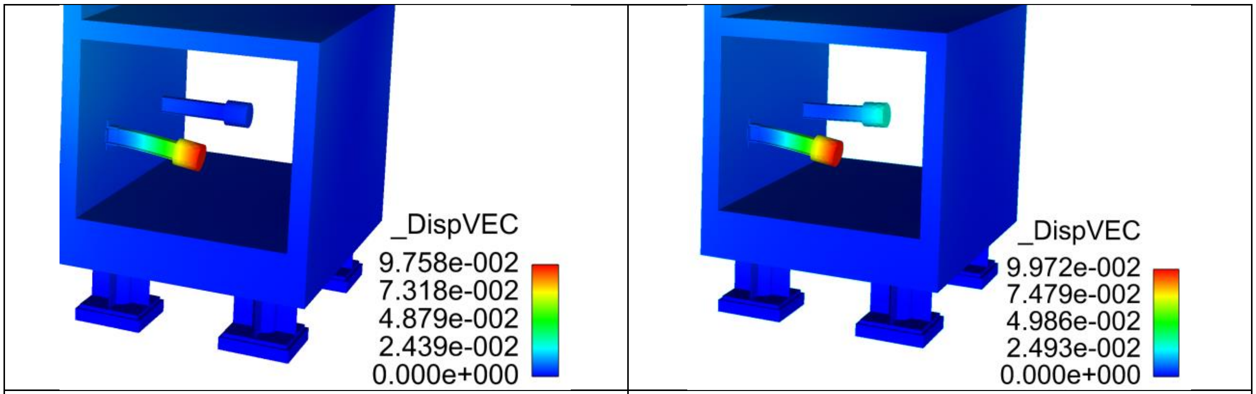

Visual displacement factor: 1000	Visual displacement factor: 1000

Figure 4-70: (Left) Mode 7: 57.4 Hz, first bending mode in orthogonal direction of first I-beam. (Right) Mode 8: 59.5 Hz, first bending mode in orthogonal direction of first I-beam.

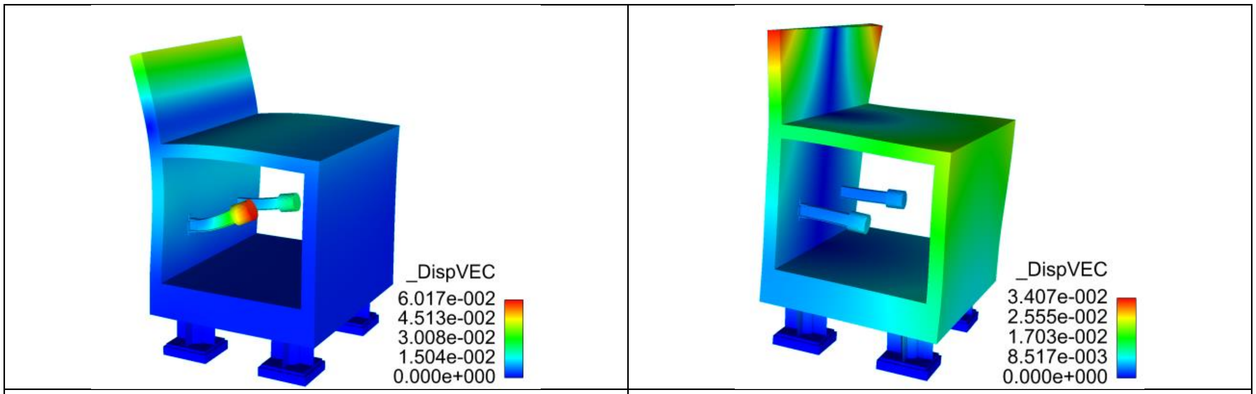

Visual displacement factor: 5000	Visual displacement factor: 5000

Figure 4-71: (Left) Mode 9: 64.6 Hz, bending mode of concrete cross-section combined with bending mode of first beam. (Right) Mode 10: 71.7 Hz, twisting mode of concrete back wall.

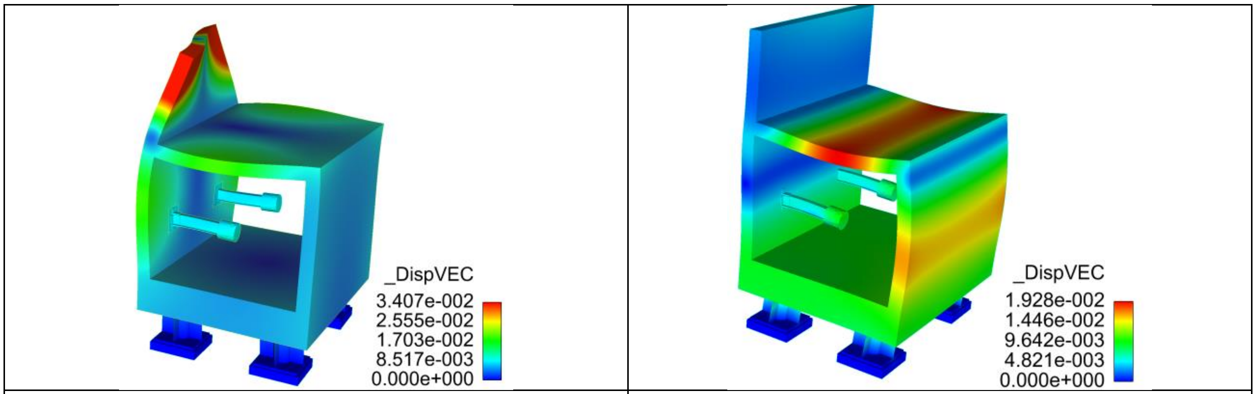

Visual displacement factor: 5000	Visual displacement factor: 5000

Figure 4-72: (Left) Mode 11: 96.8 Hz, twisting mode of concrete back wall. (Right) Mode 12: 101.3 Hz, higher order bending of concrete cross-section.

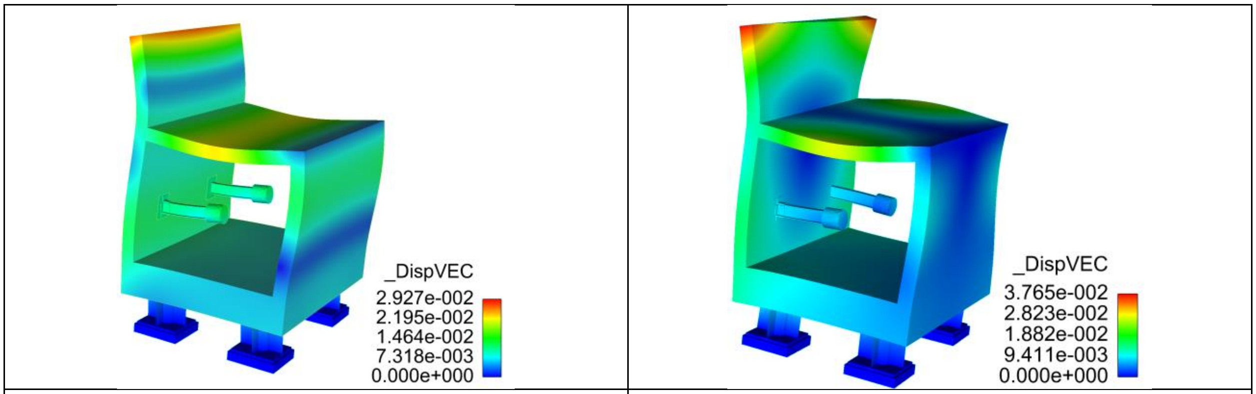

Visual displacement factor: 5000

Visual displacement factor: 5000

Figure 4-73: (Left) Mode 13: 110.6 Hz, higher order bending of concrete cross-section. (Right) Mode 14: 124.5 Hz, concrete top surface and back surface twisting in opposite directions.

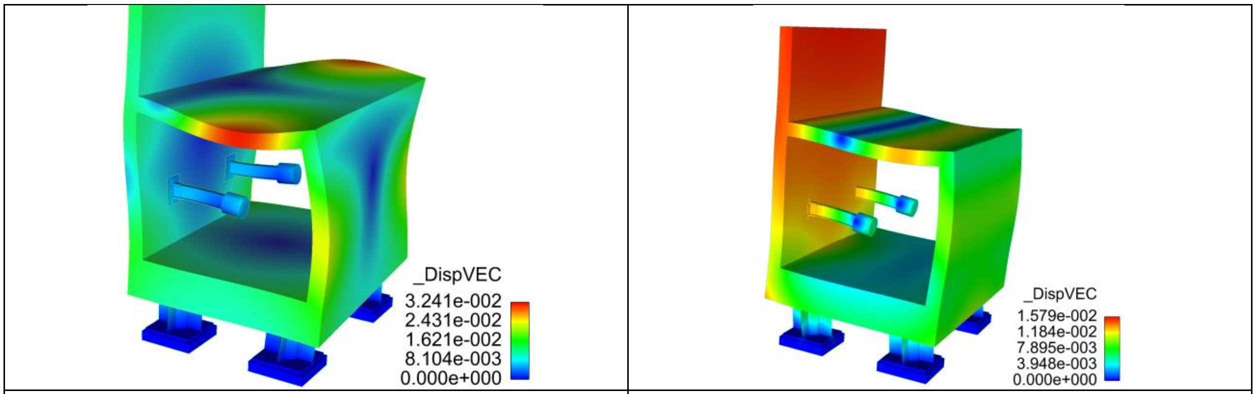

Visual displacement factor: 5000

Visual displacement factor: 5000

Figure 4-74: (Left) Mode 15: 133.5 Hz, concrete top surface twisting. (Right) Mode 16: 156.4 Hz, high order bending of concrete cross-section.

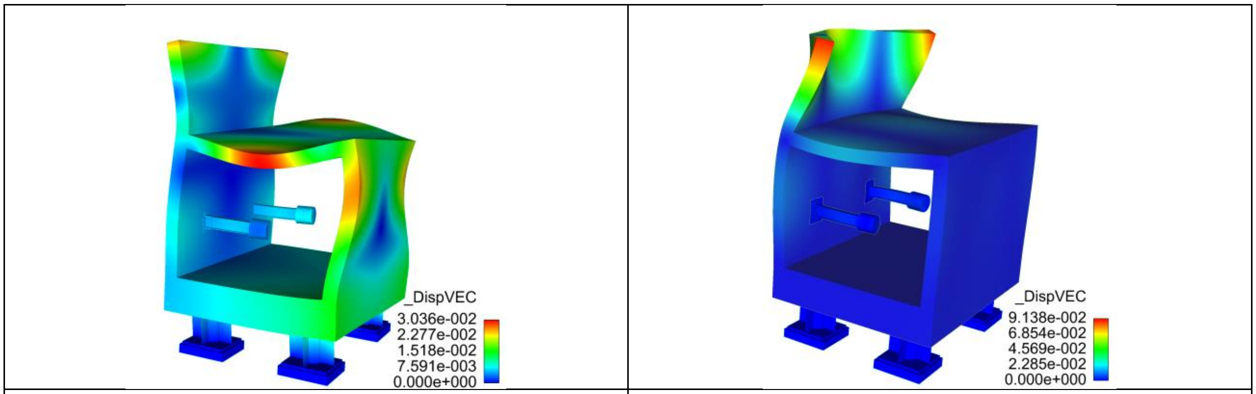

Visual displacement factor: 5000

Visual displacement factor: 5000

Figure 4-75: (Left) Mode 17: 170.8 Hz, concrete top, back, and front surface twisting. (Right) Mode 18: 179.6 Hz, combined twisting of concrete back surface with high order bending of top surface in same direction.

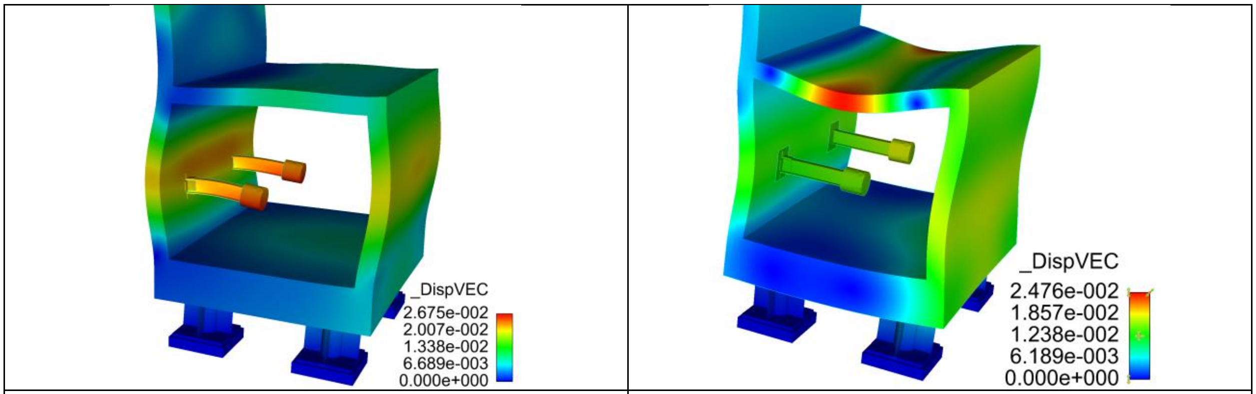

Visual displacement factor: 5000

Visual displacement factor: 5000

Figure 4-76: (Left) Mode 19: 186.0 Hz, high order bending of concrete cross-section combined with bending of I-beams. (Right) Mode 20: 201.5 Hz, high order bending of top surface.

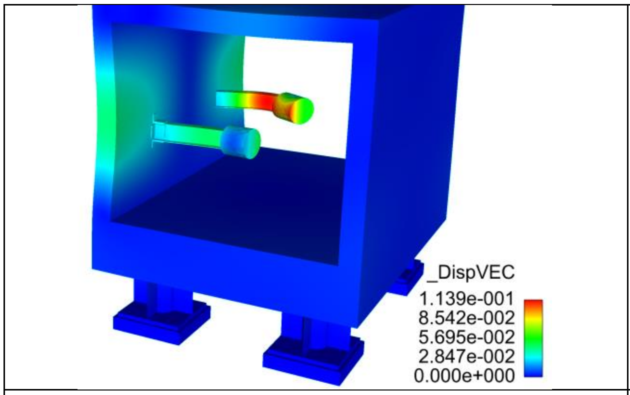	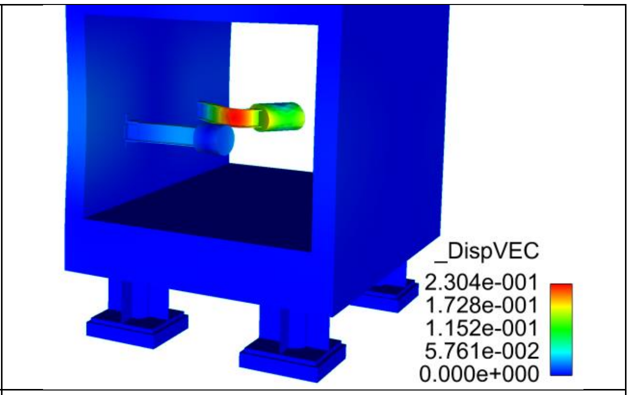
Visual displacement factor: 1000	Visual displacement factor: 1000

Figure 4-77: (Left) Mode 21: 204.8 Hz, second bending mode of second I-beam. (Right) Mode 22: 210.7 Hz, second bending mode of second I-beam.

4.4.3 Post-Processing Technique

Data is presented herein as either unfiltered or filtered. Data points were recorded at a rate of 100,000 Hz. Some data, namely accelerations but others as well, are filtered using Wolfram's *Mathematica* (Wolfram Mathematica 11.2 2018) low-pass from filter to remove numerical noise and high-frequency accelerations that were not of import to the organizing committee. Other data is filtered using a moving average to reduce noise. The typical moving average in this report averages 50 data points or 0.5 ms of data. Data filtering was discussed in detail by all teams present at the benchmark workshop in June 2017. Much of the noise in the signals was attributed to numerical error inherent in finite element analysis. Filtering the noise below a certain frequency eliminates numerical noise.

The teams at the 2017 benchmark meeting agreed that ~250 Hz was the proper frequency to filter out numerical noise for structural elements. Analysis of the results from the simulations indicated that ~1000 Hz should be the cutoff frequency for the missile, force summation immediately in the vicinity of missile impact, and accelerations. Figure 4-78 shows the acceleration of the rear of the missile during impact with raw data, data filtered below 1000 Hz, and data filtered below 250 Hz. The raw acceleration data oscillates between 20,000 m/s^2 and -5000 m/s^2; this is most likely due to numerical noise in the simulation. One possible source of noise could be individual elements folding as the nose of the missile contracts into its failed 'accordion' structure. Filtering the data below 1000 Hz results in a smooth curve with peak acceleration of ~7,500 m/s^2 and no oscillations as are found in the raw data. Filtering the data below 250 Hz also results in a smooth curve, but the curve does not accurately represent the raw data. For example, the sub-250 Hz curve has an initial acceleration of ~3,700 m/s^2 while the missile had not yet impacted the concrete. Therefore, data analysis of the acceleration of the rear missile indicates that the appropriate frequency to filter data for the missile, force summation immediately in the vicinity of missile impact, and accelerations is 1000 Hz. Structural elements such as reaction forces of the mockup supports or displacements of various positions are filtered under 250 Hz.

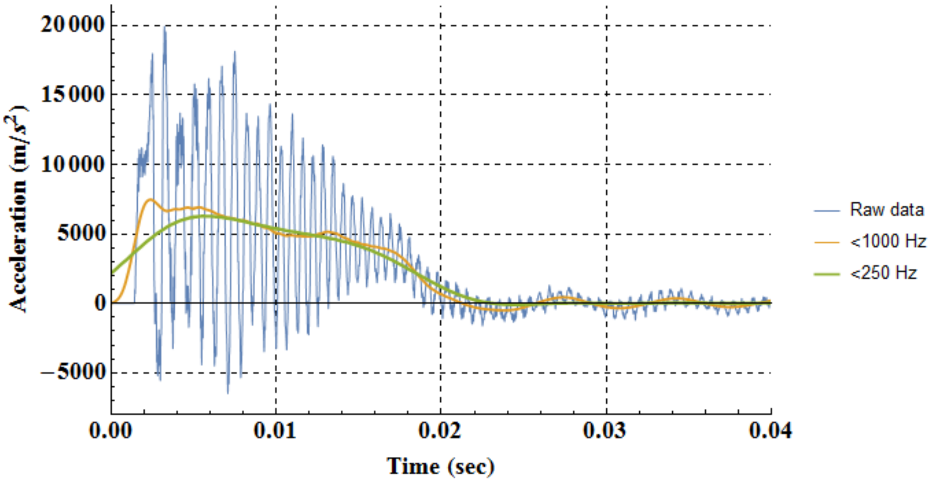

Figure 4-78: Acceleration of the rear of the missile during impact with raw data, data filtered below 1000 Hz, and data filtered below 250 Hz.

4.4.4 90 m/s Impact Velocity Results

This section contains results for the 90 m/s impact velocity test. Select results comparing simulation data vs experimental data is shown in this section. The complete collection of simulation data is included in the appendices.

4.4.4.1 Missile Results

The results of the missile are separated into general missile crushing results and time histories of the missile velocity, acceleration, impulse, and force pushing against the mockup.

4.4.4.1.1 Crushing Results

The results of the simulated 90 m/s missile impact are shown in Table 4-6 and Figure 4-79. These values were obtained using analyst judgement to determine the transition from crushed to uncrushed. The experimental crushed missiles are shown in Figure 4-80.

Table 4-6: 90 m/s Missile Impact Crush Results.

	Simulated Lengths	**Experimental Lengths**
Original length (including hemispherical head)	1625 mm	1625 mm
Total length after crush	1016 mm	851 mm
Crushed length H_T	262 mm	160 mm
Non-crushed length L_T	754 mm	691 mm

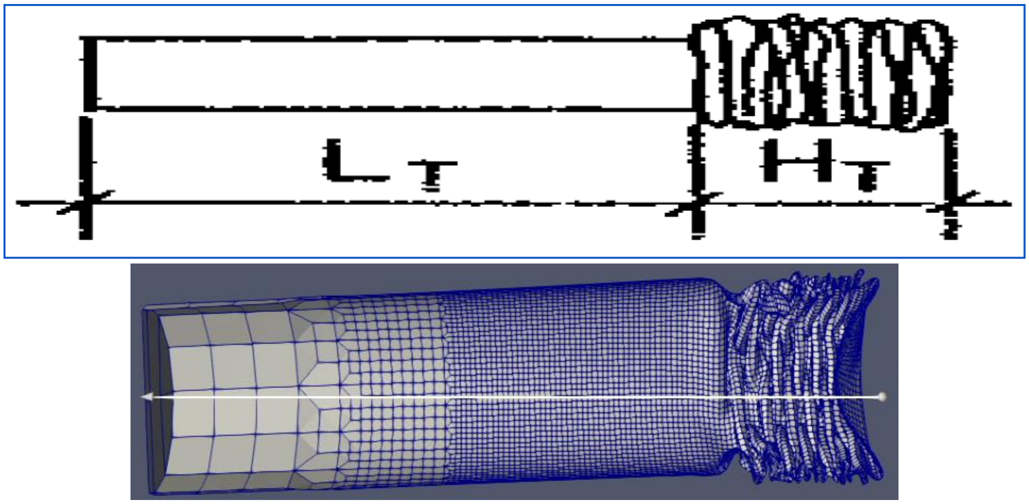

Figure 4-79: Simulated crushed 90 m/s missile.

Figure 4-80: Experimental crushed missiles. Left to right: 170 m/s, 90 m/s, 90 m/s.

4.4.4.1.2 Time Histories

The time histories of missile end velocity and acceleration are presented in Figure 4-81 and Figure 4-82. The missile velocity and accelerations cut off at 0.05 seconds since the missile was omitted from the simulation at 0.05 seconds. The contact force of the missile against the mockup is presented in Figure 4-83, and the contact force of the missile against a rigid target is presented in Figure 4-84. Similar behavior and peak forces for both the 0.5 ms averaged data and the <1000 Hz data indicate that the mockup behaved much as a rigid target for the 90 m/s missile.

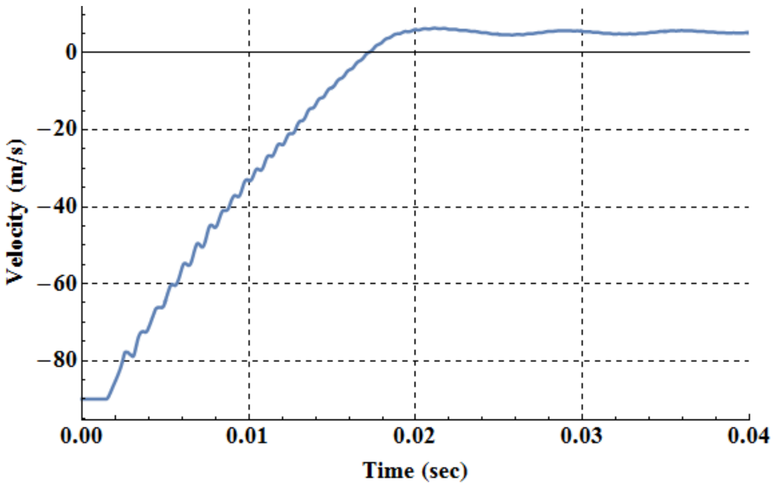

Figure 4-81: 90 m/s missile end velocity.

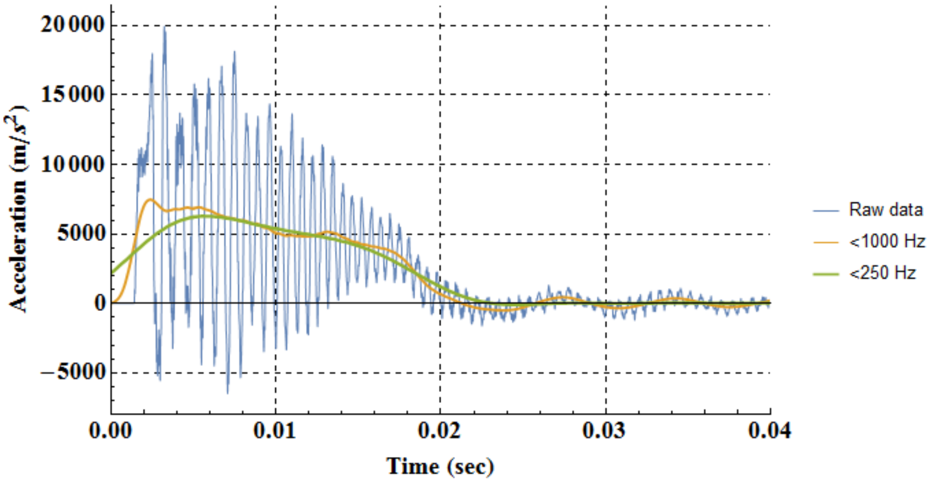

Figure 4-82: 90 m/s missile end acceleration.

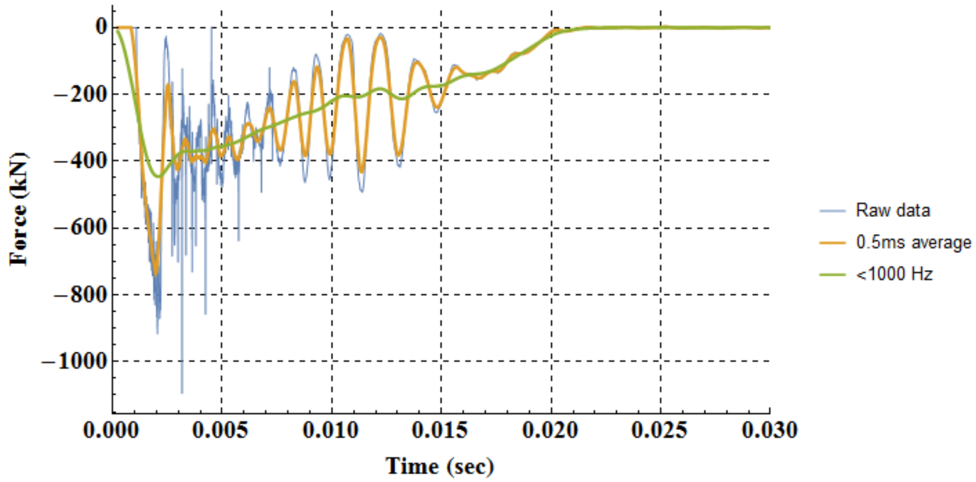

Figure 4-83: Force of the 90 m/s missile against the mockup.

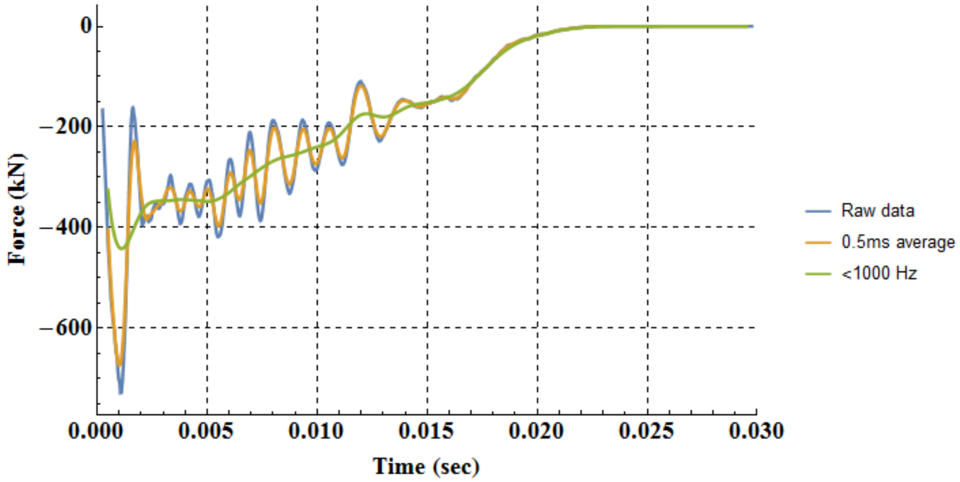

Figure 4-84: Force of the 90 m/s missile against a rigid target.

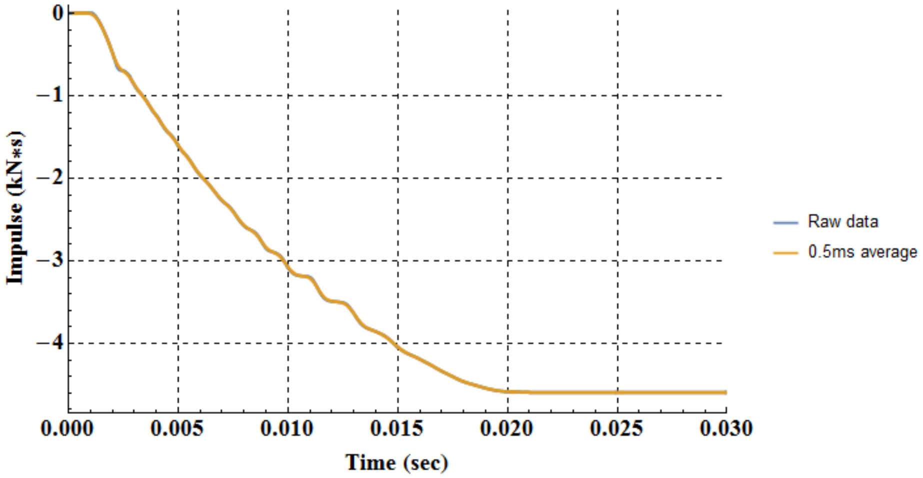

Figure 4-85: Impulse of the 90 m/s missile against the mockup.

4.4.4.2 Mockup Results

4.4.4.2.1 Global Results

Results from the 90 m/s missile impact simulation are shown in Figure 4-86 through Figure 4-90. The support pedestals and missile have been removed to better see the concrete damage. A damage factor of 2.0 indicates cracked concrete.

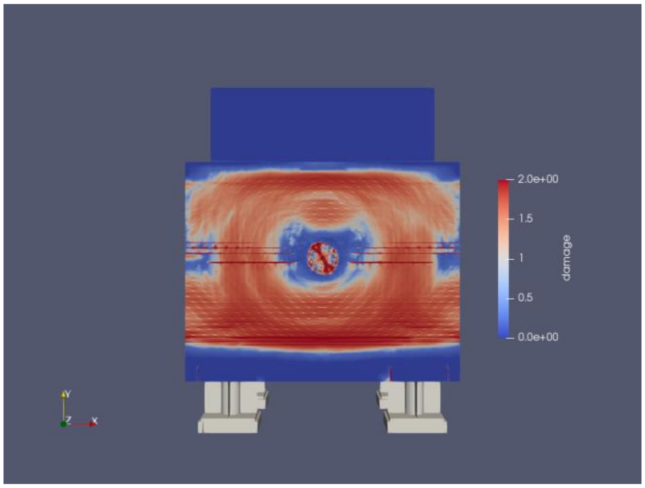

Figure 4-86: Damage on the impact face of the 90 m/s impact mockup.

The impact face of the concrete suffered crack damage immediately where the missile impacts the concrete. Flexure cracks are evident through the midheight of the impact face and likely at the base where the impact face meets the bottom slab.

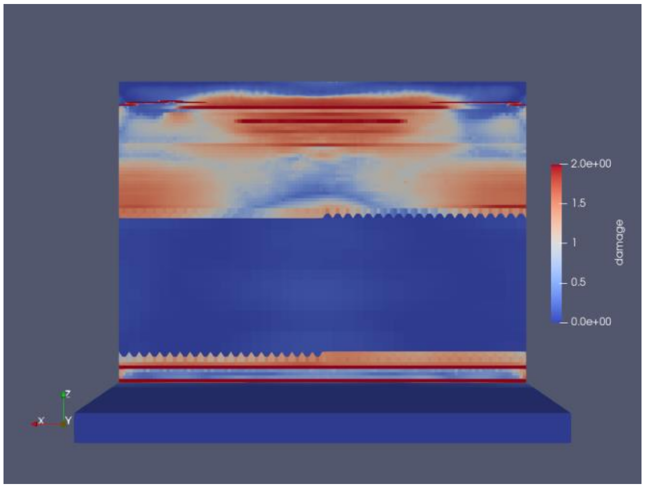

Figure 4-87: Top view of damage of the 90 m/s impact mockup.

The top of the mockup suffered cracks damage due to bending moments from the impact. A jagged row of elements show a sudden change in damage evident from the sudden color change from red-white-blue to solid blue. This row of elements was the transition between “refined” and “coarse” meshes, and the lack of damage in the “coarse” mesh was likely due to there being insufficient damage accrual in the larger elements.

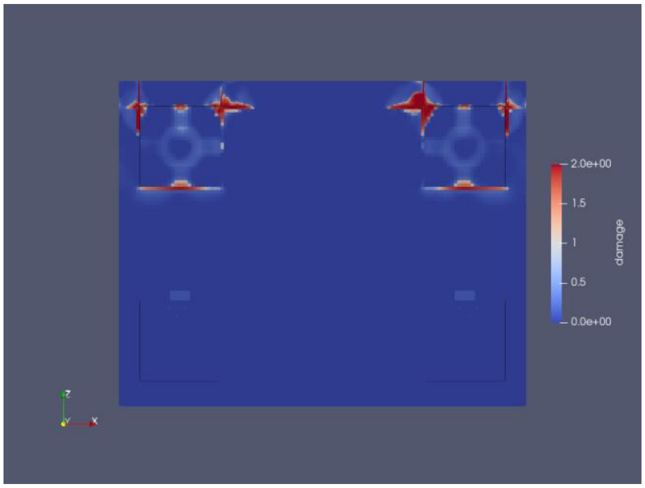

Figure 4-88: Bottom view of damage of the 90 m/s impact mockup. The edge with damage is the impact side of the mockup.

The bottom of the mockup suffered crack damage due to bending moments and possibly due to stress concentrations at the divots where the supports were attached to the concrete. The pattern with a damage of ~1 in the divots mirrors the shape of the supports suggesting large stress concentrations through the webbing and central pipe structure of the supports.

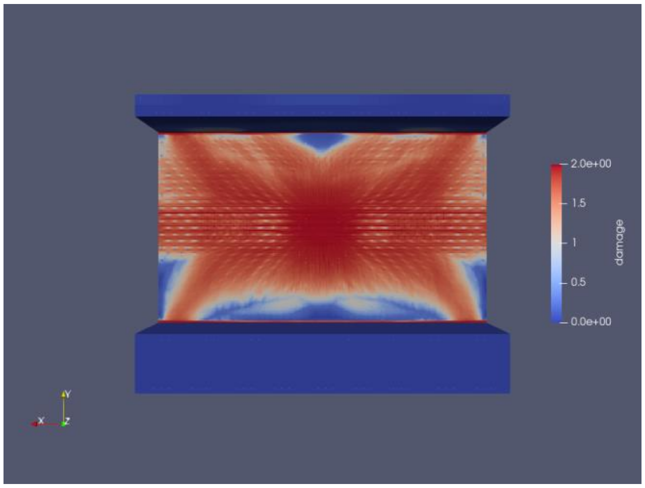

Figure 4-89: Back side of the impact face of the 90 m/s impact mockup.

The back side of the impact face suffered crack damage immediately in the vicinity of the missile impact and in an ‘X’ pattern from corner to corner.

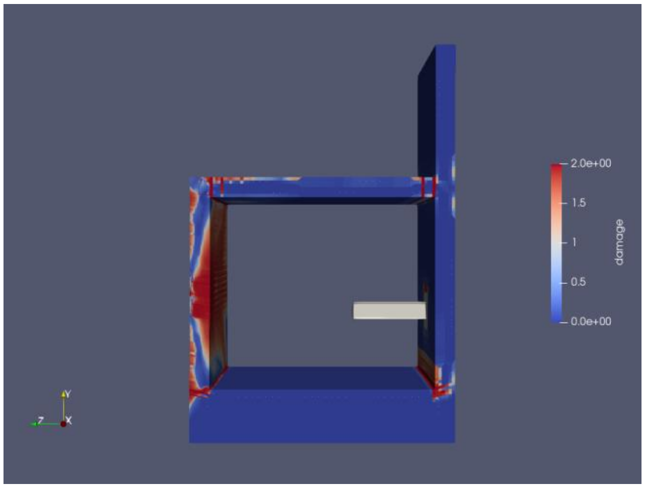

Figure 4-90: Half-cut side view of damage in the 90 m/s impact mockup.

Figure 4-90 shows half of the mockup from the side with damage originating from the center. The side view of the damage indicates that the largest concentrations of damage are immediately behind the missile impact and where the impact face meets the base of the mockup.

The final displacements of the mockup are shown in Figure 4-91 through Figure 4-93 (units are in mm).

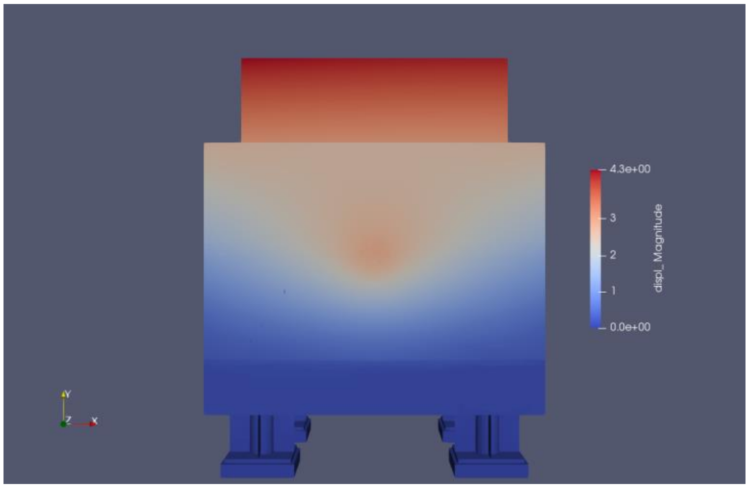

Figure 4-91: Front view of the final displacements of the 90 m/s mockup.

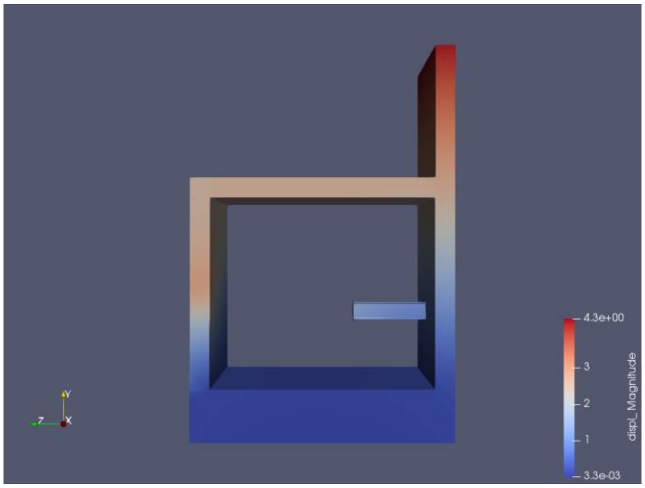

Figure 4-92: Side view of the final displacements of the 90 m/s mockup.

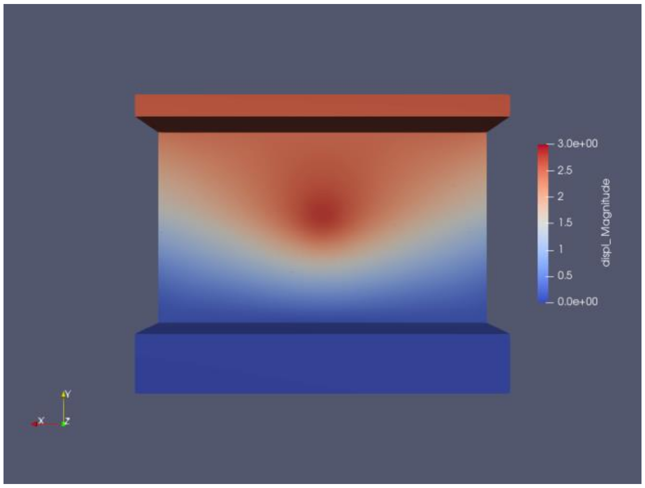

Figure 4-93: Rear side of the impact wall's final displacements in the 90 m/s mockup.

4.4.4.2.2 Reaction Forces at Supports

The Y-direction (vertical) reaction forces under each support are shown in Figure 4-94 through Figure 4-97. Peak reaction forces for each support are presented in Table 4-7. There is a notable difference between the unfiltered and filtered reaction forces in both frequency/oscillations and peak force.

Table 4-7: Peak reaction forces during the 90 m/s impact.

Support Location	Peak Force Unfiltered (kN)	Peak Force <200 Hz (kN)	Peak Experimental (kN)
Front left	424	194	357
Front right	306	169	278
Rear left	284	164	94
Rear right	-212	-143	-107

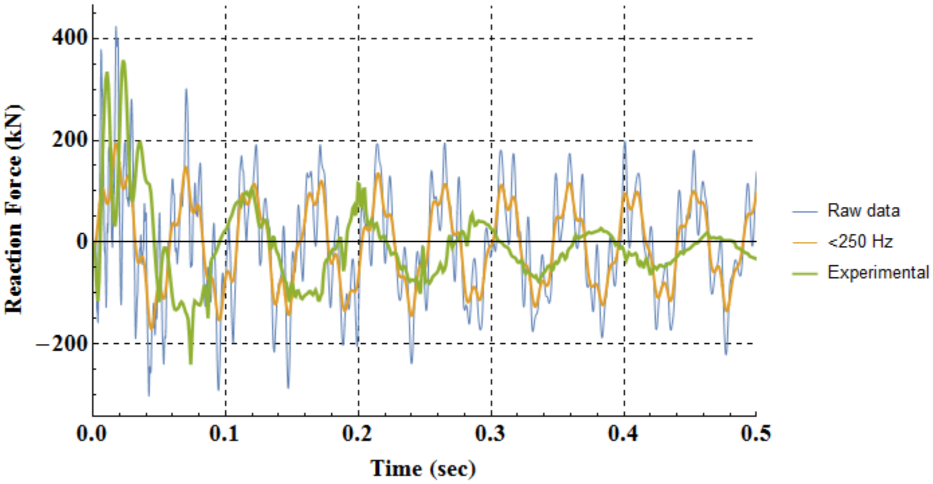

Figure 4-94: Vertical force under the front left support for the 90 m/s impact.

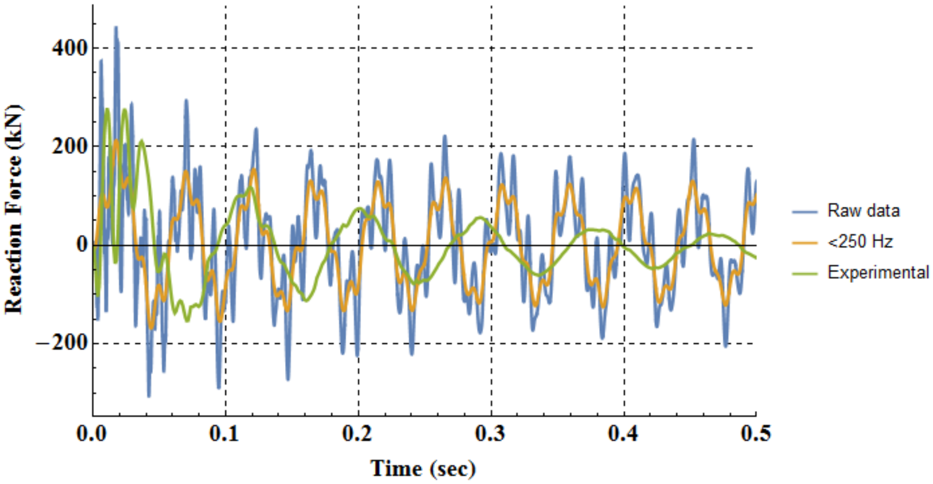

Figure 4-95: Vertical force under the front right support for the 90 m/s impact.

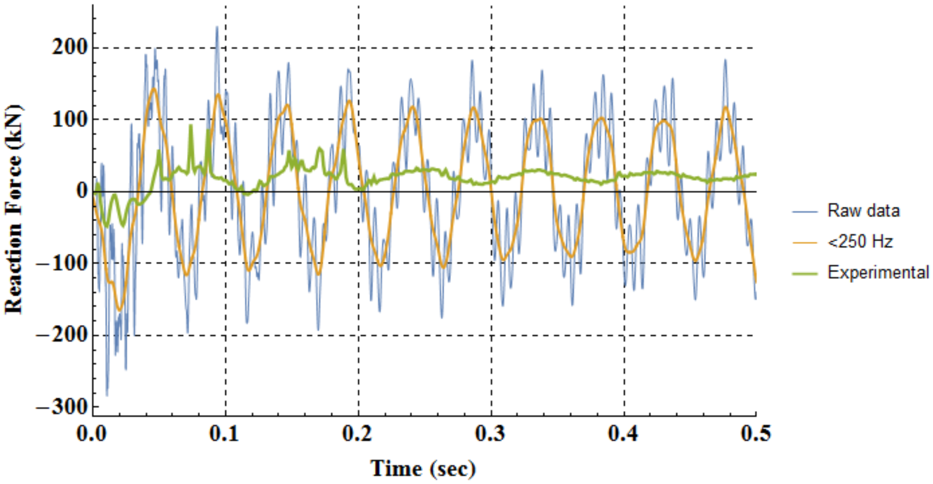

Figure 4-96: Vertical force under the rear left support for the 90 m/s impact.

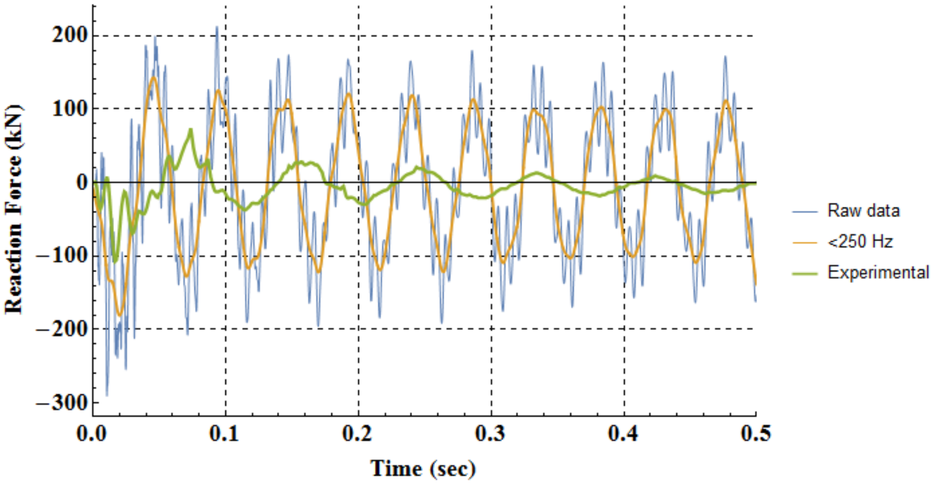

Figure 4-97: Vertical force under the rear right support for the 90 m/s impact.

Two examples of Z-reaction forces in line with the missile impact are shown in Figure 4-98 and Figure 4-99.

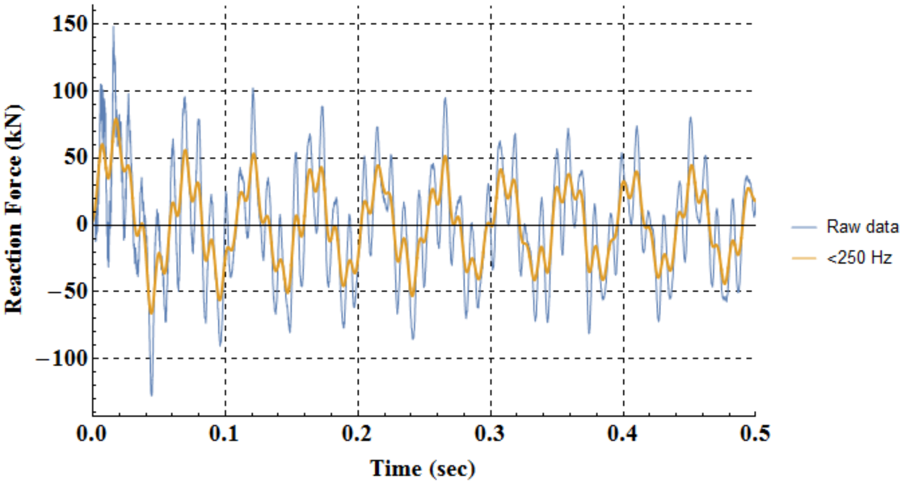

Figure 4-98: Z-reaction force (in line with the missile) under the front left support for the 90 m/s impact.

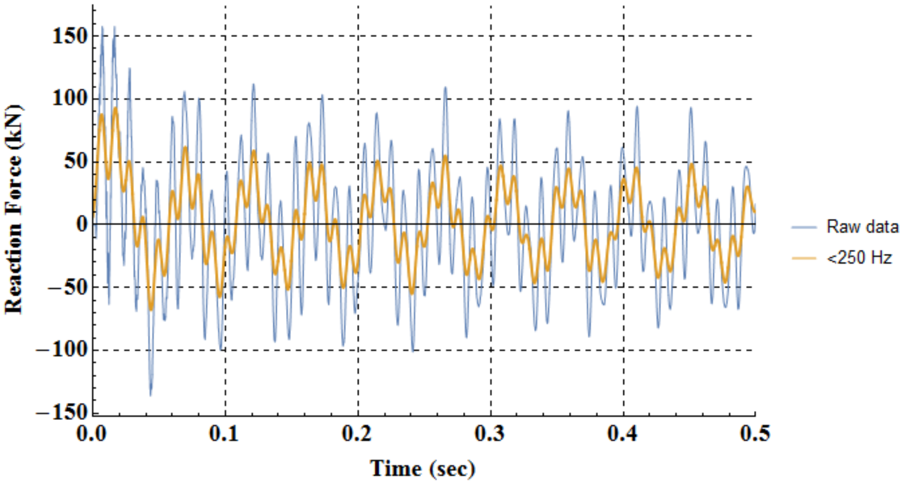

Figure 4-99: Z-reaction force (in line with the missile) under the rear left support for the 90 m/s impact.

4.4.4.2.3 Time Histories

Time histories of displacements, strains, accelerations are presented in Figure 4-100 through Figure 4-121. Accelerations are presented with unfiltered data and as filtered through a 250 Hz low-pass filter. In these figures, an apostrophe indicates a transducer on or around the welded I-beam. For example, D9 is the displacement transducer on the bolted I-beam and D9' is a displacement transducer near the welded I-beam. Some experimental data received from the IRIS organizing committee was unclear or faulty, likely due to instrumentation errors during impact. Therefore, experimental data for gage G2V is not included in the report.

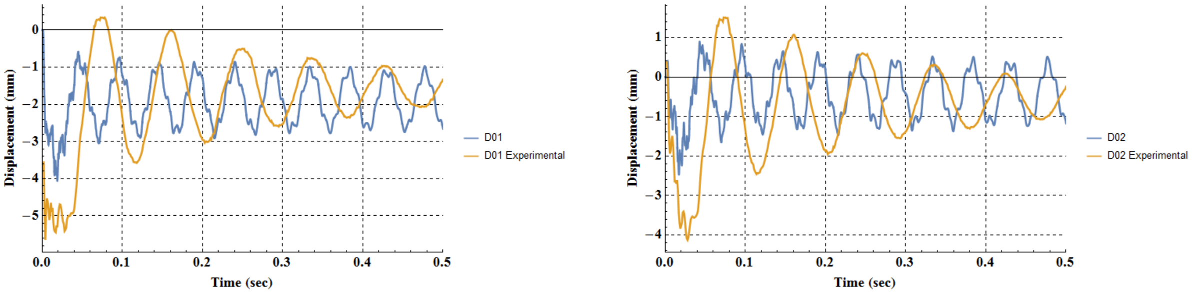

Figure 4-100: Displacement of 90 m/s transducers D01 and D02.

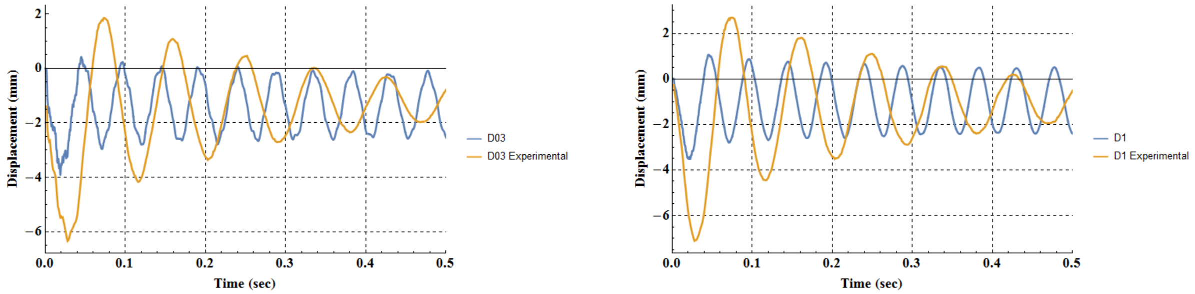

Figure 4-101: Displacement of 90 m/s transducers D03 and D1.

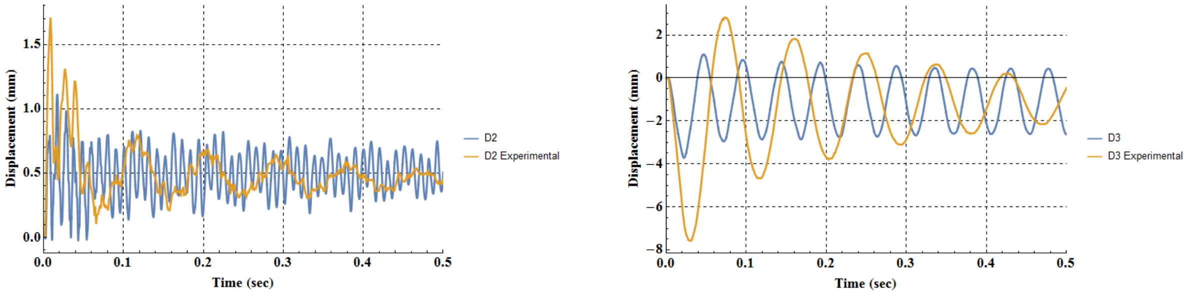

Figure 4-102: Displacement of 90 m/s transducers D2 and D3.

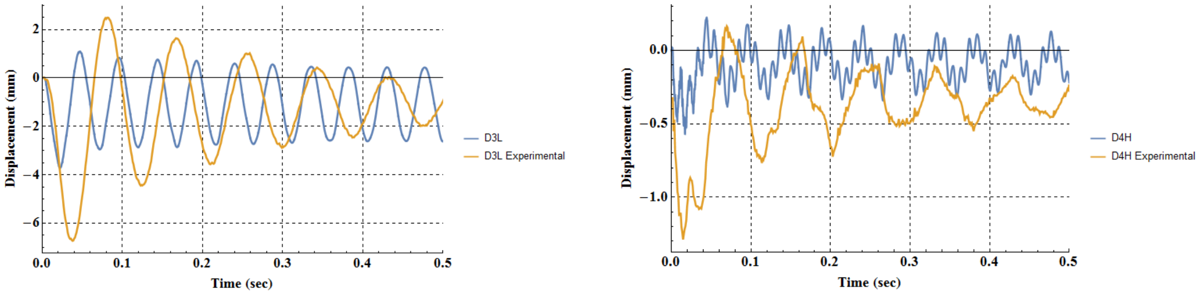

Figure 4-103: Displacement of 90 m/s transducers D3L and D4H.

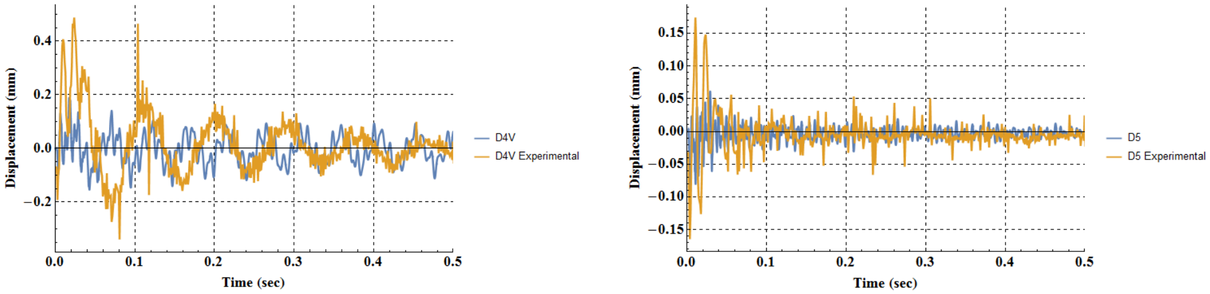

Figure 4-104: Displacement of 90 m/s transducers D4V and D5.

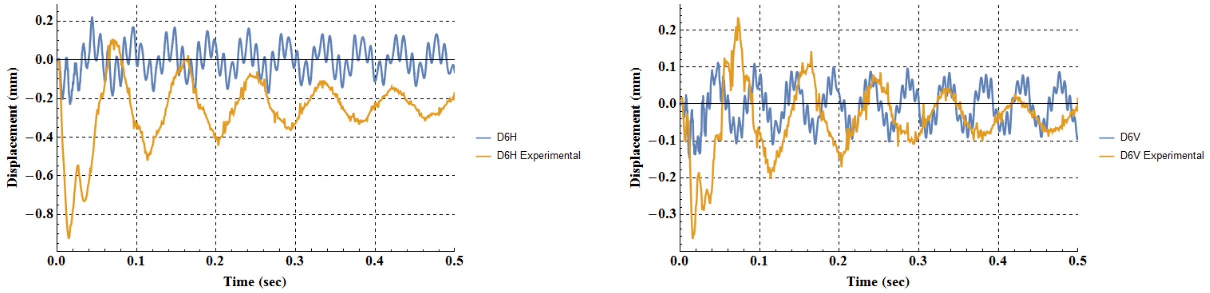

Figure 4-105: Displacement of 90 m/s transducers D6H and D6V.

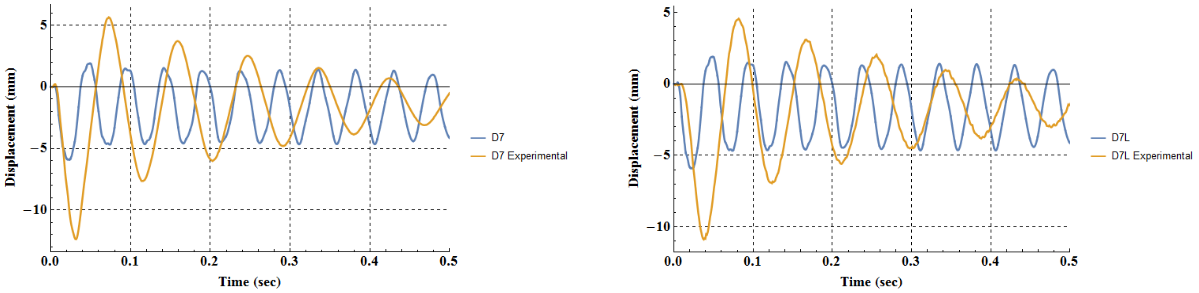

Figure 4-106: Displacement of 90 m/s transducers D7 and D7L.

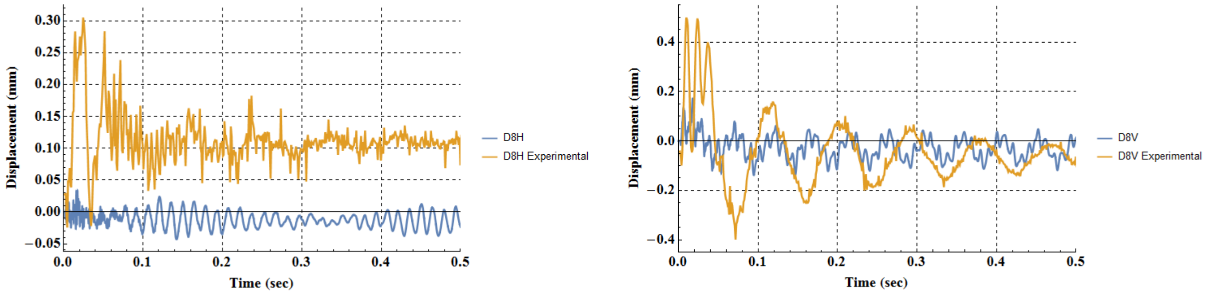

Figure 4-107: Displacement of 90 m/s transducers D8H and D8V.

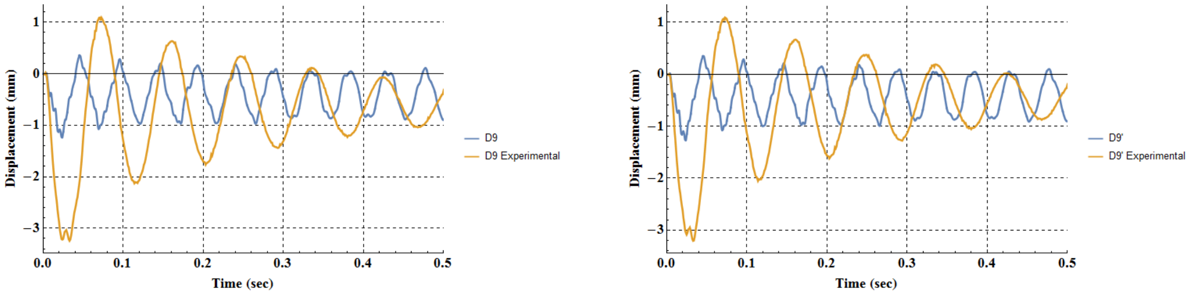

Figure 4-108: Displacement of 90 m/s transducers D9 and D9’.

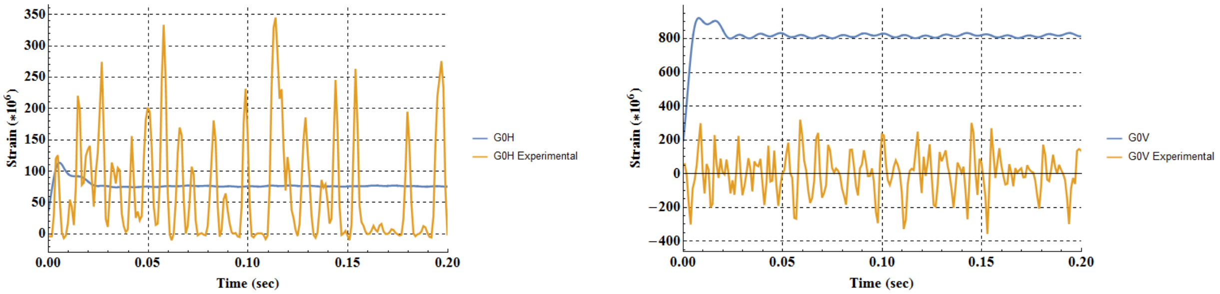

Figure 4-109: Strain of 90 m/s strain gages G0H and G0V.

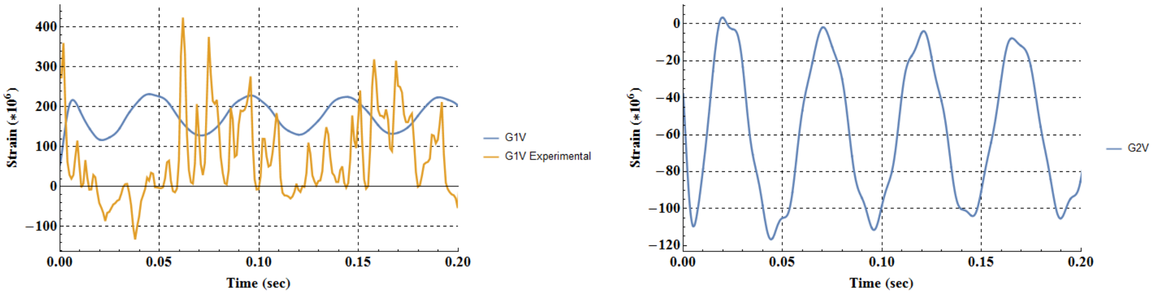

Figure 4-110: Strain of 90 m/s strain gages G1V and G2V.

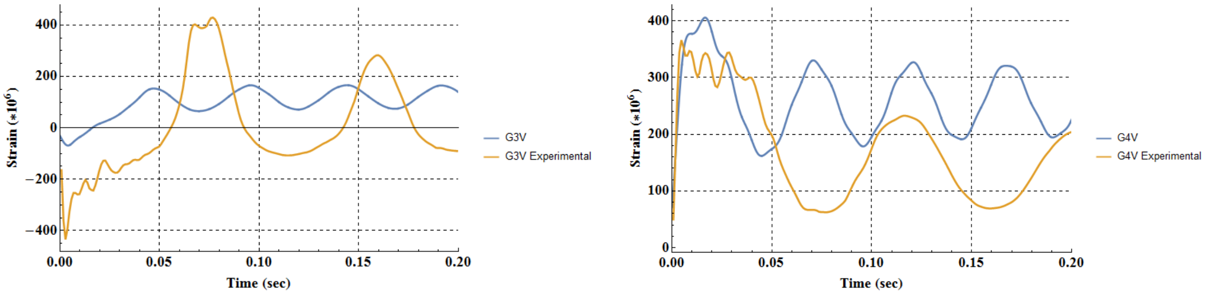

Figure 4-111: Strain of 90 m/s strain gages G3V and G4V.

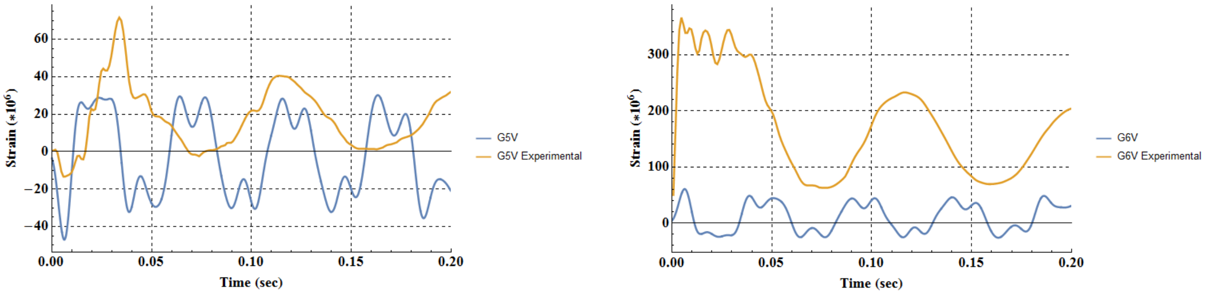

Figure 4-112: Strain of 90 m/s strain gages G5V and G6V.

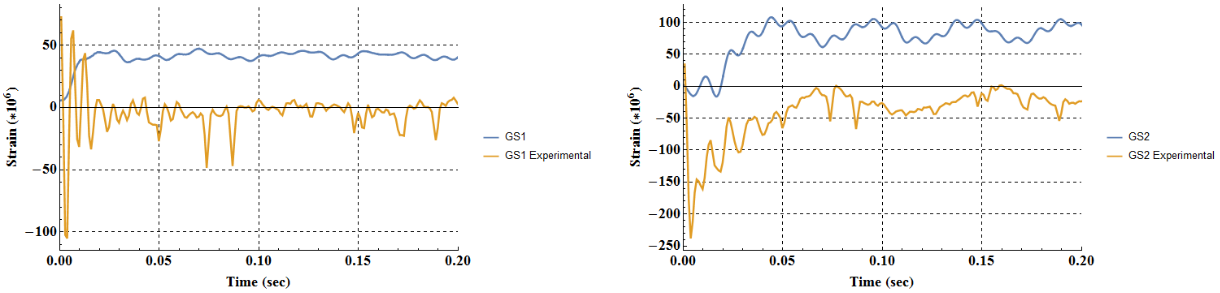

Figure 4-113: Strain of 90 m/s strain gages GS1 and GS2.

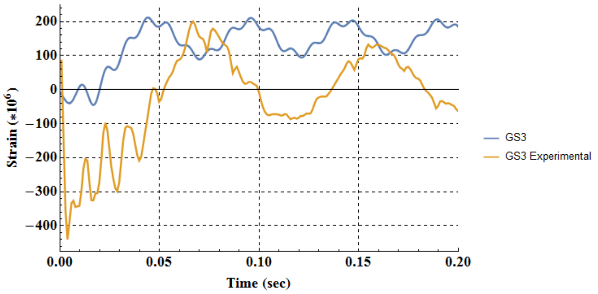

Figure 4-114: Strain of 90 m/s strain gage GS3.

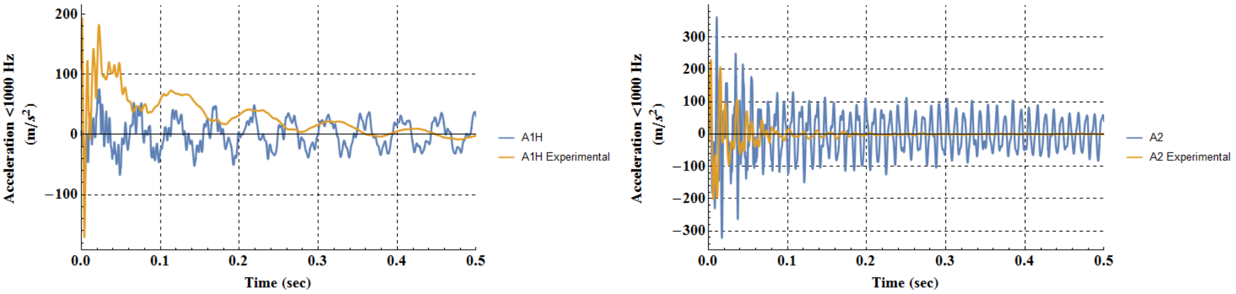

Figure 4-115: 90 m/s accelerometers A1H and A2.

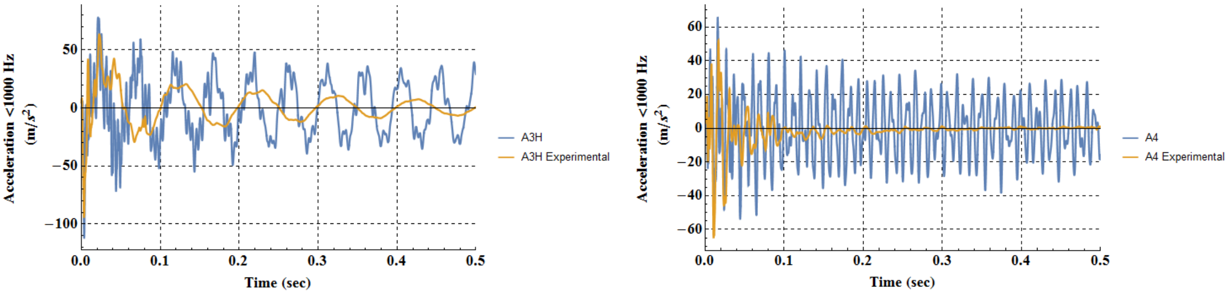

Figure 4-116: 90 m/s accelerometers A3H and A4.

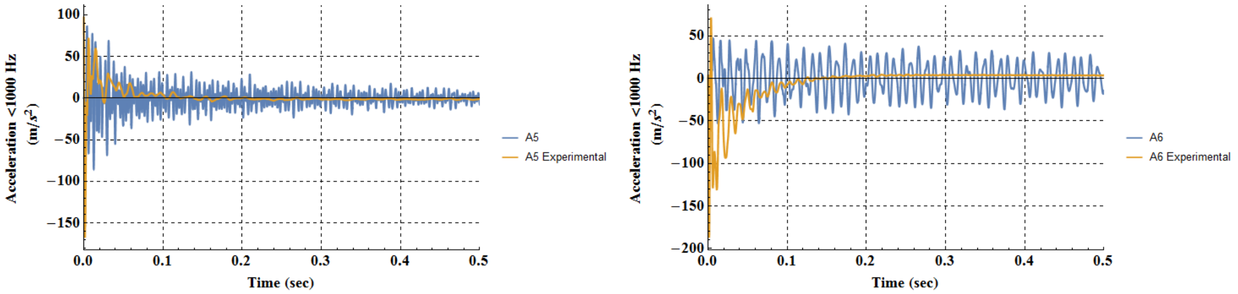

Figure 4-117: 90 m/s accelerometers A5 and A6.

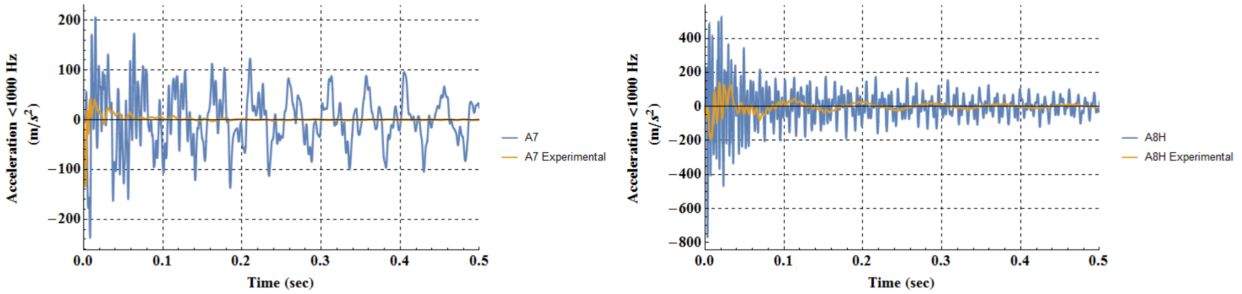

Figure 4-118: 90 m/s accelerometers A7 and A8H.

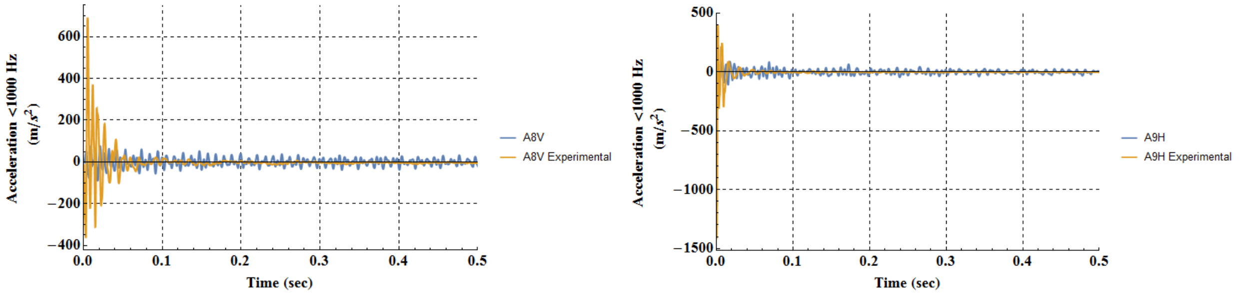

Figure 4-119: 90 m/s accelerometers A8V and A9H.

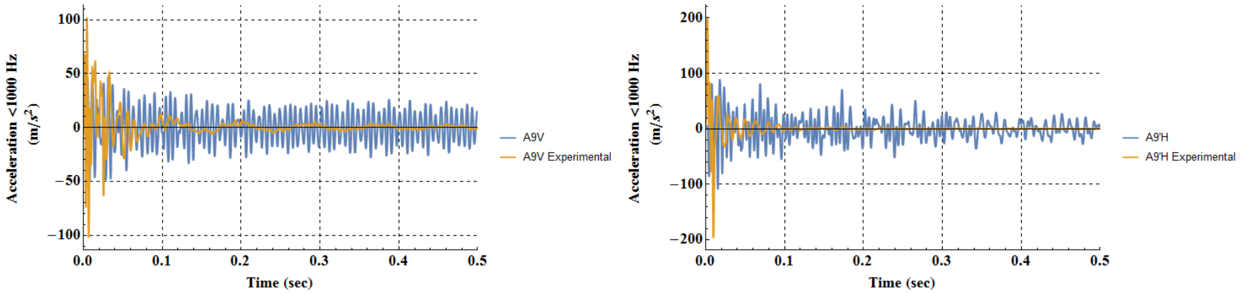

Figure 4-120: 90 m/s accelerometers A9V and A9'H.

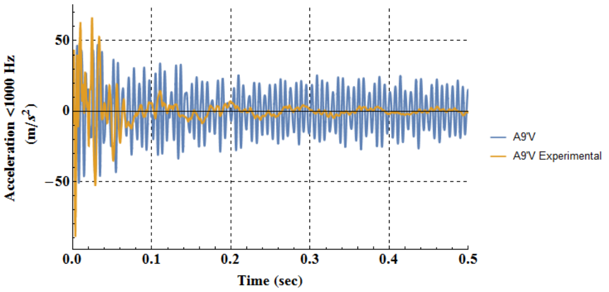

Figure 4-121: 90 m/s accelerometer A9'V.

4.4.4.3 Pseudo-Equipment Results

The pseudo-equipment displacements and accelerations are presented in Figure 4-122 through Figure 4-123. The pseudo-equipments had similar behavior despite being connected via two different methods. Comparing the two experimental graphs or the two simulation results graphs, the displacements of the bolted and welded pseudo-equipments are similar in frequency and amplitude. The initial displacement of the experimental pseudo-equipments were considerably higher than the simulation results (~5 mm vs ~1.8 mm) and the frequency of the simulation results was higher than the experimental. These comparisons suggest that 1) the simulation connections between the I-beams and the supporting plates were too rigid, 2) the simulated mockup was more stiff, or 3) a combination of the two.

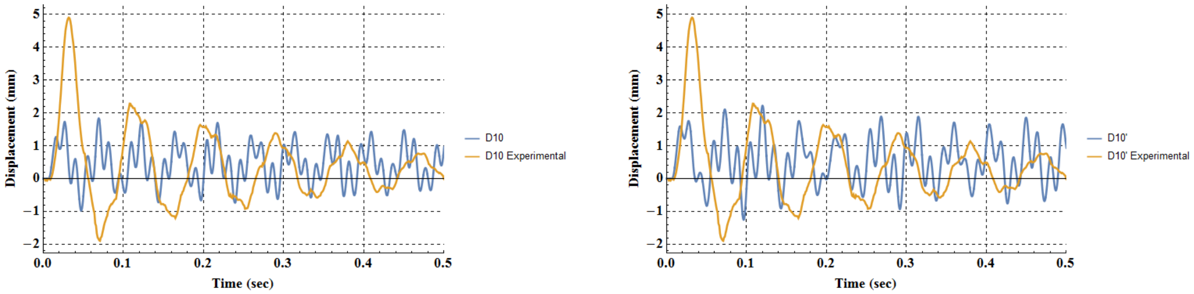

Figure 4-122: Vertical displacement of 90 m/s transducers D10 and D10'.

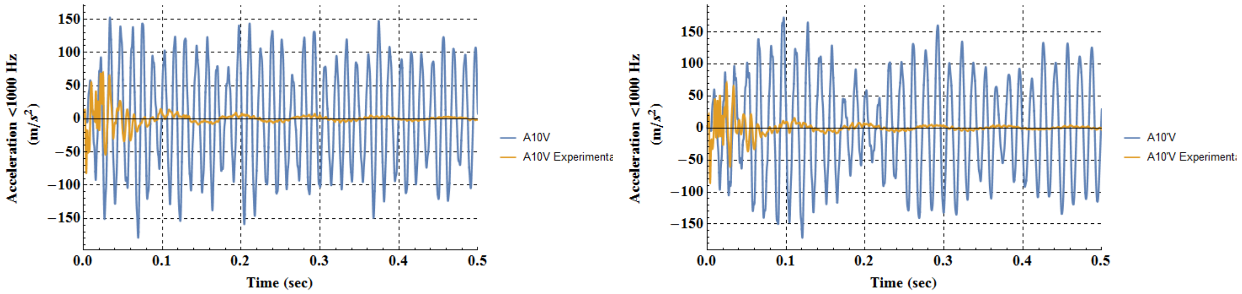

Figure 4-123: Vertical accelerations of the 90 m/s pseudo-equipments.

4.4.4.4 90 m/s Missile Impact Conclusions

The missile simulation material and structural behavior correctly represented the behavior of the experimental missile. The missiles deformed in a similar manner and to similar lengths. The simulation acceleration data of the rear end of the missile showed excess noise, but the acceleration data filtered under 1000 Hz showed a clear result with a maximum acceleration of ~7,000 m/s^2. The force of the missile against the target filtered under 1000 Hz was ~450 kN, though the smoothed data curve (moving average) showed a maximum force of ~750 kN. Results from EDF indicate that the maximum force of the experimental missile against the mockup was 400-500 kN. Therefore, the accurate method of post-processing the missile force and accelerations was to filter the data below 1000 Hz.

The missile did not penetrate the concrete in the experiment or the simulation. Damage accrued on the front wall on both faces where the missile impacted as shown in Figure 4-86 and Figure 4-89. Figure 4-90 reveals that the damage on the front face under the missile impact was shallow and limited to the first layer of elements. Damage on the rear face of the front wall likely accrued due to tensile stresses in the concrete and percolated in places all the way through the wall to meet the damage on the front face. Cracks spread in an 'X' pattern on the front wall, both on the front and rear faces. Horizontal lines of damage accrued in the mockup that may or may not be damage from the impact. Simulations dictated that the K&C concrete model required heavy hourglass stiffening to prevent instability in high gradients, e.g. during impact. The horizontal lines of damage may either be damage from the impact or element instability inherent to the K&C model.

The addition of concrete pedestals below the supports allowed for cleaner readings of reaction forces compared to efforts in the first benchmark wherein the forces were summed through the support base plates. The simulation pedestal reaction forces were almost always greater in magnitude than those of the experiment. In addition, the simulation pedestal reaction forces had a higher frequency than those of the experiment. The higher frequency in the simulation is most likely due to 1) stiffer simulated connections between the mockup and its foundation and 2) stiffer simulated connections between all mockup pieces. The rebar inside the simulated mockup was perfectly bonded to the concrete, and all supporting plates were perfectly bonded to their connecting pieces. In the experiment, all of these connections could slip if damaged.

The displacements recorded by the displacement transducers in the experiment and the simulation were of similar magnitude for all locations, though the mockup had a higher displacement frequency for previously postulated reasons. Displacement transducer D01 in Figure 4-100 (front center of the impact face) indicates that permanent deformation of 1-2 mm occurred on the front face of the concrete. Some displacements did not agree, such as displacement transducer D8H in Figure 4-107. The simulation predicted no permanent deformation while the experiment experienced permanent deformation of ~0.10 mm. The difference in this particular gage is likely due to the perfect bond between materials and components in the simulation (resulting in no permanent displacement) whereas the mockup could be permanently displaced in the experiment. The simulated strain gages G0H and G0V in Figure 4-109 indicate that the rebar in the impact wall also permanently deformed; however, experimental results seem to include excessive noise suggesting that the gages may have been damaged before or during impact. Strain gages G5V and G6V in Figure 4-112 indicate that the rebar at the base of the cantilever did not permanently deform in the simulation but may have permanently deformed in the experiment.

Accelerometer data indicates that 1000 Hz is an adequate cutoff frequency for analyzing structural accelerations as discussed in Figure 4-78. The magnitudes of accelerations in the simulation and the experiment were similar, though the simulation did not dampen the accelerations with time whereas the experimental accelerations lessened over time.

To verify that the simulation displacements, velocities, and accelerations were internally consistent, Figure 4-125 compares scaled (1/10 scale) A3H accelerometer data vs the displacements of D3. A3H and D3 were in the same location. The two curves share the same frequency but are offset by ½ period, suggesting excellent agreement between the simulation output displacements, velocities, and accelerations.

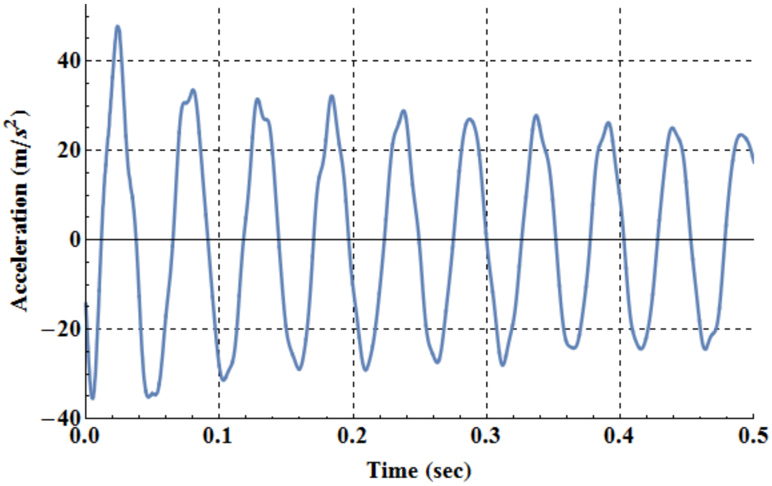

Figure 4-124: Accelerometer A3H showing only accelerations with frequencies below 1000 Hz (90 m/s).

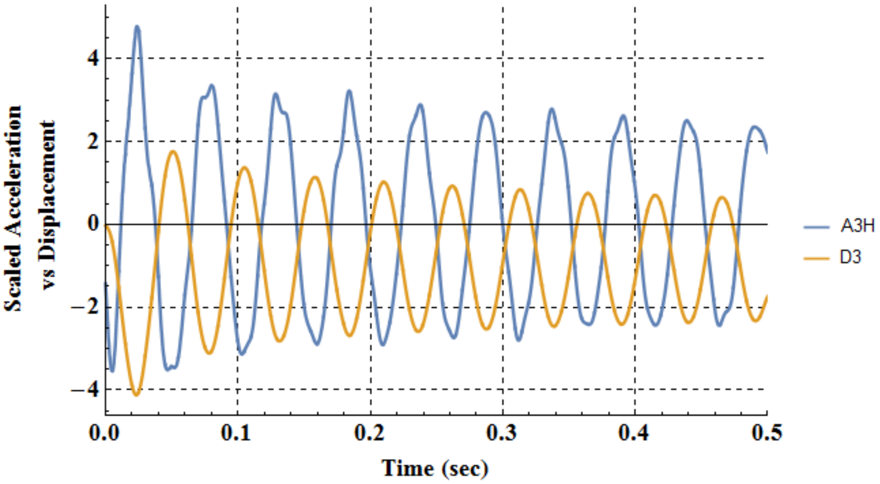

Figure 4-125: 1/10 Scaled acceleration of A3H plotted with D3 (90 m/s).

The bolted and welded pseudo-equipments behaved similarly in both the experimental and simulation results, but the experimental results were subject to higher displacements and lower oscillation frequencies. These results suggest that 1) the simulation connections between the I-beams and the supporting plates were too rigid, 2) the simulated mockup was more stiff, or 3) a combination of the two.

4.4.5 170 m/s Impact Velocity Simulation Results

4.4.5.1 Missile Results

The results of the missile are separated into general missile crushing results and time histories of the missile velocity, acceleration, impulse, and force pushing against the mockup.

4.4.5.1.1 Crushing Results

The results of the simulated 170 m/s missile impact are shown in Table 4-8 and Figure 4-126. These values were obtained using analyst judgement to determine the transition from crushed to uncrushed. Figure 4-80 shows the experimental crushed missiles.

Table 4-8: 170 m/s Missile Impact Crush Results.

	Simulated Lengths	**Experimental Lengths**
Original length (including hemispherical head)	2525 mm	2525 mm
Total length after crush	775 mm	887 mm
Crushed length H_T	470 mm	330 mm
Non-crushed length L_T	305 mm	557 mm

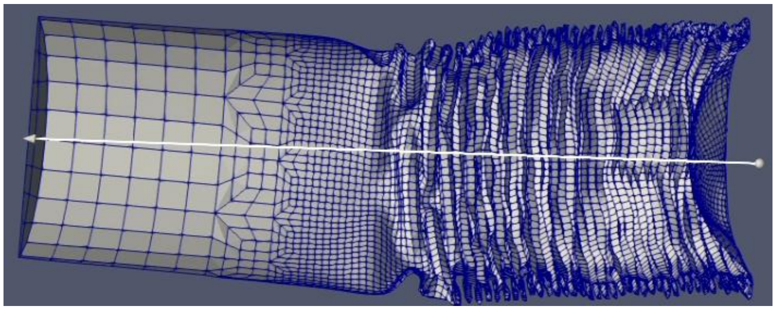

Figure 4-126: Simulated crushed 170 m/s missile.

4.4.5.1.2 Time Histories

The time histories of missile end velocity and acceleration are presented in Figure 4-127 and Figure 4-128. The missile velocity and accelerations cut off at 0.05 seconds since the missile was omitted from the simulation at 0.05 seconds. The contact force of the missile against the mockup is presented in Figure 4-129, and the contact force of the missile against a rigid target is presented in Figure 4-130; similar behavior and peak forces indicate that the mockup behaved much as a rigid target for the 170 m/s missile.

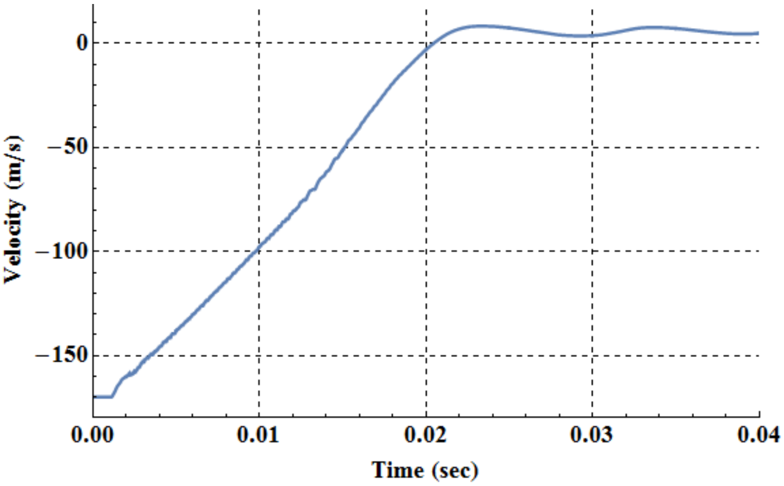

Figure 4-127: 170 m/s missile end velocity.

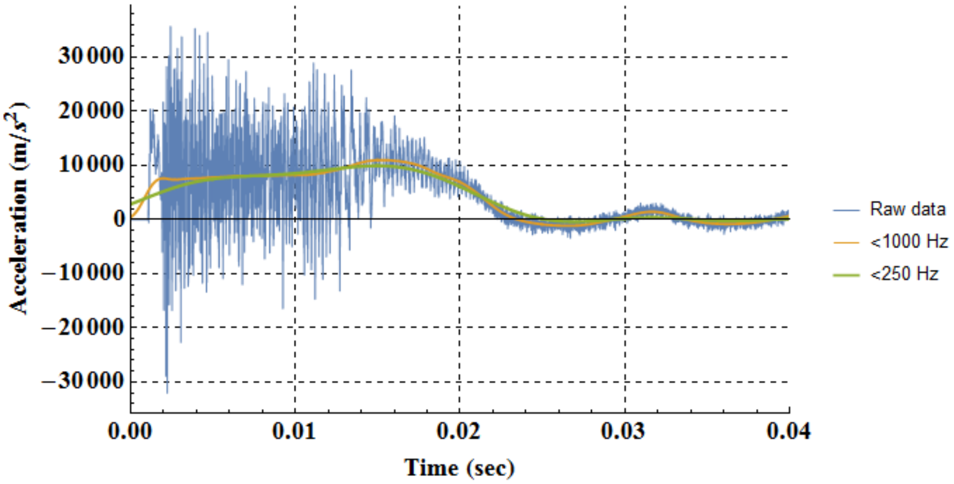

Figure 4-128: 170 m/s missile end acceleration.

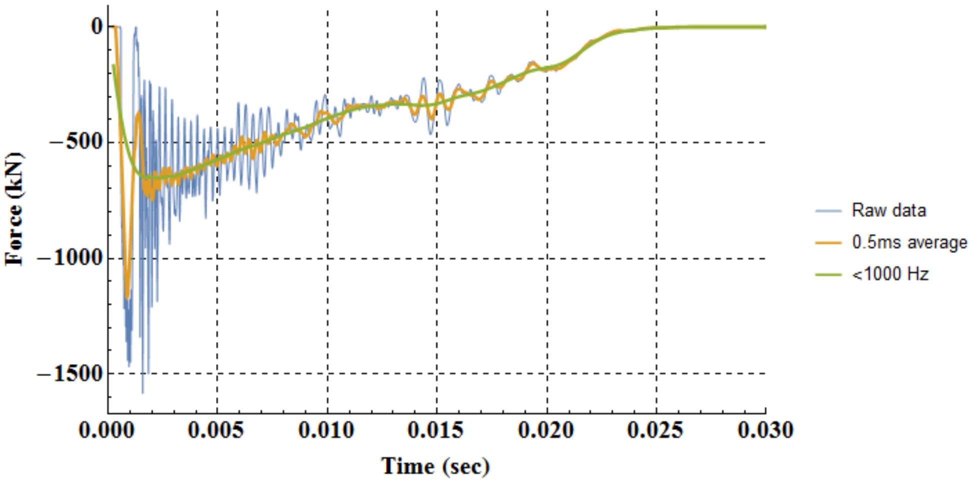

Figure 4-129: Force of the 170 m/s missile against the mockup.

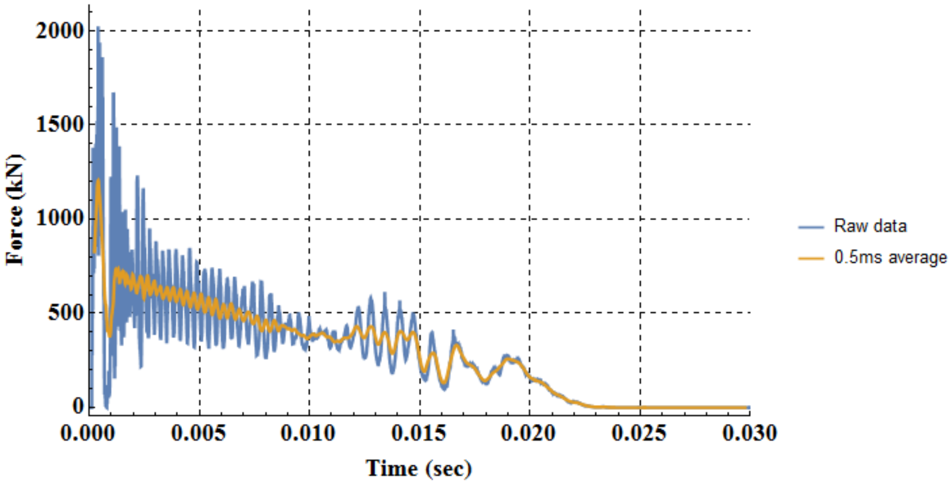

Figure 4-130: 170 m/s missile force-time history against a rigid plane.

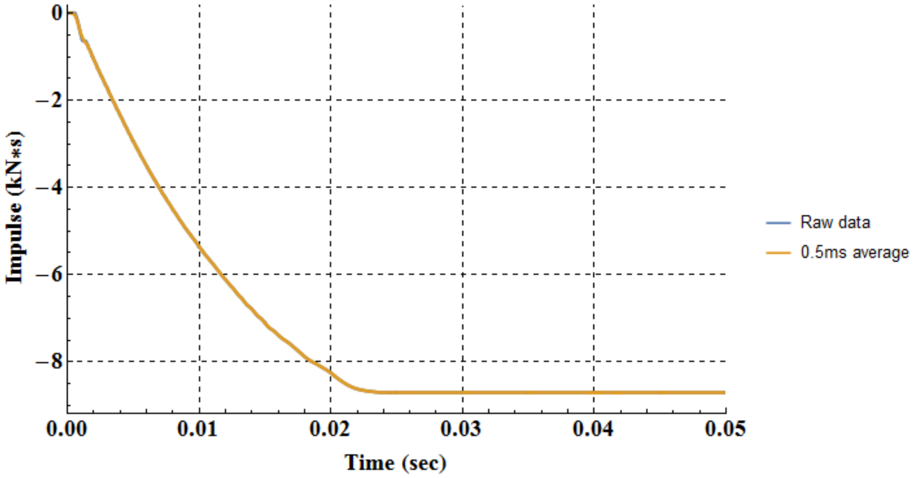

Figure 4-131: Impulse of the 170 m/s missile against the mockup.

4.4.5.2 Mockup Results

4.4.5.2.1 Global Results

Results from the 170 m/s missile impact simulation are shown in Figure 4-132 through Figure 4-136. The support pedestals and missile have been removed to better see the concrete damage. A damage factor of 2.0 indicates cracked concrete.

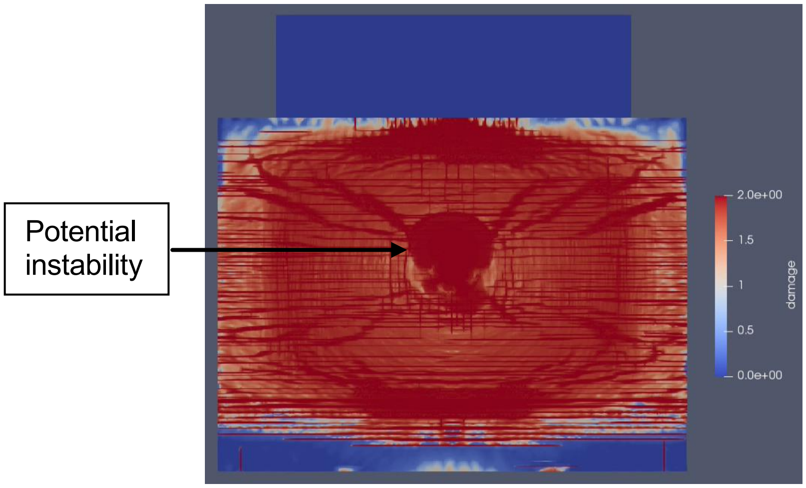

Figure 4-132: Damage on the impact face of the 170 m/s impact mockup.

The impact face of the concrete suffered crack damage immediately in the vicinity of the missile impact as shown as the deepest red shading in the center of the impact face. Cracks also formed spreading outwards from the area of impact towards the corners of the mockup. The impact face of this mockup may have developed a material instability in the vicinity of the missile impact. Hourglass stiffness and viscosity was applied to the concrete elements, but it seems that the Karagozian & Case model may develop too much damage in simulations with extremely high gradients in force or deformation.

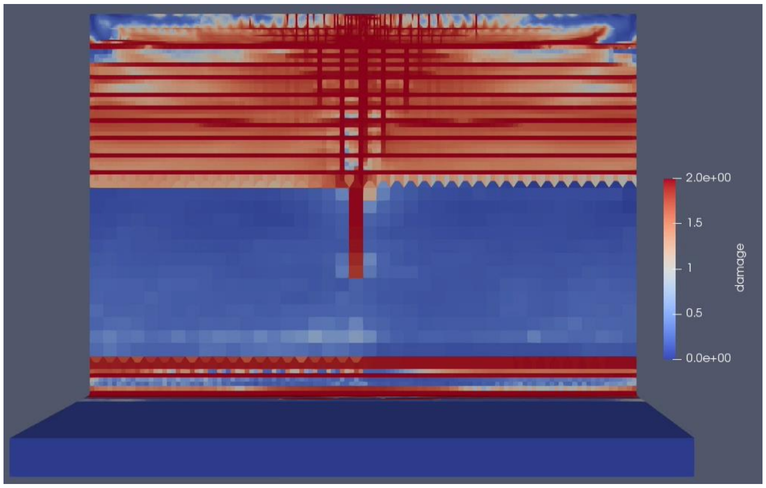

Figure 4-133: Top view of damage of the 170 m/s impact mockup.

The top of the mockup suffered cracks damage due to bending moments from the impact. It also seems apparent that material performance changed when the element size changed at halfway through the mockup (seen here as a sudden change from red to blue).

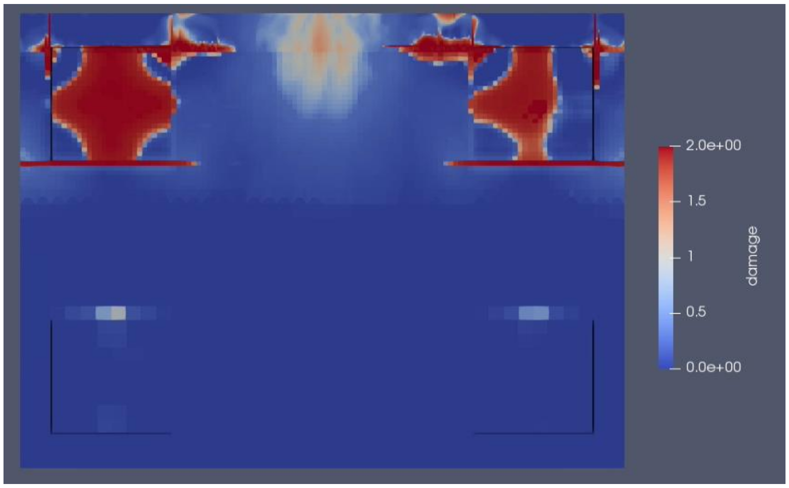

Figure 4-134: Bottom view of damage of the 170 m/s impact mockup. The edge with damage is the impact side of the mockup.

The bottom of the mockup suffered crack damage due to bending moments and possibly due to stress concentrations at the divots where the supports were attached to the concrete. Extensive damage was predicted immediately above the supports, though it is not clear if the damage is from actual damage predictions or from Karagozian & Case material model instability.

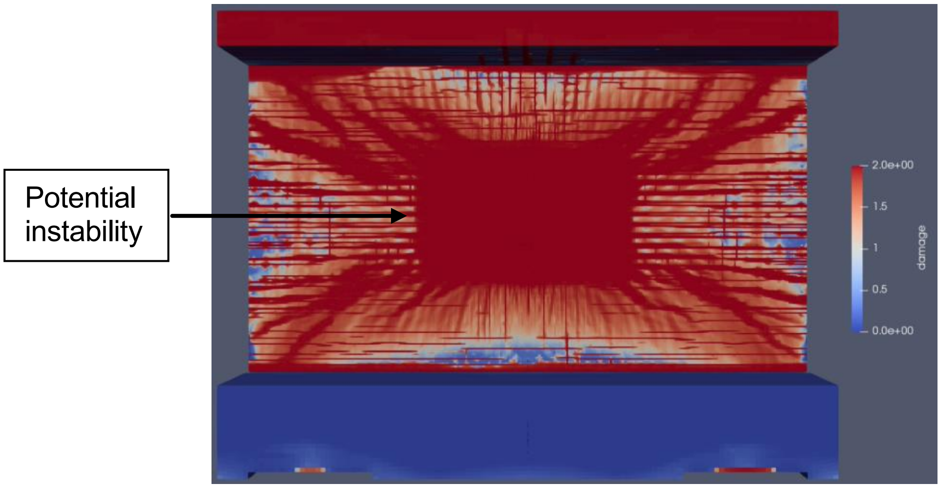

Figure 4-135: Back side of the impact face of the 170 m/s impact mockup.

The back side of the impact face suffered crack damage immediately in the vicinity of the missile impact and in an ‘X’ pattern from corner to corner. Excessive damage accrued behind the missile impact position, and it is unclear if the damage is actual material damage or an instability in the Karagozian & Case material model.

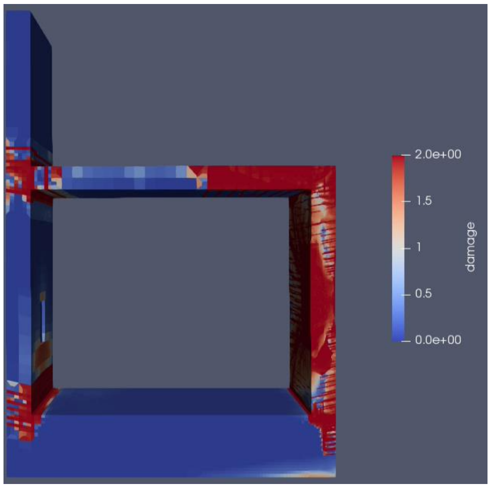

Figure 4-136: Half-cut side view of damage in the 170 m/s impact mockup.

Figure 4-136 shows half of the mockup from the side originating from the center. The side view of the damage indicates that the largest concentrations of damage are immediately behind the missile impact and at the top-front corner of the mockup.

The final displacements of the mockup are shown in Figure 4-137 through Figure 4-140 (units are in mm).

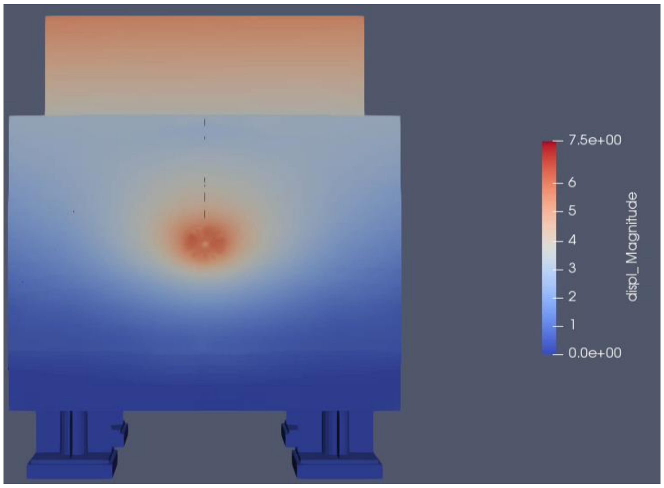

Figure 4-137: Front view of the final displacements of the 170 m/s mockup.

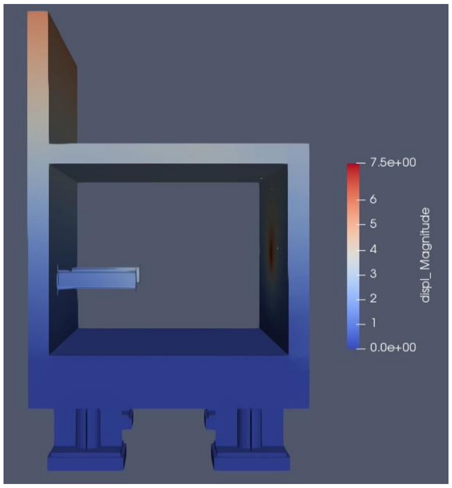

Figure 4-138: Side view of the final displacements of the 170 m/s mockup.

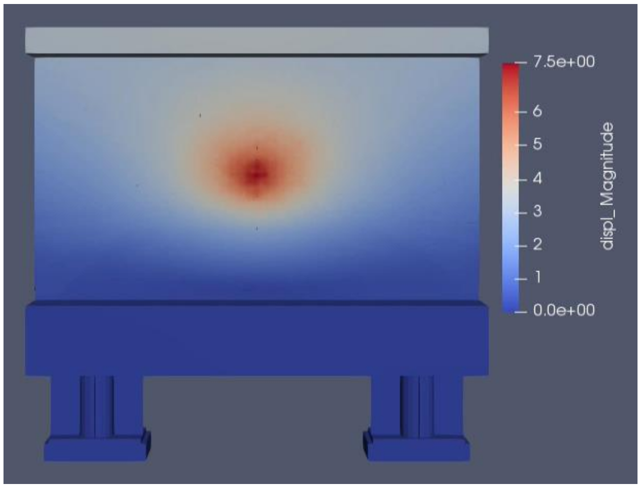

Figure 4-139: Rear side of the impact wall's final displacements in the 170 m/s mockup.

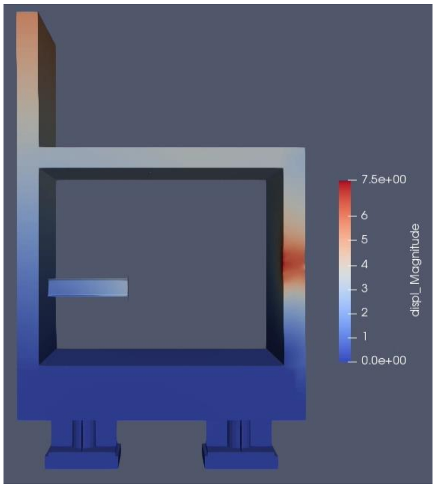

Figure 4-140: Half-cut side view of the final displacements of the 170 m/s mockup.

4.4.5.2.2 Reaction Forces at Supports

The Y-direction (vertical) reaction forces under each support are shown in Figure 4-141 through Figure 4-146. Peak reaction forces for each support are presented in Table 4-9. There is a notable difference between the unfiltered and filtered reaction forces in both frequency/oscillations and peak force.

Table 4-9: Peak reaction forces during the 170 m/s impact.

Support Location	Peak Force Unfiltered (kN)	Peak Force <200 Hz (kN)	Peak Experimental (kN)
Front left	424	296	514
Front right	423	317	469
Rear left	391	261	158
Rear right	419	286	132

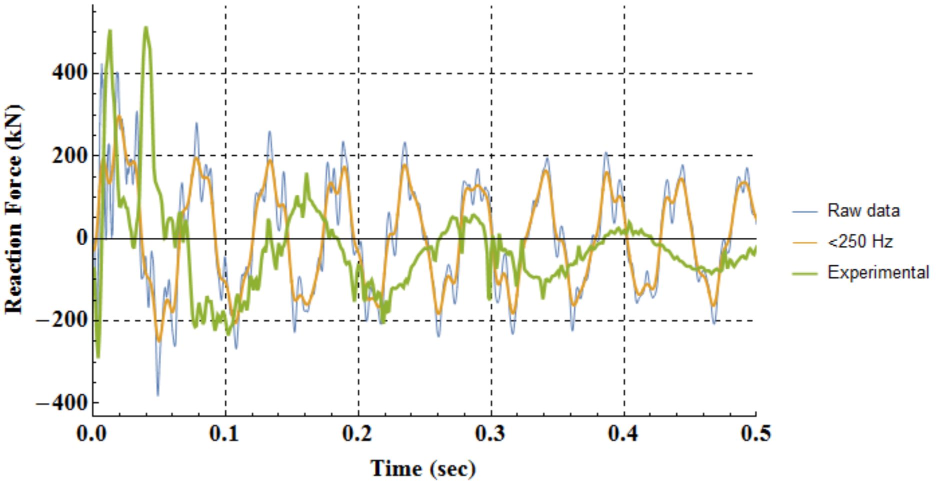

Figure 4-141: Vertical force under the front left support for the 170 m/s impact.

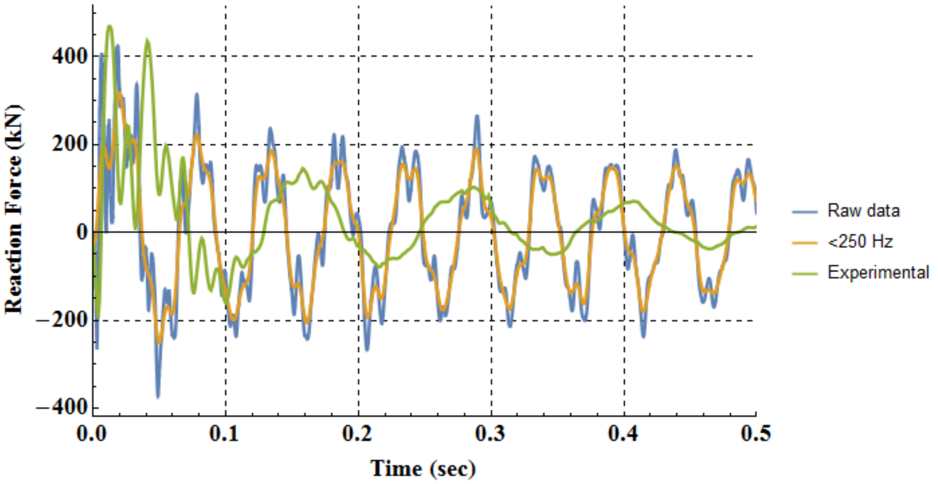

Figure 4-142: Vertical force under the front right support for the 170 m/s impact.

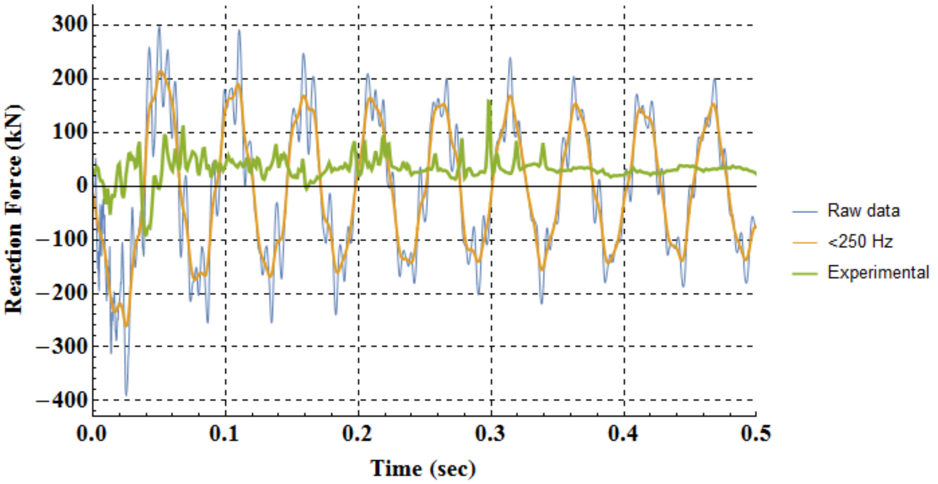

Figure 4-143: Vertical force under the rear left support for the 170 m/s impact.

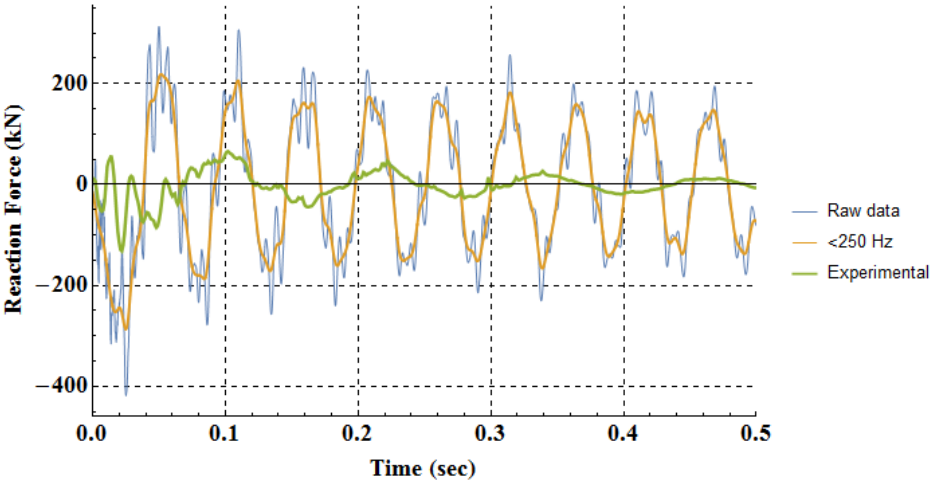

Figure 4-144: Vertical force under the rear right support for the 170 m/s impact.

Two examples of Z-reaction forces in line with the missile impact are shown in Figure 4-145 and Figure 4-146.

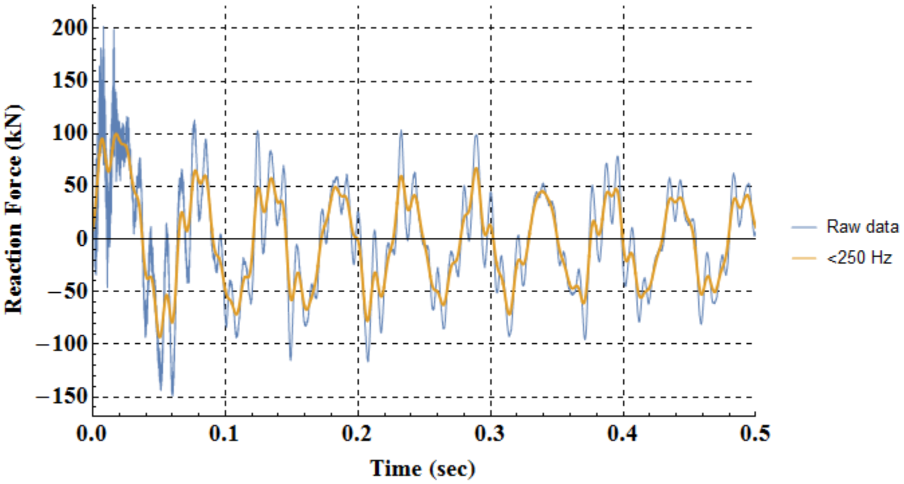

Figure 4-145: Z-reaction force (in line with the missile) under the front left support for the 170 m/s impact.

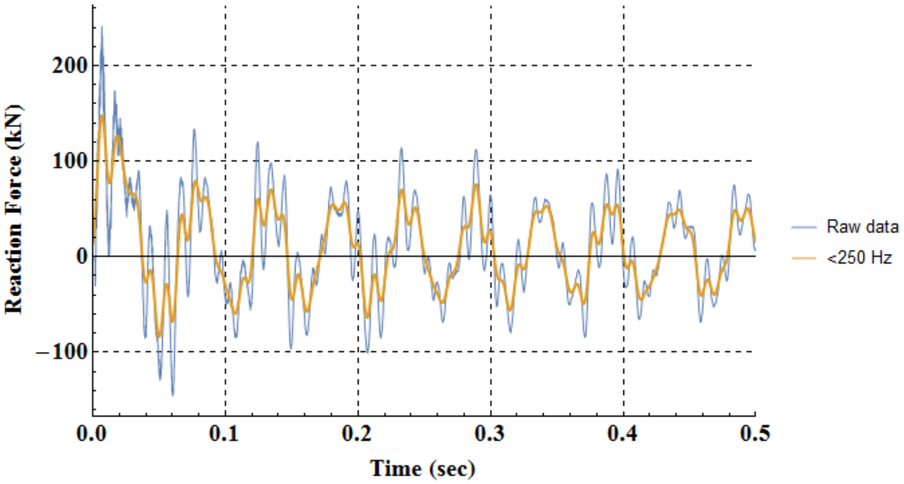

Figure 4-146: Z-reaction force (in line with the missile) under the rear left support for the 170 m/s impact.

4.4.5.2.3 Time Histories

Time histories of displacements, strains, accelerations are presented in Figure 4-147 through Figure 4-168. Accelerations are presented with unfiltered data and as filtered through a 200 Hz low-pass filter. In these figures, an apostrophe indicates a transducer on or around the welded I-beam. For example, D9 and D9L are displacement transducers on either side of the bolted I-beam and D9' is a displacement transducer near the welded I-beam.

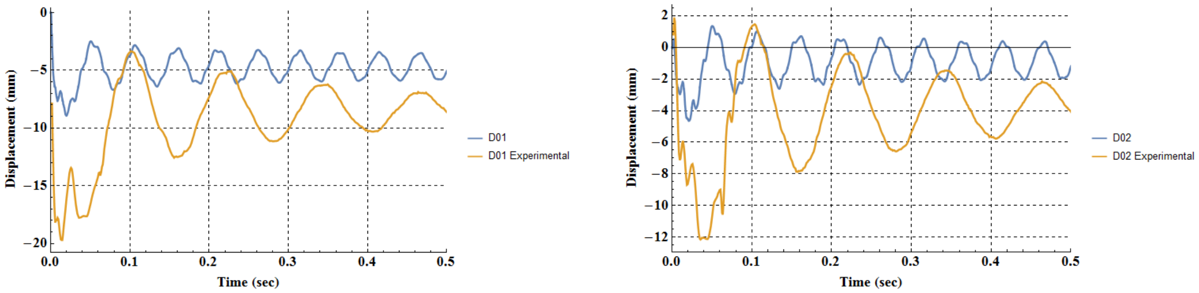

Figure 4-147: Displacement of 170 m/s transducers D01 and D02.

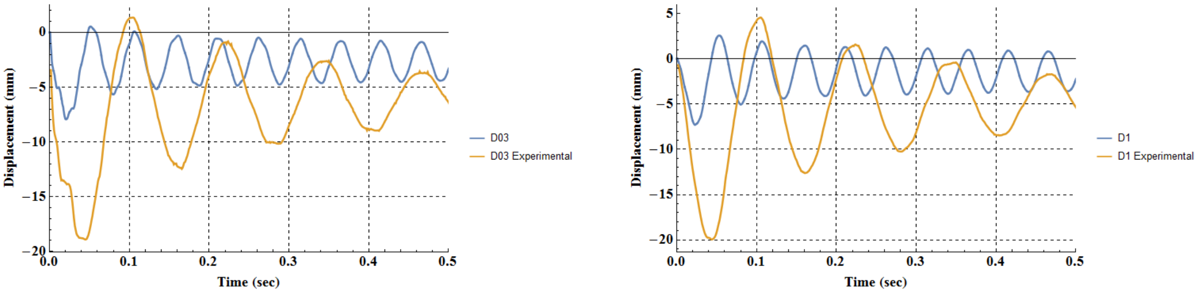

Figure 4-148: Displacement of 170 m/s transducers D03 and D1.

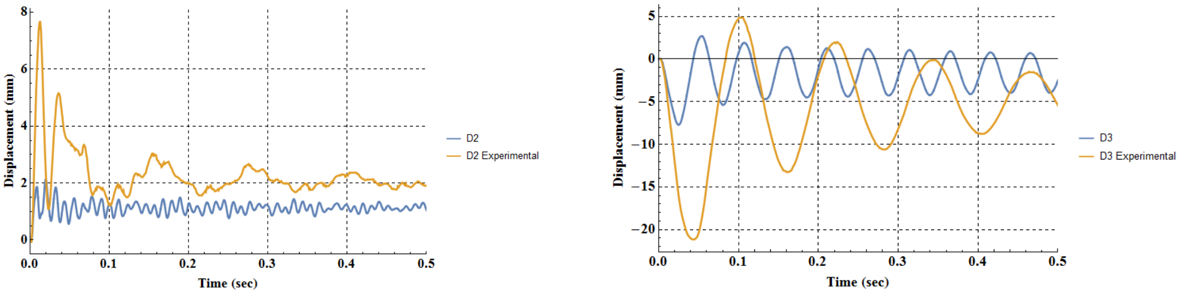

Figure 4-149: Displacement of 170 m/s transducers D2 and D3.

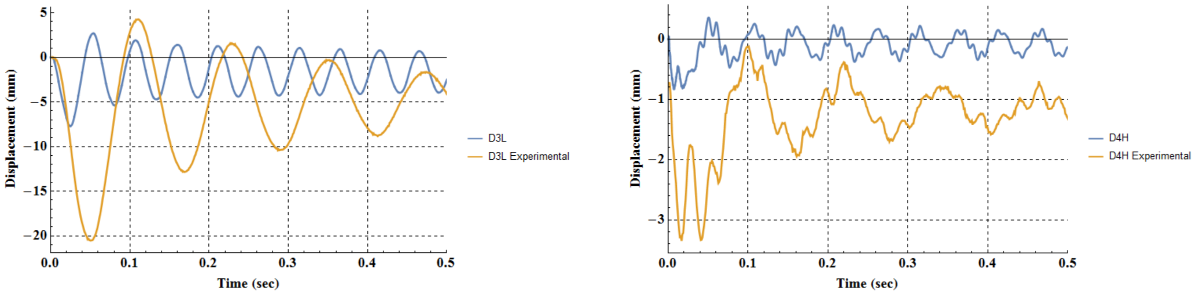

Figure 4-150: Displacement of 170 m/s transducers D3L and D4H.

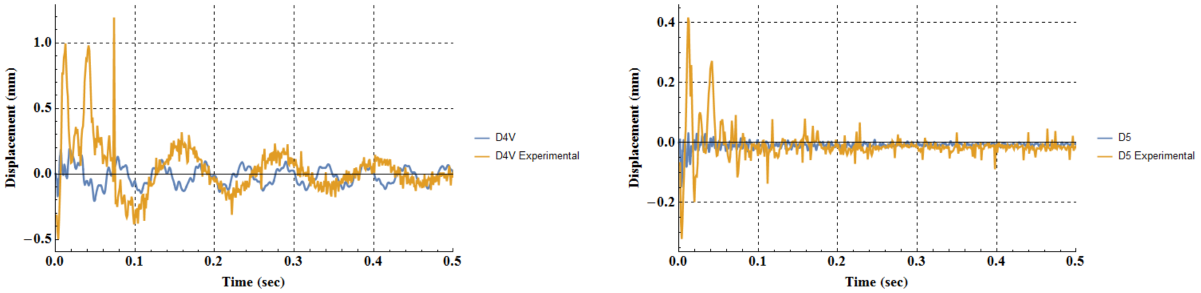

Figure 4-151: Displacement of 170 m/s transducers D4V and D5.

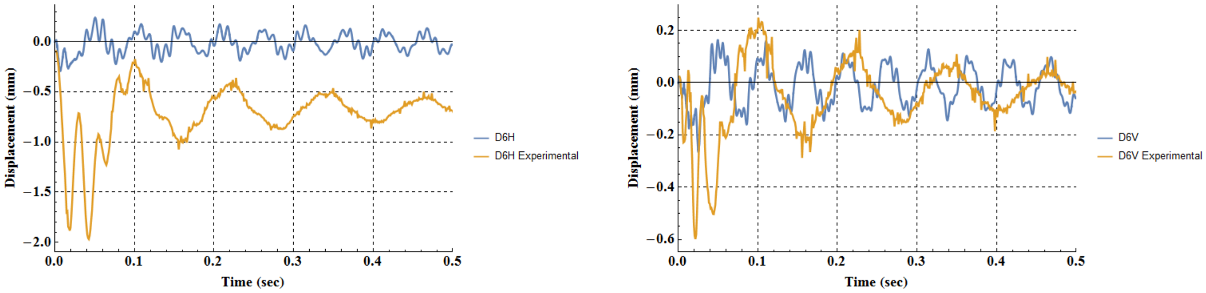

Figure 4-152: Displacement of 170 m/s transducers D6H and D6V.

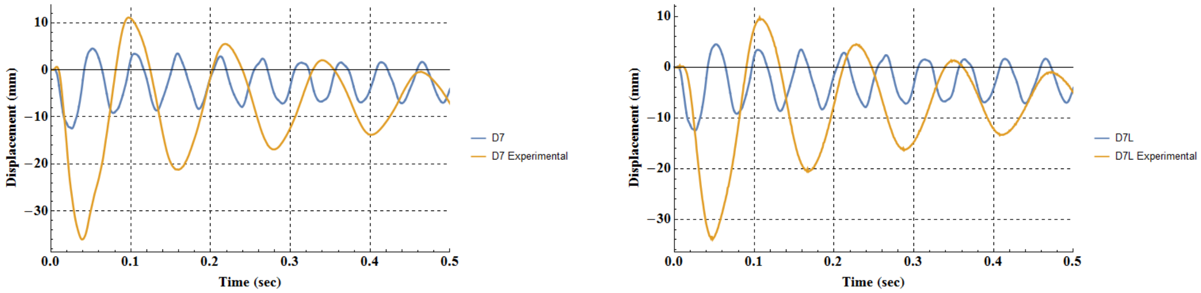

Figure 4-153: Displacement of 170 m/s transducers D7 and D7L.

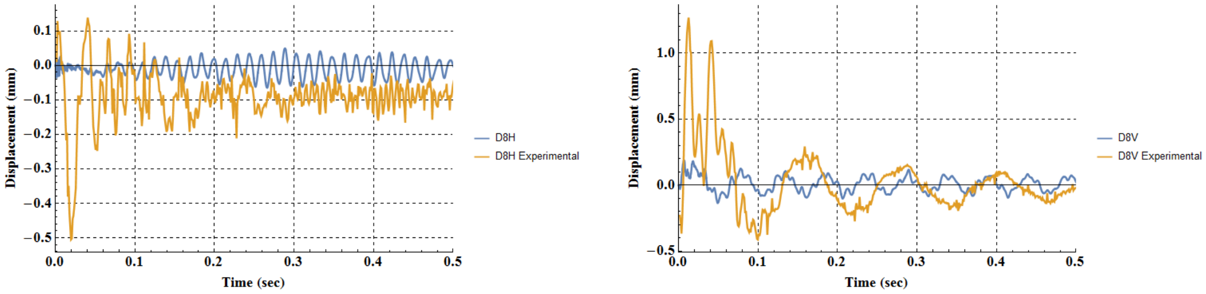

Figure 4-154: Displacement of 170 m/s transducers D8H and D8V.

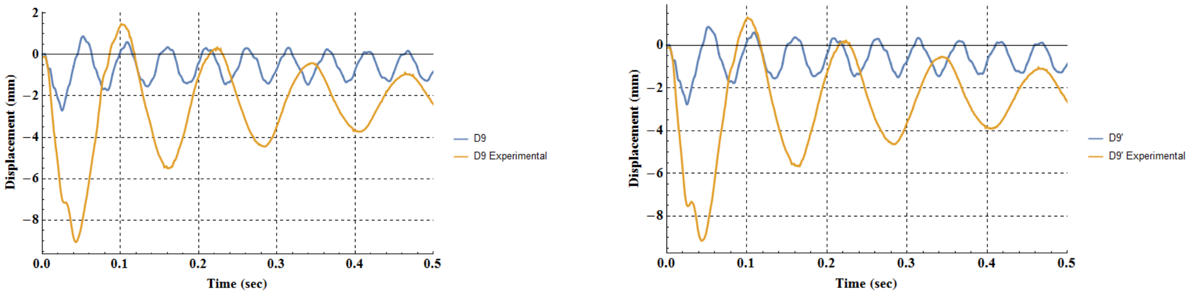

Figure 4-155: Displacement of 170 m/s transducers D9 and D9'.

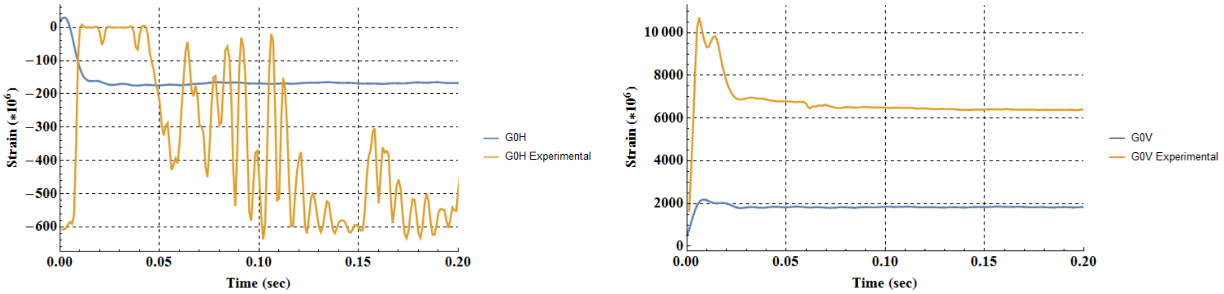

Figure 4-156: Strain of 170 m/s strain gages G0H and G0V.

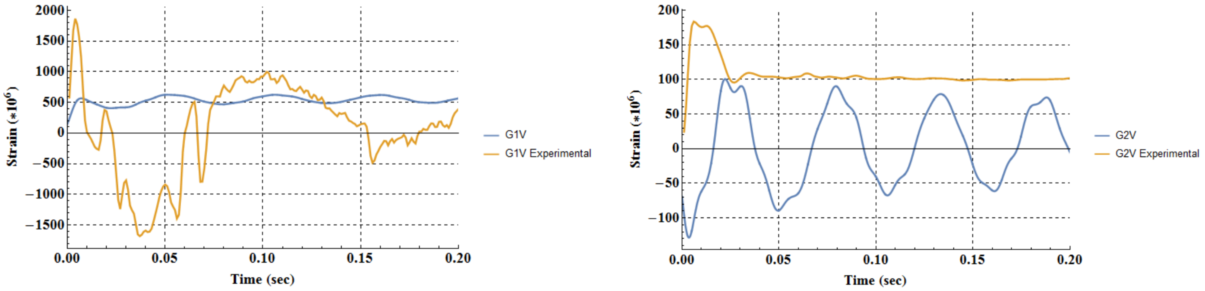

Figure 4-157: Strain of 170 m/s strain gages G1V and G2V.

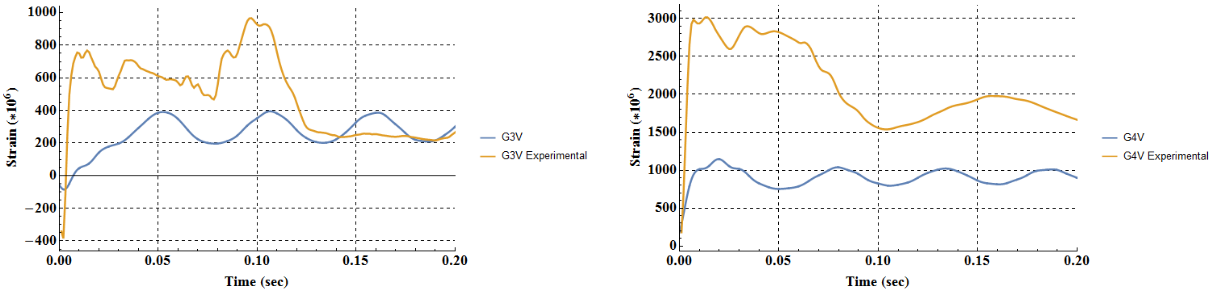

Figure 4-158: Strain of 170 m/s strain gages G3V and G4V.

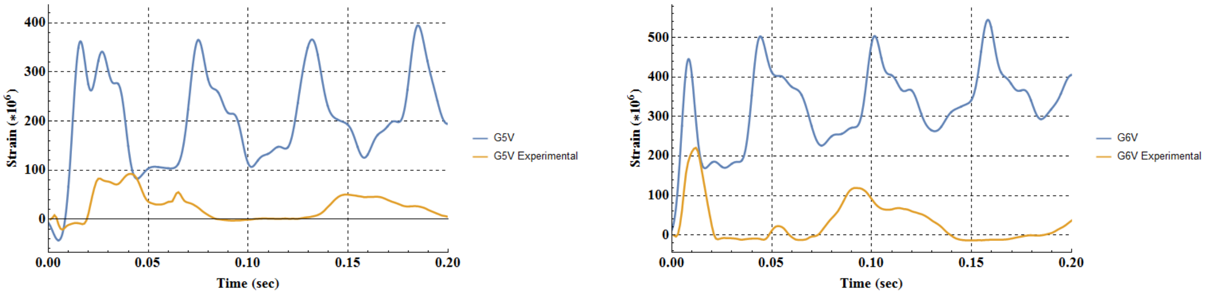

Figure 4-159: Strain of 170 m/s strain gages G5V and G6V.

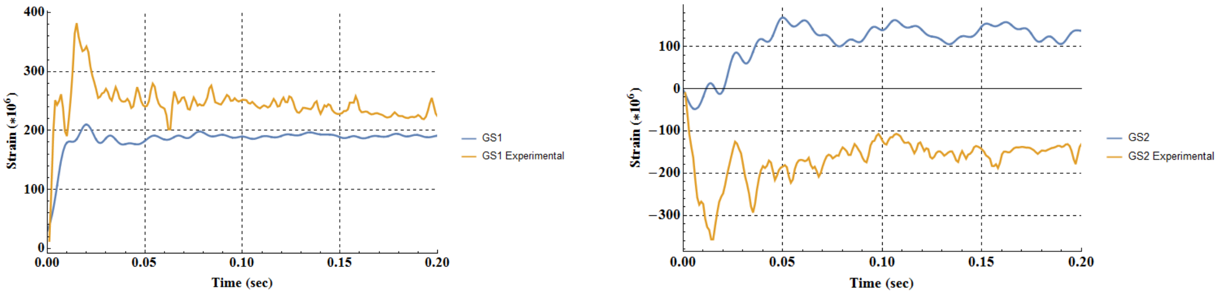

Figure 4-160: Strain of 170 m/s strain gages GS1 and GS2.

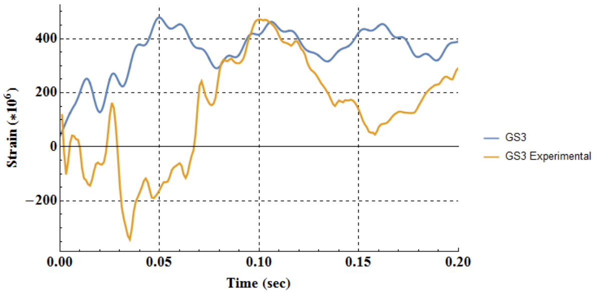

Figure 4-161: Strain of 170 m/s strain gage GS3.

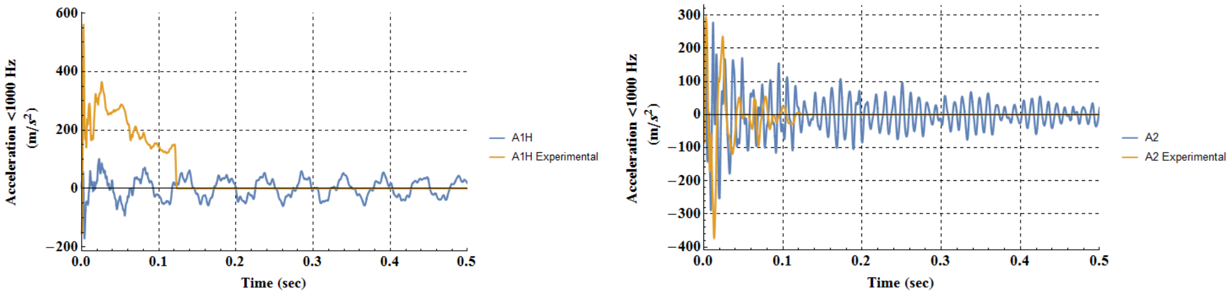

Figure 4-162: 170 m/s accelerometers A1H and A2.

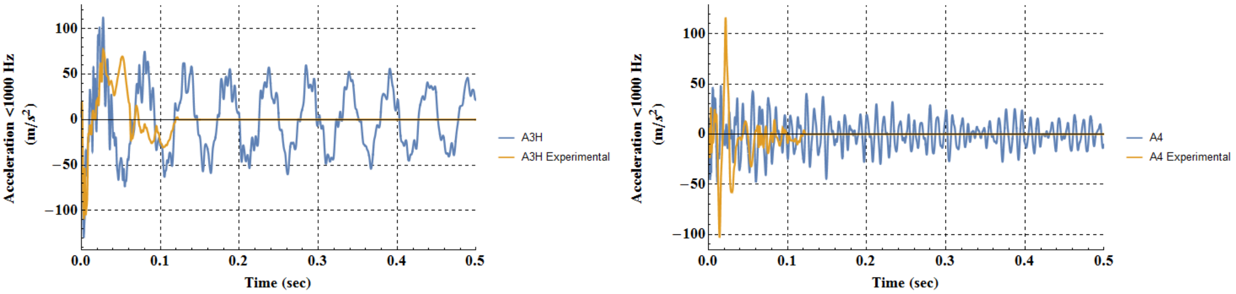

Figure 4-163: 170 m/s accelerometers A3H and A4.

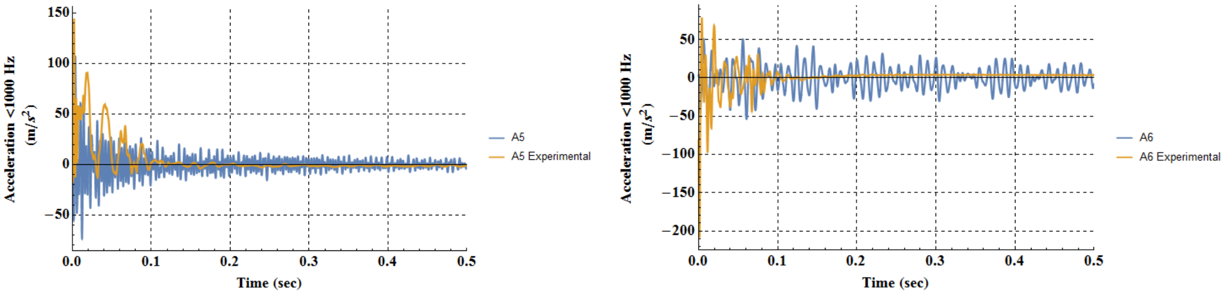

Figure 4-164: 170 m/s accelerometers A5 and A6.

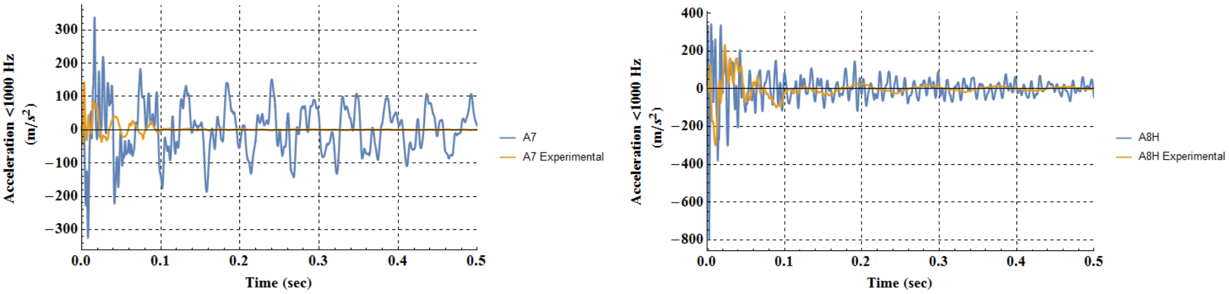

Figure 4-165: 170 m/s accelerometers A7 and A8H.

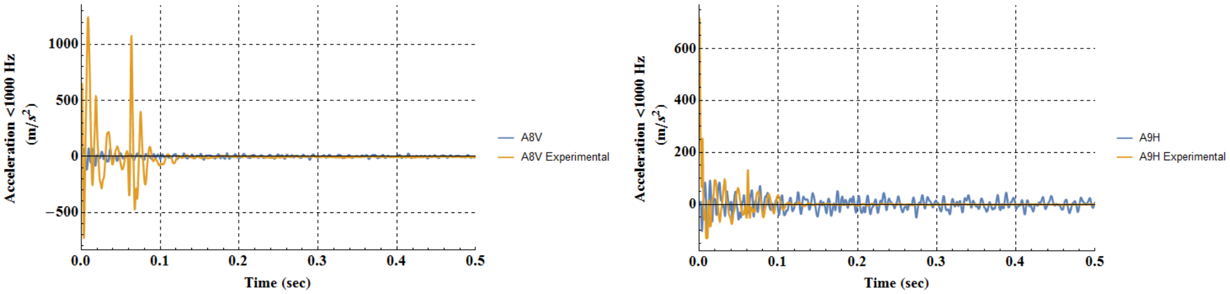

Figure 4-166: 170 m/s accelerometers A8V and A9H.

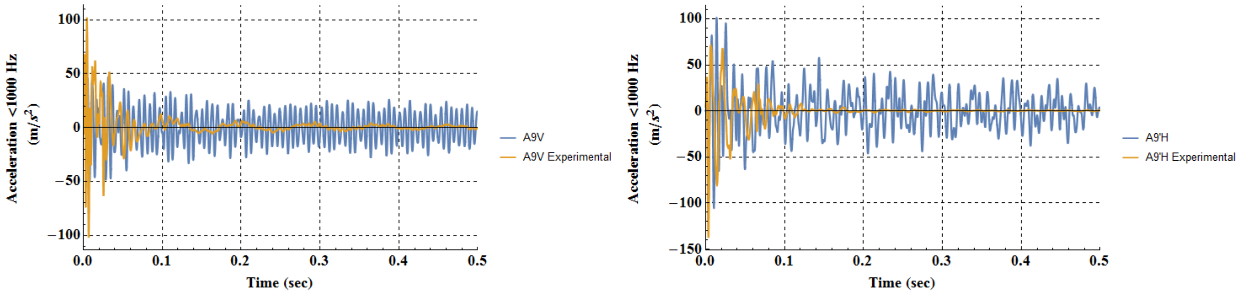

Figure 4-167: 170 m/s accelerometers A9V and A9'H.

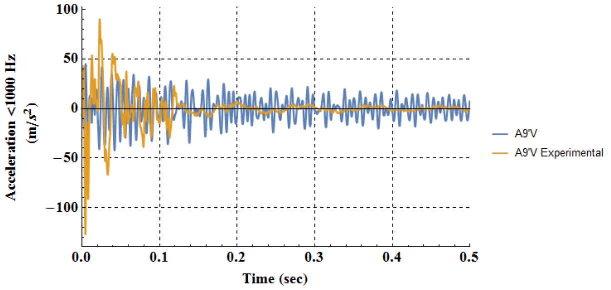

Figure 4-168: 170 m/s accelerometer A9'V.

4.4.5.3 Pseudo-Equipment Results

The pseudo-equipment displacements and accelerations are presented in Figure 4-169 and Figure 4-170. The pseudo-equipments had similar behavior despite being connected via two different methods. The displacements of the pseudo-equipments are similar in frequency and amplitude. The experimental pseudo-equipments experienced much higher initial displacements than predicted by the simulation (~14 mm vs ~4 mm, respectively) and had a slower oscillation frequency. As in the 90 m/s missile simulation, the disparity between the simulation and the experimental results suggest that perhaps 1) the connections between the I-beams and the supporting plates were too rigid, 2) the simulated mockup was more stiff, or 3) a combination of the two.

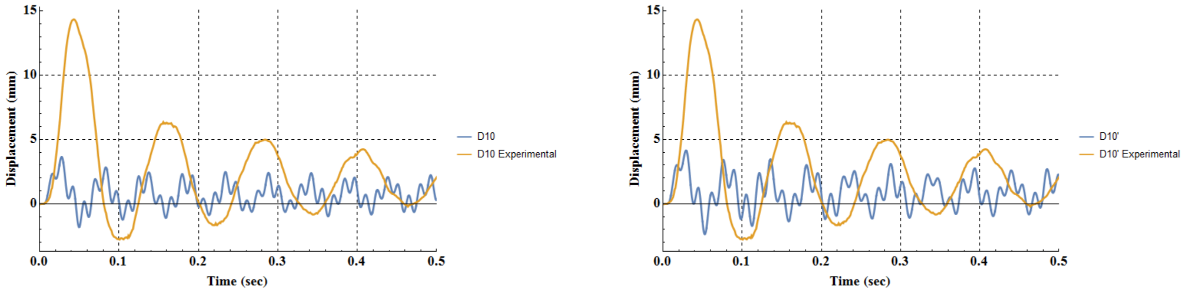

Figure 4-169: Vertical displacement of 170 m/s transducers D10 and D10’.

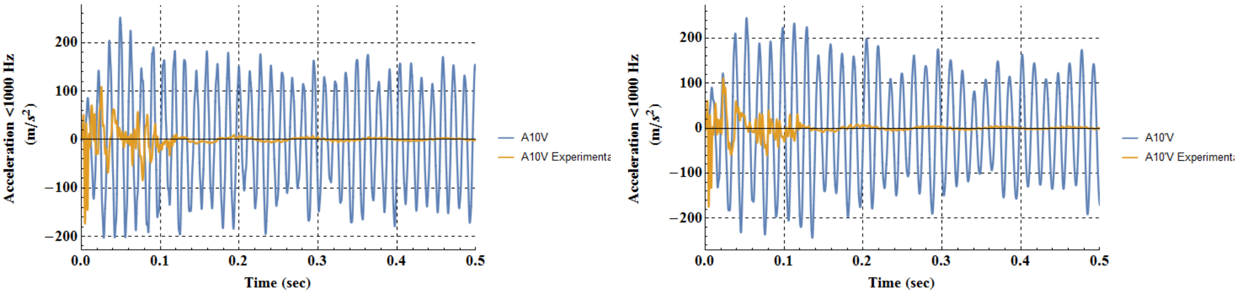

Figure 4-170: Vertical accelerations of the 170 m/s pseudo-equipments.

4.4.5.4 170 m/s Missile Impact Conclusions

The missile simulation material and structural behavior correctly represented the behavior of the experimental missile. The missiles deformed in a similar manner and to similar lengths. As discussed in the 90 m/s missile impact conclusions, the acceleration of the rear end of the was filtered under 1000 Hz. The force of the missile against the target filtered under 1000 Hz was ~700 kN. Results from EDF indicate that the maximum force of the experimental missile against the mockup was ~970.

The missile did not penetrate the concrete in the experiment or the simulation, but significant cracking occurred on both the front and back of the impact face. Damage accrued on the front wall on both faces where the missile impacted as shown in Figure 4-132 and Figure 4-135. Damage on the rear face of the front wall likely accrued due to tensile stresses in the concrete and percolated in places all the way through the wall to meet the damage on the front face. The damage on the front face of the impact wall was shallower than that of the back face. Cracks spread in an ‘X’ pattern on the front wall, both on the front and rear faces, similar to but more extreme than the 90 m/s impact. Horizontal lines of damage accrued in the mockup that may or may not be damage from the impact. Simulations dictated that the K&C concrete model required heavy hourglass stiffening to prevent instability in high gradients, e.g. during impact. The horizontal lines of damage may either be damage from the impact or element instability inherent to the K&C model. In addition, Figure 4-132 and Figure 4-135 show areas where the K&C model may have suffered severe instability leading to excess accumulated damage immediately in the vicinity of the missile impact.

The front pedestal reaction forces in the experiment had a similar magnitude to those in the simulation, but the rear pedestal reaction forces in the experiment were lower than those in the simulation. The reasons for the great disparity between the experimental and simulation results for the rear reactions forces are unknown, but Figure 4-143 provides a clue. The experimental force in Figure 4-143 does not return to or oscillate around zero. Since the final force after impact must eventually be zero, the strain gages on that pedestal may have been damaged during the impact. The simulation pedestal reaction forces had a higher frequency than those of the experiment. The higher frequency in the simulation is most likely due to 1) stiffer simulated connections between the mockup and its foundation and 2) stiffer simulated connections between all mockup pieces. The rebar inside the simulated mockup was perfectly bonded to the concrete, and all supporting plates were perfectly bonded to their connecting pieces. In the experiment, all of these connections could slip if damaged.

The displacements recorded by the displacement transducers in the experiment were almost entirely larger than those in the simulations. Displacement transducer D01 in Figure 4-147 indicates that permanent deformation occurred on the front face of the concrete; the deformation was severe enough to cause a ‘dent’ in the front of the concrete impact wall as shown in Figure 4-137 and Figure 4-139. The simulation predicted final permanent displacement of ~5 mm while the experiment resulted in ~7 mm. Strain gages G0H and G0V in Figure 4-156 indicate that the rebar in the impact wall permanently deformed; the simulation predicted roughly 1/3 of the total strain that was found in the experiment. Figure 4-159 indicates that the rebar at the base of the cantilever permanently deformed in the simulation but not in the experiment. The final damage of the mockup is shown in Figure 4-171 through Figure 4-173.

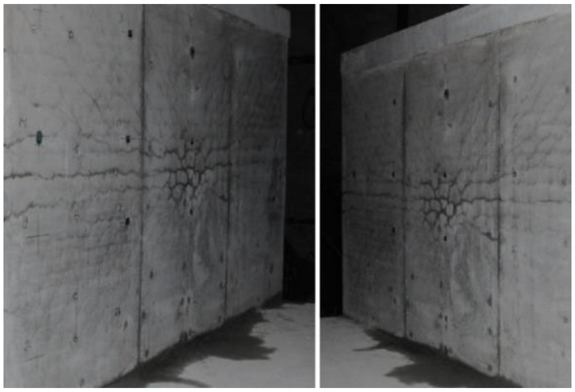

Figure 4-171: Back of the impact face of the mockup showing cracking pattern after all impacts.

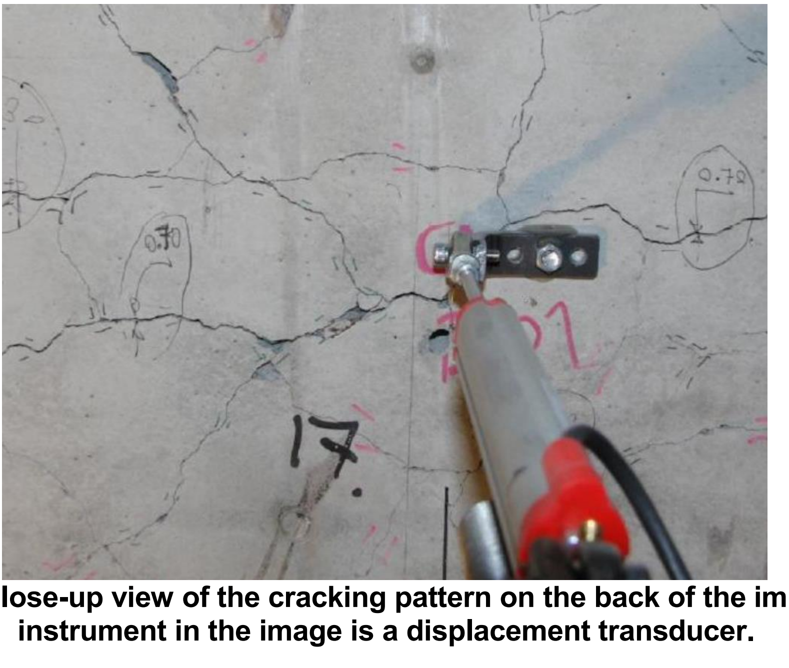

Figure 4-172: Close-up view of the cracking pattern on the back of the impact face. The instrument in the image is a displacement transducer.

Figure 4-173: Bottom of the front face where it meets the bottom of the mockup showing a complete crack through the concrete.

As in the 90 m/s simulation, the magnitudes of accelerations in the simulation and the experiment were similar, though the simulation did not dampen the accelerations with time whereas the experimental accelerations lessened over time.

5 CONCLUSIONS

The objectives of the exercises detailed in this document were to develop guidance for conducting impact analyses including issues related to computer codes, modeling approaches, and analysis techniques. The full project was comprised of three phases: Phase I, impact of walls; Phase II, impact of larger structures; and Phase III, transmission of shock and vibration to internal components.

Program IRIS consisted of three phases. Phase I included three separate tests of missile impact against a reinforced concrete wall. Phase II did not include additional missile impact tests; participating agencies were allowed to modify their FEA codes to better simulate the missile impact tests of Phase I and compile a report on the findings. Phase III included a trio of missile impact tests against a reinforced concrete structure.

5.1 Phase I Conclusions

5.1.1 LS-DYNA Riera Approach Conclusions

The major advantages versus consequences and drawbacks of the LS-DYNA Riera load function approach are discussed here.

The Riera load function approach is simple. It avoids contact models and alleviates constructing an additional finite element model of the missile. However, the crushing strength and mass distribution of the missile is challenging for the simplified Riera loading approach. Visual penetration of the target from a missile is not possible.

The Karagozian & Case concrete material model input requires only two input parameters which simplifies fitting the model to experimental data and material constants. However, the K&C model does not provide a detailed crack pattern visualization. The model does accrue damage, but the cracks that may “appear” as damaged elements begin to run together and from one solid block of damaged elements as the concrete approaches fully cracked.

A reinforcing steel bar material model based on yield strength without strain rate dependence is simple to implement and computes quickly, but dynamic increase factors are well known attributes of steel reinforcing bars used in concrete structures. A more accurate rebar material model would include strain rate dependence.

Using coincident nodes for the concrete material and the reinforcing steel permitted an orthogonal steel grid and concrete material geometric distribution. However, the steel reinforcing bar was not allowed to slip or exhibit pullout behavior. A more sophisticated contact model is needed to adequately address behavior between concrete and steel reinforcing bars. In addition, steel reinforcing bar density may not always be preserved.

The Meppen II/4 simulations used ¼ model symmetry to reduce computational resources, but ¼ model symmetry rendered the simulation unable to include angle of attack and/or angle of impact. Forced symmetry may not replicate the full response of test target behavior (e.g. radial crack pattern, measured load response at force transducers, etc.).

5.1.2 EMU Peridynamics Code Conslusions

The EMU peridynamics code did not exhibit any surprising sensitivities or pathological behavior, such as numerical instability. Although many calculations were required to reproduce the Meppen II/4 test results with reasonable fidelity, this repetition was mainly to correct input errors.

The authors consider the following to be the most likely sources of uncertainty in the predictive modeling of the Flexural Mode Test and the Punching Mode Test:

- Concrete penetration is widely thought to involve a strong size scale effect, in which small scale targets act differently (usually appearing stronger) than large targets. This effect, which is difficult to quantify and whose origin is controversial, was not considered in the EMU analysis.
- The unconfined compressive strength of concrete is an important but incomplete measure of the material response under large stress and high deformation.
- Rate effects in material response were not included explicitly in the EMU material model. These are generally measured with split Hopkinson bar tests, but these tests do not take into account confining pressure and do not relate directly to deformations with high rates of shear.

Strengths of the EMU peridynamics code for this application include the following:

- EMU utilizes a meshless Lagrangian formulation which avoids complex mesh generation requirements and problems with mesh tangling or distortion.
- It provides treatment of fracture without supplemental relations or special numerical techniques needed with finite elements.
- Its formulation inherently allows large strains and nonlinearity.
- The method lends itself to massively parallel computation.
- The contact algorithm is simple and fairly robust.
- EMU allows incorporation of any material model that can be used with finite elements (although this capability was not used in the results presented here).
- Because the formulation is nonlocal and explicitly involves a material length scale, it could potentially take into account the effect of aggregate size in localizations such as those predicted to occur on the surface of the plug in the Punching Mode Test.

Some of the EMU peridynamics code weaknesses include:

- EMU does not allow large variations in grid spacing within a model.
- It runs slower than traditional finite element method codes.
- It does not represent the bending rigidity of rebar.
- It does not treat friction at sliding interfaces.

5.2 Phase II Conclusions

In Phase II, the LS-DYNA calculations were updated to include explicit representations of the missiles rather than the Riera approach. The concrete material model parameters were updated as well. Finally, shell elements were used in Phase II for various pieces of the simulations.

5.2.1 Material Comparisons Conclusions

The LS-DYNA concrete material MAT-072R3 in conjunction with appropriate boundary conditions in a uniaxial concrete cylinder test simulation was able to reproduce the triaxial concrete test behavior shown in the experimental results. Three different target concrete models were used to predict the response of the Meppen II-4 impact scenario (*i.e.,* *MAT_072R3, *MAT_085, and *MAT_159). Three baseline calculations were completed to predict and compare with the Meppen impact test. All of the simulations assumed no strain-rate strength enhancement in the steel reinforcing bars. The Winfrith (*MAT_085) and the Continuous Surface Cap Model (CSCM or *MAT_159) concrete constitutive laws were employed without strain-rate effects. However, the Karagozian and Case concrete material model (*MAT_072R3) used a dynamic increase function to permit strain-rate effects based on the unconfined compressive cylindrical specimen strength. Both the *MAT_072R3 and *MAT_159 constitutive laws experience strain softening in compression, as opposed to the absence of any compressive strain softening witnessed in the *MAT_085 concrete model response.

5.2.2 Meppen Simulation Conclusions

The simulated target displacements show that the simulations employing the *MAT_072R3 target concrete constitutive law are closer than either the *MAT_085 or *MAT_159 (*i.e.,* Winfrith or CSCM) models at predicting target displacements. Due to a bug in the LS-DYNA version mpp971d Dev, visualization of crack patterns was not possible from the *MAT_085 simulations of the Meppen II-4 impact scenario.

5.2.3 VTT Flexural Conclusions

Comparing the displacement histories of the VTT flexural impact scenario target displacement, the *MAT_085 concrete model is consistently in less agreement with test data. Both *MAT_072R3 and *MAT_0159 LS-DYNA concrete constitutive material laws correctly capture the bending phase, which both tests reveal a peak displacement is reached at about 11.5 msec. This agreement may be related to adequate beam element discretization in the *CONSTRAINED_LAGRANGE_IN_SOLID type of steel reinforcement bar (*i.e.,* beam elements) coupling to the concrete elements (8-noded hexahedral elements), and improved concrete material model shear failure surface constructions.

Comparison of the test data and numerically computed strains at steel reinforcing bar strain gage location #15 of shows some agreement on the period of peak strain from the *MAT_072R3 concrete constitutive law, with approximately 50% error at the peak strain value. Several factors may account for this discrepancy between test data and numerically computed results: insufficient coupling of reinforcing bar (beam elements) with the concrete (solid 8-noded hexahedral elements), subsequent feature/outcome of the *CONSTRAINED_LAGRANGE_IN_SOLID methodology, discretization of the beam element grid representing the steel reinforcing bar, and/or material property characterization due to unknown strain rate behavior in the A500HW 6 millimeter outside diameter type reinforcing steel bar.

5.2.4 VTT Punching Conclusions

Three different target concrete models were used to predict the response of the VTT punching mode impact scenario (*i.e.,* *MAT_072R3, *MAT_085, and *MAT_159). Unlike to the Meppen II-4 impact scenario simulations, the VTT punching mode impact scenario simulations used no strain-rate strength enhancement in the steel reinforcement bars with the *MAT_024 only when using the *MAT_072R3 target concrete model. Both the Winfrith (*MAT_085) and the Continuous Surface Cap Model (CSCM or *MAT_159) concrete constitutive laws were employed without strain-rate effects to treat the target concrete component. However, the Karagozian and Case material model (*MAT_072R3) included a dynamic increase function to permit strain-rate effects based on the unconfined compressive cylindrical specimen strength.

The primary distinction of this scenario from the two previous simulations is the impact response resulting in penetration of the target comprised of both concrete and steel. Two of the target concrete constitutive laws (*MAT_072R3 and *MAT_085) do not permit implicit erosion control. The *MAT_159 material model has several means of controlling erosion. Another unique aspect of the VTT punching mode impact scenario is the hard type of missile - a relatively thick cylindrical vessel filled with concrete. In order to accurately capture the energy transfer of the composite missile (steel and concrete) perfect bonding between the steel and concrete components was not assumed.

Comparing the test and numerical simulations of the deformed missile shapes after impact reveals the target concrete *MAT_085 constitutive law calculation precludes any missile node bulging. This behavior is clearly in disagreement with both observed experiments and with the other two simulations (*i.e.,* those using the target concrete models: *MAT_072R3 and *MAT_159).

Comparing the displacement histories of VTT punching impact scenario target displacement sensor locations, the sensitivity calculations P1.1, P1.2, and P1.3 are the closest to the test data, but are over-predicting target displacement. However, the calculations P1, P1.4, P1.5, and P1.6 under-predict target displacement. This bounding numerical distribution is suggestive that further sensitivity studies may produce better displacement predictions.

5.3 Phase III Conclusions

The portions pertaining to Phase III describe analyses and numerical results obtained from simulations of a hollow steel missile impacting a concrete target reinforced with steel bars. Phase III was completed using the finite element analysis code SIERRA. Various material models were tested in the simulation including pure elastic, Holmquist-Johnson-Cook concrete model (Holmquist, Johnson and Cook 1993), and Karagozian & Case concrete model (Malvar, et al. 1997).

5.3.1 Material Comparisons Conclusions

Three different concrete material model inputs were compared in Phase III: 1) Karagozian & Case (K&C); 2) Holmquist, Johnson, and Cook using empirical input parameters (Empirical HJC); and 3) Holmquist, Johnson, and Cook using input parameters taken directly from the original model documentation (Original HJC). The most accurate concrete model in terms of displacements and strains on the impact face of the concrete is the K&C model. The Original HJC model inputs did not predict enough displacements or strains in the structure whereas the Empirical HJC model inputs predicted far too much damage, displacements, and strains.

5.3.2 Post-Processing Technique Conclusions

The teams at the 2017 benchmark meeting agreed that ~250 Hz was the proper frequency to filter out numerical noise for structural elements. However, analysis of the results from the simulations indicated that ~1000 Hz should be the cutoff frequency for the missile, force summation immediately in the vicinity of missile impact, and accelerations. The raw acceleration data of the end of the missile oscillates between 20,000 m/s^2 and -5000 m/s^2; this is most likely due to numerical noise in the simulation. One possible source of noise could be individual elements folding as the nose of the missile contracts into its failed ‘accordion’ structure. Accelerations inside the mockup structure also are susceptible to noise. Filtering the data below 250 Hz results in a smooth curve, but the curve does not accurately represent the raw data. For example, the sub-250 Hz curve of the acceleration in the end of the missile has an initial acceleration of ~3,700 m/s^2 while the missile had not yet impacted the concrete. Therefore, data analysis of the acceleration of the rear missile indicates that the appropriate frequency to filter data for the missile, force summation immediately in the vicinity of missile impact, and accelerations is 1000 Hz. Structural elements such as reaction forces of the mockup supports or displacements of various positions are filtered under 250 Hz.

5.3.3 Impact Test Conclusions

In both simulations, the simulated missile crushed similarly to the experimental missile. The simulated missiles had an accordion-like structure in the impact regime, as did the experimental missiles. Both the 90 m/s missile and the 170 m/s missile had similar lengths of crushed and non-crushed material. This indicates that the stiffnesses of the simulated mockup and missile materials were comparable to the stiffnesses of the experimental materials.

The addition of concrete pedestals below the supports allowed for cleaner readings of reaction forces compared to efforts in the first benchmark wherein the forces were summed through the support base plates. The simulation pedestal reaction forces had a higher frequency than those of the experiment. The higher frequency in the simulation is most likely due to 1) stiffer simulated connections between the mockup and its foundation and 2) stiffer simulated connections between all mockup pieces. The rebar inside the simulated mockup was perfectly bonded to the concrete, and all supporting plates were perfectly bonded to their connecting pieces. In the experiment, all of these connections could slip if damaged.

Accelerometer data indicates that 1000 Hz is an adequate cutoff frequency for analyzing structural accelerations. The magnitudes of accelerations in the simulation and the experiment were similar, though the simulation did not dampen the accelerations with time whereas the experimental accelerations lessened over time.

To verify that the simulation displacements, velocities, and accelerations were internally consistent, 1/10 scaled A3H accelerometer data was compared with the displacements of D3. A3H and D3 were in the same location. The two curves share the same frequency but are offset by ½ period, suggesting excellent agreement between the simulation output displacements, velocities, and accelerations.

1.1.1.1 90 m/s Impact Specific Conclusions

The missile did not penetrate the concrete in the 90 m/s experiment or the simulation. Damage accrued on the front wall on both faces where the missile impacted. Damage on the front face under the missile impact was shallow and limited to the first layer of elements. Damage on the rear face of the front wall likely accrued due to tensile stresses in the concrete and percolated in places all the way through the wall to meet the damage on the front face.

The displacements recorded by the displacement transducers in the experiment and the simulation were of similar magnitude for all locations, though the mockup had a higher displacement frequency for previously postulated reasons. Displacement transducer D01 in the front center of the impact face indicates that permanent deformation of 1-2 mm occurred on the front face of the concrete. Some displacements did not agree, such as displacement transducer D8H. The simulation predicted no permanent deformation in D8H while the experiment experienced permanent deformation of ~0.10 mm. The difference in this particular gage is likely due to the perfect bond between materials and components in the simulation (resulting in no permanent displacement) whereas the mockup could be permanently displaced in the experiment.

1.1.1.2 170 m/s Impact Specific Conclusions

The missile did not penetrate the concrete in the experiment or the simulation, but significant cracking occurred on both the front and back of the impact face. Damage accrued on the front wall on both faces where the missile impacted. Damage on the rear face of the front wall likely accrued due to tensile stresses in the concrete and percolated in places all the way through the wall to meet the damage on the front face. The damage on the front face of the impact wall was shallower than that of the back face. Cracks spread in an ‘X’ pattern on the front wall, both on the front and rear faces, similar to but more extreme than the 90 m/s impact. Horizontal lines of damage accrued in the mockup that may or may not be damage from the impact. Simulations dictated that the K&C concrete model required heavy hourglass stiffening to prevent instability in high gradients, e.g. during impact. The horizontal lines of damage may either be damage from the impact or element instability inherent to the K&C model. In addition, the K&C model may have suffered severe instability leading to excess accumulated damage immediately in the vicinity of the missile impact.

The front pedestal vertical reaction forces in the experiment had a similar magnitude to those in the simulation, but the rear pedestal vertical reaction forces in the experiment were lower than those in the simulation. The reasons for the great disparity between the experimental and simulation results for the rear reactions forces are assumed to be that the strain gages on the pedestal may have been damaged during the impact. The simulation pedestal reaction forces had a higher frequency than those of the experiment. The higher frequency in the simulation is most likely due to 1) stiffer simulated connections between the mockup and its foundation and 2) stiffer simulated connections between all mockup pieces. The rebar inside the simulated mockup was perfectly bonded to the concrete, and all supporting plates were perfectly bonded to their connecting pieces. In the experiment, all of these connections could slip if damaged.

The displacements recorded by the displacement transducers in the experiment were almost entirely larger than those in the simulations. Displacement transducer D01 in the front face of the mockup indicates that permanent deformation occurred on the front face of the concrete; the deformation was severe enough to cause a ‘dent’ in the front of the concrete impact wall. The simulation predicted final permanent displacement of ~5 mm while the experiment resulted in ~7 mm. Strain gages G0H and G0V indicate that the rebar in the impact wall permanently deformed; the simulation predicted roughly 1/3 of the total strain that was found in the experiment. The rebar at the base of the cantilever permanently deformed in the simulation but not in the 170 m/s experiment. However, the rebar at the base of the cantilever was already permanently deformed in the 90 m/s experiment, so the results from the 170 m/s experiment could indicate that these particular rebar did not deform more than what was already done in the 90 m/s experiment.

6 REFERENCES

Alexander, J. M. 1960. "An Approximate Anaysis of the Collapse of Thin Cylindrical Shells Under Axial Loading." *Quart. J. Mech. Appl. Math* 13: 10-15.

Aljawi, A. A. N. 2002. "Numerical Simulation of Axial Crushing of Circular Tubes." *JKAU: Eng. Science* 14 (2): 101-115.

ASTM. 2017. "Standard Test Method for Splitting Tensile Strength of Cylindrical Concrete Specimens." *ASTM C496.* ASTM International.

Attaway, S.W., R.V. Matalucci, S.W. Key, K.B. Morrill, L.J. Malvar, and J.E. Crawford. 2000. *Enhancements to PRONTO3D to Predict Blast Structural Response.* SAND200-1017, Albuquerque: Sandia National Laboratories, Appendix D (Section D-2, Section D-4).

Beltrán, F., D. Combescuscure, and F. Rueda. 2010. "Numerical Simulation of Meppen Test II-4, ISRN-VTT Flexural Mode Test and IRSN-CNSC-VTT Punching Mode Test." *IRIS 2010 Benchmark on Improving Robustness Assessment Methodologies for Structures Impacted By Missile.* Paris: ISRN-VTT. 6.

Bignell, John, Jonathan Rath, Ali Syed, and Richard Rivera-Lugo. 2013. "Numerical Simulation of a Hard and Soft Missile Impact into a Steel Reinforced Concrete Target: Overview of Work Performed by SNL for the US NRC in Support of the IRIS 2012 Exercise." *Structural Mechanics in Reactor Technology Conference (SMiRT-22).* San Francisco.

Brandes, Klaus. 1988. "Assessment of the Response of Reinforced Concrete Structural Members to Aircraft Crash Impact Loading." *Nuclear Engineering and Design* 110: 177-183.

CSNI. 2012. "IRIS 2012 Benchmark Numerical Simulation Guidelines and Deliverables." Comimittee on the Safety of Nuclear Installations (CSNI) Acitivity Probosal Sheet for IRIS 2012, February.

Cubit. 2011. *A Finite Element Method Meshing Tool.* Version 13.1 Build 47162. Sandia National Laboratories. Albuquerque, NM.

Cubit. 2016. *A Finite Element Method Meshing Tool.* Albuquerque, NM.

Day, J. 2011. "mat84_winfrith." Livemore Software Technology Corporation. December 07. Accessed December 07, 2011. http://ftp.lsct.com/anonymous/outgoing/jday/concrete/mat84_winfrith.

Holmquist, T. J., G. R. Johnson, and W. H. Cook. 1993. "A Computational Constitutive Model for Concrete Subjected to Large Strains, High Strain Rates, and High Pressures." *14th International Symposium on Ballistics.* Quebec, Canada. 26-29.

J. Skrzypek, A. Ganczarski. 2015. *Mechanics of Anisotropic Materials.* Springer International Publishing.

Jones, C., J. Hogancamp, G. Mata, and P. Coffin. 2017. *IRIS III Benchmark Team Report, SAND2017-0031R.* Albuquerque: Sandia National Laboratories.

LSTC. 2011. "LS-DYNA." Livermore, Califorinia.

LSTC. 2010. *LS-DYNA Keyword User's Manual Volume 1 and Volume 2.* Version 971 / Rev. 5 (Beta). Livermore, CA: Livermore Software Technology Corporation, May.

LSTC-contact. 2011. *contact-modeling-in-ls-dyna.* Livermore Software Technology Corporation. Accessed November 2011. http://www.dynasupport.com/tutorial/contact-modeling-in-ls-dyna.

Magallanes, J.M., Y. Wu, L.J. Malvar, and J.E Crawford. 2010. "Recent Improvements to Release III of the K & C Concrete Model." *11th International LS-DYNA Users Conference.* Detroit: Livermore Software Technology Corporation. 3-40 (Table 1).

Malvar, L. Javier, John E. Crawford, James W. Wesevich, and Don Simons. 1997. "A Plasticity Concrete Material Model for DYNA3D." *International Jounral of Impact Engineering* 847-873.

Meppen. 2010. *Improving Robustness Assessment Methodologies for Stuctures Impacted by Missiles.* German Military Test, Data Synthesis of Meppen Test II-4, Revision B (20 December 1977).

Nordbert, Hans. 2004. *Note on the Sensitivity of Stainless Steels to Strain Rate.* Research Report No. 04.0-1, Sheffield Hallam University, AvestaPolarit Research Foundation.

Nuclear_Energy_Agency. 2010. *IRIS_2010 Improving Robustness Assessment Methodologies for Impacted Structures.* Accessed December 14, 2011. http://www.oecd-nea.org/download/iagectg.

Peixinho, N., and A. Pinho. 2007. "Study of Viscoplasiticy Models for the Impact Behavior of High-Strength Steels." *American Society of Mechanical Engineers*, April: 120.

Rath, J., and J. Bignell. 2012. *IRIS 2012 Numerical Simulation Report, SAND2012-10505P.* Albuquerque: Sandia National Laboratories.

Rath, J., S. Silling, and J. Petti. 2010. *CSNI/NEA Phase I Benchmark Simulations using LS-DYNA and EMU: Steel projectiles impacting a reinforced concrete targets, SAND2010-8899.* Albuquerque: Sandia National Laboratories.

Schwer, Len. 2010. *Non-Linear Modellijng and Analysis of Structural Impact: Meppen and VTT Test Simulations, Brief Summary of Modelling & Results.* Windsor, CA: Schwer Engineering & Consultating Services.

Schwer, Leonard E., Samuel W. Key, Thomas A. Pučik, and Lee P. Bindeman. 2005. "An Assessment of the LS-DYNA Hourglass Formulations via the 3D Patch Test." *5th European LS-DYNA Users Conference.* Schwer Engineering & Consulting Services.

Sidney Mindess, J. Francis Young, David Darwin. 2003. *Concrete, 2nd Edition.* Upper Saddle River, NJ: Prentice Hall.

SIERRA. 2016. *A Finite Element Analysis Software.* Albuquerque, NM.

Tzikang, Chen. 2000. *Determining a Prony Series for a Viscoelastic Material From Time Varying Strain Data.* Langley, VA: NASA Langley Research Center & Army Research Lab.

Vepsä, Ari. 2010a. *Experimental Tests for Bending and Punching Behaviour of Reinforced Concrete Walls Under Impact Loading.* Confidential, Technical Research Centre of Finland (VTT); VTT-R-05587-10.

Vespä, Ari. 2010b. *Punching Behaviour Test of One 250 mm Thick Reinforced Concrete Wall Under Hard Impact Loading: Revision A.* Confidential, Technical Research Centre of Finland (VTT); VTT-R-05588-10.

VTT. 2012. *VTT Technical Research Centre of Finland in Espoo.* August 27. Accessed August 27, 2012. http://www.vtt.fi/index.jsp.

2018. "Wolfram Mathematica 11.2." Wolfram Research.

NRC FORM 335
(12-2010)
NRCMD 3.7

U.S. NUCLEAR REGULATORY COMMISSION

BIBLIOGRAPHIC DATA SHEET

(See instructions on the reverse)

1. REPORT NUMBER
(Assigned by NRC, Add Vol., Supp., Rev., and Addendum Numbers, if any.)

NUREG-XXXX

2. TITLE AND SUBTITLE

Draft Report for Program IRIS: Improving the Robustness of the

3. DATE REPORT PUBLISHED

MONTH	YEAR
Month	**Year**

4. FIN OR GRANT NUMBER

5. AUTHOR(S)

List names from Cover of NUREG Report of individuals who contributed to this publication

6. TYPE OF REPORT

Technical

7. PERIOD COVERED (Inclusive Dates)

8. PERFORMING ORGANIZATION - NAME AND ADDRESS (If NRC, provide Division, Office or Region, U. S. Nuclear Regulatory Commission, and mailing address; if contractor, provide name and mailing address.)

Performing Organization’s Name and Address

9. SPONSORING ORGANIZATION - NAME AND ADDRESS (If NRC, type "Same as above", if contractor, provide NRC Division, Office or Region, U. S. Nuclear Regulatory Commission, and mailing address.)

Sponsoring Organization’s Name and Address

10. SUPPLEMENTARY NOTES

11. ABSTRACT (200 words or less)

Copy and paste Abstract here (200 words or less)

12. KEY WORDS/DESCRIPTORS (List words or phrases that will assist researchers in locating the report.)

List of keywords or phrases that will assist researchers in locating this NUREG.

13. AVAILABILITY STATEMENT

unlimited

14. SECURITY CLASSIFICATION

(This Page)

unclassified

(This Report)

unclassified

15. NUMBER OF PAGES

16. PRICE

UNITED STATES
NUCLEAR REGULATORY COMMSSION
WASHINGTON, DC 20555-0001

OFFICIAL BUSINESS

@NRCgov

NUREG-XXXX

Draft Report for Program IRIS: Improving the Robustness of the Assessment of Structures Impacted by a Large Missile

Month Year